A TEM Investigation of Controlled Magnetic Behaviour in Thin Ferromagnetic Films

Craig Brownlie B. Sc.

Submitted for the degree of Doctor of Philosophy at the
Department of Physics and Astronomy, University of Glasgow
August 2007

This thesis is dedicated to my late grandfather Andrew S. Nelson

Acknowledgements

There are many people I would like to thank for their help, support and friendship over the course of my PhD, and I apologise in advance if I miss anyone out.

First and foremost I would like to acknowledge my supervisors Dr Stephen McVitie and Prof John Chapman for their advice and guidance over the last four years. I really couldn't have asked for better supervision and I'm very grateful. For continually repairing the CM20 after my heavy handed use and for maintaining nearly every piece of equipment in the group (with a smile I may add), I would like to thank Dr Sam McFadzean. I am also very appreciative of Colin How, Billy Smith and Brian Miller, who along with Sam, provided technical assistance, IT support and some much needed banter. Thanks also to Brian for the fabrication of my cross-sectional samples.

Also in connection with my research, I wish to acknowledge Dr Stephen Thoms and the cleanroom technicians, who, whilst running a superb laboratory, also provided advice on nanofabrication. In addition, I thank Dr Frederik Vanhelmont and Dr Hans Boeve at Philips Research and Dr Susana Cardoso at INESC-MN who supplied me with excellent multilayer samples, Prof Thomas Schrefl and Simon Bance for their collaborative work and hospitality when I visited The University of Sheffield, and Dr Bob McMichael at NIST for his helpful input to my study of domain wall trap structures. I'd also like to acknowledge Dr Mike Donahue (also at NIST) for help and information on micromagnetic simulations, Dr Ian MacLaren for acquiring the BF/DF cross-sectional images and Robin O'Neill for his continual assistance in microscopy, fabrication, and computer simulations. Special thanks go to Lucy Murray for the organisation of numerous academic trips.

As I suffer yet another hangover, I'd like to say cheers to my uni mates Paul 'Twin' and Jonny 'J-Rod' Grant, Fiona 'Fi-Box' McEwan, Paul Robb, Paolo Longo, James Wilson and Mike Finnie for their friendship and many a great night out on the town. I also wish to express gratitude to my Room 408 office mates David Eustace, Frances Docherty, Pedro Diaz, Mhairi Crawford and Xiang Kong for their support, advice and quality chat. Other friends in the SSP group I'd like to big up (who haven't already been mentioned) are Damien McGrouther, Nils Wiese, Beverley Craig, Jamie Scott, Aurélie Gentils, David Hamilton, Susan Turnbull, Tom McMullen and Donald MacLaren. I've thoroughly enjoyed your company over the years, especially during the group/departmental events, summer school, GRADschool, conference and pub crawls. I also wish to thank non-SSP group members Keith Mathieson, Liam Cunningham, Alan Moodie and Morgan Murray, who have been equally as welcoming.

I know this going on a bit, but bear with me. Out with the university, I must say a big thank you to a wonderful group of friends who have managed to keep me laughing, even during the last year of mundane thesis writing. Their banter and antics really are hilarious and I wouldn't have missed the parties, nights out or holidays for anything. So to Martin 'McStagger' McGowan, Andres 'Two-tonne' Hernandez, Craig 'Bart' Bartholomew, Iain 'Tam' Paxton, Steven 'Pierre' Ross, Andrew 'Sely' Selkirk, Craig 'Mungheid' McKay, Stewart 'P' Peutherer, David 'Hallbag' Hall, James 'Scratchy' Archibald, Ewan 'Eggy' Towie, Fraser 'Froggy' Donaldson, Kenny 'Maverick' Johnstone and Euan 'Tufty' Bell, cheers lads.

Finally, I'd like to say a huge thank you to my mum and dad who have supported me emotionally and financially over the course of my PhD. I now promise to stop being such a parasite and get a proper job as soon as possible. I'd also just like to acknowledge the rest of my family whilst I'm at it, including my younger brother David, his girlfriend Myra and their beautiful baby daughter Natalie, my Auntie Margaret, Auntie Anne, Uncle Alan and my Gran. Thanks.

Abstract

Understanding the magnetic behaviour of thin film elements is of major importance for the magnetic sensor and storage industries, but also for fundamental micromagnetics. To store digital information, each memory element must support two distinct remanent magnetisation configurations that can be switched between using an applied field. In magnetoresistive random access memory (MRAM), a low switching field and reproducible reversal behaviour are desirable properties. The low field keeps the power consumption to a minimum and the reproducility enables efficient writing and read back of data. However, simple geometric structures are able to support a variety of metastable remanent configurations which can be problematic for device applications. For example, with rectangular elements, the switching fields are history dependent, and there is the possibility of flux-closure formation on repeated switching. This means different field strengths may be required to reverse the magnetisation of the same bit (binary digit) during different field cycles, and the information stored in a cell could be accidentally lost. In addition, the miniaturisation of these elements faces the problem that the coercivity is inversely proportional to element width for a given thickness; a factor which limits their use in high density arrays. The optimum geometry for supporting the stored information is therefore an important issue. In this thesis, different element shapes designed to tackle these problems have been investigated using transmission electron microscopy (TEM) backed by micromagnetic simulations. It has been found that variations in element geometry and symmetry can lead to a greater control of the states that can be formed.

Alongside this work on patterned elements, continuous film multilayer samples in the form of magnetic tunnel junctions (MTJs) have also been studied. These multilayer structures serve as storage cells in MRAM devices so their successful operation is of the utmost importance to the development of this technology. At the most basic level, MTJs comprise two ferromagnetic layers separated by a layer of electrical insulator. Whilst one magnetic layer is fixed (pinned layer), the other is free to switch direction when an external field is applied (free layer). Ideally the free layer hysteresis loop would be centred at zero field, but because of magnetostatic interactions caused by layer roughness, the ferromagnets couple to one another and the hysteresis loop is offset. This shift means that the fields required to switch the cell in opposite directions are different. In collaboration with Philips Research in Eindhoven, the magnetic and physical structure of new MTJ stacks incorporating an artifical antiferromagnet (AAF) in the free layer were studied using TEM. An AAF consists of two ferromagnetic layers coupled anti-parallel through a thin layer of non-magnetic metal, typically Ru. These samples were found to reduce the offset field by up to 36% when compared to the basic MTJ stack. Whilst this research is valuable to the magnetic storage industry, the information it provides on these complicated magnetic systems is equally beneficial for solid state physics.

Further information

This research was performed at the Kelvin Nanocharacterisation (www.knc.gla.ac.uk) and James Watt Nanofabrication (www.jwnc.gla.ac.uk) Centres of Glasgow University, and was funded by the UK Engineering and Physical Sciences Research Council (www.epsrc.ac.uk).

EPSRC Engineering and Physical Sciences
Research Council

Declaration

This thesis is a record of the work carried out by myself in the Department of Physics and Astronomy at the University of Glasgow during the period 2003–2007. The work described herein is my own, apart from the deposition of magnetic tunnel junction films which was performed by Dr Frederik Vanhelmont at Philips Research, Eindhoven, The Netherlands and Dr Susana Cardoso at INESC-MN, Lisbon, Portugal. In addition, the fabrication and imaging of TEM cross-sections was carried out by Brian Miller and Dr Ian MacLaren at the University of Glasgow, respectively. Some of the work reported in this thesis can be found in the following papers:

1. **Lorentz microscopy studies of domain wall trap structures**, C. Brownlie, S. McVitie, J. N. Chapman and C. D. W. Wilkinson, J. Appl. Phys. **100**, 033902 (2006).

2. **Transitions between vortex and transverse walls in NiFe nano-structures**, S. Bance, T. Schrefl, G. Hrkac, D. Suess, C. Brownlie, S. McVitie, J. N. Chapman and D. A. Allwood, IEEE Trans. Magn. **42**, 2966 (2006).

The rest remains to be published. This thesis has not previously been submitted for a higher degree.

Contents

Chapter 1

Magnetism and magnetic materials

1.1 Introduction

Magnetic properties of materials originate from the magnetic moment of the constituent atoms/ions which are produced by the spin and orbital angular momenta of their electrons. As magnetic fields can be generated by the movement of charge, the perpetual motion of the bound electrons effectively acts as a current loop with an associated magnetic moment. In most materials, however, the electrons are paired in their orbitals with opposite spin and their magnetic effects cancel. In this situation the material is classed as diamagnetic and has a negative susceptibility. As the atomic orbitals are filled according to the Pauli, Hund and Aufbau principles, however, some materials have unpaired electrons and are termed paramagnetic. The magnetic moments of these electrons do not cancel and the material has a positive susceptibility. In lanthanide elements, the ions have an incomplete 4f shell which is found deep within the atom. As a result, the unpaired electrons are well-screened from the neighbouring ions and the magnetic moment can be related to both the spin and orbital angular momenta. In the transition metal elements, the unpaired electrons are found in the incomplete 3d shell on the outside of the ion. Here, the electrons are able to interact with the electric field of the neighbouring ions and the orbital moment is quenched. In effect, only the electron spin contributes to the magnetic moment.

In true paramagnetic materials the magnetic moments associated with the unpaired electron spins are randomly oriented throughout the material (Fig. 1.1a), whilst in others, spontaneous interactions force the moments (spins) to be aligned in particular orientations.

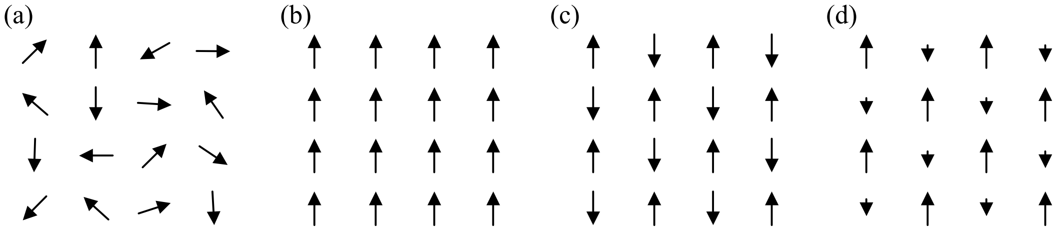

Fig. 1.1: The magnetic ordering in (a) paramagnetic, (b) ferromagnetic, (c) antiferromagnetic and (d) ferrimagnetic materials.

In ferromagnetic materials the neighbouring spins are aligned parallel to one another below the Curie temperature, T_C (Fig. 1.1b), giving a measurable magnetic moment overall, whilst in antiferromagnetic materials the adjacent spins are arranged anti-parallel below the Néel temperature, T_N (Fig. 1.1c). At zero field, this latter configuration exhibits no overall moment due to cancellation from the two magnetic sub-lattices. Above these critical temperatures thermal agitation destroys the alignment, causing transition to the paramagnetic state. In another class of material, ferrimagnets, the electron spins are aligned anti-parallel but with an unequal moment in the two sub-lattices (Fig. 1.1d). As a result, ferrimagnetic materials exhibit a net magnetic moment albeit weaker than most ferromagnets. This type of magnetic order is not seen in any pure element, but instead is found in compounds such as mixed oxides, known as ferrites. A colour-coded periodic table highlighting the magnetic state of each element at room temperature can be seen in Fig. 1.2.

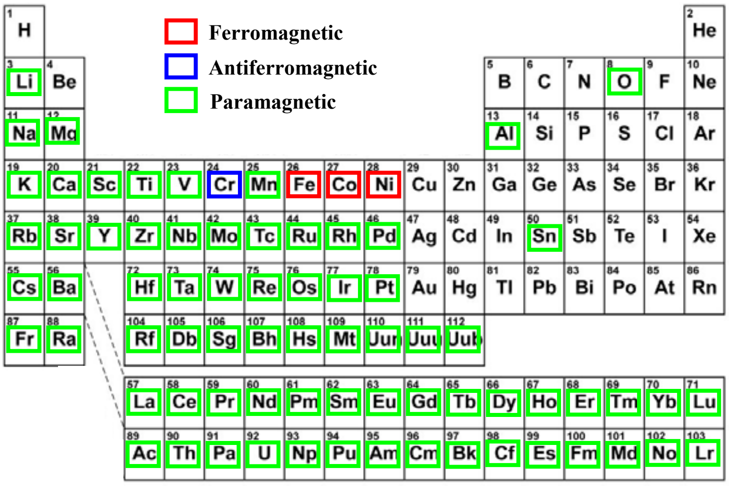

Fig. 1.2: Periodic table of elements revealing the magnetic order of each element at room temperature. **N.B.** all materials exhibit diamagnetism to some extent also.

1.2 Ferromagnetism

Of the various classes of magnetic material, ferromagnets are by far the most useful for applications due to the cooperative effect of their atomic moments. As a result, these materials are most commonly studied and will be discussed frequently throughout this thesis. Ferromagnetic behaviour is found in the transition metal and rare earth elements but also exists in the alloys, oxides and complexes of these elements.

1.2.1 Spontaneous alignment

Unlike paramagnets in which the spins align parallel only in the presence of an applied field, ferromagnetic materials exhibit a spontaneous alignment below the Curie temperature. For this to happen, there has to be a strong interaction present between the atoms/ions. In 1907 Weiss represented the interaction by an internal molecular field,

$$B_e = \lambda M \tag{1.1}$$

where λ is the molecular field constant and M is the magnetisation of the material [1]. Each atomic moment is assumed to be acted on by this field, which is proportional to the magnetisation of its environment. If a parallel alignment of moments should appear locally at any place in the lattice, the molecular field will be produced which in turn will promote further alignment of the spins. The problem with this theory was that it did not explain the origin of the field. Also, for typical ferromagnetic materials, the magnitude is calculated to be on the order of $\sim 10^7$ Oe, suggesting that an externally applied field would be insignificant in comparison and would not affect the system at all. This is clearly not the case. In 1928, Heisenberg proposed a quantum mechanical theory to explain the spontaneous alignment [2]. In this theory the interaction can be attributed to an exchange force between each atom and its nearest neighbours, caused by the overlap of electron wavefunctions. Pauli's exclusion principle for fermions [3] states that the total wavefunction for a quantum mechanical system comprising electrons must be antisymmetric . Therefore two electrons bound within the same orbital (symmetric space part) must have opposite spin (antisymmetric spin part), whilst those in different orbitals (antisymmetric space part) must have parallel spin (symmetric spin part). Since similarly charged particles repel one another, it follows that the more favourable configuration occurs with the electrons occupying different orbitals and having their spins aligned parallel to one another. In effect, the interaction responsible for ferromagnetic alignment is not magnetic as Weiss proposed, but is actually electrostatic in nature. This interaction can be represented by the Heisenberg Hamiltonian energy,

$$H_H = -2J\mathbf{s_i} \cdot \mathbf{s_j} \tag{1.2}$$

where H_H is the exchange energy of two interacting electron spins, $\mathbf{s_i}$ and $\mathbf{s_j}$, and J is the exchange integral which is material dependent. This model can also be used to describe antiferromagnetic coupling. Whilst for ferromagnets the exchange integral is positive, resulting in an energy minimum for parallel spins, antiferromagnets have a negative exchange integral, with the lowest energy when the spins are aligned anti-parallel.

1.2.2 Field and temperature dependence of M and χ

The magnetisation of a ferromagnetic material is dependent on both applied magnetic field and temperature, as shown in Fig. 1.3a and Fig. 1.3b respectively. Below the Curie temperature spontaneous alignment occurs, but overall the material exhibits no (or very little) magnetisation. This is because (as will be discussed later) the material splits up into regions of parallel alignment called domains. At zero applied field these domains are oriented randomly and the magnetic effects cancel, but as the field is increased, the domains align with one another and the magnetisation increases. The magnetisation at zero field is referred to as the remanent magnetisation and when all domains are parallel the magnetisation is a maximum and is called the saturation magnetisation. As the temperature approaches T_c, the saturation magnetisation decreases to zero as thermal agitation destroys the alignment.

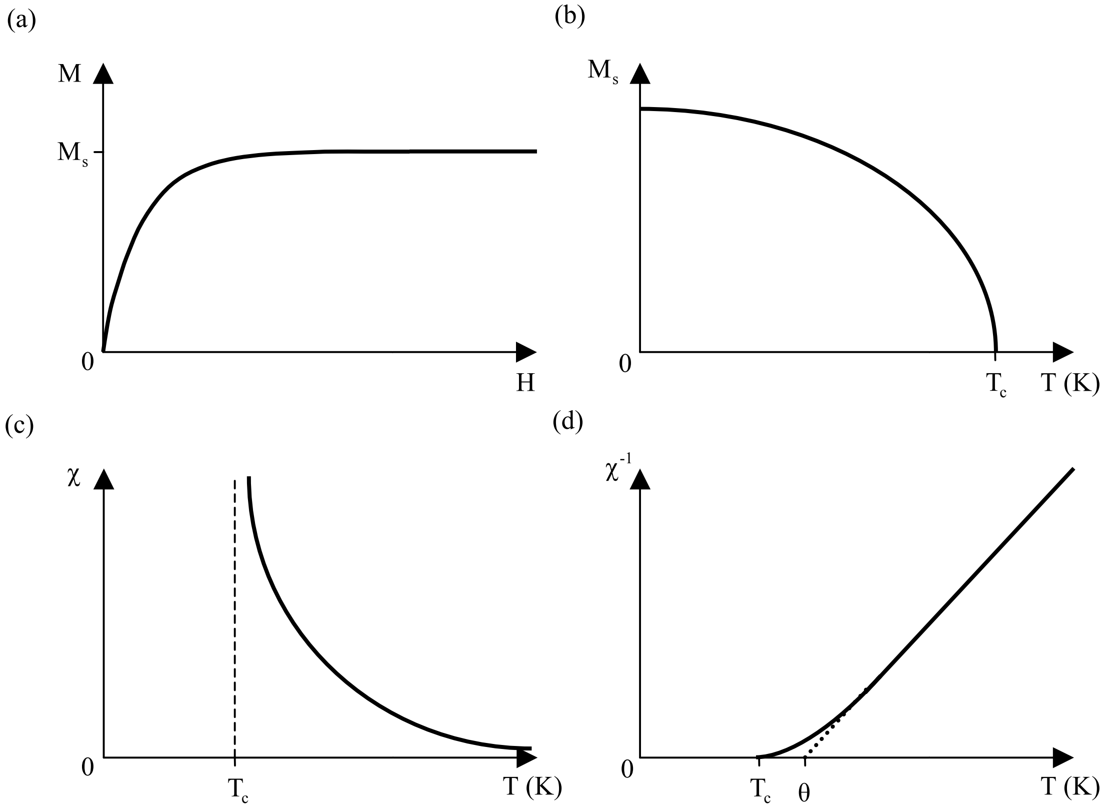

Fig. 1.3: Graphs showing (a) the variation in magnetisation with field and (b) saturation magnetisation, (c) magnetic susceptibility and (d) reciprocal susceptibility with temperature for a ferromagnetic material.

Magnetic materials are often distinguished by their (temperature dependent) magnetic susceptibility (Fig. 1.3c). The susceptibility of a material, χ, indicates how dramatically it responds to an applied field, and is defined as the ratio of the magnetisation to field,

$$\chi = \frac{M}{H} \tag{1.3}$$

At high temperatures χ is small and positive, but as the temperature is reduced it increases exponentially to infinity at T_c. This shows the ease of increasing the magnetisation by applying a field when the material is undergoing a transition between magnetic order and disorder. This temperature dependence can be described by the Curie-Weiss law,

$$\chi = \frac{C}{T - \theta} \tag{1.4}$$

where C and θ are the Curie and Weiss constants respectively. Often the straight line plot of reciprocal susceptibility with temperature is used to describe the ferromagnetic response of a material (Fig. 1.3d). The gradient of this graph is equal to C^{-1}. Deviations can be seen between experiment and theory as χ tends to infinity. Whilst the Curie-Weiss law predicts $\chi^{-1} \rightarrow 0$ at $T = \theta$, experiments show the Curie temperature to be slightly lower. This is because the theory is based on a mean-field approximation to simplify the interactions of a many-body system.

1.2.3 Gauss' law for magnetism

It is important to note that unlike electric fields which start and end on charges, magnetic B-fields are continuous and have no sources or sinks. In a closed surface therefore, every magnetic field line entering the surface, leaves the surface and this includes both stray field and magnetisation components of ferromagnetic materials. Gauss' law for magnetism (one of Maxwell's equations) expresses this as,

$$\oint_S \mathbf{B} \cdot d\mathbf{A} = 0 \tag{1.5}$$

where **B** is the magnetic induction and **A** is the outward pointing area vector normal to the surface. Physically, this equation means that magnetic field lines must be closed loops and is a mathematical formulation of the statement that there are no magnetic monopoles.

1.3 Magnetic energy terms

Although ferromagnetic materials have a net magnetic moment on the atomic scale, volumes of these materials often possess little or no net magnetisation. The magnetisation of a material is the total magnetic moment per unit volume. The reason for this, as mentioned previously, is down to the formation of magnetic domains. The exchange interaction cannot explain this behaviour and there are other energy contributions that must be taken into account.

1.3.1 Exchange energy

The Heisenberg model discussed above has to be summed over all electrons which contribute to the magnetisation. However, only the overlap between adjacent atoms gives an appreciable value for J and so only nearest neighbour interactions are considered, which simplifies the calculation. The total exchange energy for the material assuming identical atoms is,

$$\mathrm{E}_{\mathrm{ex}} = -2\mathrm{JS}^2 \sum_{\mathrm{ij}} \cos\varphi_{\mathrm{ij}} \qquad (1.6)$$

where S is the magnitude of the spin vector and φ_{ij} is the angle between the spins i and j. Taking into account the three dimensional nature of crystals and integrating over a finite volume of material, but considering only cubic systems, this expression becomes,

$$\mathrm{E}_{\mathrm{ex}} = \mathrm{A}\int_{\mathrm{V}} [(\nabla\alpha)^2 + (\nabla\beta)^2 + (\nabla\gamma)^2]\mathrm{dV} \qquad (1.7)$$

where α, β, γ are the direction cosines with respect to the crystal axes and A is the exchange stiffness constant for the material given by,

$$\mathrm{A} = \frac{\mathrm{kJS}^2}{\mathrm{a}} \qquad (1.8)$$

with k a structure-dependent constant (1 for simple cubic, 2 for body-centred cubic and 4 for face-centred cubic materials) and a the lattice parameter.

1.3.2 Anisotropy energy

Anisotropy relates to the fact that the properties of a magnetic material depend on the directions in which they are measured. This is because the direction of magnetisation is influenced by the structure of the material, which forces the spins to lie in certain directions. There are two main types of anisotropy: magnetocrystalline and shape anisotropy.

Magnetocrystalline anisotropy

The crystal structure of a material induces preferred directions for the magnetic moments. Magnetocrystalline anisotropy is caused by the spin-orbit interaction. In general, atomic orbitals are non-spherical in shape and are linked to the crystalline structure. As a result, these orbitals are oriented along certain crystallographic directions and can overlap with one another. The orbitals then couple to the electron spins and force them to align along well-defined axes. The preferred directions for the magnetisation are called the ‘easy directions’ and the directions in which it is most difficult to align the magnetisation are called the ‘hard directions’. To rotate the magnetisation away from the easy direction costs energy. This anisotropy energy depends on the structure of the lattice. For hexagonal systems there is a uniaxial anisotropy with energy,

$$E_k = \int_V (K_1 \sin^2\theta + K_2 \sin^4\theta)\,dV \tag{1.9}$$

or using direction cosines,

$$E_k = \int_V [K_1(1-\gamma^2) + K_2(1-\gamma^2)^2]\,dV \tag{1.10}$$

where K_1 and K_2 are the anisotropy constants for the material, θ is the angle between the easy direction and the magnetisation, and V is the volume of material. This system therefore has one easy axis with two energy minima separated by energy maxima. For cubic systems with cubic anisotropy, the energy is given by,

$$E_k = \int_V [K_1(\alpha^2\beta^2 + \beta^2\gamma^2 + \gamma^2\alpha^2) + K_2\alpha^2\beta^2\gamma^2]dV \tag{1.11}$$

In the above expression α, β, γ are the directional cosines referred to the crystallographic axes. In polycrystalline materials, however, the magnetisation has no overall preferred axis because the crystallites are randomly oriented. Instead, the anisotropy direction varies between crystallites, resulting in local easy axes which manifest themselves in the Fresnel and DPC images as magnetisation ripple [4]. Despite this, anisotropy can be induced during or after film growth using special processing techniques. For example, growing the material in a large applied field or annealing the sample in a large field after deposition can have this effect. Growing the film on top of a buffer layer is another commonly used method in the fabrication of multilayer structures.

Shape anisotropy

This type of anisotropy is related to the magnetostatic effects of the system rather than the overlap of electron orbitals, but is vitally important to the magnetic configurations of thin film elements and must be described. When a magnetic body is uniformly magnetised, magnetic ‘free poles’ build up at the surface of the material. These poles are referred to as north and south (N and S) but are often represented by positive and negative charges (+ and -). In this situation, field lines connect the opposite poles both inside and outside of the material. Inside the body, this demagnetising field, H_d, is opposite in direction to the magnetisation and the shape anisotropy energy increases as H_d increases.

By considering an anisotropic 3D shape such as an ellipsoid (Fig. 1.4) magnetised along the long and short axes, it can be seen that free poles are separated by relatively long and short distances respectively [5]. As a result, magnetising the material along the long axis leads to smaller values of H_d and a lower energy than when it is magnetised along the short axis. In this case the energy expression has a similar form to the uniaxial crystalline anisotropy,

$$E_k = -\int_V K_{eff} \sin^2\theta dV \tag{1.12}$$

with

$$K_{eff} = 1/2(N_b - N_a)M^2 \tag{1.13}$$

where θ is the angle between the long axis of the sample and the magnetisation direction, M is the magnetisation and N_a and N_b are demagnetising factors in the long and short axes respectively. N_a and N_b depend on the sample geometry and are uniform for an ellipsoid.

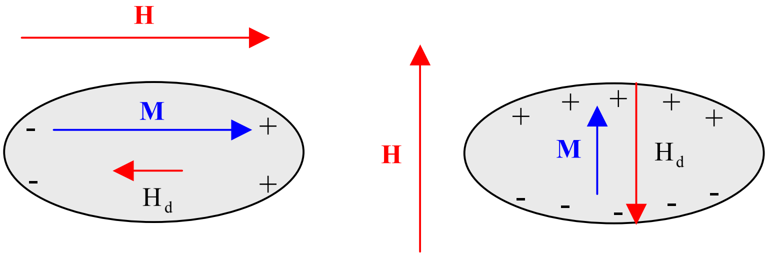

Fig. 1.4: The shape anisotropy energy is greatly affected by the sample shape and is dependant on the size of the demagnetising field.

1.3.3 Magnetostatic energy

Magnetostatic effects are a natural consequence arising from any magnetisation distribution which results from the build up of magnetic charge at the surfaces of a magnetic material and also from within the volume when the magnetisation distribution is discontinuous or divergent. As mentioned in the previous section, these poles generate field which exists both inside (demagnetising field) and outside (stray field) the material, with H_d opposing the magnetisation. The surface magnetic charge density, σ, is given by,

$$\sigma = \mathbf{M} \cdot \mathbf{n} \tag{1.14}$$

and the volume magnetic charge density, ρ, by,

$$\rho = -\nabla \cdot \mathbf{M} \tag{1.15}$$

where **M** is the magnetisation vector and **n** is the outward pointing unit vector normal to the surface. The energy associated with these surface and volume charges arises from the interaction between the field and magnetisation, and is expressed as,

$$E_d = -\frac{\mu_0}{2} \int_V \mathbf{M} \cdot \mathbf{H_d} dV \tag{1.16}$$

and μ_0 is the permeability of free space. As the magnetostatic field originates from the surface (S) and volume (V) charges, it is represented by,

$$\mathbf{H_d} = \frac{1}{4\pi}\int_V \frac{-\nabla \cdot \mathbf{M}}{r^2} dV + \frac{1}{4\pi}\int_S \frac{\mathbf{M} \cdot \mathbf{n}}{r^2} dS \tag{1.17}$$

where **r** is the position vector for the point at which the field from the charge is evaluated. The magnetostatic energy of the system can be reduced by decreasing the amount of stray field generated at the edges of the material. This is achieved by the formation of domains and is discussed later in the chapter.

1.3.4 Zeeman energy

In the presence of an externally applied magnetic field, the moments within the material will attempt to align parallel to the field direction. The Zeeman energy takes into account the orientation of the magnetisation with respect to the applied field and is given by,

$$E_z = -\mu_0 \int_V \mathbf{M} \cdot \mathbf{H} dV \tag{1.18}$$

where **H** is the external magnetic field.

1.3.5 Magnetostrictive energy

When a ferromagnetic material is magnetised, there may be a change in the dimensions of the material. This effect is termed magnetostriction. Conversely, applying stress to the material changes its magnetisation. The reason for this behaviour relates to the atomic structure of the material. When atoms bond to form a crystal, the shape of the electron orbitals changes and they deviate from their spherical form. Since the atomic moments are dependant on both the spin and orbital components of angular momentum and the magnetisation on the overlap of neighbouring orbitals, the magnetic properties are affected by the atomic spacing. When an external field is applied, the magnetic moments try to align with the field and the orbitals distort. This effectively changes the atomic positions within the material and creates mechanical strain. The specimen either expands (positive magnetostriction) or contracts (negative magnetostriction) in the direction of the magnetisation. Likewise, when a physical stress is applied, the atoms in the material are displaced, effectively causing changes in the magnetisation. The magnetostriction, λ, is defined as the fractional change in length,

$$\lambda = \frac{\delta l}{l} \tag{1.19}$$

and has a maximum value, λ_s, when the magnetisation is saturated in the direction of an applied field. The related energy term, called the magnetostrictive energy, is associated with the strain induced in the material and is given by,

$$E_\lambda = \int_V (3/2\lambda_s \sigma \sin^2 \alpha) dV \tag{1.20}$$

where α is the angle between the saturation magnetisation and the stress, σ. Therefore, by magnetising a material in a specific direction there is a magnetostrictive energy cost. The size and sign of λ_s depends on the crystal symmetry and the direction in which the material is magnetised.

1.3.6 Total energy

The total energy of a ferromagnetic specimen is the sum of the individual energy terms discussed,

$$E_{tot} = E_{ex} + E_k + E_d + E_z + E_\lambda \tag{1.21}$$

and the magnetic states supported are a direct consequence of its local or global minimisation.

1.4 Magnetic domains and domain walls

Ferromagnetic materials can be regarded as a collection of exchange-coupled magnetic dipoles [6]. They are fixed to one point but are free to rotate. The magnetisation distribution (patterns) supported are determined by the different energy terms of the system. The problem can be visualised more simply by considering the basic forces acting on the moments as a result of the different interactions. The exchange interaction tries to align adjacent spins parallel to one another (Fig. 1.5a), whilst the magnetostatic interaction pushes them in opposite directions (Fig. 1.5b). Meanwhile any material anisotropy and magnetostrictive stress (Fig. 1.5c) bias the magnetisation in one particular direction and an applied field forces it in another (Fig. 1.5d). The orientation of the dipoles within a particular domain is therefore a balance between the exchange and magnetostatic interactions. At small length scales (10nm) the exchange force is greater and the spins are nearly parallel, but at length scales of 100nm and above, the magnetostatic coupling dominates and the spins may be oriented in opposite directions.

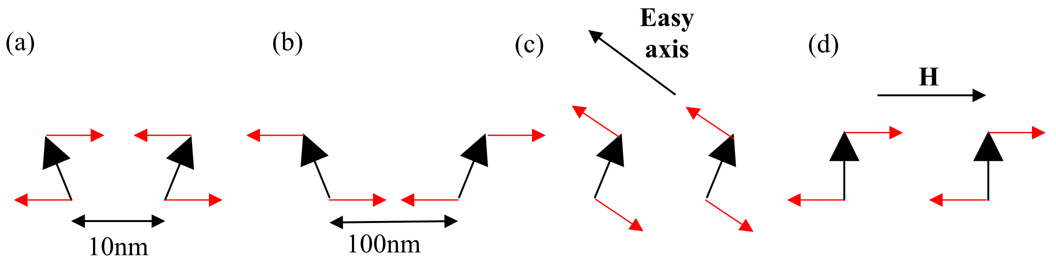

Fig. 1.5: The directions of torque (red) acting on the magnetic moments as a result of (a) exchange, (b) magnetostatic, (c) anisotropy/magnetostriction and (d) applied field interactions.

1.4.1 Domain configurations

As an example, consider a square piece of material sufficiently thin that the magnetisation preferentially lies in the film plane. If the magnetisation is saturated along one axis (Fig. 1.6a) the exchange energy is minimised by the parallel spins, but there is a large build up of surface charge and associated magnetostatic energy. In reality, this state could only be achieved if the element was very small, if there was a large field present or there was a high uniaxial anisotropy or magnetostrictive stress. In any other situation, the system would break up into domains [7,8] to reduce the magnetostatic energy at the expense of some ‘domain wall’ energy (Fig. 1.6b). These walls (as will be discussed in the next section) have associated exchange, anisotropy and magnetostatic contributions. As with the first configuration, the vertical orientation of spins would only occur under particular conditions. Without these conditions the magnetisation would likely rotate to form a flux closure structure (Fig. 1.6c). This state generates little surface charge but has exchange energy and some domain wall energy. With uniaxial (magnetocrystalline) anisotropy or magnetostrictive stress present, a low energy configuration might be that shown in Fig. 1.6d where multiple domains are present and surface charge is reduced. Instead of magnetocrystalline anisotropy or magnetostriction, favourable orientations can be induced by introducing shape anisotropy. In Fig. 1.6e the shape symmetry aligns the magnetisation parallel to the long (or easy) axis. As discussed, this configuration reduces the demagnetising field and magnetostatic energy. In summary therefore, it can be seen that whilst the exchange energy tries to oppose domain formation, the magnetostatic energy favours it. In addition, anisotropy, magnetostriction and applied fields limit the possible orientations of these domains, but do not directly favour or oppose their formation.

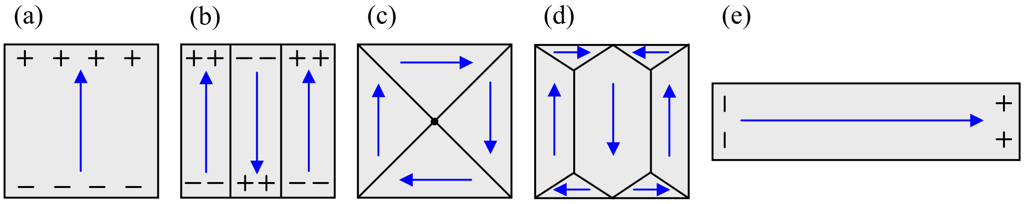

Fig. 1.6: Hypothetical domain configurations supported by a square thin film element. These include (a) single domain and (b) multi-domain states with large magnetostatic energy, (c) magnetocrystalline isotropic and (d) anisotropic flux closure configurations and a (e) single domain (shape) anisotropic state.

In most cases for a ferromagnetic film there are a large number of different magnetic states that the system can relax into, often with different energies [9]. The lowest energy state is referred to as the ground state, and represents the global minimum. Configurations with higher energy are called metastable states and are the local minima for the system. The configuration supported by a sample depends on the history of the material as well as the applied field strength and direction. Applying a particular field will often change the configuration from one state to another. In many cases, however, the various configurations are similar in energy and are considerably more complicated than those shown in Fig. 1.6.

1.4.2 Domain wall configurations

Two regions of different magnetisation are separated by boundaries known as domain walls. Within the wall, the magnetic moments of the material rotate smoothly between the two directions of magnetisation. As the rotation occurs gradually over many atoms, the domain wall width is given by,

$$w = Na \tag{1.22}$$

where N is the number of atoms and a is the atomic spacing. However, as the walls introduce additional exchange, anisotropy and magnetostatic energy to the system, their width is an important consideration and depends on a balance between the different terms. Narrow walls have a considerable exchange energy because the rotation from one spin to the next is large, whilst wide walls deviate a larger fraction of the magnetisation away from the easy axis and introduce a large anisotropy component. The magnetostatic contribution, however, depends on the thickness of the film. In thin films the upper and lower surfaces are closer together, so the free poles create a large demagnetising field compared with thicker films. This effect also determines the type of wall that forms.

Walls are characterised according to their spin configuration and angle through which the magnetisation rotates on going from one domain to the next. There are two basic types of domain wall: namely Néel walls (Fig. 1.7a) and Bloch walls (Fig. 1.7b). In Néel walls, the magnetisation rotates in the plane of the film, whilst in Bloch walls the rotation is out-of-plane. With Bloch walls there is no divergence of the magnetisation. Therefore in thicker films (> 90nm), the associated stray field is small and Bloch walls are favourable. If the thickness is reduced (<30nm) and the out-of-plane magnetisation intersects the surface, free poles are generated and this type of wall becomes unfavourable. Instead Néel walls are formed. Since the spins rotate in the sample plane, magnetic charge builds up inside the material and not on the surface. Taking into account the different energy terms, the width of a Bloch wall is dependent only on the exchange and anisotropy contributions and is related to the anisotropic exchange length,

$$\delta_{ex,k} = \sqrt{\frac{A}{K}} \tag{1.23}$$

with A and K being are the exchange and anisotropy constants for the material. The width of a Néel wall on the other hand is dependent on the exchange, anisotropy and magnetostatic energy terms. As the magnetostatic energy is more dominant than the anisotropy energy, however, the width is related to the magnetostatic exchange length,

$$\delta_{ex,d} = \sqrt{\frac{2A}{\mu_0 M_s{}^2}} \tag{1.24}$$

where M_s is the saturation magnetisation.

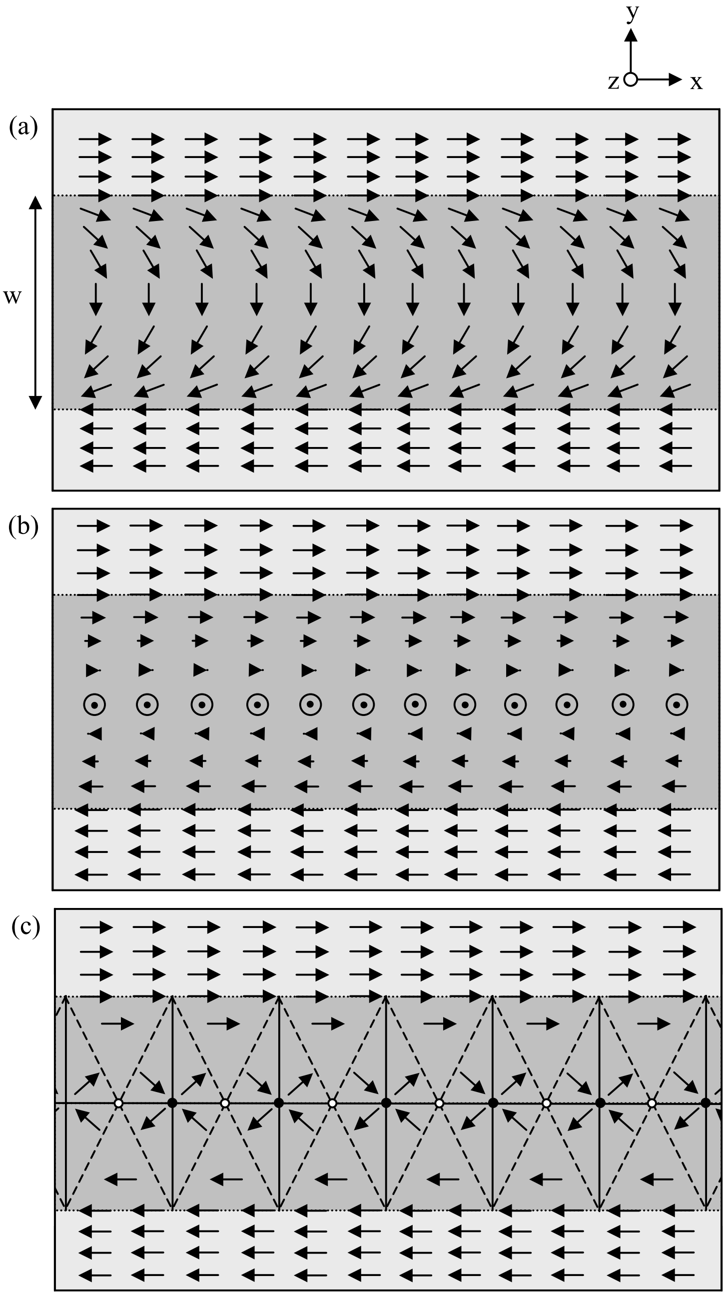

Fig. 1.7: (a) Néel, (b) Bloch and (c) cross-tie domain walls (shaded region) found in ferromagnetic films.

Fig. 1.8 shows a simulated phase diagram for permalloy films [10], which illustrates the variation of wall energy density, σ_w, with film thickness. In real materials a variety of different domain wall configurations are possible by combining the basic Néel and Bloch type walls. These more complicated structures occur as the system tries to minimise the total energy. One common example is a cross-tie wall [11] (Fig. 1.7c) which, from Fig. 1.8, is found in film thicknesses of between 30 and 90nm. Solid lines in the schematic represent 90° Néel walls and dashed lines 45° Néel walls. The circles in Fig. 1.7c indicate Bloch lines, where the magnetisation is out-of-plane. They exist where the in-plane direction is undefined and are called singularities [12]. As the distance increases from the centre of a singularity, the magnetisation relaxes into the plane of the film. The black circles are cross Bloch lines (or cross-ties) and the white circles circular Bloch lines (or vortex cores). Magnetisation vortices are found frequently in ferromagnetic films because they reduce the magnetostatic energy of the system. The magnetisation rotates around the core with the spins becoming tighter as the radius of curvature decreases. This tightening increases the exchange energy to the extent that the spins point out-of-plane at the centre of the vortex, decreasing the exchange energy at the cost of some magnetostatic energy. Other examples of complex domain wall configurations include 360° domain wall loops and head-to-head vortex and transverse walls. These will be discussed in detail in the relevant sections of this thesis.

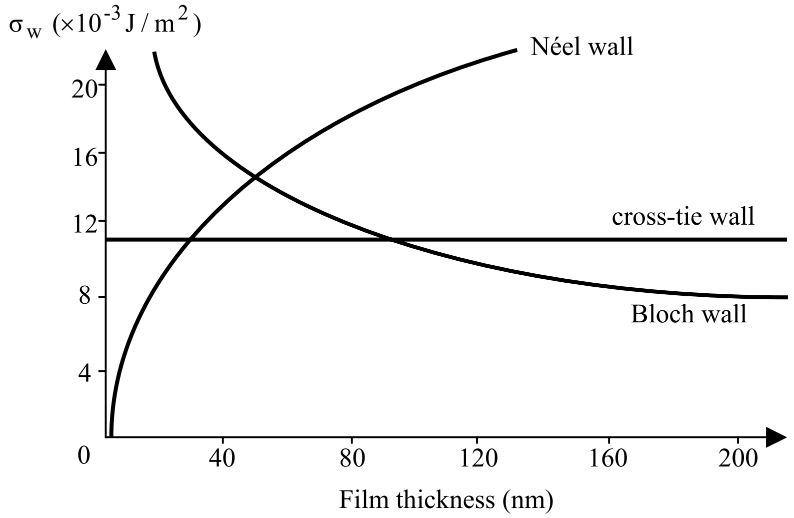

Fig. 1.8: Domain wall phase diagram for permalloy showing the energy density of Néel, Bloch and cross-tie walls as a function of film thickness.

1.5 Hysteresis

The magnetisation of ferromagnetic materials depends not only on the applied field, but also on the previous magnetic history [13]. This behaviour is called hysteresis. The macroscopic field response is considered first and is depicted in Fig. 1.9. If we take an isotropic ferromagnetic material in the as-grown state, where the sample has never been exposed to an external field, the domains within the material will be arranged such that the net magnetisation is zero (1). By then applying a field, a net magnetisation is induced in the field direction (2). As this field is increased, the magnetisation increases until saturation, M_s (3), when all the moments are aligned with the applied field, H_s. When this field is removed, the magnetisation then drops to a value known as the remanant magnetisation (or remanance), M_r (4). The remanent magnetisation can range from zero to near M_s depending on the material. A field applied in the opposite direction will then reduce the magnetisation to zero (5) with the field strength at which this occurs known as the coercive field, H_c (or the coercivity). Increasing the negative field saturates the magnetisation in the opposite direction (6) before field removal allows the system to reach remanance again (7). Application of a positive field then demagnetises the sample as before (8). The M-H graph produced as the field is swept between positive and negative values is known as a hysteresis loop. The area of the loop is a measure of the work required to take the material through one complete magnetisation cycle. Note, however, that the initial increase of the magnetisation from zero to M_s between field values of zero and H_s (1) – (3) is never repeated. This type of hyteresis loop is called a major loop since the magnetisation is driven between saturation in opposite directions. On the other hand, cycling between smaller field values results in minor loops of which there can be an infinite number. With anisotropic samples the direction of applied field is also a consideration, and so hysteresis loops for different directions of applied field must be obtained for proper characterisation. Often plots of magnetic induction against applied field (B-H) are determined instead of M-H loops. Magnetic induction is given by,

$$\mathbf{B} = \mu_0(\mathbf{M} + \mathbf{H}) \tag{1.25}$$

For linear materials, substituting M from equation (1.3) gives,

$$B = \mu_0 \mu_r H \tag{1.26}$$

where μ_0 is the permeability of free space and μ_r is the relative permeability. The latter is the relative difference in magnetic field inside and outside of the material.

The quantities M_r and H_c provide the principal characterisation of a magnetic material for device applications. For example, in permanent magnets the material must exhibit a high M_r and H_c so that it maintains a large magnetisation and is difficult to demagnetise. Materials with a high or low H_c are referred to as hard and soft magnetic materials respectively. For transformer cores, the material should be soft with a low M_r. This is achieved using amorphous materials. On the other hand, magnetic memory and storage applications require a thin film with large M_r and intermediate H_c. The large M_r enables differentiation between two binary states ($+M_r$ and $-M_r$) whilst the coercivity allows the material to be written to without accidental demagnetisation (memory loss).

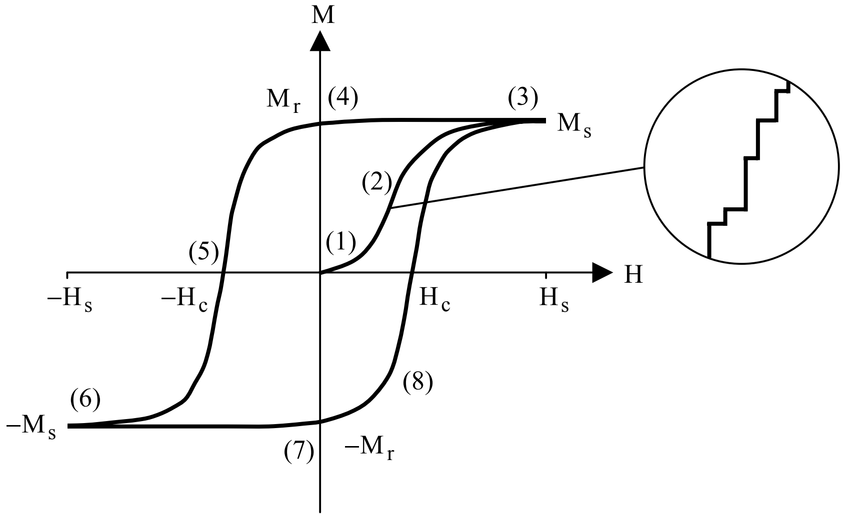

Fig. 1.9: Typical hysteresis loop for a ferromagnetic material. The enlarged region shows steps in the response known as the Barkhausen effect.

1.6 Magnetisation reversal

When an external field is applied, the magnetisation can change direction to align with the field in two different ways. One mechanism is coherent rotation. In this situation, the magnetisation vector rotates smoothly from one direction to the other and occurs in films possessing uniaxial anisotropy. Stoner and Wohlfarth [14] developed a model to describe this mechanism in small single-domain particles. Although this model places a single domain constraint on the system, it can be used in a modified form to deal with more complicated problems [15]. However, in larger systems it may be more energetically favourable for reversal to occur through domain processes. This mechanism involves the nucleation of domains and domain walls, and subsequent domain wall motion. Such behaviour can be predicted using micromagnetic simulations. In systems supporting multiple domains prior to field application, similar domain processes can occur without the need to nucleate new domains/domain walls. By considering a rectangular thin film element exhibiting initial flux closure (Fig. 1.10a) and applying a field parallel to the long axis, the domain aligned with the field increases in size at the expense of the others (Fig. 1.10b). This process is reversible. As the field is increased, however, domain wall annihilation occurs and the domain unfavourably aligned with the field is removed (Fig. 1.10c). This is an irreversible step. Domains oriented close to the applied field direction rotate to align with the field. At larger fields, further domain wall annihilation occurs and a single-domain state is reached (Fig. 1.10d). In general, the growth and reduction of domains are reversible processes, whilst domain wall annihilation is irreversible. It is the irreversible steps that are responsible for hysteresis in ferromagnetic materials. In addition, the small magnetisation jumps that occur in hysteresis loops (Barkhausen effect) are due to irreversible domain wall motion (Fig. 1.9).

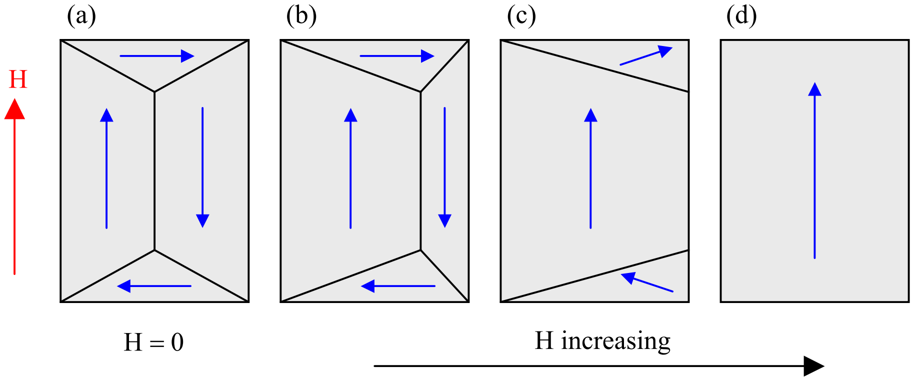

Fig. 1.10: Typical domain process observed in a rectangular thin film element during field application.

1.7 Tunnelling magnetoresistance

Magnetoresistance is the property of some materials to change the value of their electrical resistance when an external magnetic field is applied. The effect, later called ordinary magnetoresistance (OMR), was first discovered by William Thomson (Lord Kelvin) in 1856 [16] but only exhibited changes in resistance of up to 5%. Since then, however, other types of magnetoresistance have been discovered including anisotropic (AMR) [17], giant (GMR) [18], tunnelling (TMR) [19] and colossal magnetoresistance (CMR) [20], which have been shown to give larger effects. Only TMR is considered here, as it forms the basis for the structure and operation of magnetic tunnel junctions (MTJs).

MTJs (Fig. 1.11), at the simplest level, consist of two layers of ferromagnetic metal separated by an ultrathin layer of insulator, typically aluminium oxide with a thickness of about 1nm [21]. The insulating layer is thin enough that electrons can tunnel through the barrier if a bias voltage is applied between the metal electrodes. A dramatic change in tunnelling current occurs when the magnetisation of the ferromagnetic layers change their alignment. This TMR effect was first observed by Julliere in 1975. In order for MTJs to be used as effective memory cells it must be possible to vary the alignment of the layers between a parallel and anti-parallel configuration using an applied field, whilst for magnetic sensors, all possible orientations are required.

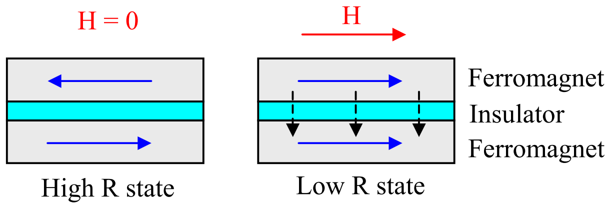

Fig. 1.11: Changes in the MTJ resistance occur when the relative orientation of the layers is altered by an external magnetic field. Dashed arrows in the low R state represent tunnelling electrons.

TMR is a consequence of spin-dependent tunnelling (SDT), a phenomenon discovered in 1970 by Tedrow and Meservey [22]. It arises from the fact that in ferromagnetic metals, electronic energy bands are exchange split, resulting in a difference in the density of states at the Fermi level for the spin-up and spin-down electrons. Therefore, the number of electrons that can tunnel through the barrier and also the tunnelling conductance, depend on the electron spin. Julliere's model (Fig. 1.12) helps to explain this further and is based on two assumptions. Firstly, it is assumed that the spin of the electrons is conserved during the tunnelling process and that the tunnelling of spin-up and spin-down electrons can be considered as two independent processes (spin channels). Therefore electrons of one spin state from the first ferromagnetic layer are accepted by unfilled states of the same spin in the second ferromagnetic layer. When the two layers are aligned parallel, the majority spins tunnel to the majority states and the minority spins to the minority states. In effect, the spin-aligned electrons have a higher probablility of tunnelling through the insulating layer and we have a low-resistance state. On the other hand, when the two ferromagnetic layers are aligned anti-parallel, the identity of the majority and minority spin electrons is reversed and the majority spin electrons tunnel to the minority states and vice versa. In this situation, the tunnelling probability of both spin-up and spin-down electrons is reduced and we have a high-resistance state. The second assumption of Julliere's model is that the conductance for a particular spin orientation is proportional to the product of the density of states of the two ferromagnetic layers. Therefore, the TMR can be written as,

$$\mathrm{TMR} = \frac{R_{\uparrow\downarrow} - R_{\uparrow\uparrow}}{R_{\uparrow\uparrow}} = \frac{I_{\uparrow\uparrow} - I_{\uparrow\downarrow}}{I_{\uparrow\downarrow}} = \frac{2P_1P_2}{1 - P_1P_2} \tag{1.27}$$

with

$$P = \frac{D_{\uparrow} - D_{\downarrow}}{D_{\uparrow} + D_{\downarrow}} \tag{1.28}$$

where R is the resistance, I is the tunnelling current, P is the spin polarisation for the top (1) and bottom (2) ferromagnetic layers and D is the density of states at the Fermi level. The arrows in equation 1.27 show the alignment of the magnetic electrodes whilst in equation 1.28 indicate spin-up and spin-down electrons.

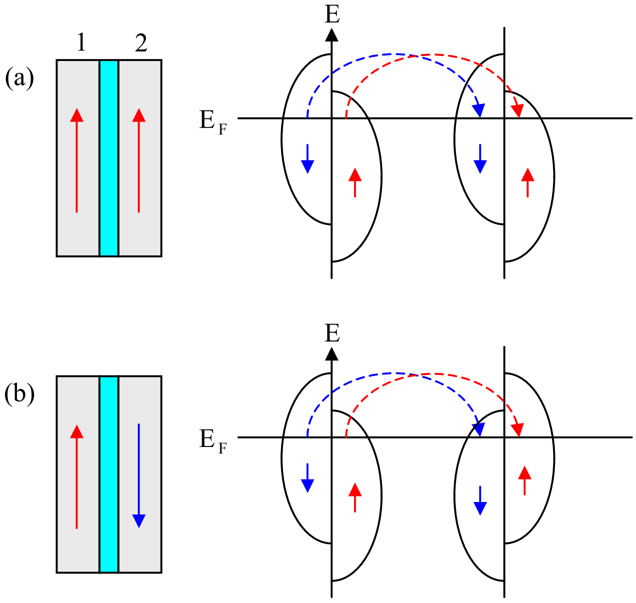

Fig. 1.12: Julliere’s model of TMR showing the variation in density of states for spin-up and spin-down electrons when the ferromagnetic layers of a MTJ are aligned (a) parallel and (b) anti-parallel.

1.8 Interlayer coupling

For storing information, it should be possible to vary the alignment of the MTJ ferromagnets (FM) between a parallel and anti-parallel orientation using a modest applied field. By using an antiferromagnetic (AFM) layer in contact with one of the FM electrodes, the direction of magnetisation in this FM layer is fixed. This layer is known as the pinned layer. The other FM, however, is able to change its magnetisation direction to align with the field and is termed the free layer. A common specification for applications is a good control over the low field properties of the free layer. Its orientation should be sensitive to the applied field with a large resulting change in TMR as its direction changes with respect to the pinned layer. Ideally the free layer hysteresis loop would be centred around zero field, but this is rarely the case. As a result of various interlayer coupling mechanisms between the free and pinned layers, the centre of the hysteresis loop is shifted away from zero field and changes in the free layer coercivity can occur [23].

In general, the different coupling mechanisms cause a parallel (FM) or anti-parallel (AFM) alignment between adjacent FM layers. This alignment depends on the dominant mechanism and the particular materials involved, and is described as ‘bilinear’ because the coupling energy is linear in both of the magnetisation directions [24],

$$E_{\mathrm{bil}} = -J_1 \mathbf{m_1} \cdot \mathbf{m_2} \qquad (1.29)$$

where J_1 is the coupling constant and $\mathbf{m_1}$ and $\mathbf{m_2}$ are the magnetisation vectors of the adjacent FM layers. With this form of interaction, positive values of the coupling constant favour parallel alignment and negative values favour anti-parallel alignment. Although this model can successfully describe the interactions for most samples, some specimens have been known to exhibit a non-linear magnetisation curve and a perpendicular alignment of the magnetisation vectors at zero field. This alignment can be explained by the presence of physical defects and disorder in the structure. Studies have shown that one origin is spatial fluctuations in the interlayer coupling through the spacer layer as a result of terraces at the FM/spacer interface. A phenomenological way to describe this behaviour is through the use of a ‘biquadratic’ term in the energy expression,

$$E_{\mathrm{biq}} = -J_2 (\mathbf{m_1} \cdot \mathbf{m_2})^2 \qquad (1.30)$$

It is called biquadratic because the energy is quadratic in both of the magnetisation directions. All found values of the coupling constant, J_2, are negative, favouring a perpendicular orientation of the magnetisation vectors. Most of the different coupling interactions played a part in the magnetic structure of the MTJs in chapter 8, and will be described briefly. A schematic diagram of the type of stack studied is given in Fig. 1.13, but will be discussed in detail later. The various coupling types can be split into two main categories, namely exchange interactions and magnetostatic interactions.

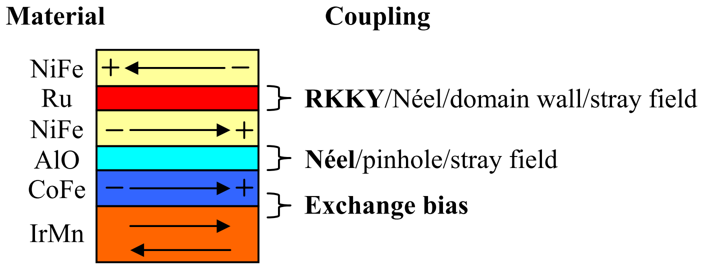

Fig. 1.13: Schematic diagram of the MTJs studied in chapter 8 showing the different layers deposited and the type of coupling present between each magnetic layer. The dominant mechanism at each interface is highlighted in bold.

1.8.1 Exchange interactions

There are four different exchange interactions that affect the behaviour of multilayer films. These include interlayer exchange coupling (IEC), exchange bias, pinhole coupling and Ruderman-Kittel-Kasuya-Yosida (RKKY) coupling. IEC [25,26] is an indirect exchange coupling effect caused by spin-polarised electrons tunnelling across the insulating barrier when a voltage is applied to the stack (Fig. 1.14a). These electrons exert a spin torque from one film to the other which acts to align the FM layers parallel provided the barrier is free from defects and impurities. Exchange bias (or exchange anisotropy) [27,28] is a direct exchange interaction that exists at the interface of any FM and AFM material (Fig. 1.14b) and is characterised by a shifted hysteresis loop (H_E) and enhanced coercivity (H_C) for the FM. With thin film AFM-FM bilayers, the exchange bias is set by cooling the film through T_N from $T_N < T < T_C$ in the presence of an applied field (cooling field). As a result of the loop shift, different coercivity values are experienced for positive and negative field. All effects, however, vanish above the blocking temperature, T_B, of the system, which is dependent on the AFM T_N. Pinhole coupling [29,30] is a direct FM exchange interaction via magnetic bridges through the insulating barrier (Fig. 1.14c). These bridges are formed when the upper FM material is deposited onto a spacer layer containing gaps. The density of pinholes is affected by fundamental growth processes and by substrate dislocations and morphology. RKKY coupling [31] occurs when the two FM layers are separated by a metallic paramagnetic (PM) spacer and is caused by an indirect exchange interaction through conduction electrons of the spacer layer (Fig. 1.14d). The conduction electrons are magnetised in the vicinity of one FM and the second FM perceives this magnetisation. For transition metals, the interaction is AFM and the conduction electrons try to screen the spin by spin-polarising in alternating directions. Close to the FM the spins are aligned in the opposite direction, but favour a parallel orientation further away. The second FM then aligns itself anti-parallel to the spins of its adjacent conduction electrons.

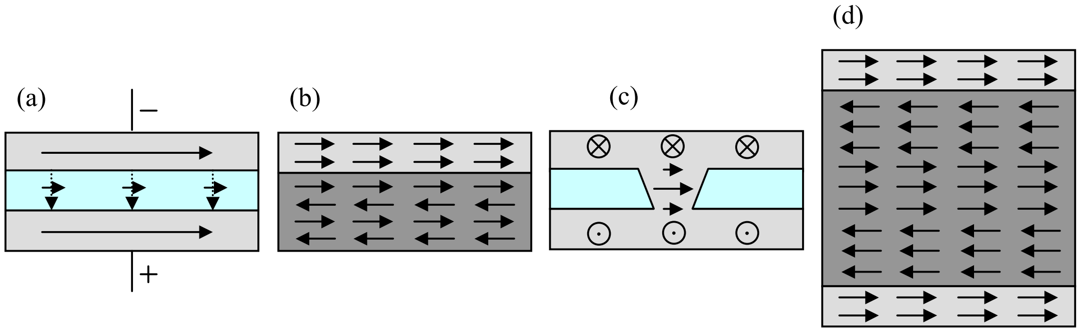

Fig. 1.14: The (a) IEC, (b) exchange bias, (c) pinhole and (d) RKKY exchange coupling interactions between the layers of a MTJ.

1.8.2 Magnetostatic interactions

There are also three magnetostatic coupling effects. These include Néel (or orange-peel) coupling, domain wall coupling and stray field coupling. Orange peel coupling [32-35] is a dipole-dipole interaction that occurs in multilayer FM films when the surface is rough and there is intralayer exchange coupling. Under these conditions, magnetic surface charge develops at the interfaces because the magnetisation cannot follow the surface profile (Fig. 1.15a). When the roughness has a conformal or correlated waviness (implying no phase, amplitude or correlation length differences in topology between the various layer surfaces) through a spacer layer of uniform thickness, the interface normals are locally opposite. With the layers magnetised in the same direction, the poles of opposite polarity in adjacent films are closer together than if the magnetisation was anti-parallel. In this situation stray field lines connect both inter and intralayer magnetic charges. When the magnetisation is anti-parallel, none of the field lines cross the spacer layer and the field energy is larger. Therefore, orange-peel coupling favours a FM alignment. Domain wall coupling [36-40], on the other hand, is found in multilayer FM films that reverse by domain wall motion. Domains walls in one film couple with those in the adjacent film and exert an ‘escape field’ which pins the second wall in place (Fig. 1.15b). In the pinned configuration the magnetostatic energy is lowered when the sense of rotation in each of the walls is opposite, otherwise wall displacement occurs [41]. This coupling phenomenon affects not only the domain and domain wall configurations supported by the films, but also the material coercivity. In patterned magnetic multilayers, magnetostatic interactions occur between the free and pinned layers as a result of stray field from the magnetic charges at the edges of the element (Fig. 1.15c). This stray field coupling [42-45] encourages an energetically favourable anti-parallel orientation of the magnetisation vectors, which promotes reversal of the free layer to the anti-parallel state but opposes its switch back to the parallel configuration. The stray field itself radiates from the charge and has both parallel and perpendicular components which influence the magnetisation of the adjacent film.

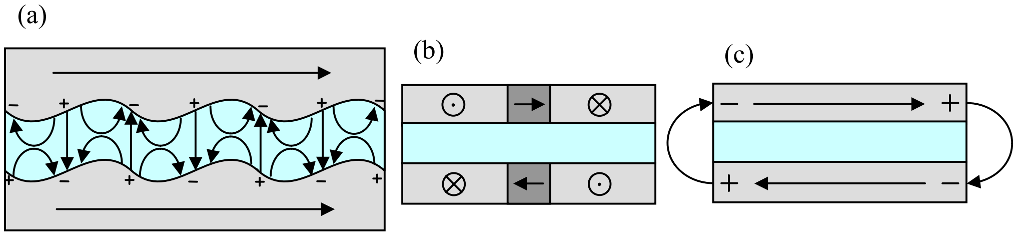

Fig. 1.15: The (a) orange-peel, (b) domain wall and (c) stray field magnetostatic coupling interactions between the layers of a MTJ.

Although interlayer coupling is useful in some circumstances, exchange bias for example, many of the interactions adversely affect the behaviour of TMR memory and sensor elements. Direct consequences include reduced TMR and field sensitivity, unstable magnetic states and in extreme cases, complete failure of the device. Therefore, these interactions are not just minor complications but must be given a great deal of consideration if TMR devices are to be successful in the future.

Chapter 2

Instrumentation and experimental techniques

2.1 Introduction

Microscopy is a technique used to produce visible images of structures too small to be seen by the human eye. The microscope itself has to accomplish three tasks: it must be able to produce a magnified image of the specimen, resolve features in the image and render the details visible to the eye or camera. The technique has evolved with the development of optical technology and there are now three main branches: optical, electron and scanning probe microscopy. Only electron microscopy is discussed in this thesis.

2.2 Electron microscopy

2.2.1 The transmission electron microscope (TEM)

As the resolution of a microscope is limited by the wavelength of its illumination, optical microscopes are only able to resolve features down to ~300nm at best [46]. To understand the properties of modern materials, however, it is necessary to study features that are on a length scale well below this resolution limit, if possible at the atomic level. In 1925 Louis de Broglie hypothesised that electrons exhibit wave-like characteristics, with a wavelength far shorter than visible light. As moving charged particles were already known to be deflected by magnetic fields, it was not long afterwards that the idea of an electron microscope was proposed. The first electron microscope (transmission) was built in 1933 by German physicists Ernst Ruska and Max Knoll and was similar in design to the optical microscope. Using electromagnetic lenses to focus a beam of electrons, this instrument was capable of magnifying objects 400 times. Electron microscopes have come a long way since this model, with modern versions being able to resolve individual columns of atoms in crystals with magnifications of several million times [47].

The wavelength, λ, of electrons is related to their energy, and when accelerated by a potential difference, V, is given by,

$$\lambda = \frac{h}{p} = \frac{h}{(2m_0eV)^{1/2}} \tag{2.1}$$

where h is Planck's constant and m_0 and e are the electron rest mass and charge respectively. This equation ignores the relativistic correction for the kinetic energy of electrons, and by taking this into consideration, becomes,

$$\lambda = \frac{h}{[2m_0eV(1+\frac{eV}{2m_0c^2})]^{1/2}} \tag{2.2}$$

where c is the speed of light in vacuum. By substituting a typical value for the accelerating voltage of 200kV, the wavelength is found to be 0.0025nm (or 2.5pm). This value can be reduced slightly by increasing the accelerating voltage, but higher energy electrons can introduce greater specimen damage which is often undesirable. Although the above value is far smaller than interatomic distances, electron microscopes are not able to achieve this wavelength limit of resolution due to aberrations in the electromagnetic lenses. Current work is being done to develop aberration correctors, however, and so far a resolution of 0.5Å has been achieved [47].

The original form of electron microscopy, transmission electron microscopy [48], involves a high voltage electron beam emitted by a triode electron gun and focussed by electromagnetic lenses (Fig. 2.1). The beam is partially transmitted through a very thin specimen, carrying information about its physical structure. Modern techniques also allow the user to extract details of the sample chemistry and electric or magnetic properties. Like optical microscopy, the spatial variation in the illumination is then magnified by a series of lenses to be observed or recorded.

For thermionic sources, a tungsten or LaB_6 filament is heated resistively until the electrons have sufficient energy to escape into the vacuum, before they are focussed using an electrostatic lens (Wehnelt) and accelerated down the column by an anode. With field emission guns (FEGs), two anodes are used. The first acts as an intense electric field to extract electrons before the second accelerates the beam. The combined fields of the anodes produce a fine point source. Following electron production, a condenser system involving two condenser lenses and an aperture diaphragm are used to control the electron intensity, spot size and convergence at the specimen. For TEM analysis the sample must be electron transparent. Therefore with 200kV electrons, the maximum specimen thickness cannot exceed ~100nm. Below the sample, a short focal length objective lens is used for imaging. Focussing is achieved by varying this distance on the optic axis. For magnetic lenses, adjustment of the focal length is easily performed by changing the current through the windings of the electromagnet. Intermediate and projector lenses are then used for magnification, producing a final real image on a fluorescent screen or CCD camera. Due to interactions between the electrons and air molecules, the complete TEM column must be operated under high vacuum ($\sim 10^{-7}$ torr) to reduce scattering to a negligible level.

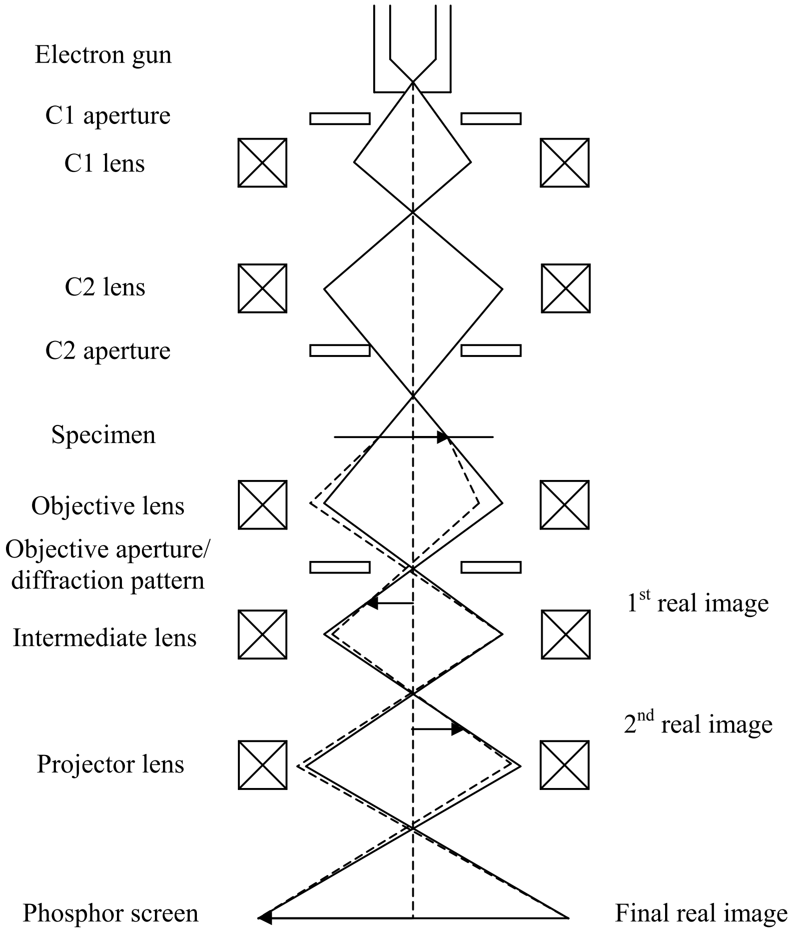

Fig. 2.1: A typical transmission electron microscope. A series of electromagnetic lenses are used to magnify a real image onto the phosphor screen.

2.2.2 The scanning electron microscope (SEM)

As well as the evolution of transmission electron microscopy, two other types of electron microscope have developed rapidly. These are the scanning electron microscope (SEM) and the scanning transmission electron microscope (STEM). Scanning electron microscopes [49] (Fig. 2.2) are mainly used to study surface morphology and use a finely focussed beam which is scanned across the surface of the specimen in synchronism with a spot in a cathode ray tube (CRT).

When the electron beam hits the sample, backscattered (BSE), secondary (SE) and Auger electrons (AE) can be produced as well as x-rays. As the beam scans in a raster pattern a detector monitors the intensity of the secondary signal, which is then converted electronically, amplified and used to control the CRT spot on the display monitor. Because the image is built up serially, the imaging process in SEM is much slower than in TEM, which occurs in parallel. An advantage SEM has over TEM, however, is the ability to image thicker samples, and it is possible to control the depth to which the electron penetrates the specimen by adjusting the accelerating voltage. As this affects the type of secondary signal produced, there is a lot of control over the nature of the final image.

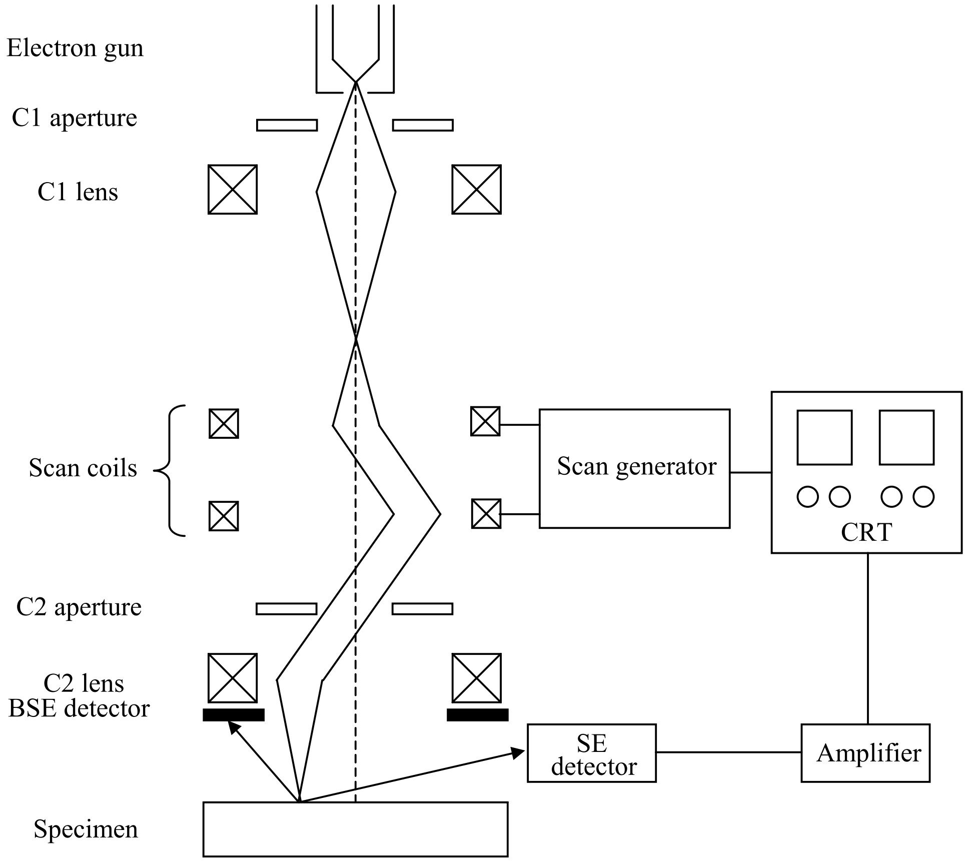

Fig. 2.2: Schematic diagram of a scanning electron microscope highlighting the important components that make up the system.

As with TEM, an electron gun emits divergent electrons which are then controlled by a condenser system. The first condenser lens, C1, demagnifies the gun crossover and the second condenser lens converges the beam to a final crossover at the specimen plane. The upper condenser controls the spot size and effectively the resolution of the microscope whilst focussing is achieved by adjusting C2. A condenser aperture is used to control the convergence angle of the beam at the sample surface. As before, the aperture reduces the beam current by stopping many of the electrons from reaching the specimen.

Unfortunately it also reduces the microscope resolution since diffraction at the aperture edge increases the spot size. Between the lenses, two sets of deflection coils are used to scan the beam about the specimen surface. An SEM was used in this project to determine specimen quality immediately after fabrication.

2.2.3 The scanning transmission electron microscope (STEM)

The scanning transmission electron microscope [50] is a hybrid of the TEM and SEM which uses deflection coils to scan a fine electron probe across the surface of a thin specimen, and is generally used to localise signals at very high resolution. Often the deflection coils are built into modern TEM systems to enable STEM imaging in addition to the usual TEM modes of microscopy, but dedicated STEMs are also available. One method of converging the beam on the specimen is to adjust the C2 lens so that the focal point is at the specimen plane instead of below the sample (Fig. 2.3a). However, we often require a spot diameter of <10nm to obtain the most useful information from the sample, and the C1 and C2 lenses are not able to achieve this. Instead, the upper objective polepiece may be used to converge the beam with C2 switched off. This configuration (Fig. 2.3b) can provide a highly focussed probe.

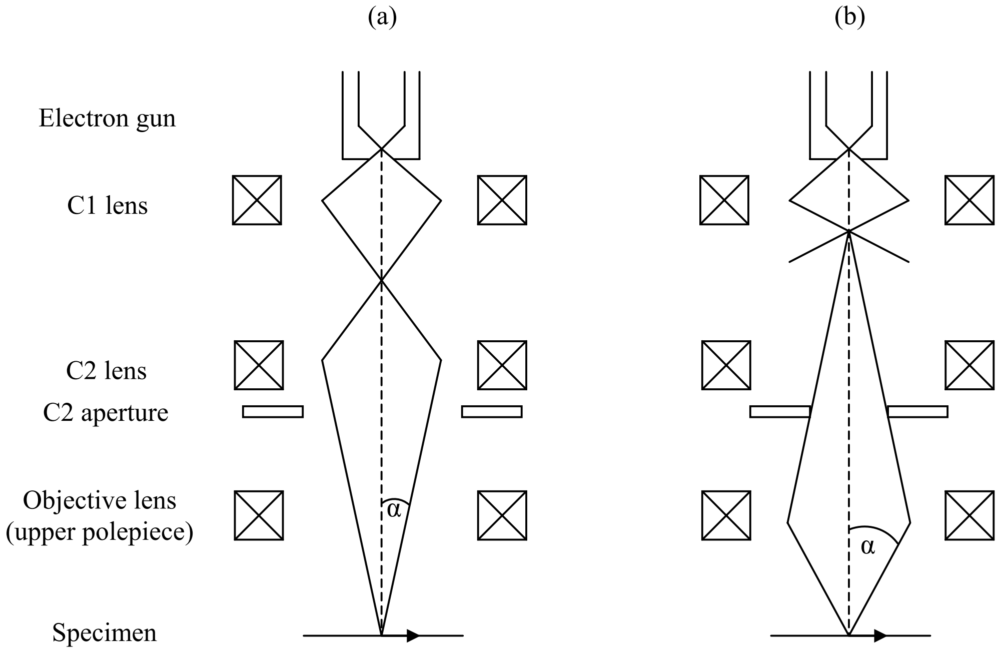

Fig. 2.3: (a) A small area of the specimen can be illuminated by focussing the C2 lens on the surface of the specimen, but for high resolution STEM imaging, (b) the upper polepiece of the objective lens is used to converge the beam to a fine probe.

Scan coils between the condenser and objective lenses control the beam on the surface of the sample whilst descan coils below the specimen ensure the electrons are centred on the detector as the beam scans. Instead of using an objective aperture to select the electrons contributing to the image, an electron detector is used. The detector sits below the projector lens and is composed of two separate parts: the bright field (BF) and annular dark field (ADF) detectors. Direct, unscattered electrons are incident on the BF detector whilst Bragg scattered electrons register on the ADF detector (which is situated around the BF section). Some STEMs also incorporate BSE and SE detectors similar to those used in SEM. One advantage STEM has over TEM is resolution. In STEM, the resolution of the system is determined by the probe size at the specimen and not by the imaging lenses which are strongly affected by aberrations. However, as spherical aberration affects the condenser system, the achievable probe size and resolution are still limited by the lenses. In both SEM and STEM scanning systems, the magnification is controlled by the scan dimensions on the specimen and not by the lenses.

2.3 Electromagnetic lenses

2.3.1 Focussing electrons

Electromagnetic lenses used in electron microscopes (Fig. 2.4) incorporate a cylindrically symmetric core (or yoke) of soft iron called a polepiece, with a hole drilled through the centre called the bore (‘b’ in diagram).

There are normally two polepieces in a lens known as the upper and lower polepieces, separated by a critical distance called the gap (‘g’ in diagram). The ratio of the bore to gap size is very important, as it controls the density of field lines at the focussing region and therefore the action of the lens. A coil of copper wire is wound around each polepiece to carry current and create an axially symmetric magnetic field in the bore. As the current flows through the coil the copper heats up resistively, so the lenses have to be cooled using a water recirculating system. The field produced magnetises the core, increasing the magnetic flux at the gap. It is important to be able to produce large fields because the strength controls the ray paths of the electrons. The field is weakest on axis and increases in strength towards the sides of the polepiece, providing a strong deflection to the electrons that travel off-axis.

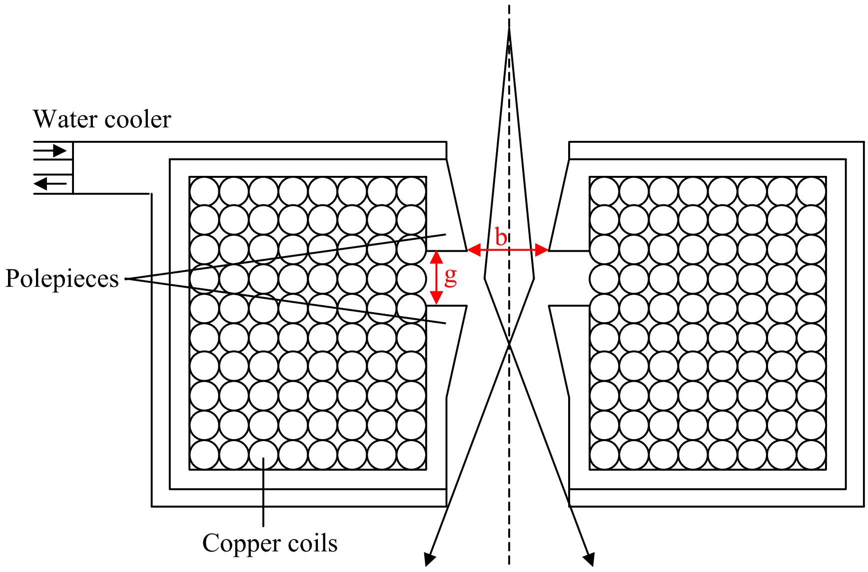

Fig. 2.4: An electromagnetic lens used to focus a beam of electrons.

2.3.2 Lens aberrations

If the lenses in a microscope were optically perfect, they would be able to transfer each point in the object to an equivalent point in the image and give a geometrically accurate 2D projection of the specimen. In reality, however, lens defects or aberrations affect the ability of the lens to form an image. These aberrations are present in both optical (glass) and electromagnetic lenses, but rotation of the image caused by the electron trajectory in a magnetic field results in additional terms for electron microscopes. Most aberrations are related to the orientation of the wavefront and focal plane with respect to the optic axis, and these affect the image clarity. This type of aberration can be split into two different classes: on-axis and off-axis aberrations. On-axis aberrations include chromatic and spherical aberration whilst off-axis terms include coma, astigmatism and field curvature.

In addition to these, other optical problems exist that do not affect the resolution, but instead distort the image. Geometrical distortion causes both barrel and pincushion effects, whilst as stated above, electron trajectories introduce rotation to the image. Some of these lens defects will now be explained in more detail.

Chromatic aberration

Chromatic aberration (Fig. 2.5) is related to the wavelength of the illumination. In light optics the different wavelengths of light are refracted differently, causing a dispersion spectrum. In glass lenses this effect results in each colour having a different focal point along the optic axis. In the image, this manifests itself as coloured fringes around the features and a disc of least confusion instead of a point focus. In electron microscopes, modern electron guns are capable of reducing the spread in electron energies and before they hit the specimen, the electrons can be regarded as monochromatic. However, after specimen interaction, some of these electrons lose energy and therefore chromatic aberration exists in the post-specimen lenses.

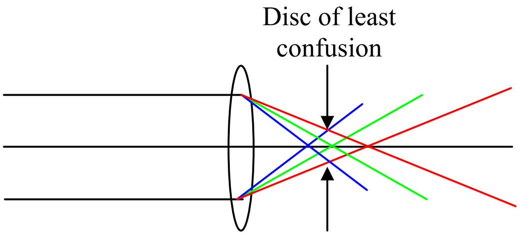

Fig. 2.5: Different wavelengths of light or electrons are brought to focus at different points on the optic axis giving rise to chromatic aberration.

Spherical aberration

Even with monochromatic illumination, on-axis rays can be poorly focussed. This is due to spherical aberration (Fig. 2.6), which results in rays passing through the outside of the lens being focussed more strongly than those passing through the centre. Spherical aberration is caused by differences in path length for the various rays and shows up in images as a series of diffraction rings around a focused spot. Effectively, a point object is imaged as a disc of finite size which reduces the resolution of the system and limits the ability to magnify detail.

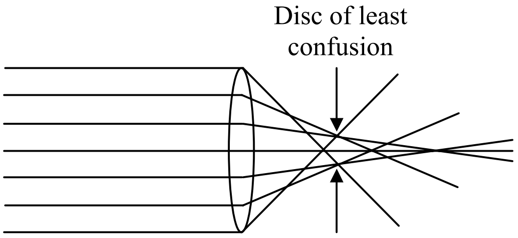

Fig. 2.6: The outer regions of the lens focus illumination more strongly than the centre, resulting in multiple focal points for the various rays.

Astigmatism

Astigmatism (Fig. 2.7) affects the focussing of off-axis points in an image. It is caused by differing degrees of focus for rays that propagate in two perpendicular planes. In electron lenses, a nonuniform field caused by microstructural and engineering defects in the polepieces or by unclean apertures gives this effect. The focal points for the tangential (yz-plane) and sagittal (xz-plane) rays occur at different distances along the z-axis and are called the tangential and sagittal foci respectively. As a result of this aberration, an off-axis point on the object appears as a short line oriented along the x-axis at the tangential focus and as a second line oriented along the y-axis at the sagittal focus. In between these two foci, a disc of least confusion is formed which represents the best compromise in an optical system with astigmatism. As the two focal points move closer together, the image shape changes between linear, elliptical and circular.

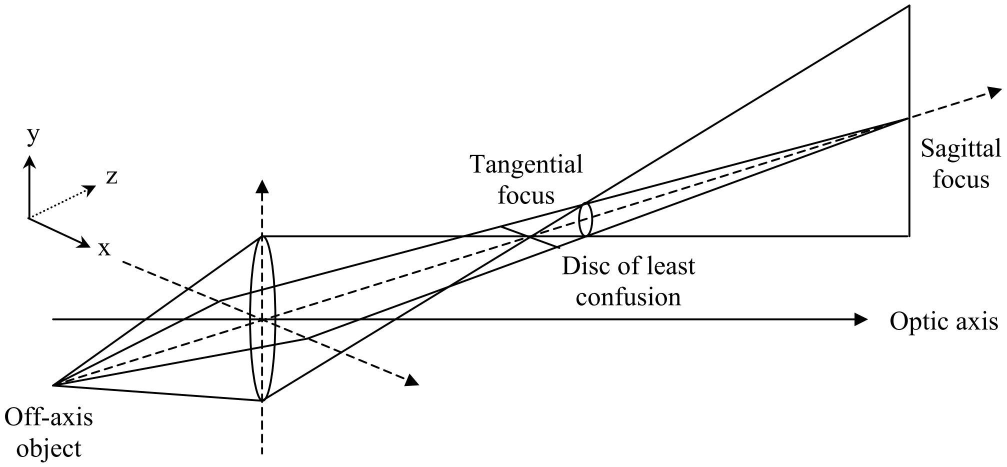

Fig. 2.7: Different focal points for tangential and sagittal rays produce astigmatism in the image.

Image rotation

In electromagnetic lenses, the magnetic field causes electrons to spiral around the optic axis. The number of turns the electron makes whilst traversing the lens is determined by the field strength and is rarely an integer. As a result, the lens acts not only to invert the image, but also to rotate it about the optic axis.

2.3.3 Resolution

The resolving power of the microscope is its ability to make adjacent points in the object discernible in the image. The resolution is therefore the shortest distance between these points on the object that can still be distinguished by the observer. An approximate value for the smallest resolvable distance (theoretical) can be calculated using Rayleigh's criterion,

$$r_{th} = \frac{0.61\lambda}{n \sin \alpha} \tag{2.3}$$

where λ is the wavelength of the radiation, n is the refractive index of the viewing medium and α is the objective lens semi-collection angle. The resolving power of a lens is ultimately limited by diffraction. When the illumination passes through the lens aperture, it interferes with itself to produce a ring-shaped diffraction pattern with points in the object being imaged as discs (Airy discs). This interference therefore blurs the image and smears out the features. The theoretical approximation also has to be adjusted due to the lens aberrations, and unfortunately, the practical resolution is not as good as Rayleigh's equation predicts.

Spherical aberration, as stated earlier, prevents the rays being focussed at a single point and instead focusses those close to the optic axis at the Gaussian image plane and those off-axis before the Gaussian image plane. The disc of least confusion is the smallest dimension of the cone of rays and is found between these foci. At the Gaussian image plane, a second, larger disc exists called the spherical aberration disc. The radius of this is given by,

$$r_{sph} = C_s \alpha^3 \tag{2.4}$$

where C_s is the spherical aberration coefficient of the lens and α is the lens semi-collection angle. This is used to define the effect of spherical aberration on resolution. Similar image degradation is caused by chromatic aberration and astigmatism with radii defined as,

$$r_{chr} = \frac{C_c \Delta E \alpha}{E_0} \tag{2.5}$$

$$r_{ast} = \alpha \Delta f \tag{2.6}$$

where C_c is the chromatic aberration coefficient of the lens, ΔE is the energy loss of the electrons, E_0 is the initial beam energy and Δf is the maximum difference in focus induced by the astimatism. However, in electron microscopy the high accelerating voltages and thin film specimens can reduce the chromatic aberration considerably, whilst stigmator coils can be used to introduce compensating fields to balance the inhomogeneities. An approximate practical resolution at Scherzer defocus can therefore be found by taking the theoretical and spherical aberration expressions into account and ignoring the astigmatism and chromatic aberration [48]. These are added in quadrature,

$$r = [(\frac{0.61\lambda}{\alpha})^2 + (C_s\alpha^3)^2]^{1/2} \tag{2.7}$$

and used to calculate an optimum value for α which minimises r,

$$\alpha_{opt} = \frac{0.77\lambda^{1/4}}{C_s^{1/4}} \tag{2.8}$$

Substituting this into equation 2.3 then gives the practical resolution, r_p,

$$r_p = 0.91(C_s\lambda^3)^{1/4} \tag{2.9}$$

Typical values of λ and C_s, 2.5pm and 1.2mm respectively, give a point-to-point resolution of 3.4Å.

2.4 Structural characterisation

2.4.1 Electron-specimen interactions and image contrast

In order to be able to see details of a specimen in the TEM, we rely on image contrast. Contrast is defined as the difference in intensity between two neighbouring areas and is given by the equation,

$$C = \frac{I_1 - I_2}{I_2} = \frac{\Delta I}{I_2} \tag{2.10}$$

where I_1 and I_2 are the intensities of the adjacent areas and ΔI is the intensity variation. This difference in intensity is caused by electron-specimen interactions. When the incident beam travels through the sample, some electrons pass straight through unaffected by the specimen whilst a fraction are scattered by a variety of processes, affecting both the spatial and angular distribution. These interactions produce forward and backscattered electrons, as well as a large number of secondary signals (Fig. 2.8). In effect, an initial uniform distribution of illumination emerges from the sample with a non-uniform intensity, and this is what allows details of the specimen to be observed.

The human eye is not able to detect changes in intensity of less than ~5% [48], so specimen contrast must exceed this threshold unless electronic processing techniques are applied to digital images. Electrons can undergo changes in both amplitude and phase, and as a result, there are two fundamental types of contrast in the image: amplitude contrast and phase contrast. Normally both types of contrast contribute to the image but one may dominate. Specimens that alter the amplitude of transmitted radiation are referred to as 'amplitude objects' and can be observed in the microscope as a consequence of their ability to absorb or scatter the illumination. The greater the degree of scattering from a given region of the specimen, the darker the corresponding area of the image appears. In TEM/STEM the three main types of amplitude contrast in the images are mass-thickness, Z and diffraction contrast.

Many specimens, however, do not produce significant amplitude contrast so different techniques are required to image their detail. Phase contrast microscopy overcomes this problem by making use of the change in phase incurred by the illumination from specimens called 'phase objects'. In electron microscopy, phase changes are often produced by changes in electric and magnetic field. They occur when the incident wavefront at a particular region in the sample is slightly advanced or retarded relative to the surrounding area, giving constructive and destructive interference. For phase contrast microscopy to work, however, the illumination must have a degree of coherency that is preserved throughout the imaging system so that this phase change can be transferred to the image plane. Examples of phase contrast include lattice fringes (High resolution TEM), Moiré fringes and Fresnel contrast.

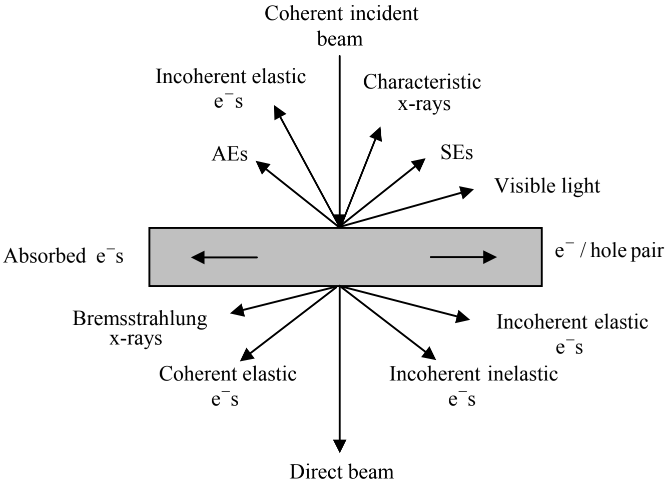

Fig. 2.8: The various electron-specimen interactions produce forward and backscattered electrons as well as a large number of secondary signals.

2.4.2 FEI Tecnai T20 TEM

The structural characterisation in this thesis was performed using an FEI Tecnai T20 TEM [51] (Appendix Fig. A.1). This is a fairly standard commercial microscope which uses a LaB_6 electron source, but includes a couple of additional features. Built into the lower polepiece of the objective lens (sketched below this lens in the diagram) is a Lorentz lens which enables imaging of magnetic specimens in a field-free environment. This will be discussed in the next section, where similar lenses installed in the CM20 TEM/STEM were used for magnetic imaging. In addition, below the microscope column, a Gatan Image Filter (GIF) has been installed to allow energy filtered imaging. On passing through the GIF aperture, electrons are deflected by a magnetic prism and a chosen energy range is selected using the energy slit. This enables the user to map specific elements by allowing only those electrons that have suffered a corresponding energy loss to contribute to the image. Following selection, a final lens projects the image onto a CCD or off-axis TV camera. Energy filtering was not required for this work, but the GIF was used for capturing BF and DF images of the continuous film samples.

2.4.3 Bright-field and dark-field imaging

The two fundamental operations of a TEM are the formation of an image and electron diffraction pattern on the viewing screen. To observe an image of the specimen, the intermediate lens is set so that the object of this lens is the image of the objective lens produced at the first image plane. On the other hand, if the diffraction pattern is required, then the intermediate lens is weakened so that the back focal plane of the objective lens (at which the DP is formed) becomes the object.

When the diffraction pattern is projected onto the viewing screen it contains a bright central spot produced by the direct electrons and several spots or rings produced by the scattered electrons. The diffracted electron beams can be selected using the objective aperture to produce either bright-field (BF) or dark-field (DF) images. To produce a BF image, the aperture is centred around the direct beam, allowing only the unscattered electrons to contribute to the image (Fig. 2.9a).

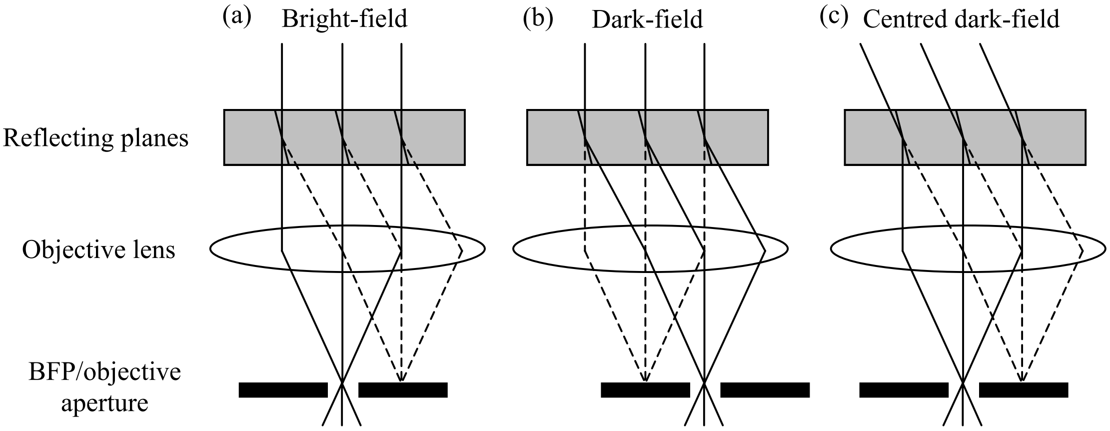

Fig. 2.9: The formation of BF and DF images is achieved by centering the objective aperture around the (a) central and (b) diffracted beams respectively. (c) A CDF image can be formed by tilting the incident beam to the Bragg angle.

If this aperture is moved and centred around one (or some) of the diffracted beams, then a DF image is produced (Fig. 2.9b). In this DF arrangement, however, the selected electrons travel off-axis and suffer from aberrations and astigmatism. This is avoided by tilting the incident beam onto the specimen at an angle equal to the Bragg angle. In this situation, the scattered electrons travel down the optic axis and the direct electrons off-axis. The objective aperture is centred around the scattered beam to produce a centred dark-field (CDF) image (Fig. 2.9c). BF and (220) DF images of the polycrystalline grains in a MTJ film are shown in Fig. 2.10 as an example.

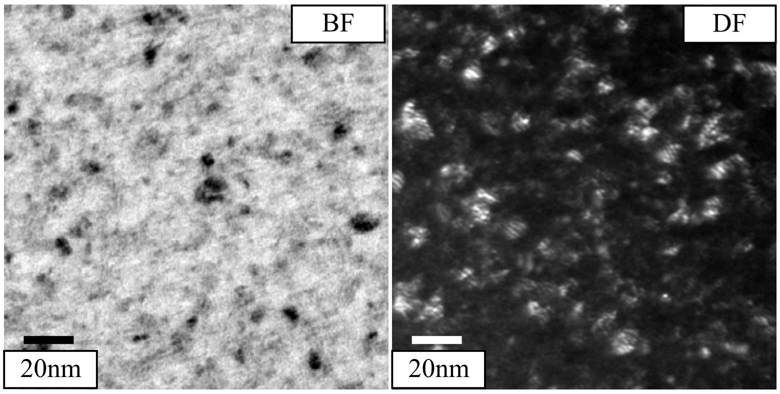

Fig. 2.10: Plan-view BF/DF images of polycrystalline grains in a continuous film MTJ stack. These images were acquired using the central and (220) spots from the fcc diffraction pattern.

2.4.4 Electron diffraction

Diffraction is a term which refers to the bending of waves on passing through an aperture. It occurs with any type of wave and results in the formation of an interference pattern behind the scattering object. When the pattern is produced at a large distance from the object, the rays are effectively parallel and the diffraction is referred to as Fraunhofer diffraction, but when the pattern is close to the diffracting object, the parallel beam approximation cannot be used and the diffraction is called Fresnel diffraction.

Here, the emphasis is on Fraunhofer diffraction produced when electrons in the TEM interact with the specimen and are scattered elastically to produce intense coherent beams. The electron waves are scattered by the periodic arrangement of atoms in the crystal with each atom acting as a point source of spherical wavefronts. When the electrons interact with the electron clouds of the atoms, they can be scattered at various angles. However, some electrons in this beam are incident on the atomic planes at a critical angle (Bragg angle) and are 'reflected' in-phase with electrons from neighbouring planes, resulting in constructive interference of significant intensity.

If two waves are incident at angle, θ, on a set of lattice planes, denoted by Miller indices (hkl), within the crystal, they will be reflected at an equal angle and will interfere with one another. As can be seen in Fig. 2.11, if these planes have spacing, d, then the path difference between the two waves is 2dsinθ. For constructive interference to occur, Bragg's law must be satisfied,

$$n\lambda = 2d\sin\theta \tag{2.11}$$

It is important to note here that since $\sin\theta \le 1$, Bragg reflection can only occur for $\lambda \le 2d$ which is why it is not possible to produce diffraction patterns from crystals using visible light.

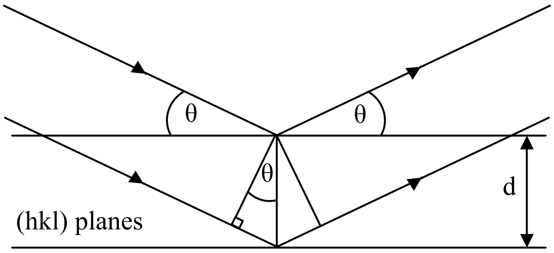

Fig. 2.11: Two electrons waves incident on a set of lattice planes (hkl) are reflected in-phase when their path difference is equal to an integer number of wavelengths.

Within a crystal, each set of atomic planes has a different inter-plane spacing, d. For a cubic lattice, this spacing is given by,

$$d = \frac{a}{\sqrt{h^2 + k^2 + l^2}} \tag{2.12}$$

where a is the lattice parameter and h, k, l are the Miller indices for the set of lattice planes. Electrons that are Bragg scattered emerge from the crystal suffering a deflection of 2θ with respect to the incident beam direction (Fig. 2.12). Since all electrons that pass through the specimen are brought to focus in the back focal plane of the objective lens, the diffraction pattern is produced in this plane.

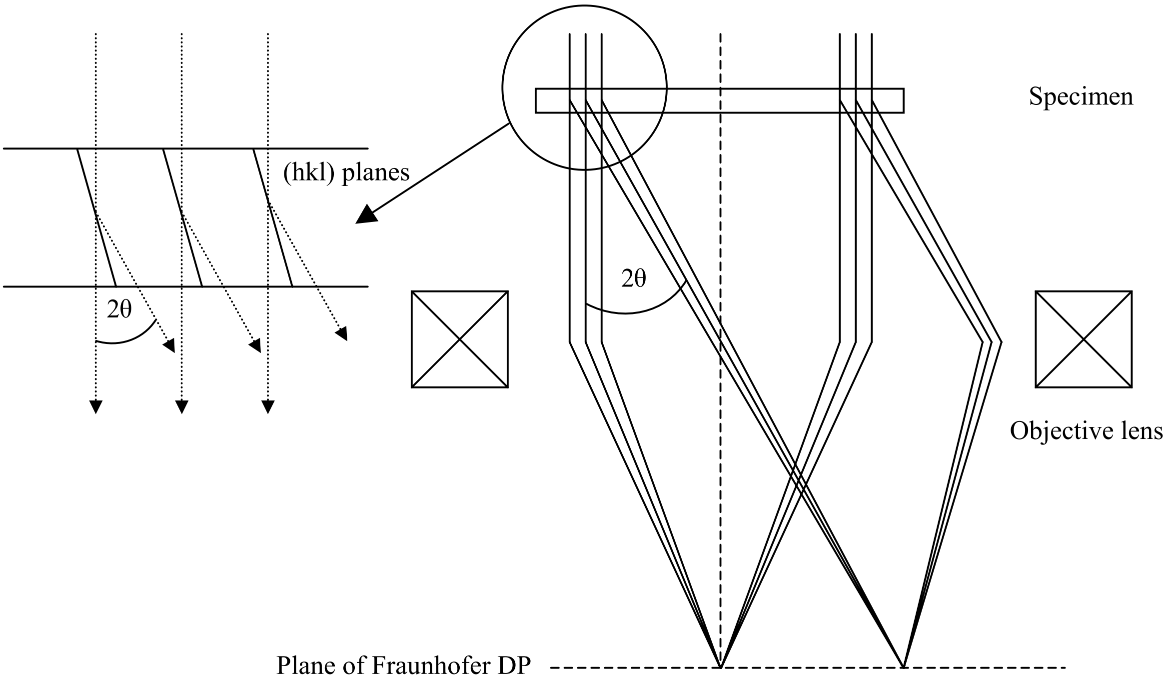

Fig. 2.12: Parallel rays entering the objective lens are brought to focus at the back focal plane. The Bragg scattered electrons therefore form a diffraction pattern in this plane.

In a single crystal diffraction experiment, the electron wavelength, beam direction and d-spacing for each set of planes are fixed. Therefore, only certain lattice planes are able to satisfy the Bragg condition and produce an intense beam. The beams for each of these allowed reflections results in a series of spots being produced (Fig. 2.13a). By tilting the specimen, different (hkl) planes are able to produce Bragg scattering and the diffraction pattern changes.

With polycrystalline samples however, all possible orientations of crystallite are present and a ring pattern is produced (Fig. 2.13b). This pattern appears as a superposition of many single crystal spot patterns. If the grain size in the material is small then continuous rings are produced, but if larger grains are present the rings are made up of discrete spots and appear speckled. Also, as the probability of scattering decreases with angle, the spots and rings decrease in intensity the further they are from the centre.

Crystalline texturing is the distribution of crystallographic orientations of the grains in a polycrystalline material [52]. Texturing is present in the sample when some preferred orientation exists, and the degree of texturing is dependent on the percentage of crystallites with that particular orientation. When tilting a non-textured polycrystalline specimen the diffraction pattern remains constant. If texturing is present, however, then the intensity varies within the rings and arcs are produced (Fig. 2.13c). This pattern exists because, despite the texturing in one dimension, the crystallites are still randomly oriented about this direction. Also, when tilting a textured sample, the intensity along the tilt axis remains constant. This occurs because the plane spacing is unaltered relative to the incident beam direction.

Diffraction can also be performed with amorphous materials. Amorphous solids are non-crystalline and have no long range order. When electrons are scattered from an amorphous material a series of fuzzy rings are produced (Fig. 2.13d) with the ratio of these rings being related to the average nearest neighbour distances in the material.

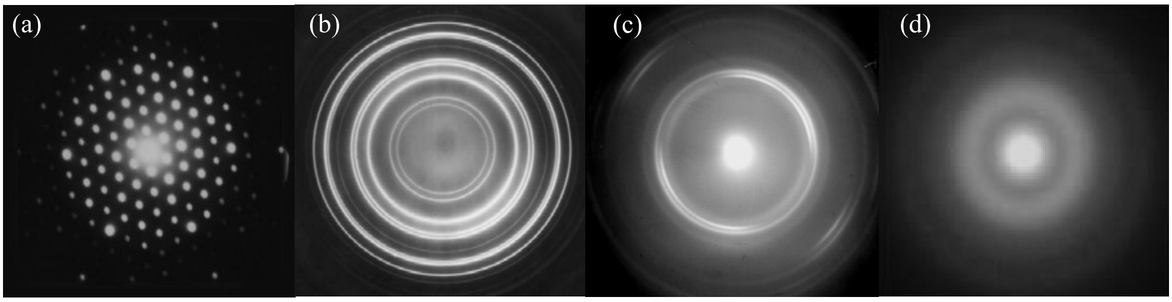

Fig. 2.13: Typical electron diffraction patterns produced by (a) single crystal, (b) non-textured polycrystalline, (c) textured polycrystalline and (d) amorphous materials.

2.5 Magnetic characterisation

2.5.1 Electron-specimen interactions

The way in which electrons interact with a ferromagnetic specimen is of great importance to this thesis. This interaction can be described using both classical and quantum mechanical approaches [53].

Classical approach

As mentioned earlier, electrons in the beam are deflected by magnetic fields, which is why electromagnetic lenses are used for focussing. However, this Lorentz force is also present when the electrons encounter a magnetic specimen, and this enables us to image the magnetic structure. Fig. 2.14 shows electrons passing through a thin ferromagnetic film which is split into three domains separated by two 180° domain walls. The directions of magnetisation are in the plane of the specimen as indicated.

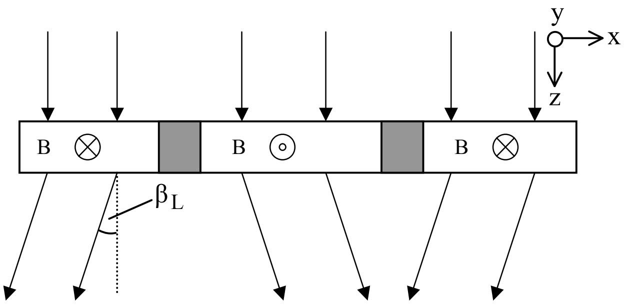

Fig. 2.14: The Lorentz deflection of an incident electron beam as it passes through a uniform thin ferromagnetic film.

A parallel beam, incident perpendicular to the plane of the film along the z-axis, experiences a deflection in the x-direction at angle β_L given by,

$$\beta_L(x) = \frac{e\lambda}{h}\int_{-\infty}^{\infty} B_y(x,y)dz \qquad (2.13)$$

where $B_y(x,y)$ is the y-component of magnetic induction at point (x,y), e is the electron charge, λ is the electron wavelength and h is Planck's constant. If stray field effects are ignored, the magnetisation is uniform (M_s) and the specimen is of constant thickness, t, equation 2.1 can be simplified to,

$$\beta_L = \frac{eB_0\lambda t}{h} \tag{2.14}$$

where B_s is the saturation induction $(B_s = \mu_0 M_s)$. For 200kV electrons passing through a 20nm thick film with a saturation induction of 1T, $\beta_L \sim 1.2 \times 10^{-5}\,\mathrm{rad}$. This is far smaller than a typical first order Bragg angle of $\sim 10^{-2}\,\mathrm{rad}$.

Quantum mechanical approach

A quantum mechanical description of this interaction is necessary when quantitative analysis is required or when interference effects must be considered. If two electrons originating from the same point travel different equidistant paths and rejoin, they will suffer a phase difference which is proportional to the magnetic flux through the surface defined by the two paths. This phase shift $\Delta\varphi$ is given by,

$$\Delta\varphi = \frac{2\pi e N}{h} \tag{2.15}$$

where N is the flux enclosed. In the case of a plane wave incident on the thin ferromagnetic film considered above, the phase shift between any two points x_1 and x_2 will be,

$$\Delta\varphi(x) = \frac{2\pi e t}{h}\int_{x_1}^{x_2} B_y(x)\,dx \tag{2.16}$$

As a result, a ferromagnetic specimen can be treated to first order as a pure phase object to the electron beam, and any amplitude modulation due to the physical structure of the material is neglected. Lorentz microscopy is therefore a branch of phase contrast microscopy.

2.5.2 Creating a field-free environment

The main imaging lens in most microscopes is the objective lens and this determines the overall resolution and performance of the instrument. When imaging non-magnetic materials, the specimen is normally located at the centre of the objective lens. However, in this region of the microscope a large field exists to focus the beam which makes it unsuitable for imaging magnetic samples. This field would destroy the magnetic information which is to be studied so the objective lens has to be modified to allow for this type of imaging.

One way to achieve this is by using a three pole-piece setup with two gaps [54]. The central pole-piece acts to create a magnetic shield around the specimen, leaving the sample in field-free space. With this arrangement the objective lens can still be used for focusing and the resolution does not suffer too much. Another way of achieving field-free conditions is by incorporating additional Lorentz lenses into the upper and lower objective lens pole-pieces [55]. In this situation the objective is switched off and the Lorentz lenses are used for focusing. As these are not as strong as the objective lens, however, the resolution of the system is compromised. An advantage of this latter setup is that whilst imaging with the Lorentz lenses, the objective can be weakly excited to provide a controllable field in the specimen region, allowing in-situ magnetising experiments to be performed.

2.5.3 Philips CM20 TEM/STEM

The Philips CM20 TEM/STEM [56] (Appendix Fig. A.2) used for all of the magnetic imaging in this project has been highly modified with respect to the basic commercial microscope. This FEG system makes use of the upper and lower Lorentz lenses to enable in-situ imaging of magnetic specimens in both the Fresnel and differential phase contrast (DPC) modes of microscopy. In addition, the gap between the objective lens pole-pieces has been widened to allow a magnetising stage or specialised rods to be used for more complicated experiments. Below the projector lenses of the microscope there is an 8-segment detector for modified DPC (see later) as well as a CCD camera for CTEM experiments and a BF/ADF split detector for normal STEM imaging using the objective lens.

2.5.4 Fresnel imaging

The Fresnel mode of Lorentz microscopy [57] is a qualitative technique used to image the domain walls within a ferromagnetic film. To observe magnetic contrast, the imaging lens is defocused by an amount $\pm\Delta z$. This has the effect of raising or lowering the object plane relative to the specimen depending on whether the lens is under-focused or over-focused respectively. Referring to Fig. 2.15, the Lorentz deflection causes convergence and divergence of the electron beam at the domain walls.

If the electron source is sufficiently coherent (as with a FEG), fringes may be observed at large defocus due to the interference effects of the convergent electron wavefront. By positioning the object plane below the sample, dark and bright bands representing the domain walls (and edges of the material) are transferred to the image plane, whilst the domains themselves appear as regions of (near) uniform electron intensity. Focusing on the object plane above the specimen rather than below inverts the contrast. By extrapolating the rays back through the film, the regions of convergence and divergence are reversed and a virtual object is formed.

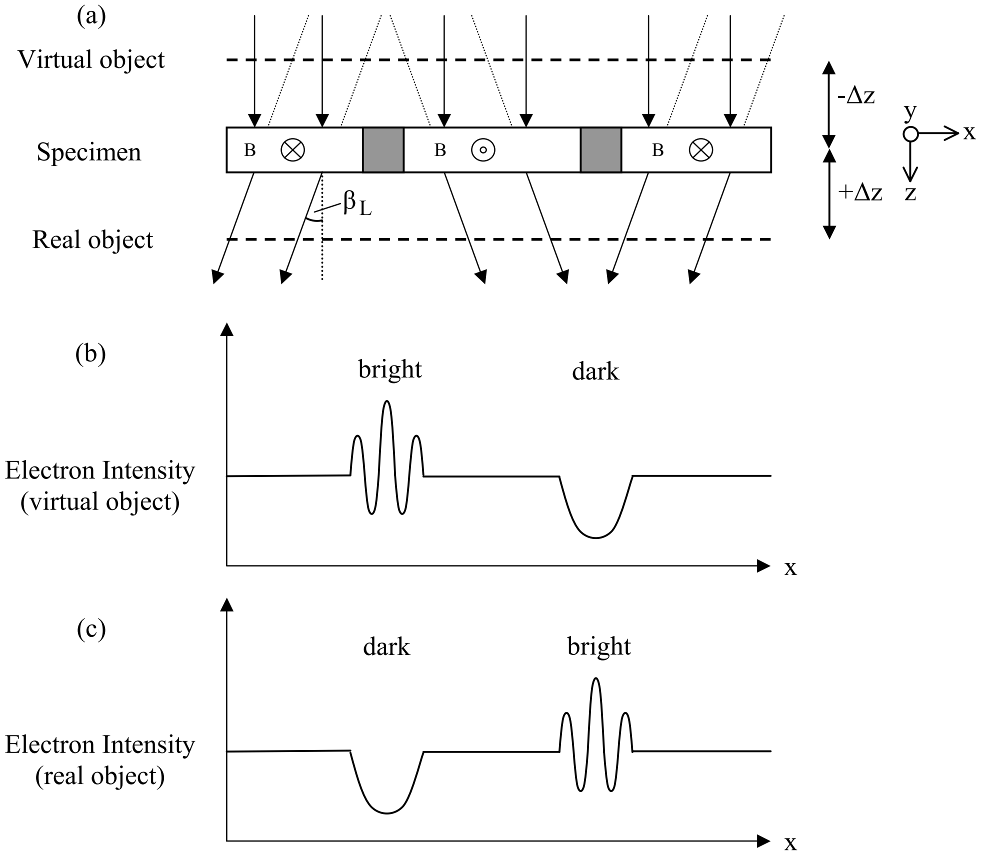

Fig. 2.15: (a) Domain wall contrast is observed in the Fresnel mode of Lorentz microscopy when the imaging lens is defocused. Under-focusing produces a (b) virtual object above the specimen and associated electron intensity whilst over-focusing produces a (c) real object below the specimen.

The level of contrast produced is highly dependent on the value of defocus. Large Δz values increase the contrast but also smear the information and reduce the resolution, whilst small Δz values make it difficult to observe the details of the magnetic state. A compromise is therefore required to obtain the best imaging conditions. In addition to the domain wall contrast, intensity variations exist at the edges of magnetic specimens as a result of magnetic and electrostatic phase contributions (Fig. 2.16a). This edge contrast can dominate the images of small features, drowning out the domain wall information. For this reason and the limited resolution of the technique, Fresnel is unsuitable for the observation of very small patterned elements with dimensions of < 200nm. However, the technique is particularly useful for studying the magnetic behaviour of continuous film specimens. In such samples magnetisation ripple is present within the domains, and this can be imaged in addition to the domain walls (Fig. 2.16b). As the direction of ripple lies perpendicular to the net moment of the domain, it is possible to deduce the axis of magnetisation.

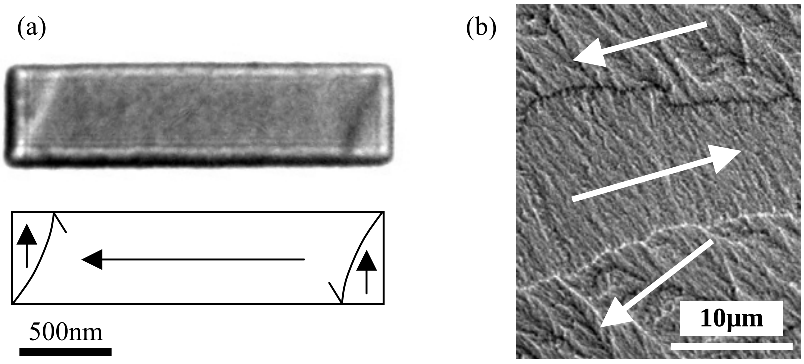

Fig. 2.16: Fresnel images of a (a) rectangular thin film element and a (b) continuous film multilayer specimen.

By knowing whether the lens is over or under-focused, however, it is also possible to determine the absolute directions of magnetisation. This is done using the domain wall contrast with the magnetisation ripple in continuous film specimens. In thin film elements without visible magnetisation ripple, the domain wall and edge contrast is required.

The advantages of Fresnel imaging for studying magnetic specimens include its ease of operation and the high levels of contrast. It is also well-suited to real-time in-situ imaging, allowing reversal sequences to be recorded during magnetising experiments. However, as previously mentioned, this technique is limited by poor resolution, which prevents the imaging of ultra small structures and makes it difficult to relate magnetic detail to topographic contrast. In addition, the non-linear relationship between intensity and magnetic induction mean that quantitative information is hard to obtain.

2.5.5 Differential phase contrast (DPC) imaging

Differential phase contrast imaging [58,59], unlike Fresnel, is performed in a STEM. This technique is used to observe and provide quantitative information on the magnetic induction of thin film samples [60,61]. After the probe passes through the specimen, the electrons emerge as a cone of illumination which is projected onto a circular quadrant detector. If a non-magnetic specimen is placed in the path of the beam the disc is centred on the detector. Alternatively, if a magnetic sample is used, the Lorentz force deflects the electrons and shifts the disc to a position that is no longer concentric (Fig. 2.17). Since each segment of the detector measures a separate electron intensity, difference signals taken from opposite segments provide information on the induction as contrast in the image. The (A + D) – (B + C), (A + B) – (C + D), A – C and B – D signals are acquired to map the induction in 45° directions. As the Lorentz force is perpendicular to both the induction and beam directions, the difference signals provide orthogonal maps of induction perpendicular to the deflection. In addition, by summing the signals from all four quadrants, a bright field image can also be produced.

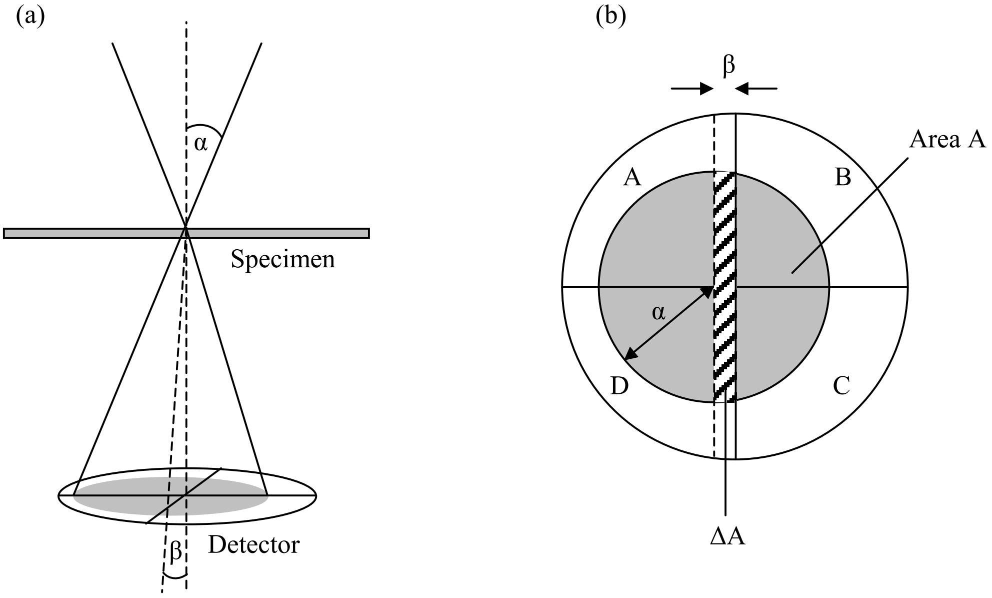

Fig. 2.17: (a) Magnetic specimens cause deflection of the beam which (b) shifts the disc on the surface of the quadrant detector.

The angle that the incident beam makes with the normal to the surface is denoted by α and is proportional to the radius of the disc on the detector. The deflection angle of the beam is again denoted by β. Therefore, when the disc is shifted a distance β on the detector, the area covered on region (B + C) decreases by ~2αβ. Likewise, this same area is transferred to region (A + D) resulting in an area difference, ΔA, of 4αβ between the two regions. The difference signal is given by,

$$S = \frac{I\Delta A}{A} \tag{2.17}$$

where I is the electron intensity and A is the total area of the spot on the detector. This can therefore be rewritten as,

$$S = \frac{I}{\pi\alpha^2}[(\frac{\pi\alpha^2}{2} + 2\alpha\beta) - (\frac{\pi\alpha^2}{2} - 2\alpha\beta)] = \frac{4I\beta}{\pi\alpha} \qquad (2.18)$$

The main implication of this calculation is that the difference signal produced is linearly proportional to the Lorentz deflection which, as was shown earlier, is directly related to the integrated magnetic induction. Therefore, making the same assumptions about the sample as before, we have,

$$S = \frac{4IeB_s\lambda t}{\pi\alpha h} \qquad (2.19)$$

It is important to note that this relationship only holds when the deflection is small, i.e. $\beta < \alpha/10$. If the deflection is larger than this, linear imaging is not possible. The resolution of the image produced is approximately equal to the diameter of the probe, which varies depending on whether the system is being used in the high magnification scanning (HMS) or low magnification scanning (LMS) modes (Fig. 2.18).

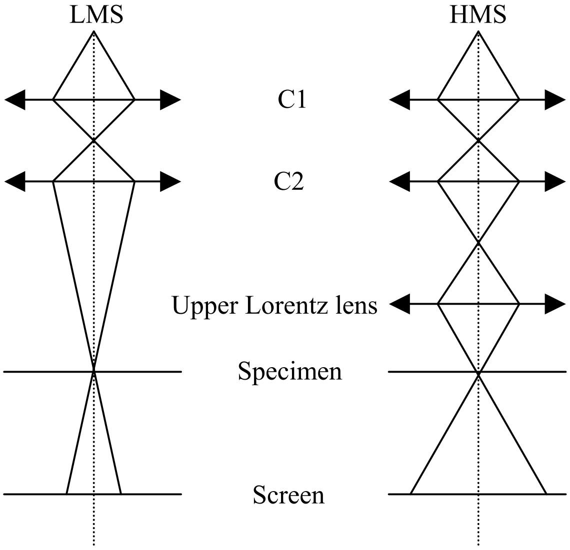

Fig. 2.18: LMS DPC uses the C1 and C2 lenses to form the probe whilst HMS requires the use of the upper Lorentz lens to condense the beam further.

A greater useful magnification is achievable in HMS by scanning a smaller area of the sample with a finer probe. In LMS the upper Lorentz lens is turned off, resulting in a larger probe at the specimen and smaller probe angle. With this setup a resolution of ~ 30nm is common. Also, since $\beta \sim \alpha/10$ (depending on magnetic sample), the DPC signal is very sensitive to changes in magnetic induction and high contrast is produced. In HMS the use of the upper Lorentz lens forms a small probe with large probe angle. However, as, $\beta \sim \alpha/1000$, the signal is less sensitive to changes in induction and the contrast suffers. The resolution of DPC is limited by two factors: the coherent and incoherent limits. The coherent limit was discussed earlier and is imposed by diffraction and spherical aberration. Remembering that the probe size, P, is proportional to $\lambda / \alpha + C_s \alpha^3$, the probe angle, α, can be chosen to minimise P (Fig. 2.19a). The incoherent limit, however, arises from the fact that the probe cannot be demagnetised to a point, but has a finite size. Of the two effects, this has the largest contribution and confines the probe size to just less than 10nm.

When performing DPC, it is necessary for the beam to remain stationary with respect to the detector whilst scanning. This ensures that deflections caused by the magnetic induction are the only shifts of the beam from the central position. To achieve this, descan coils are used after the beam has passed through the specimen (Fig. 2.19b).

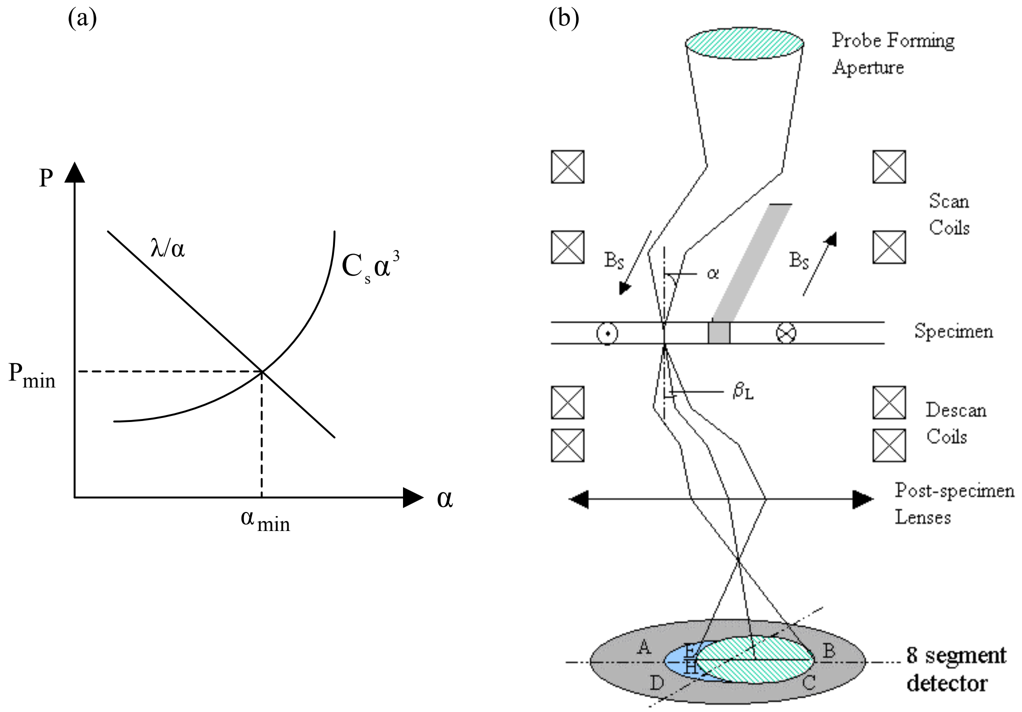

Fig. 2.19: (a) The probe size can be minimised by varying the incidence angle, α. (b) Descan coils below the specimen ensure that the only shift of the spot on the detector is due to the Lorentz deflection.

2.5.6 Modified differential phase contrast (MDPC) imaging

Despite the ability of DPC imaging to provide quantitative magnetic information, there is an inherent problem with the system: the data obtained from a real specimen contains both magnetic and non-magnetic components such as physical microstructure and crystalline potentials. These contributions often conceal some of the magnetic data. This problem is reduced with the use of an 8-segment detector (Fig. 2.20a) instead of its quadrant counterpart, which changes the efficiency with which different spatial frequencies are transferred to the image [62]. Since the spatial frequency of the crystallite contrast is greater than that of the magnetic contrast, detection of these lower frequencies with greater efficiency results in a boost of the magnetic signal at the expense of the crystallite signal (noise). The only parts of the electron distribution which carry information in the difference signal are those involved in the overlap of the scattered and unscattered beams. For low frequency magnetic components, this overlap is at the edge of the unscattered cone. Therefore, by collecting difference signals from the annular quadrants of the detector, the magnetic signal is preferentially detected. When implementing this technique, an important consideration is the value of κ, defined as,

$$\kappa = \frac{k_i}{k_\alpha} \tag{2.20}$$

where k_i and k_α are the radii of the inner annulus and the bright field cone respectively (Fig. 2.20b). The variation in signal to noise with reduced spatial frequency, k_r, in one dimension is given in Fig. 2.20c, where,

$$k_r = \frac{k_x}{k_\alpha} \tag{2.21}$$

and k_x is the spatial frequency along the x-axis. As κ is increased, the high frequency contribution is suppressed and the signal to noise ratio enhanced. Therefore κ should be set close to 1 so that the disc impinges only slightly onto the outer quadrants; achieved simply by adjusting the post-specimen lenses.

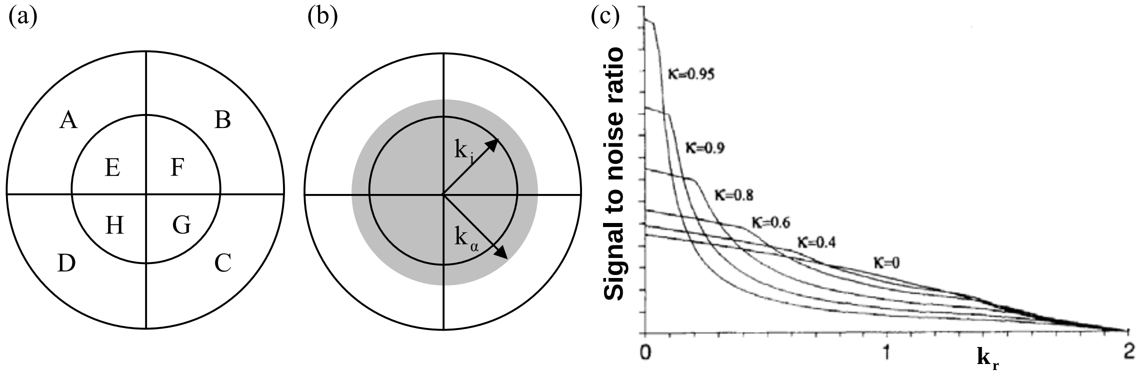

Fig. 2.20: (a) The 8-segment detector and (b) spatial frequency vectors for MDPC. (c) The variation of signal to noise with reduced spatial frequency for different values of κ.

The advantages of using DPC to study ferromagnetic films are that it can be used to recover quantitative magnetic information at a resolution of below 10nm. Due to the phase gradient experienced by the electron beam between areas containing the magnetic film and those with only the supporting substrate, however, edge contrast is also present in DPC images. As it is an in-focus technique though, these fringing effects are smaller than in Fresnel images, so DPC is the preferred option for the study of sub-micron sized elements. The main disadvantage is that the instrumental setup is a lengthy procedure, so the average DPC experiment requires far more time to complete than those performed in the Fresnel mode. Fig. 2.21 shows MDPC images of a thin film element and continuous film specimen.

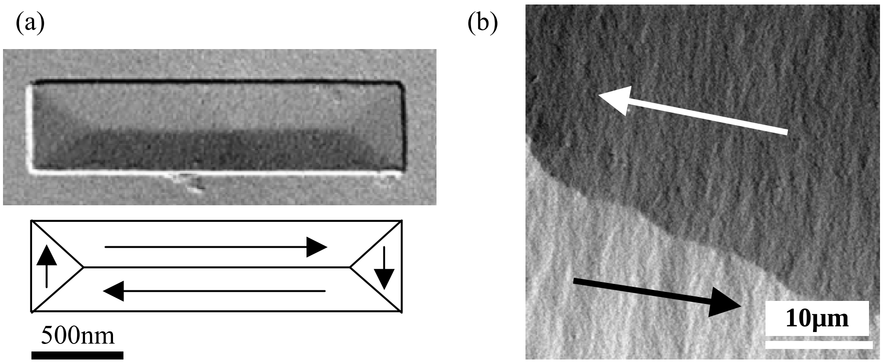

Fig. 2.21: DPC images of a (a) rectangular thin film element and (b) continuous film multilayer specimen.

2.5.7 In-situ magnetising experiments

To study the dynamic behaviour of ferromagnetic films, fields were applied in-situ. This is achieved in the Philips CM20 by weakly exciting the objective lens to provide a field and using the Lorentz lenses to image. When current is passed through the lens coils a vertical field, **H**, is produced in the specimen region. The direction of this field (up or down) can be controlled by passing the current through the coils in the forward or reverse directions respectively. With the specimen held in the horizontal position (0° tilt) the field is perpendicular to the plane of the film and there is no in-plane component. However, when the specimen is tilted at an angle, θ°, it encounters a field component parallel to the specimen plane, $\mathbf{H}_{||}$, given by,

$$\mathbf{H}_{||} = \mathbf{H}\sin\theta \tag{2.22}$$

Therefore, the in-plane field can be controlled by tilting the specimen to different angles (Fig. 2.22). The maximum field, experienced at 90° tilt, is determined by the current through the objective lens and can have any value up to ~7000 Oe. A problem associated with this technique though, is that the component of field perpendicular to the sample, $\mathbf{H}_{\perp}$, can affect the magnetisation. This sensitivity to the perpendicular component lowers the in-plane field necessary to reverse the magnetisation and can allow the formation of magnetic states which would otherwise be difficult to form.

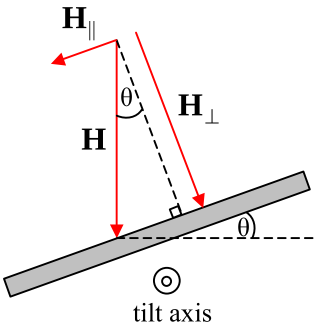

Fig. 2.22: Tilting of the specimen about the rod axis introduces a variable field component in the plane of the film. The magnitude of this component is determined by the vertical field produced by the objective lens coils and the angle of tilt.

Chapter 3

Fabrication of thin film elements and continuous film specimens

3.1 Introduction

Nanotechnology [63] is a multi-disciplinary science that deals with the production of materials and devices at the nanometre scale. The fabrication involved incorporates a variety of subjects including physics, chemistry, engineering and computer science amongst others, and pushes existing methodologies to the limit. In general, nanofabrication techniques fall into two main classes called ‘top-down’ and ‘bottom-up’. Top-down fabrication [64] is the more traditional approach and includes lithography, soft-lithography and masked deposition. It can be thought of as carving away material from a larger component to build smaller structures. Although these techniques are becoming reasonably well understood and have demonstrated major success, resolution and reproducibility problems are being encountered as smaller feature sizes are required. Bottom-up techniques [65] on the other hand create structures by assembling smaller components, and include molecular assembly, nanoparticle formation and probe lithography. This approach can be used to fabricate smaller features, but the techniques themselves are still relatively new and it is difficult to create more complex patterns. Attempts are currently being made to integrate top-down and bottom-up techniques to develop a more reliable method of fabricating nanoscale structures.

Nanofabrication has to be performed in a specially constructed and environmentally controlled laboratory called a cleanroom. Cleanroom facilities use air filters and continuous circulation to produce levels of air borne particles that are far lower than normal atmospheric dust levels. The cleanliness of a cleanroom is represented by its class. A class 1 area has less than 1 particle/ft^3 greater than 0.5μm in size whilst a class 100 area has less than 100 particles/ft^3. In general, cleanroom levels begin at 100,000 particles/ft^3, but the better the class the smaller the structures are that can be fabricated without contamination. As well as cleanliness, cleanrooms are designed to control tempertaure, humidity, air pressure, vibration, noise and lighting, all of which are factors that greatly affect the fabrication procedures. The majority of the fabrication performed in this thesis was carried out in the James Watt Nanofabrication Centre (JWNC) at Glasgow University, a newly built, top of the range facility with rooms ranging from class 10,000 to class 10.

During processing of the substrate it is necessary to keep the surface as clean as possible without any material residue, as this can seriously reduce the quality of the finished sample. To clean the substrate, high purity organic solvents are used. These strip off most organic matter and any particles of dust. The wafer is first immersed in acetone and the beaker placed into a hot water bath. Following this, the sample is transferred to a beaker of isopropyl alcohol (IPA) and returned to the bath. IPA dissolves the acetone on the substrate surface without leaving drying marks. Finally, a fast jet of nitrogen gas is used to blow-dry the surface. If different solvents with higher boiling points are used for cleaning, then an oven can be used for drying after the nitrogen gas.

3.2 Electron transparent substrates

A lot of the experimental work in this project involved characterisation of the magnetic behaviour of both thin film elements and continuous film specimens using TEM. To enable TEM analysis, the samples have to be thin enough to ensure electron transparency. Normally films thinner than 100nm are suitable for use with 200kV electrons, and these must be supported on a substrate that allows the passage of electrons through the regions of interest whilst remaining strong enough to withstand handling.

3.2.1 TEM membranes

The substrate of choice is a 50nm thick, $100 \times 100\,\mu\text{m}^2$ Si_3N_4 membrane 'window' supported on 500μm thick bulk silicon [66]. These samples are made in two main sizes, $2 \times 2\,\text{mm}^2$ single membranes for deposition of continuous films or patterning with a focused ion beam (FIB) and $9 \times 9\,\text{mm}^2$ blocks of 4 for electron beam lithography. Schematics of these specimens are given in Fig. 3.1. The bulk silicon is wet etched through a mask of Si_3N_4 on the back of the substrate to leave the Si_3N_4 membrane on the opposite side. For lithography, an etched topographic cross and markers are used to direct the electron beam to the transparent regions, whilst cleave lines allow separation of the individual membrane substrates for subsequent TEM analysis.

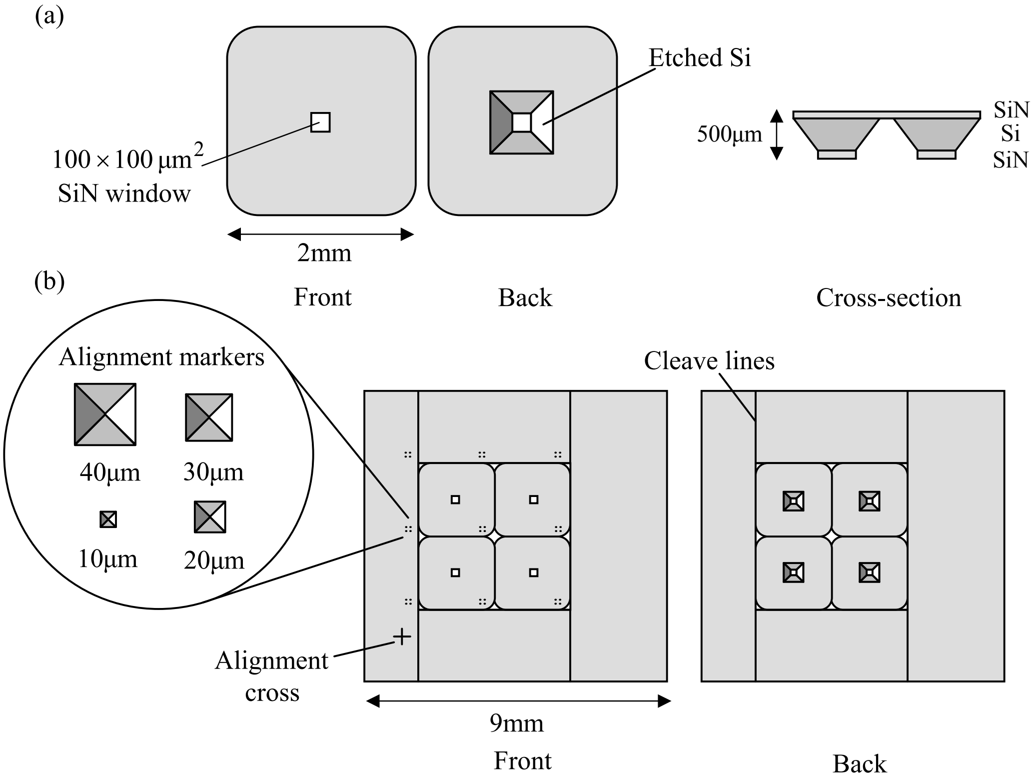

Fig. 3.1: (a) Front, back and cross-section schematic diagrams of a single SiN membrane substrate. (b) Block of 4 membranes used for electron beam lithography.

The membrane substrates are made in bulk quantities by Kelvin Nanotechnology Ltd (KNT) based in the Department of Electronics and Electrical Engineering at the University of Glasgow. Generally, two 4-inch (100) Si wafers are used to produce 90 $9 \times 9\,\mathrm{mm}^2$ blocks and 600 $2 \times 2\,\mathrm{mm}^2$ singles, assuming 100% yield. In reality, however, accidental damage by handling and cleaving reduces the number of useable substrates.

3.2.2 TEM cross-sections

To properly understand the magnetic behaviour of thin film samples, it is often a requirement to characterise the physical structure of the material. Currently, multilayer samples that exhibit novel electronic, magnetic, mechanical and optical properties are of great interest. To a large extent these properties are dependent on the quality of the interface between the different layers of the structure and frequently, their composition varies widely on the nanometre scale. The MTJ samples discussed in this work are examples of this kind of specimen and so structural characterisation was performed to compliment the magnetic study. As well as examining these samples in-plane, TEM cross-sections were fabricated to enable a detailed understanding of their physical make-up. The encapsulation technique [67] (Fig. 3.2) used to make the cross-sections uses conventional fabrication methods and does not require the use of a cleanroom facility. This was performed by Mr Brian Miller in the Department of Physics and Astronomy at the University of Glasgow.

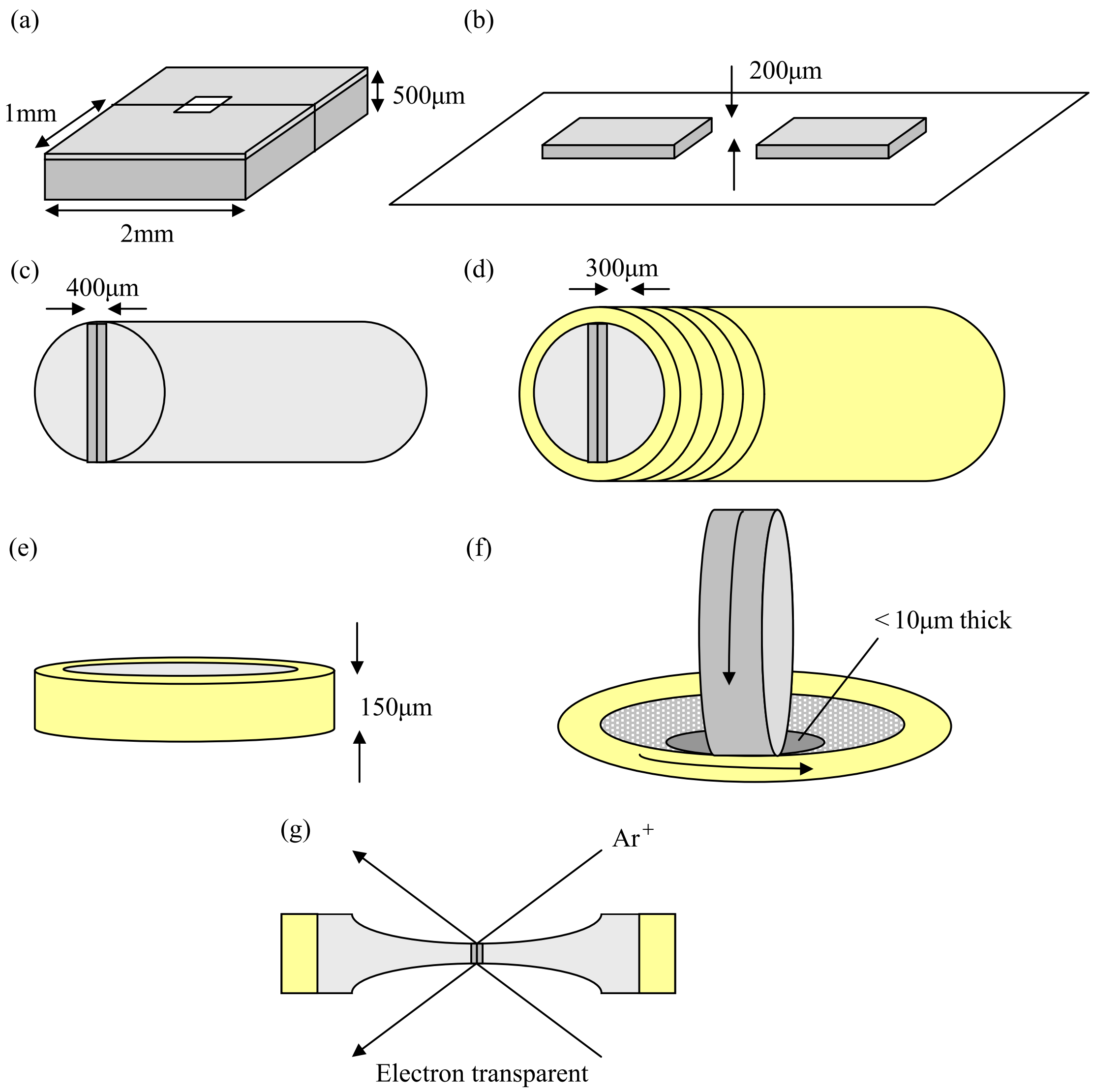

Fig. 3.2: The membrane substrate is (a) cleaved into halves and (b) ground to fit inside a slot cut from a (c) Mo rod. The pieces are then glued and encapsulated by a (d) brass tube before being sliced into (e) thin discs. The discs are ground, (f) dimpled and (g) ion milled until they are electron transparent.

First the membrane substrates (onto which the films of interest are deposited) are cleaved in half (Fig. 3.2a) and ground until both pieces are of equal length and width. The 500μm thick pieces are then placed onto a glass slide and thinned to 200μm using a hand grinder (Fig. 3.2b) before being glued face-to-face with an epoxy resin and held together in a 400μm wide slot cut from a molybdenum rod (Fig. 3.2c). This assembly is then coated in epoxy, slid into a brass tube (Fig. 3.2d) and cured at 130°C to set the glue. Once cooled, 300μm thick discs are cut from the tube and ground on both sides until a total thickness of 150μm is achieved (Fig. 3.2e). To reach electron transparency, a dimple grinder and precision ion polishing system (PIPS) are required. Dimple grinding from either side produces a 10μm thick spherical indentation (Fig. 3.2f) before ion milling gently thins the remaining material during the latter fragile stages (Fig. 3.2g).

3.3 Lithography

Lithography [68] was originally defined as a process of obtaining prints from a stone or metal surface. These days, however, it refers to the transfer of a pattern of geometric shapes from a physical or electronic mask onto the surface of a substrate, often a semiconductor. The designed pattern is written onto an intermediate organic compound called a resist which is applied to the surface of the substrate, exposed to a beam of particles or electromagnetic radiation and developed. Following development, the substrate is etched or metallised to produce the pattern using the resist profile. A variety of different techniques have been developed to enable micro and nano scale lithography using different sources of radiation. These include photo or optical lithography (UV), particle lithography (electrons, protons), x-ray lithography and ion-beam lithography (Ga^{+}). Each has particular advantages/disadvantages in terms of resolution, registration and pattern transfer time.

3.3.1 Electron beam lithography

Electron beam lithography (EBL) as the name suggests, uses a beam of electrons to expose the resist and offers major advantages over photolithography. The resist itself is sensitive to electrons and not electromagnetic radiation. As the wavelength of the electrons is much shorter (10^{-12} m) than that of UV (10^{-7} m), an electron beam is capable of patterning at a far higher resolution, allowing features down to ~10nm to be written, taking into account spherical and chromatic aberrations. Instead of using a physical mask to define the pattern, the beam is computer controlled and exposes regions as determined by an electronic computer-aided design (CAD) mask. Although the ability to create any pattern electronically without the need to fabricate expensive mask plates makes e-beam a highly flexible tool, the exposure process occurs serially, pixel-by-pixel, resulting in a large writing time. This, together with the high equipment and maintenance costs are the main drawbacks of the technique. As well as being able to write single step jobs, electron beamwriters are capable of aligning a substrate (registration) to within ~50nm, allowing users to write multiple lithography steps for more complex samples. This is a further improvement on photolithography which uses a mask aligner to set the wafer to within ~1µm.

3.3.2 E-beam system

Electron beamwriters in general are very similar in design to scanning electron microscopes. The tool used for this work was a Leica-Cambridge Electron Beam Pattern Generator (EBPG5 HR100), capable of accelerating voltages of up to 100kV [69]. A schematic diagram of this system is given in Fig. 3.3 indicating the main components.

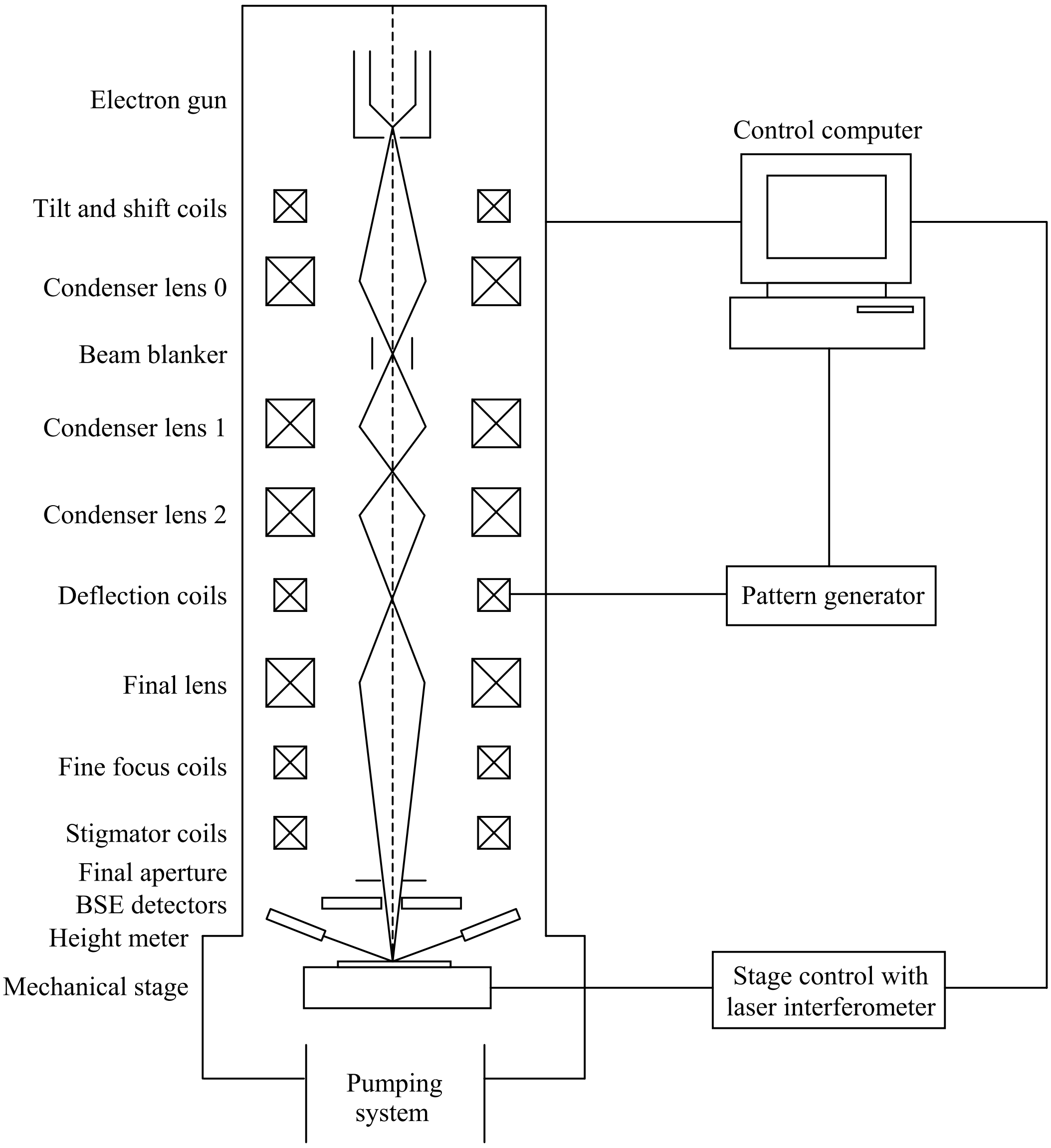

Fig. 3.3: The EBPG5 HR100 beamwriter used for electron beam lithography.

The electrons are generated by a LaB_6 source at the top of the column and are directed along the optic axis by tilt and shift coils. Following this, condenser lens 0 focuses the beam onto a blanking plate which switches the beam on and off during exposure. Two further condenser lenses, 1 and 2, are used to control the beam diameter on the substrate whilst deflection coils scan the probe across the surface under computer control. A final (objective) lens provides focusing of the spot and fine focus coils offer correction for beam deflections and sample height variation. Below these, stigmator coils are used to correct any astigmatism in the deflected beam and a final aperture controls the current density of the electron probe. In addition to the lenses and apertures used to control the beam, the column is fitted with backscattered electron (BSE) detectors for imaging, as well as a height meter to ensure the substrates lie flat with respect to the specimen stage. Here a laser beam is reflected off the surface to measure changes in distance between the sample and final lens. Below the sample, a mechanical stage is able to move the substrate in two dimensions under precise control using a laser interferometer. The complete system operates under high vacuum and a series of pumps are located below the stage to evacuate any gaseous contamination.

3.3.3 Design and layout files

In order to pattern a substrate using the electron beamwriter, the control computer must have the design and job layout files. In this work the CAD program L-Edit was used to produce the pattern (.gds file). Within the one file, L-Edit allows the user to create several individual cells or structures which can be brought together to make up the final design. In addition, several layers can be specified if multiple lithography steps are required. However, .gds files (as produced by most CAD programs) are not beamwriter compatible, as the machine is only able to handle primitive shapes. Additional processing steps are therefore required to convert the file to a suitable format (Fig. 3.4).

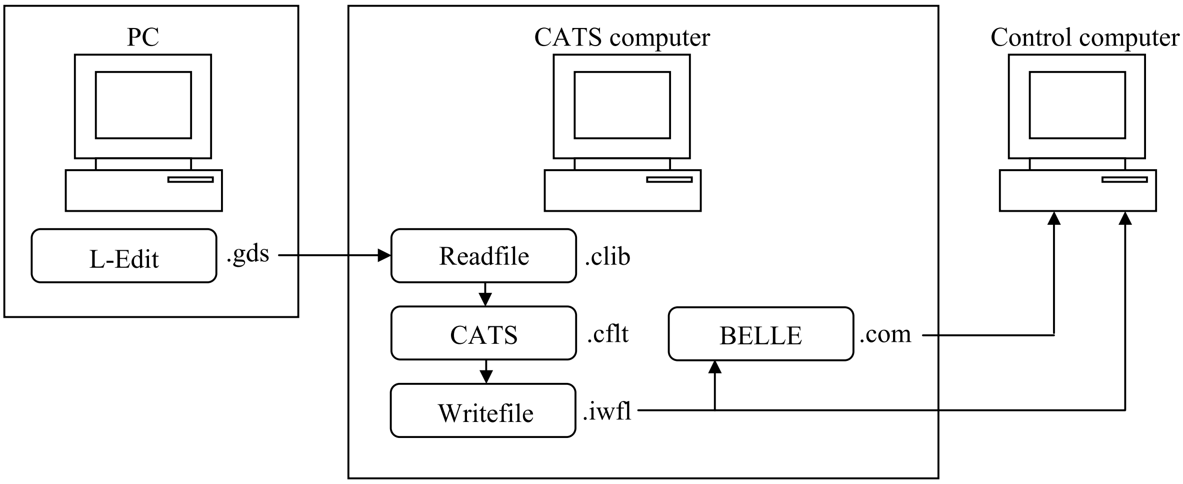

Fig. 3.4: File processing required before patterning can begin.

The L-Edit output is transferred to a computer (CATS computer) which runs a program called CATS (Computer Aided Transcription System). Once a series of input parameters have been provided along with the .gds file, CATS fractures the design into trapezia with sides of maximum length 6.4μm. The computer converts the .gds file into a .clib readfile and CATS uses this to create .cflt, .dat, .cinc, .log and .log-long files. These are then combined by the computer to produce a final .iwfl file which is sent to both the beamwriter control computer and the job layout program BELLE (Beamwriter Exposure Layout for Lithographic Engineers), which is the next step in the conversion process. BELLE requires the .iwfl file complete with all of the patterning information to produce a final job layout (.com) file. In addition, the program calculates an approximate writing time using Equation 3.1.

$$\text{job time} = \frac{\text{total charge}}{\text{beam current}} = \frac{\text{area} \times \text{dose (charge/area)}}{\text{beam current}} \tag{3.1}$$

Finally, the layout file is sent to the control computer and together with the design file, is used by the beamwriter to pattern the substrate. Screenshots of the (a) CATS and (b) BELLE interface are shown in Fig. 3.5.

(a)

```
  Format:5HR50       Function:VOID        Resolution:0.05
   Units:MICRON       Justify:CENTER          Height:800 [16000]
 Compact:NO           Reverse:NO               Width:800 [16000]
 Pregrid:NO          Overlaps:NO                Grow:0
  Precut:YES          Produce:CFLT              Rule:SQUARE     Border:OUTSIDE
    Join:YES           Select:NO            Twosided:YES
                         Keep:NO                 Tag:


       Input:($TED/transcript_db.clib)
   Structure:
      Layers:
      Limits:

      Sizing:0
       Scale:1
 Orientation:0
      Outpt:($TED/cbtranscri_db.cflt)
CATS 10:19:01 SunOS 5.7 RELEASE
Copyright 1986-2000 Transcription Enterprises Limited, Los Gatos, CA
$TEC/start_up.cinc setting PREGRID to NO
Command
```

(b)

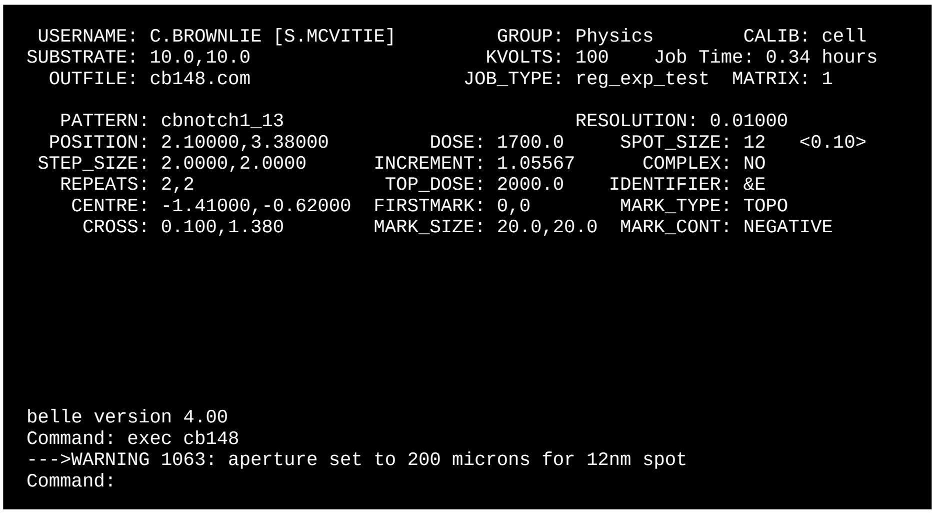

```
 USERNAME: C.BROWNLIE [S.MCVITIE]        GROUP: Physics        CALIB: cell
SUBSTRATE: 10.0,10.0                    KVOLTS: 100    Job Time: 0.34 hours
  OUTFILE: cb148.com                  JOB_TYPE: reg_exp_test  MATRIX: 1

   PATTERN: cbnotch1_13                          RESOLUTION: 0.01000
  POSITION: 2.10000,3.38000         DOSE: 1700.0     SPOT_SIZE: 12   <0.10>
 STEP_SIZE: 2.0000,2.0000      INCREMENT: 1.05567      COMPLEX: NO
   REPEATS: 2,2                 TOP_DOSE: 2000.0    IDENTIFIER: &E
    CENTRE: -1.41000,-0.62000  FIRSTMARK: 0,0        MARK_TYPE: TOPO
     CROSS: 0.100,1.380        MARK_SIZE: 20.0,20.0  MARK_CONT: NEGATIVE








belle version 4.00
Command: exec cb148
--->WARNING 1063: aperture set to 200 microns for 12nm spot
Command:
```

Fig. 3.5: Screenshots taken from the (a) CATS and (b) BELLE programs.

3.3.4 Pattern writing

When the resist layer(s) have been spun and the design and layout files submitted to the beamwriter control computer, the substrates can be loaded for patterning. The samples are clamped into special holders depending on their size and then multiple holders are loaded into cassettes. The cassettes are placed into the beamwriter and each holder is positioned separately onto the mechanical stage by the operator. At this point the backscattered electron detectors are used to check the sample alignment before exposure. During the job layout procedure, pattern resolution, spot size and cell dimensions are specified. For finer features small Gaussian spots are required, whilst for less critical areas, larger spots and even shaped beams can be used. The actual size of the spot on the sample is dependent on the size of the final aperture, and this is selected automatically. The EBPG5 at Glasgow University has 200, 400 and 800µm apertures available, allowing users to pattern with spot sizes ranging from 12nm (at 100kV) up to 300nm (at 50kV). An important point to note, however, is that a reduction in spot size results in a reduction in beam current, and so smaller features take far longer to write than larger ones.

During exposure, the electron beam is vector-scanned by directing the beam only to the desired areas of the sample and blanking in-between. As mentioned earlier, exposure occurs pixel-by-pixel with each cell equal to the resolution set in CATS and BELLE. However, because the deflection coils are only able to deflect the beam by ±400µm, the pattern is also split up into blocks, each of size 32,000 resolution steps. For patterns larger than this, fine control of the mechanical stage is used to move the next block below the beam, but although the blocks are positioned as accurately as possible, stitching errors can occur at block boundaries. For the work considered here, the patterns were designed to fit within the 100µm TEM windows so stitching errors were not a problem.

As the pattern is exposed as a series of beam steps, it is to be expected that not all of the designed shapes will be transferred to the resist with the same level of edge quality. Despite the overlap of adjacent steps, features with straight edges transfer well, whilst those with rounded edges, as can be seen in Fig. 3.6, do not.

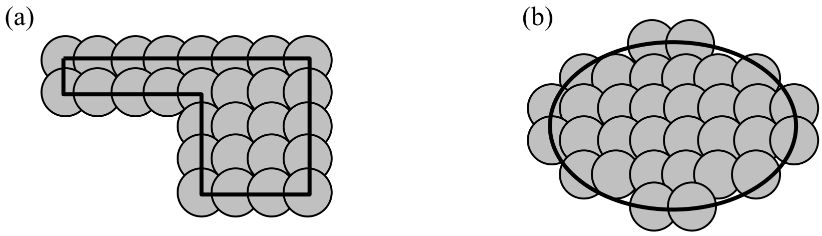

Fig. 3.6: The patterning of features with (a) straight edges and those with (b) rounded edges.

3.3.5 Proximity effect

When the electron beam interacts with a sample, both forward and backscattering events occur. This ‘double exposure’ can result in a uniform exposure giving rise to a non-uniform distribution in the patterned area and is commonly referred to as the proximity effect [70]. This non-uniformity can cause both a variation between patterned elements and also a variation within a patterned element, thus reducing the quality of the finished sample. Between elements, the received exposure varies with geometry and distribution, with smaller elements receiving smaller doses than larger ones and isolated elements receiving smaller doses than those in densely packed regions. Within a single shape, the exposure in the pattern centre tends to be larger than at the edges. To take this additional exposure into account, the beam can be seperated into forward and backscattered components, with the radial function given by a double Gaussian approximation,

$$f(r) = \frac{1}{\pi(1+\eta)}\left[\frac{1}{\alpha^2}\exp\left(\frac{-r^2}{\alpha^2}\right) + \frac{\eta}{\beta^2}\exp\left(\frac{-r^2}{\beta^2}\right)\right] \qquad (3.2)$$

where α and β are the radii of the forward and backscattered beams respectively and η is their ratio. A program called Proxecco can then be used to apply a range of doses instead of a single base dose, depending on the designed geometries (Fig. 3.7). This proximity correction (.pec file) also considers the substrate material, resist thickness and beam energy. A number of ready-made .pec files were used during the fabrication of the magnetic thin film elements. The .pec file is added to the design file in CATS before submission of the job.

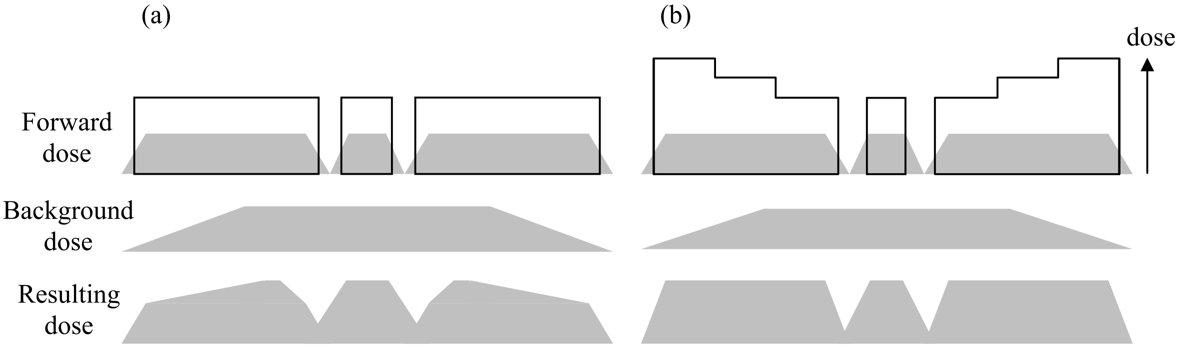

Fig. 3.7: Effects of (a) uniform and (b) modulated doses on the exposure profile. The applied and effective exposure is shown as unfilled and grey regions respectively.

3.4 Resist technology

A resist [71,72] is any material which defines a pattern after exposure to radiation. Generally carbon-chain polymers are used in photo and electron beam lithography but less conventional materials such as spin-on-glass and self-assembled monolayers can be patterned also. With polymers, many monomer building blocks are polymerised into large molecules with molecular weights of up to hundreds of thousands of atomic mass units (amu). These monomers can be identical in structure, producing a homopolymer, but may be different, producing a copolymer. The radiation exposure changes the chemical and physical properties of the resist in such a way that a replica of the mask is left on the surface of the substrate after the fabrication process is complete. Resists can be divided into two main categories depending on their polarity, namely positive tone and negative tone (Fig. 3.8).

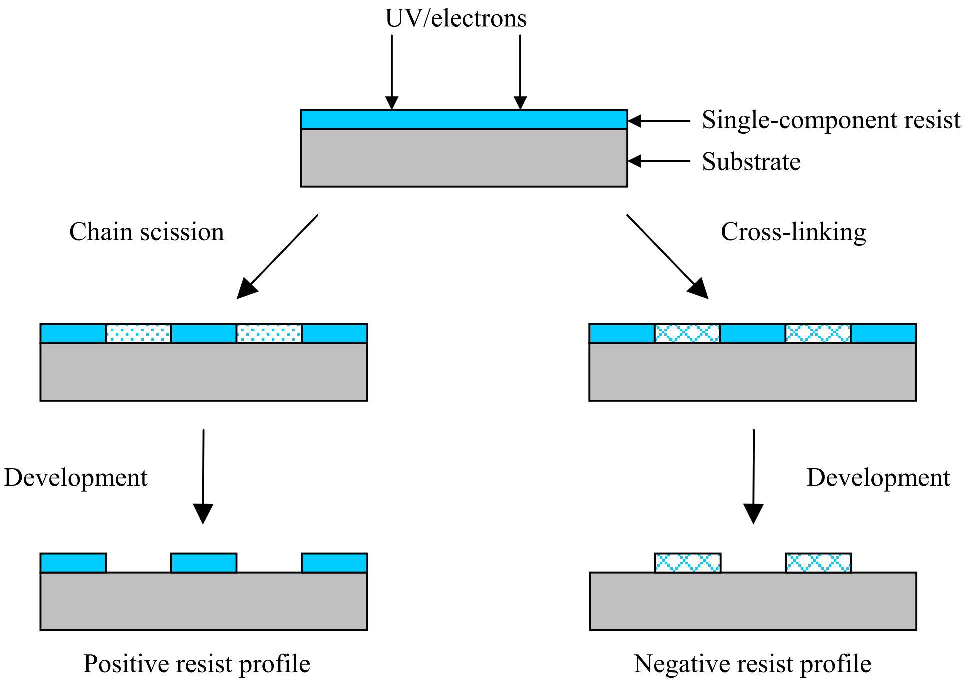

Fig. 3.8: The exposure and development processes involved in the patterning of positive and negative tone single-component resists.

With positive resists, the exposure step breaks up the long chain polymer (chain scission) to produce organic molecules of lower molecular weight. These products are more soluble in the developer than the unexposed resist and as a result, the patterned region is removed during development. With negative resists, exposure causes the polymer chains to join together (cross-linking), strengthening the material and reducing the solubility. During development it is the surrounding regions that are removed, leaving only the patterned resist on the substrate.

Currently there are a large number of different resists available for use in photo and electron beam lithography. When selecting a particular resist to use, careful consideration must be given to the processing conditions and applications involved, and there are several important properties that must be assessed. The sensitivity of a resist affects the minimum dose required to pattern the substrate and the greater this is, the faster the sample can be written. It is also important to select the correct polarity for a given job. Positive resists tend to be better for smaller features as negative polymers can absorb solvent during development causing them to swell and distort the pattern. The development stage also greatly affects the resist contrast and profile. For the fabrication of very fine features (e.g. diffraction gratings), the resist resolution must be very high. Often dry etching is required for this type of work and therefore the level of resistance to the reactive species is a priority if the pattern is to remain intact. Following deposition, the resist should be easily removed (stripped) without too many additional steps. Further factors including shelf-life, storage conditions, ease of handling, toxicity, cost and integration are also important considerations.

3.5 Lift-off

In order to produce the elements described in this thesis, a magnetic thin film has to be divided into discrete structures. Typically, there are two different methods used to achieve this, namely lift-off (an additive process) [73] and etching (a subtractive process) [74,75]. The lift-off technique (Fig. 3.9) was used routinely in this work. It is a relatively simple method that is well-suited to the creation of metallic patterns, especially films of noble metals that are difficult to etch. First, a layer of photo or electron sensitive resist is spun onto the substrate, exposed and then developed to define the pattern. Following this, a metal layer is deposited (preferably by evaporation over a large working distance), covering the resist and areas where the polymer has been cleared. The sample is then immersed in a solvent which dissolves the resist but does not attack the metal film. This step strips the polymer and any overlying metal, leaving only the film that was deposited directly onto the substrate in the shape of the designed pattern.

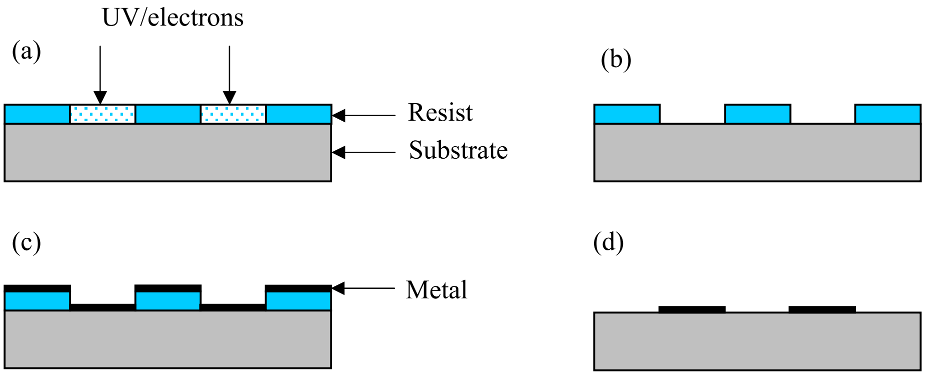

Fig. 3.9: The various stages involved in the lift-off fabrication process include (a) exposure, (b) development, (c) metallisation and (d) lift-off.

The lift-off process, however, is very dependent on the resist profile after pattern development. For large features the resist can be removed in minutes, but for smaller features, in particular those with low aspect ratio, resist removal will take far longer, if occurring at all. This problem is made worse when a single resist layer is used to define the pattern, as can be seen in Fig. 3.10a. After exposure and development, the metal is deposited on the surface of the sample and also on the sidewalls of the resist, producing a continuous film. Not only does this inhibit lift-off, but the metal coating the sidewalls adheres to the substrate, even after resist removal. This build up of excess metal is known as ‘flagging’ and occurs more prominently when the incoming material hits the sample at an angle to the normal. The problem is made worse if the metal is sputtered, due to omnidirectional deposition from the target.

3.5.1 Lift-off enhancement

To improve the quality of the lift-off process, an undercut resist profile can be used. This technique forces the metal film to become discontinuous, lying only on the surface of the sample and not on the sidewalls of the resist. Thick resist layers develop a natural undercut due to scattering, particularly in electron beam lithography. As the beam patterns the polymer, electrons experience small angle (forward scattering) and large angle (backscattering) scattering events. Unfortunately, forward scattering tends to broaden the initial beam diameter,

$$d_f = 0.9\left(\frac{R_t}{V_b}\right)^{1.5} \tag{3.3}$$

where d_f is the effective beam diameter, R_t is the resist thickness (nm) and V_b is the accelerating voltage (kV) [69]. For a resist thickness of 200nm exposed at 50kV a 7.2nm beam diameter is achieved, but for 400nm thick resist this value increases to 20.4nm, reducing the pattern resolution. It is therefore important to use a layer of resist that is thin enough to minimise the effect. Different techniques must be employed to create an undercut in thin layers of resist.

To achieve this with photoresists, the sample is soaked in a solvent called chlorobenzene [76] after the resist has been baked. This process hardens the surface of the resist, reducing its dissolution in the developer (Fig. 3.10b). With electron-sensitive resists, however, solvent soaks can dissolve the polymer, and are therefore not an option. Instead, a bilayer of different molecular weight resists is used. Those of lower molecular weight are more sensitive to electron exposure and give larger line widths for a given dose than resists of higher molecular weight. Therefore, by using a more sensitive resist at the bottom of a bilayer, it is possible to create a significant undercut (Fig. 3.10c).

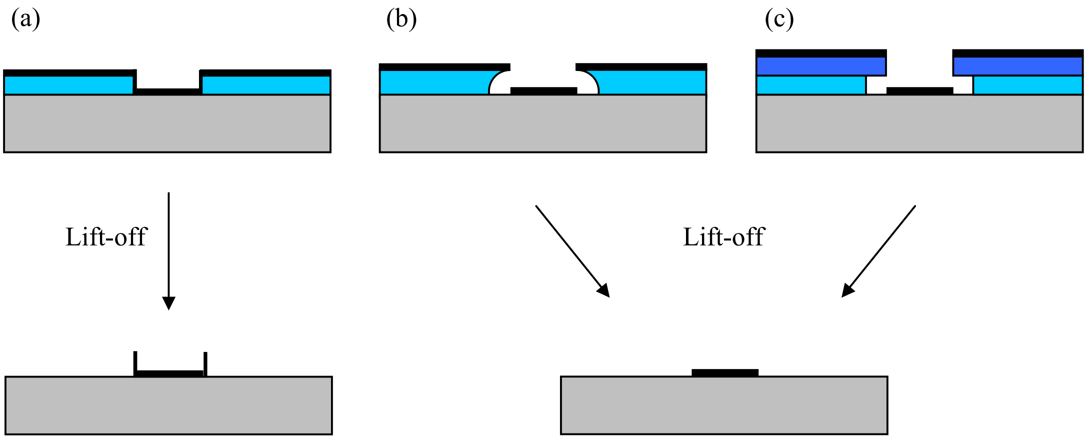

Fig. 3.10: The different profiles achieved with (a) a single layer of resist, (b) photoresist soaked in chlorobenzene and (c) a bilayer of electron sensitive resist.

3.5.2 Additional problems

Although the lift-off procedure is simple in design and is widely used in the fabrication of metal features on semiconductor substrates, some problems can arise whilst trying to remove the metal. On occasion, pieces of material that have been removed travel through the solvent and resettle elsewhere on the surface. This will often render a sample useless and is most problematic in the fabrication of electronic devices where it can create shorts. In the fabrication of magnetic elements, metal flakes can affect the magnetic behaviour and contribute to unwanted contrast in the TEM. Surface contamination in this form can be avoided by frequently changing the solvent and using a pipette to remove the flakes. Gentle agitation can also help to dislodge the metal. A further problem with this technique is that during immersion in the solvent, the entire layer of metal can be stripped. This is caused by poor adhesion to the surface but can be eliminated by allowing the metal to bond to the surface overnight before lift-off.

3.6 Deposition

During sample preparation it is necessary to deposit thin films of material using physical and chemical processes. For coating the substrate with a metal film, physical deposition techniques such as evaporation and sputtering can be used. Evaporation involves heating the material to be deposited whilst sputtering makes use of energetic ion bombardment. Other materials such as insulating or semiconducting films, however, are not well suited to these techniques and chemical deposition is one of the methods employed instead [78].

The basic principles involved in evaporation and sputtering will be described in the next two sections.

3.6.1 Evaporation

The simplest evaporator consists of a high-vacuum chamber within which the material to be deposited is heated to the point of evaporation. The atoms of the vapour travel through the vacuum in a straight line until they reach a surface where they accumulate as a film. The sample placed inside the chamber is exposed to the material until the desired thickness is deposited. The evaporation chamber itself is evacuated using diffusion and rotary pumps. A schematic diagram of the system used in this work can be seen in Fig. 3.22a. The rotary pump is first used to rough the chamber to $\sim 10^{-1}$ torr before backing the oil diffusion pump which reduces the pressure to $\sim 10^{-6}$ torr. This high vacuum ensures that the vapour travels directly from the target to the substrate and also minimises contamination from other materials.

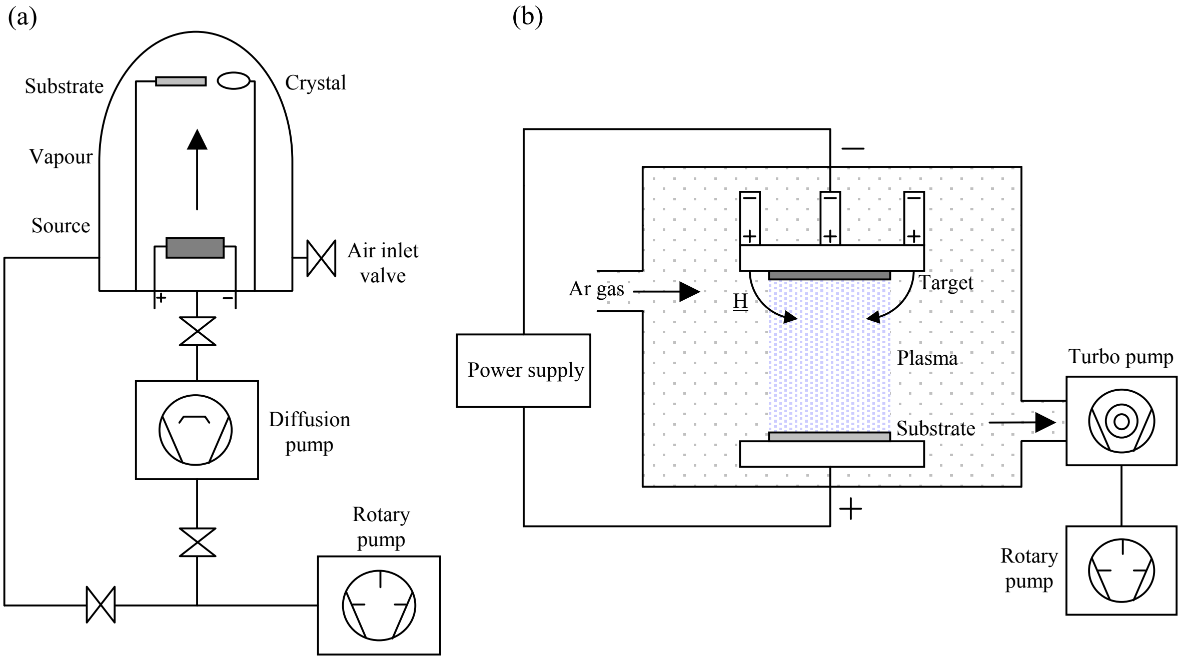

Fig. 3.22: (a) Thermal evaporation and (b) parallel-plate magnetron sputtering systems used to deposit thin metal films onto a substrate.

The target material is loaded into a ceramic boat or crucible and heated using a large current (resistive heating). Once any surface oxide is evaporated and a steady deposition rate is achieved, a protective shield is removed, exposing the sample to the vapour. This particular system is capable of containing two crucibles to allow the deposition of bilayers or alloys of various composition without breaking vacuum. It can also accommodate several substrates which are clamped in place ~20cm above the crucibles. Controlling the composition of compound materials using evaporation is very difficult due to differences in vapour pressure, but this problem can be alleviated using coevaporation or sequential deposition techniques.

The deposition rate is monitored using a quartz crystal device. This is a plate that undergoes mechanical oscillation at a measured resonant frequency. As the mass of deposited material on the plate increases, the resonant frequency decreases. For each material, the frequency of vibration is calibrated with material thickness giving an accurate indication of the thickness of the layer on the substrate.

3.6.2 Sputtering

Sputtering is the main alternative to evaporation for metal deposition and is far better for producing layers of compound material and alloys. The material to be deposited is removed from a target by the impact of energetic ions in a glow discharge plasma. The atoms removed then land on the surface of the substrate, building up to form layers. A plasma is a partially ionised gas (typically argon) within which exists dissociated atoms or molecular fragments called radicals, and ions in the atomic or molecular form. Typically radicals and charged species account for 1% and 0.01% of the total plasma respectively. The plasma is created by applying a large voltage between two electrodes in the presence of the gas at low pressure. Once formed, the positive ions are accelerated towards the cathode where they strike the surface and release secondary electrons. These electrons then accelerate towards the anode, colliding with neutral gaseous atoms along the way. These collisions cause atomic excitation, producing a characteristic glow when the atoms decay or ionisation if the energy transfer is sufficient, increasing the number of ions within the plasma.

When an energetic ion strikes the surface of a target at sputtering energies (between 10eV and 10keV depending on the ion and target material), bond breaking and physical displacement occurs. The ion will travel several atomic layers into the material until it hits an atom head-on and is deflected through a large angle. This interaction can free target atoms on the surface and break bonds in the surrounding material allowing subsequent collisions to eject individual atoms or atomic clusters.

To increase the ion density further and thus the sputtering rate of the system, magnetron sputtering can be utilised. This technique involves the use of permanent magnets behind the target electrode to produce a toroidal field of a few hundred Oersted.

The magnetic field causes secondary electrons to spiral around the field lines, confining the plasma over the target. The orbital motion of the electrons increases the probability of colliding with neutral atoms in the gas. A planar magnetron sputtering system can be seen in Fig. 3.22b. The MTJ films (discussed in Chapter 8) were deposited under ultra high vacuum (UHV) conditions in a multi-target DC magnetron sputtering system. This was performed by Dr Frederik Vanhelmont at Philips Research Laboratories, Eindhoven, The Netherlands.

3.7 Development of the lift-off fabrication process

To produce well-defined magnetic elements with nanoscale features using lift-off, it is necessary to use a bilayer of high resolution resist that can be exposed and developed to give an undercut profile. The pattern itself is written in the top layer of resist (imaging layer) with the bottom layer (undercut layer) used to ensure that the metal pattern is clearly separated from the resist and overlying metal. In this way the structures avoid contact and are not disturbed by the lift-off step. As a general rule of thumb, the bottom layer of resist should be thicker than the layer of evaporated metal.

3.7.1 PMMA procedure

A commonly used e-beam resist for this type of fabrication is poly(methylmethacrylate) (PMMA). The chemical structure of this homopolymer can be seen in Fig. 3.11a.

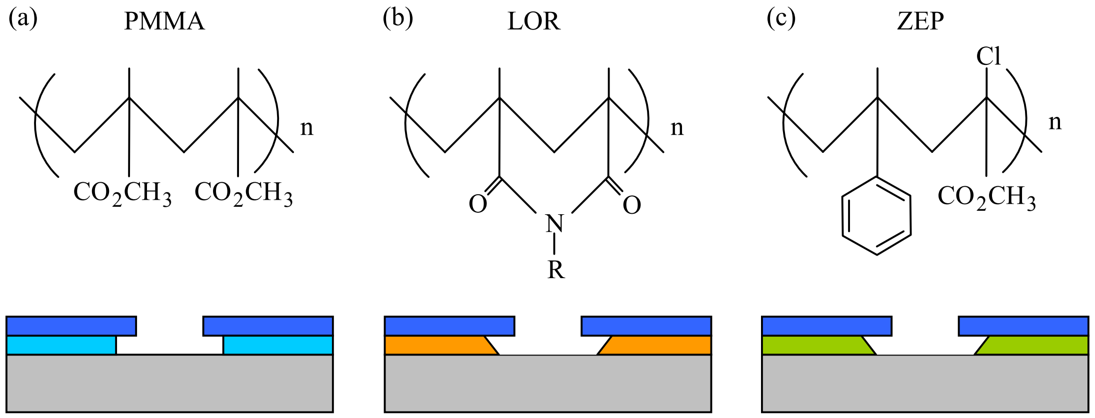

Fig. 3.11: Chemical structure and undercut profile of the (a) PMMA, (b) LOR and (c) ZEP polymers used in this work.

PMMA is a positive tone, single component resist and is supplied as a powder and then dissolved in o-xylene to provide different concentrations (%). As the % increases, the film thickness increases. Following an initial concentration/spin speed/spin time calibration, the desired film thickness can be achieved. In addition, PMMA comes in various molecular weights (MW) with 2010 (MW of 90,000amu) and 2041 (MW of 345,000amu) available for use in the JWNC. As the lower MW resist is more sensitive to electron exposure, it is used as the bottom layer in the stack. PMMA can be developed anisotropically in methyl isobutyl ketone (MIBK):IPA solutions of various concentrations (determined by feature size, resist thickness and feature density) and later removed with acetone during the lift-off step.

As an initial attempt to fabricate elements, a bilayer of PMMA was spun onto a clean membrane block and baked. Both layers of resist were ~100nm in thickness. The substrate was then patterned at 50kV in the design of a test pattern (Fig. 3.12), containing a series of basic geometric shapes. Following exposure and development, a 20nm thick layer of permalloy was evaporated before the polymer was dissolved. Finally a 4nm gold coating was sputtered onto the sample to prevent charging of the otherwise insulating substrates in the TEM/SEM. If samples are allowed to charge as a result of electron exposure, unwanted contrast, specimen drift and substrate damage can occur.

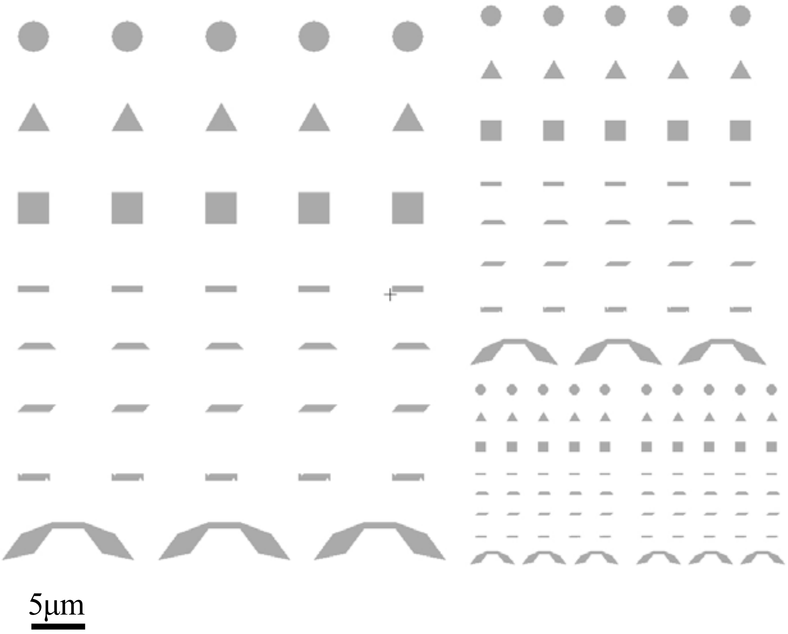

Fig. 3.12: Test pattern created in L-Edit. The smallest squares are 1µm in size with the sub-pattern repeated at two and three times magnification.

3.7.2 Problems encountered

During the subsequent SEM/TEM inspection, however, a number of problems were discovered. The first of these was pattern definition. Despite using a finely focussed electron beam and ultra high resolution resist, the shape of the elements deviated from the designed pattern, with the elements exhibiting rounded corners (Fig 3.13).

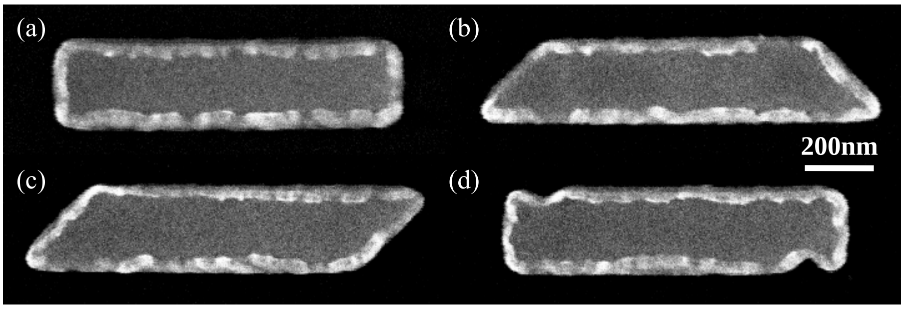

Fig. 3.13: SEM images of a (a) rectangle, (b) trapezium, (c) parallelogram and (d) notched rectangle. The notches in (d) have been reduced in width as a result of poor resolution and the corners of the other geometries less pointed than intended. Flagging is also visible around the edges of each element.

Although this does not vary the geometry so much in larger elements with in-plane dimensions of a few microns, the magnetic behaviour of smaller features (in the few hundred nanometer range for example) could be strongly affected as a result of these changes in element shape. Round features are not able to pin domain walls in the same way that sharp features can, whilst changes in edge structure can vary the element coercivity and reversal behaviour [77]. Poor definition also makes comparison between different element geometries more difficult.

A second problem was metal flagging around some of the element edges (Figs. 3.13, 3.14). This occurs when there is an insufficient undercut and some of the metal lands on the sides of the resist. Once the resist is dissolved, this metal falls onto the surface creating regions of thicker material, and is problematic. Edge flags can act as nucleation points for domain walls and may have large associated stray fields. Because contrast from the thicker material dominates the image, they also inhibit magnetic imaging.

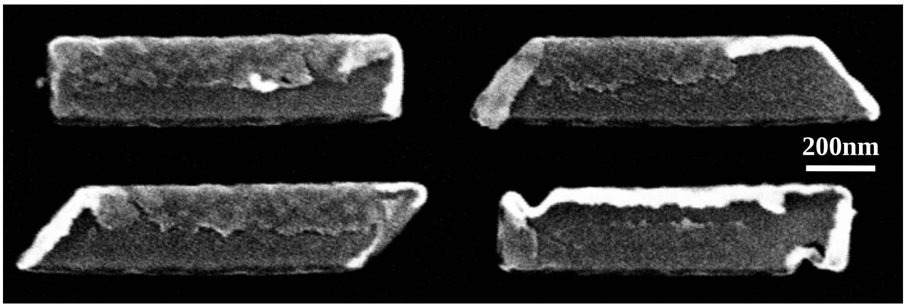

Fig. 3.14: Flags of metal can be seen around several of the element edges and was present on almost all of the structures.

The third problem was resist residue found beneath the elements using TEM. This is caused by incomplete exposure or development and/or overly strong adhesion of the polymer to the substrate. Although this does not affect the magnetic properties of the elements, it inhibits the magnetic contrast in the microscope (Fig. 3.15). Unlike edge flags, this additional contrast does not just appear at the edges of the structures, but can be found anywhere below the metal, severely reducing the quality of the images obtainable.

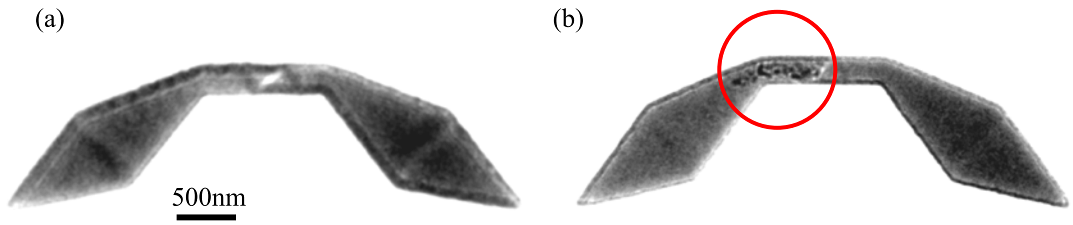

Fig. 3.15: Fresnel images of a domain wall trap element taken on the CM20 TEM. A head-to-head vortex domain wall can be seen in the centre of the strip in (a) whilst in (b) this contrast is inhibited by resist residue (circled in red).

3.7.3 Possible solutions

Following poor element definition, the .log file was checked. This is an output file produced by the beamwriter control computer which lets the user know how well a particular job ran. An important feature of this file is a height map of the substrate which is calculated at 9 points on the surface using the laser height meter attached to the column of the beamwriter. With a flat substrate, the electron beam can be focussed accurately on the surface, but if the substrate is tilted slightly then the pattern transfer suffers. Inspection of the height map for this sample showed that the laser was unable to provide a reading at any of the 9 points. This was believed to be the result of poor reflection from the SiN surface and to improve this, a coating of aluminium on top of the resist bilayer was recommended. As Si_3N_4 is electrically insulating, this metal coating may also help to reduce the build up of negative charge on the substrate during exposure. It was hoped that this might improve the resolution further by decreasing the level of Coulombic repulsion. In addition, a 100kV beam was chosen to pattern the resist instead of the original 50kV beam. The higher accelerating voltage reduces the spherical aberration and spot size without much increase in backscattered electrons when membrane substrates are used. A further idea to improve the pattern resolution was to use a thinner imaging layer of 2041 PMMA. As electron-solid interactions tend to broaden the beam diameter, thinning of the resist should reduce this effect. As a result, a 40nm thick top layer was chosen as a comparison to the original 100nm layer.

To eliminate the edge flags around the element edges, a bilayer of resist with a larger undercut than PMMA is required. As a result, two different types of resist were chosen to replace the 2010 PMMA at the bottom of the stack. The first of these resists was LOR-10A (Lift-Off Resist) which is based on the poly(dimethylglutarimide) (PMGI) platform and produced by MicroChem. LOR (Fig. 3.11b) is diluted in cyclopentanone to provide different concentrations and can be used with a variety of positive resists without intermixing. PMGI is another homopolymer like PMMA but is not sensitive to electrons (or UV). Instead, it acts as a sacrificial layer and can be wet-etched in CD26 developer following processing of the imaging layer. The development occurs isotropically with time, resulting in a controllable undercut. With thin layers, a re-entrant sidewall profile is achieved which is ideal for lift-off processes. Lift-off of LOR is performed using SVC-14. In addition, due to its poor adhesion to silicon, pre-application surface modification using an oxygen plasma asher (see below) can be required. The second resist to be tested in combination with 2041 PMMA was ZEP 520A (Fig. 3.11c), a copolymer of α-chloromethacrylate and α-methylstyrene produced by Nippon Zeon. This resist is a single component electron sensitive polymer with higher sensitivity than PMMA. It is also positive tone with ultra high resolution and excellent dry etch resistance. ZEP is diluted in anisole, developed in o-xylene and stripped using acetone. As with LOR, ZEP develops isotropically to produce a re-entrant sidewall in the resist. Surface modification can also be required to enable the resist to stick to the surface of the substrate.

To address the problem of resist residue, an oxygen plasma asher was recommended for use after development of the resist. Oxygen ashers generate oxygen ions in a plasma to bombard and react with the surface material. These systems are very efficient at removing organic films and contamination from wafers and can be used for post-development residue removal as well as surface cleaning prior to resist application.

3.7.4 Other resist issues

In relation to the ideal thickness of each of the layers in the resist stack, resist adhesion and mechanical stability must be taken into account. As stated previously, the bottom layer should be thicker than the deposited metal to create discontinuities in the film whilst the top layer should be thin enough to minimise forward scattering yet strong enough to support itself at the undercut regions. Experiments have shown that with the strongest resists an aspect ratio of 3:1 can be achieved at best (i.e. 100nm tall, 33nm wide).

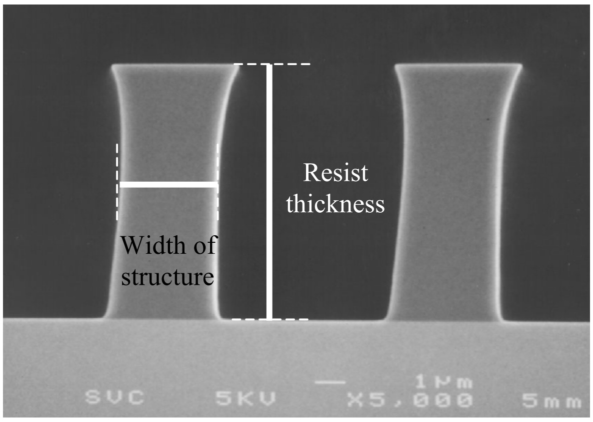

Fig. 3.16: Tilted SEM image of resist columns after exposure and development. The height-to-width aspect ratio should not exceed 3:1 or mechanical stability can be a problem.

As a result, the patterned feature size and resist thickness (Fig. 3.16) is critical to the quality of the fabricated structures and care must be taken not to pattern a thick resist with closely packed features. In addition, thinner layers of resist have been found to bond more strongly to the substrate than thicker layers and are therefore harder to remove in the lift-off stage of the procedure. In effect, although a thicker bottom layer is desirable for ease of lift-off, this can reduce the mechanical stability.

3.7.5 Resist tests

To determine the effects of these changes, 18 different bilayers of resist were exposed in the shape of the test pattern. Six of these were 2010 PMMA/2041 PMMA, six were LOR-10A/2041 PMMA and six were ZEP 520A/2041 PMMA. The thickness of the bottom layer was varied from 40nm to 100nm and 200nm whilst 40nm and 100nm thick PMMA was spun on top. A constant development time of 60 seconds was used at 21°C for each of the samples. Variation of the development time and temperature could have been used to fine tune the process for each stack but was not performed here due to time limitations. As the membrane substrates are relatively expensive, it was not possible to use these for the resist tests. Instead, a (100) silicon wafer was coated in a 50nm thick Si_3N_4 layer and cleaved into $10\times10\,\text{mm}^2$ pieces. It was hoped that despite the obvious backscattering and consequent decrease in required dose associated with bulk material, the majority of the fabrication parameters would be very similar to those used in the patterning of the membranes. For each of the samples, a dose test was run to determine the optimum exposure. Following this, new samples were patterned at this dose and fabricated using the detailed procedures given in Appendix Tables A.1-A.3. Once completed, each sample was imaged using optical microscopy to establish the rough percentage yield of fabricated elements. With visible light it is not possible to characterise the pattern in much detail, but optical microscopy is useful for determining if any of the structures are missing, badly damaged or contaminated with unwanted material (resist, metal, solvent scum etc). Afterwards, the samples were imaged using SEM. A Hitachi S4700II microscope was used to examine the elements in more detail with particular emphasis on edge definition. An accelerating voltage of 5kV was used to allow imaging of both edge and surface detail. Higher energy electrons are able to penetrate deeper into the sample but were not required for this work. During inspection, any problems discovered in the images (edge flagging, rounding, contamination etc.) were noted. The results from these resist tests are presented in Table 3.1.

Bilayer		**Optical analysis**			**SEM analysis**	
Bottom	*Top*	*Best dose μC/cm^2*	*% elements*	*Problems*	*Edge definition*	*Problems*
40nm PMMA	40nm PMMA	270	99		good	edge flags
100nm PMMA	40nm PMMA	270	98		good	edge flags
200nm PMMA	40nm PMMA	270	99		OK	edge flags, rounding
40nm PMMA	100nm PMMA	270	96		good	edge flags
100nm PMMA	100nm PMMA	270	98		good	edge flags
200nm PMMA	100nm PMMA	270	98		OK	edge flags, rounding
40nm LOR	40nm PMMA	330	93		good	contamination
100nm LOR	40nm PMMA	330	79	missing elements, surrounding flags	good	
200nm LOR	40nm PMMA	330	45	missing elements, surrounding flags	good	
40nm LOR	100nm PMMA	330	58	missing elements	OK	edge flags, contamination, rounding
100nm LOR	100nm PMMA	330	93	missing elements	OK	edge flags, contamination, rounding
200nm LOR	100nm PMMA	330	89		OK	edge flags, contamination, rounding
40nm ZEP	40nm PMMA	200	92		OK	edge flags, rounding
100nm ZEP	40nm PMMA	200	99		good	edge flags
200nm ZEP	40nm PMMA	200	92	contamination	OK	edge flags, rounding
40nm ZEP	100nm PMMA	200	98		good	edge flags
100nm ZEP	100nm PMMA	200	89		good	edge flags
200nm ZEP	100nm PMMA	200	86	contamination	good	edge flags

Table 3.1: Experimental results from the various different resist bilayers.

It was found from the optical analysis that the PMMA/PMMA bilayers produced the highest yield of elements free from bulk contamination. The LOR/PMMA samples, on the other hand, displayed a number of missing elements and metal build-up around the edges of some of the structures (Fig. 3.17).

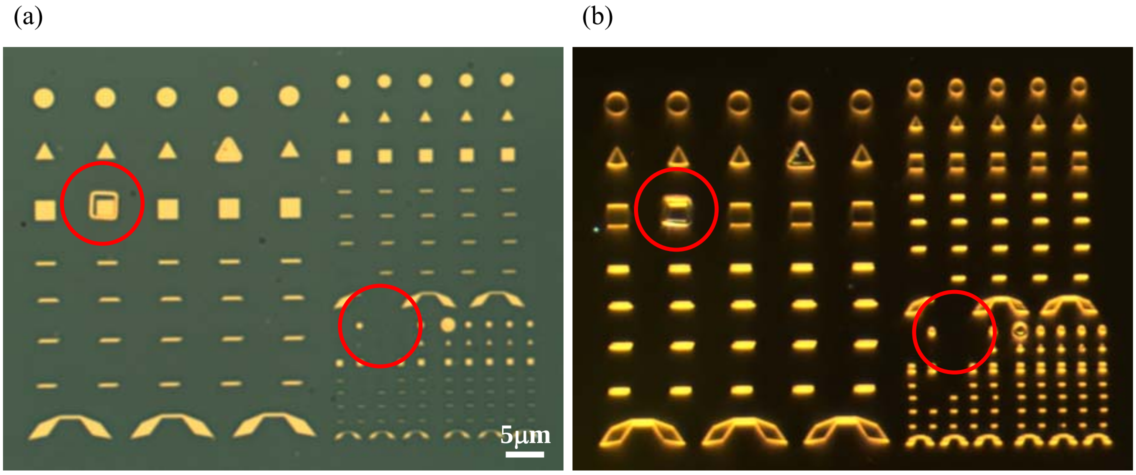

Fig. 3.17: Optical (a) bright field and (b) dark field images of a sample fabricated using 200nm LOR/40nm PMMA. Surrounding flags and missing elements are visible in the images (circled red).

It is possible that the missing elements were the result of an incomplete development. If a thin layer of resist was present on the substrate before the metal was deposited, then these elements would be removed during the subsequent lift-off step. The build-up of metal around the elements (surrounding flags) may also have been caused by incomplete development. If, due to the time-dependent isotropic development of LOR, the resist closest to the substrate (which is removed last) was not sufficiently dissolved, it would have been coated with metal, leaving flags around the element after stripping (Fig. 3.18).

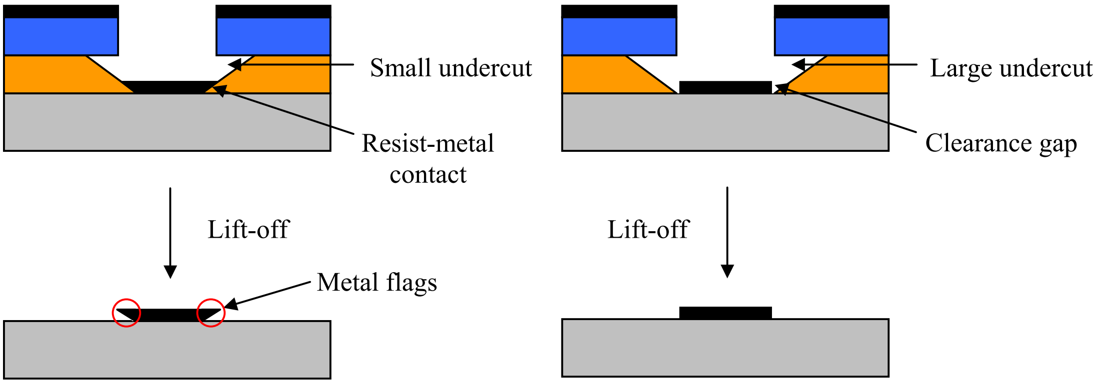

Fig. 3.18: (a) Small development times may lead to surrounding flags of metal caused by resist-metal contact. (b) Clearance gaps are produced by longer development and can reduce this effect.

With the ZEP/PMMA samples, most of the pattern appeared fine. However, on two specimens there appeared to be significant contamination across the whole surface (Fig. 3.19). This may simply be the result of slightly unclean tweezers, glassware or solvents used during the fabrication of these particular samples. As it was not present on any of the other samples it is unlikely to be a problem with the resist itself.

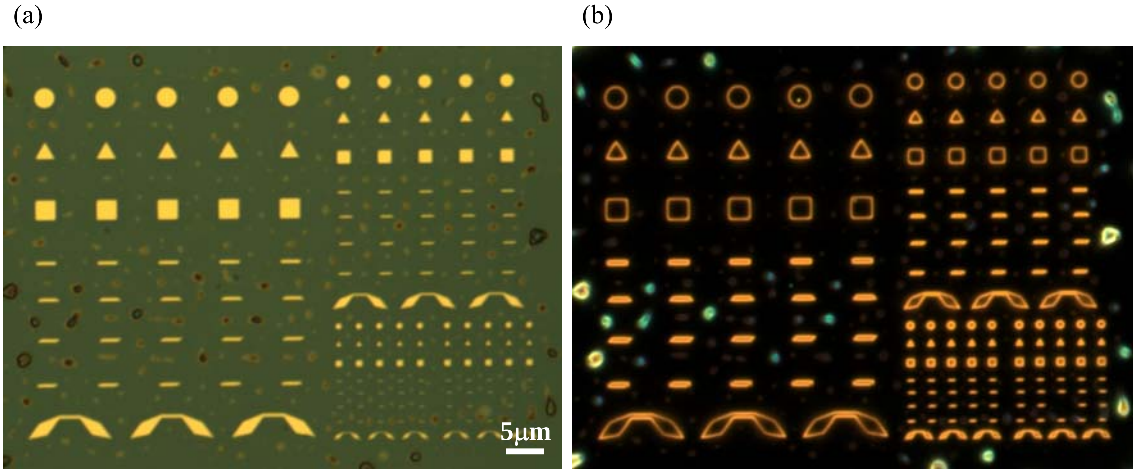

Fig. 3.19: Unknown contamination was found on the surface of some of the ZEP/PMMA samples as can be seen in the optical (a) BF and (b) DF images. This was present around the elements only, without actually affecting the structures themselves.

When the samples were imaged in the SEM, a greater number of problems emerged. Edge flags were present on all samples apart from the three LOR specimens with 40nm imaging resist layers. Therefore, despite the high sensitivity of ZEP and its isotropic development, this resist proved unsuccessful in eliminating the flags of metal. In general, edge definition of the elements was good, although some corner rounding was observed with two specimens. The 100nm PMMA layer on top of LOR seemed to reduce the pattern resolution as expected, but this trend was not observed with the other resists. In fact, the thickest bottom layer of PMMA seemed to reduce the resolution whilst in the ZEP/PMMA samples, a decrease in edge definition was seen with a 40nm top layer. A further observation was a slight contamination across the surface of four of the LOR samples (Fig. 3.20). This may again be associated with unclean utensils or solvents and could be minimised with proper care.

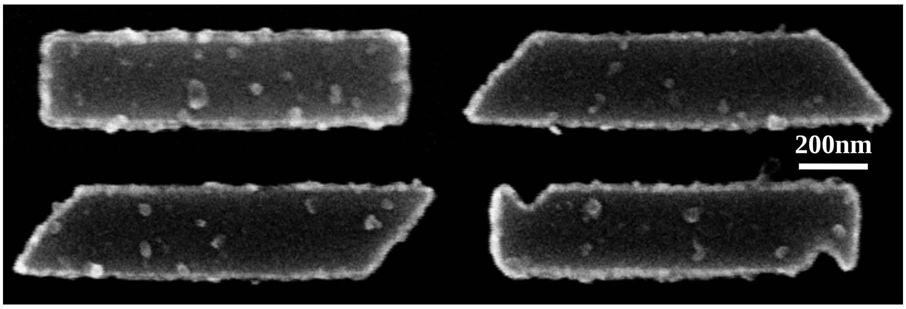

Fig. 3.20: Small particles of contamination were found on some of the elements fabricated using an LOR/PMMA bilayer.

In summary of these experiments, the most successful resist bilayer in the fabrication of thin film magnetic elements was the 40nm LOR/40nm PMMA stack. This proved capable of eliminating edge flags with no decrease in the pattern resolution. Additionally, a 93% element yield was achieved without missing structures or surrounding flags of metal. The only consideration, however, is the small amount of contamination that was present on the surface. This resist combination was used for fabrication in the remainder of this thesis. An example of a successfully fabricated element can be seen in Fig. 3.21.

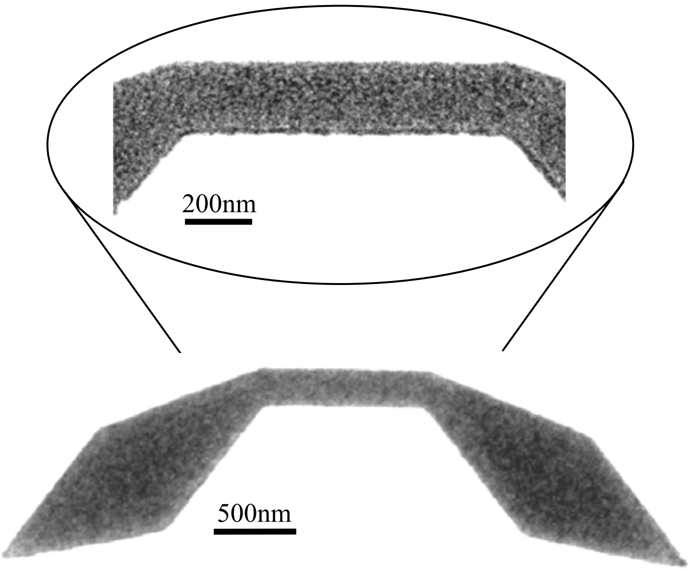

Fig. 3.21: A successfully fabricated domain wall trap element imaged using bright field TEM. The structure closely resembles the designed geometry and is free from metal flagging and contamination.

This ‘domain wall trap’ element has been imaged using bright field TEM. From these images, no metal flagging around the element edges can be observed and the film is free from resist residue and/or other contamination. In addition, the edges are smooth and the shape well-defined. Further examples can be seen in the Fresnel and DPC images of Chapters 5, 6 and 7.

Chapter 4

Micromagnetic simulations and image calculation

4.1 Introduction

The field of micromagnetics started in 1935 with a paper by Landau and Lifshitz [79] on the structure of a wall between two anti-parallel domains. Following this, Brown published several papers [80-84] deriving a set of differential equations which allow the calculation of static magnetisation states. A detailed account of micromagnetism is given in Brown's 1963 book [85]. The aim of micromagnetics is to determine the magnetisation distribution that minimises the total system energy, and for many years Brown's equations were solved analytically for systems with ideal geometry. Around the mid 1980s, however, the increase in large-scale computing power has allowed the study of more realistic problems using numerical methods. During this time it was found that the energy minimisation approach combined with classical nucleation theory (Stoner-Wohlfarth for example) was unable to correctly predict the state of the system after magnetisation reversal. As a result, a lot of work has gone into the development of dynamic approaches based on the Landau-Lifshitz equation of motion.

4.2 Magnetisation dynamics

When an external magnetic field is applied, the magnetic moment precesses around the field direction. Torque is the rate of change of angular momentum,

$$\boldsymbol{\tau} = \frac{\mathrm{d}\mathbf{l}}{\mathrm{dt}} \tag{4.1}$$

and for a magnetic moment in an external field is given by,

$$\boldsymbol{\tau} = \mathbf{m} \times \mathbf{H} \tag{4.2}$$

The magnetic moment is linked to the angular momentum by the gyromagnetic ratio, γ,

$$\mathbf{l} = -\frac{\mu_0 \mathbf{m}}{\gamma} \tag{4.3}$$

with $$\gamma = \frac{\mu_0 ge}{2m_e} \tag{4.4}$$

where g is the Landé g-factor, e is the electron charge, m_e is the electron mass and μ_0 is the permeability of free space. By including μ_0 in the expression for γ, the equation of motion for the moment of one electron is,

$$\frac{d\mathbf{m}}{dt} = -\gamma \mathbf{m} \times \mathbf{H} \tag{4.5}$$

For a many-body system, we replace the electron magnetic moment by the magnetisation, **M**, and the applied field by an effective field, $\mathbf{H_{eff}}$, which takes into account the exchange, anisotropy, magnetostatic and applied field interactions. The effective field is defined by,

$$\mathbf{H_{eff}} = -\frac{1}{\mu_0} \frac{dE_{tot}}{d\mathbf{M}} \tag{4.6}$$

where E_{tot} is the total system energy. As the magnetoelastic term can be expressed in a similar mathematical form to the magnetocrystalline anisotropy, it is effectively included also. We therefore obtain the expression,

$$\frac{d\mathbf{M}}{dt} = -\gamma \mathbf{M} \times \mathbf{H_{eff}} \tag{4.7}$$

which describes the precession of the magnetisation vector about the field direction (Fig. 4.1). Since this equation does not include a damping term, however, the precession is eternal and does not lead to an equilibrium state with the magnetisation parallel to the field. Experiments show that the changes in magnetisation decay with time, so Landau and Lifshitz included a second term which describes the dissipation of energy. This gives the Landau-Lifshitz (LL) equation,

$$\frac{d\mathbf{M}}{dt} = -\gamma \mathbf{M} \times \mathbf{H_{eff}} - \frac{\lambda}{M_s} \mathbf{M} \times (\mathbf{M} \times \mathbf{H_{eff}}) \tag{4.8}$$

where λ is a dimensionless damping parameter.

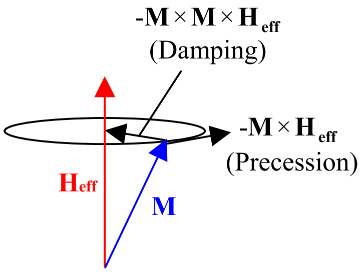

Fig. 4.1: Larmor precession with damping.

Gilbert later proposed a different damping term [86] to give the Landau-Lifshitz-Gilbert (LLG) equation,

$$\frac{d\mathbf{M}}{dt} = -\gamma\mathbf{M}\times\mathbf{H}_{\mathrm{eff}} + \frac{\alpha}{M_s}\mathbf{M}\times\frac{d\mathbf{M}}{dt} \tag{4.9}$$

with damping coefficient, α. Mathematically, these expressions are very similar. LL can be derived directly from LLG and is often rewritten as,

$$\frac{d\mathbf{M}}{dt} = -\frac{\gamma}{(1+\alpha^2)}\mathbf{M}\times\mathbf{H}_{\mathrm{eff}} - \frac{\alpha\gamma}{(1+\alpha^2)M_s}\mathbf{M}\times(\mathbf{M}\times\mathbf{H}_{\mathrm{eff}}) \tag{4.10}$$

which is the Landau-Lifshitz equation in Gilbert form. This is equivalent to LL provided $\gamma' = \gamma/1+\alpha^2$ and $\lambda = \alpha\gamma/1+\alpha^2$ where γ' is the LL gyromagnetic ratio. In the limit of small damping $(\lambda, \alpha \to 0)$ the LL and LLG equations are equivalent, but in highly damped systems $(\lambda, \alpha \to \infty)$ they give $d\mathbf{M}/dt \to \infty$ and $d\mathbf{M}/dt \to 0$ respectively. As high damping greatly minimises precessional motion, LLG is therefore more physically correct [87].

The LLG equation of motion describes the time evolution of the magnetisation if α is known. Experiments show that α is not constant, but depends non-linearly on the magnetisation [88]. It is usually determined from the line broadening in ferromagnetic resonance measurements, but for numerical convenience in simulations is normally set to a value between 0.1 and 1, which reduces the computation time. The origins of the damping process are not yet completely understood, but are thought to be the result of microscopic physical processes involving interactions between the magnetisation and the crystal lattice.

As the damping cannot be derived rigorously from basic principles therefore, the physical processes are accommodated into this single parameter.

4.3 Performing micromagnetic calculations

Micromagnetic simulation software allows the user to determine the magnetisation distribution in a 'nanomagnet' of a particular size and shape based on the various energy contributions. However, a realistic simulation of every atomic moment in the material is not possible, as it would require huge amounts of computer time and power beyond current capabilities [88]. Instead, the problem is broken down into a manageable size by defining small cells of uniform magnetisation. The cell size itself is very important to the results and can be varied by the user. Typically, cells smaller than the magnetostatic exchange length are required to find solutions that are independent of the mesh used. For the simulations performed in this thesis, cells with 5nm sides in the plane of the film were chosen. By decreasing this value, it is possible to obtain more realistic results, but the increased calculation time makes this impractical. Increasing the cell size beyond 5nm, on the other hand, speeds up the calculation, but provides a less realistic simulation of the material.

The numerical technique essentially involves the determination of the effective field at every point in the mesh, followed by a calculation of the magnetisation changes using the LLG equation. Starting from an initial state, the spins are adjusted to take into account the physical geometry and effective field before the total energy is evaluated. The whole system is updated simultaneously with each spin iteration (time step), and this procedure repeated until the magnetisation evolves into an equilibrium state. Equilibrium may be specified as the point when the torque or $d\mathbf{M}/dt$ falls below a critical value. Alternatively, the control point can be determined by a maximum iteration count or simulation time. Once the magnetisation has reached equilibrium, the system is said to have converged. Because the external field is applied in a stepwise manner, this process has to be repeated with every perturbation.

There are two parts of this procedure which are problematic, however. The first is determination of the local field. Since magnetostatic effects give rise to magnetisation structures on a length scale orders of magnitude greater than atomic spacing, it is impossible to deal with both magnetostatic and exchange effects rigorously with the current computer facilities. The second problem is in the physical microstructure of the material itself. For this, approximations have to be made in order to make the problem accessible to numerical calculations whilst still retaining some physical realism. As a result, a large number of micromagnetic programs are available which tackle the problems using slightly different mathematical treatments. The techniques fall into two main categories: finite difference and finite element methods [89]. These will be described briefly.

4.3.1 The finite difference method

The finite difference (FD) method is a widely used numerical technique for finding approximate values of solutions of problems involving partial differential equations. The basic idea consists of replacing any differential operators (space and time) by FD operators. On doing this, a partial differential equation is converted to a system of algebraic equations which can be solved numerically by an iterative process. Therefore, in the case of magnetic systems, the various energy contributions have to be approximated to their FD counterparts before the effective field and LLG equations can be solved. One problem with this technique is that it requires the use of a square mesh (Fig. 4.2). This makes it difficult to handle complicated geometries with curved boundaries and irregular microstructures. To deal with these systems, the finite element approach is more favourable. The FD program used in this work was OOMMF – Object Oriented Micromagnetic Framework, a public domain package developed by Dr Michael Donahue and Dr Donald Porter at the National Institute of Standards and Technology (NIST) in the United States [90].

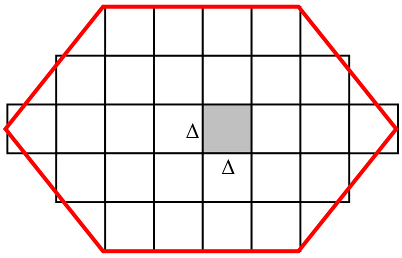

Fig 4.2: Discretisation of a 2D domain into FD cells of side Δ in which the micromagnetic equations are satisfied. The red outline shows the boundary of a particle that is problematic for FD simulations to deal with.

4.3.2 The finite element method

The finite element (FE) method [91] is a more complex mathematical technique used for modelling arbitrary geometries. As with FD simulations, the partial differential equation is discretised into a finite number of algebraic equations to reduce the problem of finding a continuous solution to one with finite dimensionality. The solution is then approximated by piecewise continuous polynomials with the aim of the process to determine the unknown coefficients in such a way that the distance from the exact solution is minimised. Instead of replacing the differential operators of the energy equations by FD operators, they are transformed to an integral representation of the system variables. The use of different shaped cells (triangles, squares or rectangles in 2D and tetrahedra, cubes or hexahedra in 3D) allows more accurate simulation of finite, inhomogeneous structures (Fig. 4.3). A further advantage of FE over FD is the use of parallel processing power. Whilst FD programs are run on stand-alone machines, FE calculations can be performed using a computer network which enables the simulation of larger problems.

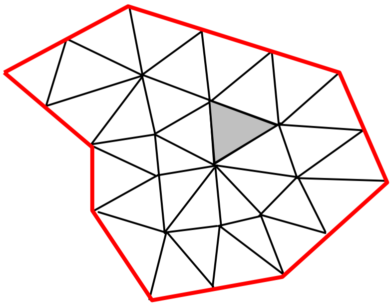

Fig 4.3: Sub-division of a 2D domain into a triangular FE mesh allows the simulation of more complicated structures.

The FE program Magpar was used as part of a collaboration with Prof Thomas Schrefl at the University of Sheffield, UK. This software was developed by Werner Scholz, Prof Josef Fidler and Prof Schrefl at the Vienna University of Technology in Austria.

It must be noted, however, that although micromagnetic simulations act as a guide between theory and experiment, they do not provide a perfectly reliable predictive tool. FD simulations often use geometrically perfect elements with uniform thickness and regular edges, whereas in reality, the structures are less perfectly defined. In addition, most programs neglect thermal effects and the time dependence of the magnetisation, which in fabricated structures, have a considerable impact on both the switching field and the supported states. A further difference is the simulation of hysteresis loops. In simulations, external fields are applied in a step-wise manner as opposed to the gradual increase or decrease of field applicable in experiment. As a result of these factors, it is expected that simulated and experimental results will differ at some level. Despite this, micromagnetic simulations are a useful tool in understanding observed behaviour and can also provide information that is experimentally inaccessible.

4.4 Image formation

4.4.1 Image formation in the TEM

Image formation in the TEM [53] can be understood by considering the Abbe theory. Objects illuminated by a plane wave form diffraction patterns in the back focal plane (BFP) of the imaging lens. A diffraction pattern divides an optical signal into its spatial frequencies with a varying intensity distribution, and can therefore be expressed as a Fourier transform. Likewise, the image amplitude is obtained by taking the inverse Fourier transform of the diffraction pattern. As the electron source is small and situated far from the specimen, the electron wave can be considered as a plane wave of the form,

$$\psi(x,y) = \exp(2\pi ikz) \tag{4.11}$$

where k is the wavenumber defined as $1/\lambda$. Here (x,y) is in the sample plane which is perpendicular to the direction of electrons (z). A typical specimen will modulate both the amplitude and phase of the wave, but for a thin ferromagnetic film of uniform thickness, we can ignore the amplitude modulation. As a result, the wavefunction leaving the specimen is given by,

$$\psi'(x,y) = f(x,y)\exp(2\pi ikz) \tag{4.12}$$

with specimen transmittance,

$$f(x,y) = \exp[i\varphi(x,y)] \tag{4.13}$$

where φ is the phase change caused by the sample. In the BFP of the image forming lens, the electron disturbance can be described by the Fourier transform of the specimen transmittance,

$$g(k_x k_y) = \iint f(x,y)\exp[-2\pi i(k_x x + k_y y)]dxdy \tag{4.14}$$

where k_x and k_y are the x and y components of spatial frequency and are directly proportional to the reciprocal dimensions. As all magnetic lenses suffer from aberrations, the wave is further modified by the transfer function, $t(k_x, k_y)$, where,

$$t(k_x,k_y) = A(k_x,k_y)\exp[-\pi i C_s \lambda^3 (k_x^2 + k_y^2)^2/2]\exp[-\pi i \Delta\lambda(k_x^2 + k_y^2)] \qquad (4.15)$$

$A(k_x,k_y)$ is the 'top-hat' aperture function, $\exp[-\pi i C_s \lambda^3 (k_x^2 + k_y^2)^2/2]$ is the contribution from spherical aberration and $\exp[-\pi i \Delta\lambda(k_x^2 + k_y^2)]$ is the lens defocus effect. The transfer function is necessary if phase variations in the object are to be changed into perceptible intensity variations in the image. In the Fresnel imaging mode the objective aperture is normally removed, and the effect of spherical aberration is insignificant in comparison to the lens defocus. Therefore, to a good approximation,

$$t(k_x,k_y) = \exp[-\pi i \Delta z \lambda({k_x}^2 + {k_y}^2)] \qquad (4.16)$$

Finally, the electron disturbance in the image plane is given by an inverse Fourier transform,

$$i(x,y) = \int\int g(k_x,k_y)t(k_x,k_y)\exp[2\pi i(k_x x + k_y y)]dk_x dk_y \qquad (4.17)$$

with intensity,

$$I(x,y) = |i(x,y)|^2 \qquad (4.18)$$

As equation (4.17) is a nonlinear integral, it is not always possible to interpret an image in terms of the detailed induction distribution within the specimen. Therefore Fresnel, as described earlier, is largely a qualitative technique.

4.4.2 Image formation in the STEM

Image formation in the STEM [53] differs markedly from that in the TEM. In TEM, the imaging lens combines the transmitted electrons into an image, whilst in STEM, the detector selects electrons from a focussed beam and records information. Also, contrast in TEM is determined by the condenser and objective apertures, with the latter positioned in the BFP of the imaging lens after the specimen. In STEM, it is controlled by an aperture in the BFP of the probe-forming lens before the specimen, and the detector collection angle. However, the imaging theory can be made very similar if we take into account a general reciprocity theorem. This states that, hypothetically, indistinguishable images can be obtained in the TEM and STEM provided (i) the imaging lens of the TEM is identical to the probe forming lens of the STEM, (ii) the current density distribution in the TEM electron source is identical to the detector response function in the STEM, and (iii) the response function of the TEM recording medium is identical to the current density distribution in the STEM electron source.

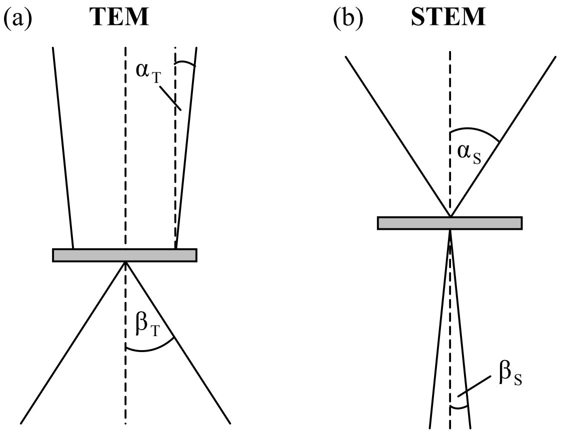

Fig. 4.4: The important beam convergence and divergence angles in (a) TEM and (b) STEM.

With reference to Fig. 4.4, the TEM convergence semiangle is defined as α_T and the objective aperture collection semiangle as β_T [48]. For STEM, the equivalent angles are the beam-convergence angle α_S and the detector collection angle β_S. Therefore, as long as the electron paths contain equivalent angles of convergence and collection at some point in the optical system, the image contrast in TEM and STEM will be the same. This is achieved by making $\alpha_T = \beta_S$ and $\alpha_S = \beta_T$. In this situation the electrons undergo equivalent angular constraints, just not at equivalent points in the system. The reciprocal relationship arises from considering the TEM image resolution and the size of the incident probe in STEM [50]. The transfer function which relates a point in the TEM image to a point on the specimen exit surface has the same form as that which describes the STEM probe on the specimen entrance surface in terms of the electron source. Consequently, it is possible to reverse the ray directions in a TEM optical schematic to obtain a diagram depicting image formation in the STEM (Fig. 4.5). In reality though, there is more freedom in STEM image formation due to variations in the detector geometry and response function.

Assuming a plane wave, $\psi(k_x, k_y)$, illuminates the aperture in the BFP of the probe-forming lens, the electron disturbance is given by the transfer function, $t(k_x, k_y)$, as before. At the specimen plane, this may be written as the inverse Fourier transform,

$$u(x,y) = \iint t(k_x,k_y)\exp[2\pi i(k_x x + k_y y)]dk_x dk_y \tag{4.19}$$

The electron probe is scanned across the surface of the sample, but for mathematical convenience we assume it remains stationary and centred on the optic axis whilst the specimen is scanned. When a point on the specimen with co-ordinates (x_0, y_0) is coincident with the optic axis, the disturbance leaving the specimen is given by,

$$u'(x,y) = f(x - x_0, y - y_0)u(x,y) \tag{4.20}$$

The wave arriving at the detector plane is the Fourier transform of this,

$$v(k_x,k_y) = \iint f(x - x_0, y - y_0)u(x,y)\exp[-2\pi i(k_x x + k_y y)]dxdy \tag{4.21}$$

with intensity,

$$I(k_x,k_y) = \left|v(k_x,k_y)\right|^2 \tag{4.22}$$

However, the image signal is also dependent on the detector response, which interprets the phase information from the beam. For a response function, $R(k_x,k_y)$, the image signal is expressed as,

$$i(x_0,y_0) = \iint I(k_x,k_y)R(k_x,k_y)dk_x dk_y \tag{4.23}$$

In DPC, the difference signal is proportional to the corresponding component of the electron intensity distribution. As was discussed in chapter 2, this is proportional to the perpendicular component of magnetic induction, rendering DPC a quantitative technique.

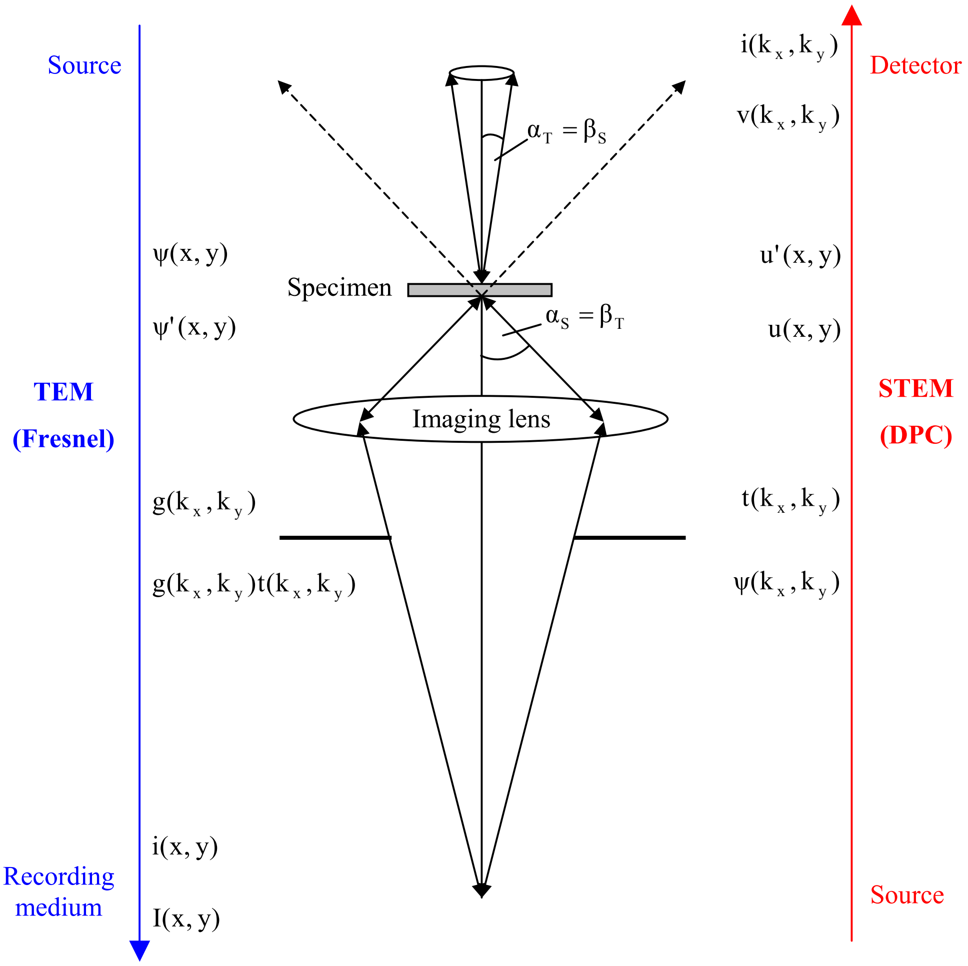

Fig. 4.5: The principle of reciprocity in the TEM/STEM.

4.5 Lorentz image calculations

Lorentz imaging involves deflection of the electron beam by the magnetic induction associated with the sample. To recall, the deflection, β, is given by,

$$\beta = \frac{e\lambda}{h}\int_{-\infty}^{\infty}(\mathbf{B}\times\hat{\mathbf{n}})dz \tag{4.24}$$

where e is the magnitude of the electronic charge, λ is the electron wavelength, **B** is the magnetic induction, $\hat{\mathbf{n}}$ is the unit vector parallel to the beam and h is Planck's constant. Considering the quantum mechanical approach, the phase change incurred by the electron on passing through the material is given by,

$$\varphi(\mathbf{r}) = -\frac{e}{\hbar}\int_{-\infty}^{\infty}(\mathbf{A}\cdot\hat{\mathbf{n}})dz \tag{4.25}$$

where **A** is the magnetic vector potential [92]. In real space **A** can be written as,

$$\mathbf{A}(\mathbf{r}) = \frac{1}{4\pi}\int_{V'} \frac{\nabla \times \mathbf{B}(\mathbf{r'})}{|\mathbf{r} - \mathbf{r'}|} dV' \tag{4.26}$$

which is a convolution of $\nabla \times \mathbf{B}(\mathbf{r})$ and $\frac{1}{4\pi r}$,

$$\mathbf{A}(\mathbf{r}) = \frac{1}{4\pi r} \otimes \nabla \times \mathbf{B}(\mathbf{r}) \tag{4.27}$$

However, $\nabla \times \mathbf{B}(\mathbf{r})$ can be written in terms of the conduction, $\mathbf{J_C}$, displacement, $\mathbf{J_D}$, and Amperian current densities, $\mathbf{J_M}$,

$$\begin{aligned} \nabla \times \mathbf{B} &= \mu_0(\nabla \times \mathbf{H}) + \mu_0(\nabla \times \mathbf{M}) \\ &= \mu_0(\mathbf{J_C} + \mathbf{J_D}) + \mu_0 \mathbf{J_M} \end{aligned} \tag{4.28}$$

Typically in the TEM, there are no conduction or displacement currents, and so $\mathbf{A}(\mathbf{r})$ can be rewritten as,

$$\mathbf{A}(\mathbf{r}) = \frac{\mu_0}{4\pi r} \otimes \nabla \times \mathbf{M}(\mathbf{r}) \tag{4.29}$$

Inserting this into the phase equation, we have,

$$\varphi(\mathbf{r}) = -\frac{e\mu_0}{4\pi r\hbar} \otimes \int_{-\infty}^{\infty} (\nabla \times \mathbf{M}) \cdot \hat{\mathbf{n}} dz \tag{4.30}$$

Assuming the film lies in the xy-plane, the beam is incident along the z-direction and the magnetisation is constant through the thickness of the film, t,

$$\varphi(\mathbf{r}) = -\frac{e\mu_0 t}{4\pi r\hbar} \otimes (\nabla \times \mathbf{M}) \cdot \hat{\mathbf{z}} \tag{4.31}$$

Therefore Lorentz microscopy can be considered as Amperian current microscopy, with the electron phase dependent on the local magnetisation curl component parallel to the electron beam direction [93,94].

4.5.1 DPC image calculations

With reference to the previous section on image formation in the TEM and STEM, it is clear that the final image depends on both the electron-specimen interaction and also the transfer function of the imaging system. In DPC, an in-focus image is built up as the probe is scanned across the specimen surface. The contrast in the final image is generated by the segmented detector which converts the phase changes to intensity variations. Therefore, in this mode of microscopy the image is affected mainly by the Lorentz force, so the aperture, defocus and spherical aberration terms of the contrast transfer function can be neglected. Electrostatic phase contributions and Bragg scattering from the crystallites also affect the image, but these have been excluded for simplification. Taking equation 4.25, the DPC signal is found by taking the 2D derivative perpendicular to the electron beam,

$$\nabla_{\perp}\varphi(\mathbf{r}) = -\frac{e}{\hbar}\int_{-\infty}^{\infty}(\nabla\times\mathbf{A})\times\hat{\mathbf{n}}\,dz \tag{4.32}$$

As $\mathbf{B} = \nabla\times\mathbf{A}$, this can be rewritten as,

$$\nabla_{\perp}\varphi(\mathbf{r}) = -\frac{e}{\hbar}\int_{-\infty}^{\infty}(\mathbf{B}\times\hat{\mathbf{n}})\,dz \tag{4.33}$$

So the DPC image is related to the integrated magnetic induction component perpendicular to the beam [95].

4.5.2 Fresnel image calculations

In the Fresnel mode, a defocused image is projected directly onto the viewing screen. In this situation, the electron wave is affected by both the specimen interaction and the defocus term of the transfer function [96]. Although Fresnel imaging of domain walls is generally considered to be a non-linear imaging mode, under certain conditions the information can be linearly interpreted and used directly in a quantitative manner [97]. In the linear regime, the Fresnel image intensity is given by,

$$I(\mathbf{r},\Delta) = 1 - \frac{\Delta\lambda}{2\pi}\nabla_{\perp}^{2}\varphi(\mathbf{r}) \tag{4.34}$$

where Δ is the defocus distance and $\nabla_{\perp}^{2}$ is the Laplacian relating to the in-plane coordinates only [98-100]. The derivation of this equation assumes that higher order defocus terms are neglected and a small angle approximation is applied to the transfer function [101]. The spatial frequencies in the image determine the extent with which this equation can be applied for a given defocus. For the images considered in this thesis, the magnetic resolution may be determined by the domain wall width. Therefore, in a 200kV microscope a defocus value of $\leqslant 200\mu m$ should enable linear imaging. Assuming these conditions and noting that,

$$\varphi(\mathbf{r}) = -\frac{e}{\hbar}\int_{-\infty}^{\infty}(\mathbf{A}\cdot\hat{\mathbf{n}})dz \qquad \text{and} \qquad \nabla_{\perp}\varphi(\mathbf{r}) = -\frac{e}{\hbar}\int_{-\infty}^{\infty}(\mathbf{B}\times\hat{\mathbf{n}})dz\,,$$

the Laplacian can be expressed as,

$$\begin{aligned}\nabla_{\perp}^{2}\varphi(\mathbf{r}) &= -\frac{e}{\hbar}\int_{-\infty}^{\infty}\nabla\cdot(\mathbf{B}\times\hat{\mathbf{n}})dz \\ &= -\frac{e}{\hbar}\int_{-\infty}^{\infty}(\nabla\times\mathbf{B})\cdot\hat{\mathbf{n}}dz\end{aligned} \tag{4.35}$$

Again, ignoring conduction and displacement currents,

$$\nabla_{\perp}^{2}\varphi(\mathbf{r}) = -\frac{e\mu_0}{\hbar}\int_{-\infty}^{\infty}(\nabla\times\mathbf{M})\cdot\hat{\mathbf{n}}dz \tag{4.36}$$

Inserting the Laplacian into equation 4.34 then gives,

$$I(r,\Delta) = 1 + \frac{e\mu_0\Delta\lambda}{h}\int_{-\infty}^{\infty}(\nabla\times\mathbf{M})\cdot\hat{\mathbf{n}}dz \tag{4.37}$$

Therefore, assuming linear behaviour, the Fresnel image can be expressed as the integrated magnetisation curl component parallel to the electron beam [101]. In practice, however, small values of defocus present problems with the signal to noise ratio, especially when there are non-magnetic contributions to the image contrast. For this reason, defocus values of greater than 200μm were used to acquire the experimental Fresnel images.

In order to calculate the Lorentz images from the magnetisation distribution, it is necessary to consider the phase in terms of the magnetic vector potential. In real space, this expression involves a convolution which is difficult to calculate. This problem, however, becomes far easier to compute when we convert to Fourier space. In Fourier space, a convolution can be written as a straight multiplication of the Fourier transforms of the two functions, allowing faster processing. The Fourier transform produces a complex number valued output image that can be displayed as separate real and imaginary parts. All image calculations were performed using the Fast Fourier Transform (FFT) algorithm available on the TEM software package, Digital Micrograph. The scripts themselves were written by Dr Stephen McVitie and Gordon White at the University of Glasgow. The FFT technique involves a decomposition of the discrete Fourier transform which reduces the number of calculations from N^2 to $\mathrm{N}\log_2 \mathrm{N}$, where N is the number of real image pixels in one dimension. In this case, N corresponds to the cell size of the micromagnetic simulation. Typically, FFT algorithms restrict the size of the input image to a square of side $\mathrm{N} = 2^{\mathrm{n}}$, where n is an integer. As a result, the area around the magnetic structure has to be padded out with pixels of zero intensity. Here, such a constraint is advantageous, as it allows the observation of stray field outside of the element.

As the stray field contributes to the image contrast in DPC, it is useful to consider the field sources in the sample. These are the surface charge associated with the out-of-plane magnetisation component, M_z, and the volume charge produced by the divergence of the in-plane magnetisation, $-\nabla \cdot \mathbf{M}_{\|}$. As DPC is sensitive to the integrated induction in the plane of the specimen, only the latter affects the image. Also, in 20nm thick films, the magnetisation can be assumed to lie predominantly in the plane of the film (xy-plane), so the main sources of field are the domain walls and element edges. Calculation of the in-plane field provides a visual comparison between the OOMMF magnetisation maps and the simulated DPC images. The stray field calculation is intensive in real space, however,

$$\mathbf{H}(\mathbf{r}) = \frac{1}{4\pi} \int_{\mathrm{V}'} \frac{-[\nabla \cdot \mathbf{M}_{\|}(\mathbf{r}')](\mathbf{r} - \mathbf{r}')}{|\mathbf{r} - \mathbf{r}'|^3} \mathrm{dV}' \qquad (4.38)$$

so it is performed in the Fourier domain [102,103] to simplify the expression and reduce the computation time. Alternatively, for a reasonable approximation of the in-plane field it is possible to calculate $-\nabla \cdot \mathbf{M}_{\|}$ from the magnetisation data.

4.6 Simulation of a square element

To demonstrate the use of these Lorentz image calculations, a 20nm thick square element of side 2μm has been considered. The ground state for this element is a flux-closure configuration and the corresponding magnetisation vector image is shown in Fig. 4.6a. By mapping the magnetisation along orthogonal axes, the images in Fig. 4.6b were produced. The electron phase was then determined using equation 4.31 in Fourier form. This calculation requires the magnetisation to be periodic, and this was implemented using an algorithm proposed by Mansuripur [104] which represents the magnetisation by a Fourier series. The phase image is presented in Fig. 4.6c. Following this, the phase was differentiated along the x and y directions to produce the calculated DPC images shown in Fig. 4.6d. As a direct comparison, experimental DPC images are included in Fig. 4.6e which show an excellent agreement. The DPC simulations appear very similar to the in-plane magnetisation components in Fig. 4.6b. This is because the magnetisation contributes greatly to the phase gradient image, with very small stray field effects as a result of the flux-closure. However, subtle differences can be noticed around the domain wall regions. These field effects become apparent when we consider the components of integrated field intensity (Fig. 4.6f), which are dependent on the in-plane divergence of the magnetisation (Fig. 4.6g). Although rather weak, the field is strongest at the domain walls and acts against the magnetisation, reducing the integrated induction relative to that in the centre of the domains.

For the Fresnel simulation, the phase Laplacian in equation 4.34 was calculated for a defocus value of 200μm. Following this, the transfer function was taken into account using a standard wave optical treatment [105,106]. Alternatively, a close representation can be obtained from the out-of-plane curl of the magnetisation as indicated by equation 4.37. Calculated Fresnel and $\nabla \times \mathbf{M}_\perp$ images are shown in Fig. 4.6h and Fig. 4.6i respectively. For comparison, an experimental Fresnel image is presented in Fig. 4.6j. The strong contrast at the centre of the element arises from rotation of the magnetisation and is not related to M_z, which makes no contribution to $\nabla \times \mathbf{M}_\perp$. As can be seen, these images agree well, although the $\nabla \times \mathbf{M}_\perp$ image is less physically correct. Additionally, the high spatial frequency ringing around the element edges in some of the simulated images results from the fact that the calculations were performed using Fourier transforms and the edges are abrupt.

In this project, Fresnel and DPC image calculations were used as a useful guide to the contrast that could be expected during the setup of the experimental imaging conditions. They have also been helpful in interpreting experimental images containing magnetic information obscured by contamination and physical defects. Although the effects of electrostatic phase and Bragg scattering were not taken into account here, they can be included in the simulations if required. Related work involving the transport of intensity equation (TIE) have shown that phase reconstruction is possible using experimental Fresnel images taken at different values of defocus [101,107,108]. Such calculations allow quantitative information to be obtained on the magnetic induction, but have not been used in this study.

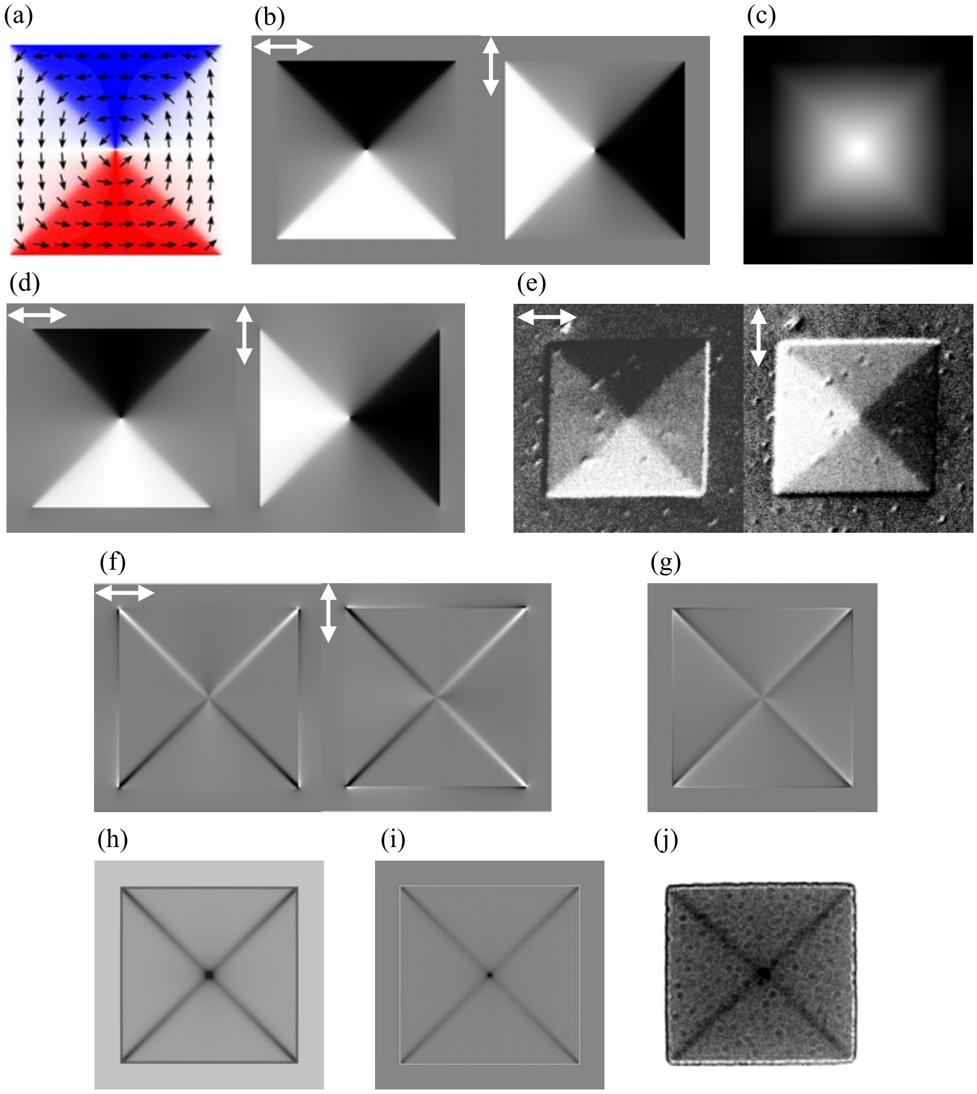

Fig. 4.6: (a) Simulation of a square element in the flux-closure state and the corresponding (b) x and y components of magnetisation. (c) The phase must be determined before (d) in-plane induction maps can be calculated for comparison to (e) experimental DPC images. (f) Orthogonal integrated field distributions show the difference between the magnetisation and induction calculations which are dependent on the (g) in-plane magnetisation divergence. Simulated (h) Fresnel and (i) out-of-plane magnetisation curl images agree favourably with an (j) experimental Fresnel image. Arrows in the figure show the directions of the integrated components.

Chapter 5

Breaking the symmetry of thin film elements to tailor their magnetic properties

5.1 Introduction

A low switching field and reproducible reversal behaviour are desirable properties of MRAM storage cells. With magnetic thin film elements, however, simple geometric structures can support a large number of different remanent configurations [109] which can result in history-dependent switching fields [110,111] and the formation of flux-closure states [112,113]. Their miniaturisation also faces the problem that the coercivity is inversely proportional to element width [114].

Rectangular 'bar' elements [115-123] are able to support near-single domain states in so-called 'C' and 'S' configurations with almost identical energy. The states consist of near-uniform magnetisation along the main axis of the element, with the domains at either end orientated nearly perpendicular to this. The principal difference between the C and S configurations is the relative direction of these end vectors, where they lie parallel in the S-state and anti-parallel in the C state. Similar configurations are possible where vortex end domains replace the transverse regions. As described in chapter 1, magnetisation vortices involve the rotation of spins around a circular Bloch line or vortex core. These spins become tighter as the radius of curvature decreases until, at the centre of the vortex, they point out-of-plane. When vortices exist at the ends of a thin film element, they usually appear as part of an asymmetric domain structure, shown schematically in Fig. 5.1. The similarity in energy means that on repeated magnetic switching it is possible to form either a C or an S state. Each of the states mentioned above have been simulated and are presented in Fig. 5.2.

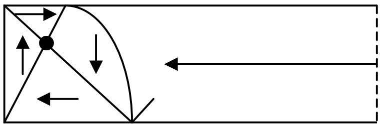

Fig. 5.1: The typical domain structure of a magnetisation vortex formed at the end of a thin film element.

(a) Transverse S $(3.2 \times 10^{-17}\,\mathrm{J})$

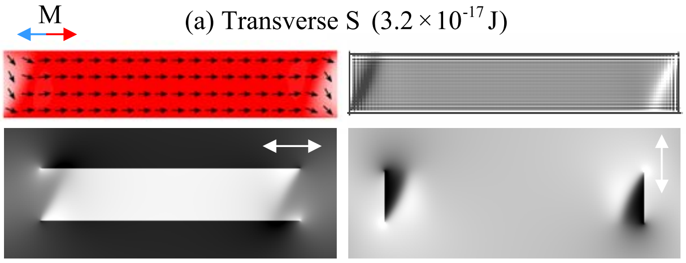

(b) Transverse C $(3.2 \times 10^{-17}\,\mathrm{J})$

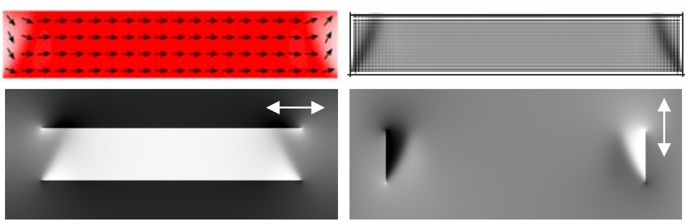

(c) Vortex S $(3.8 \times 10^{-17}\,\mathrm{J})$

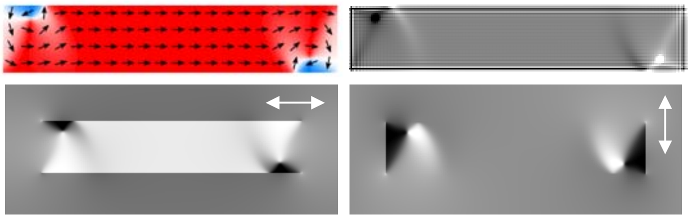

(d) Vortex C $(3.8 \times 10^{-17}\,\mathrm{J})$

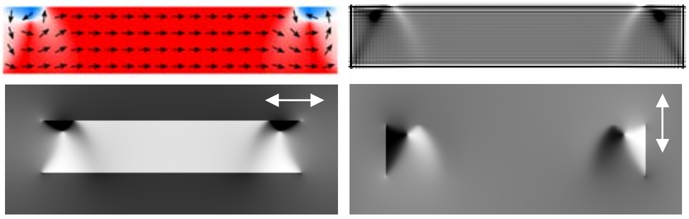

Fig. 5.2: The (a), (b) transverse and (c), (d) vortex ‘S’ and ‘C’ configurations supported by rectangular thin film elements. Equivalent states also exist with the end vectors oriented in the opposite direction. Arrows in the simulations denote the magnetisation vectors. Also shown are calculated Fresnel (top right) and DPC images for each state. The white arrows in the DPC images indicate the direction of sensitivity of the mapped induction components. Pixel colouring represents the x-component of magnetisation as shown.

Magnetising experiments (later) have shown that vortex C states can lead to a flux-closure configuration whilst transverse C, S and vortex S states tend to retain their configuration after switching (Fig. 5.3). Vortex formation is clearly undesirable and can be problematic for the intended single mode switching of elements.

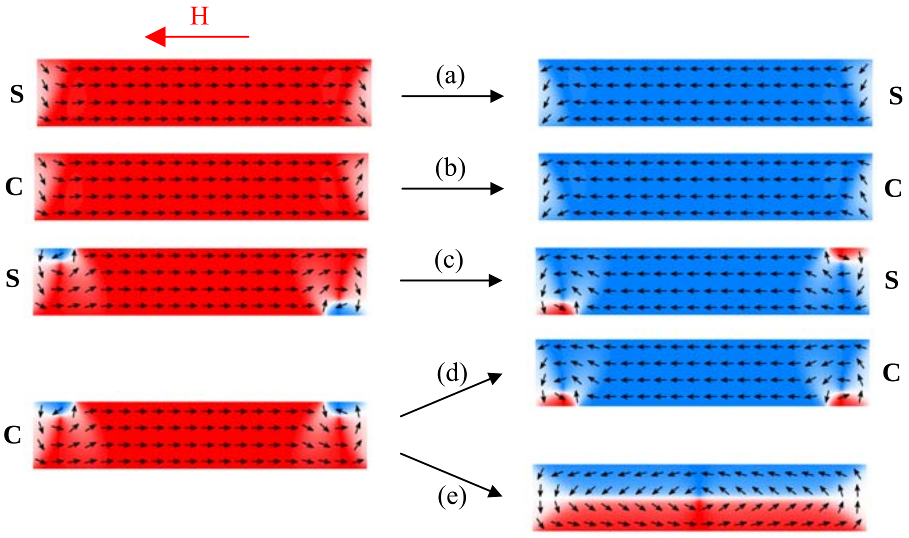

Fig. 5.3: The different transitions that occur **in experiment** with rectangular elements. These simulated elements were of size $1000 \times 200 \times 20\text{nm}^3$. Whilst the transverse (a) S, (b) C and (c) vortex S states retain their configuration after switching, the vortex C state either switches to form (d) an equivalent configuration or (e) undergoes transition to a flux-closure state.

5.2 Possible solutions

In an attempt to overcome the irreproducible switching behaviour of the rectangle, elements with tapered and elliptical ends have been studied in the past [124-130]. In the tapered element (Fig. 5.4a), the end domains responsible for degenerate ground states are suppressed, resulting in a single domain configuration. Experimental and theoretical work on this structure has shown that when a field is applied to switch the magnetisation, reversal begins at the 'corners' between the body of the element and the triangular tip [124]. With the elliptical geometry (Fig. 5.4b), however, different studies have revealed contrasting behaviour. One investigation [130] has shown the element supporting confined end domains that initiate reversal at higher fields, whilst a separate study [127] showed no end domains and reversal nucleated in the centre of the element.

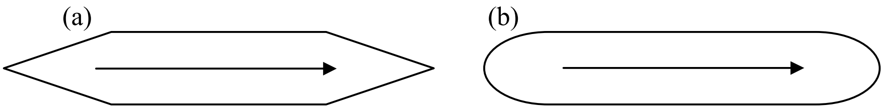

Fig. 5.4: Elements with (a) tapered and (b) elliptical ends have been found to support single domain states provided the end regions are sufficiently narrow.

Therefore, provided the ends of these elements are sufficiently narrow, reproducible switching between single domain states can be achieved. The drawback, however, is an increase in switching field associated with the smaller perpendicular component of magnetisation [130].

In this project, different structures designed to undergo single mode switching between two equivalent configurations were tested using Lorentz microscopy and backed by micromagnetic simulations. By breaking the rectangular symmetry, geometries which support the C or the S state as the ground configuration have been identified. A rectangle has mirror planes parallel to both the long and short axes and 180° rotational symmetry. The new elements, however, have a lower symmetry, with a trapezoidal structure (Fig. 5.5a) exhibiting only the one mirror plane and no rotational symmetry, and a parallelogram (Fig. 5.5b) with a 180° rotational axis and no mirror planes. The states supported are highly dependent on the shape anisotropy and the magnetisation tends to lie parallel to the edges of the element. The decision to experiment with asymmetric geometries was based on recent micromagnetic simulations by Arrott [131], who used a distorted super-octagon structure (Fig. 5.5c). This shape was found to support a C state as the remanent ground configuration offering a possible solution to the selectivity problem. The fabrication of rounded features using an electron beamwriter, however, has its limitations as outlined in chapter 3, and the basic trapezoid and parallelogram geometries were the preferred options. Since this work was started, other groups have also had success with similar structures. Lower aspect-ratio trapezoids and cut-edge shapes (Fig. 5.5d) have been tested with TMR measurements [132] whilst pairs of parallelograms as multibit MRAM cells (Fig. 5.5e) have been studied using finite element simulations [133].

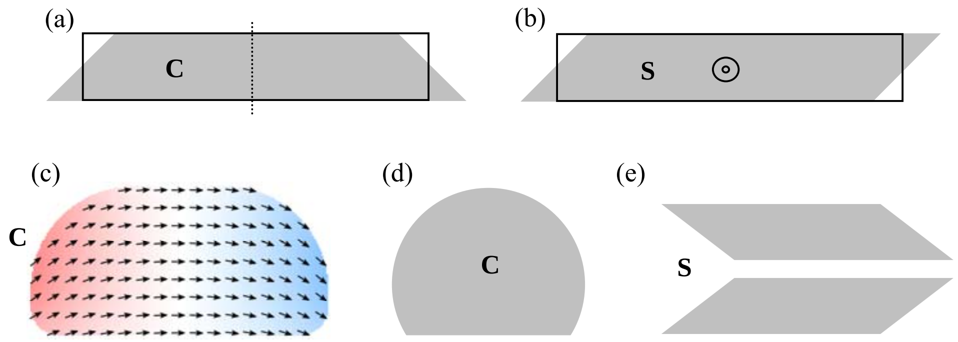

Fig. 5.5: (a) The trapezium and (b) parallelogram shaped elements used in these experiments, both with an identical volume to the rectangle (unfilled). (c) The distorted super-octagon and (d) cut-edge geometries support a remanent C state ground configuration whilst (e) parallelogram-shaped elements exhibit an S state at zero field and have been considered as MRAM storage bits.

5.3 Micromagnetic simulations

Initial simulations [90] were performed on the rectangle, trapezoid and parallelogram, using the rectangular cell as the starting point. On tilting the ends of the $1000 \times 200 \times 20\,\mathrm{nm}^3$ rectangle by 45°, the trapezium and parallelogram were created with an identical volume. In each case, the element was relaxed from several initial conditions to identify some of the possible metastable states that could be supported by the different geometries. Using these as the initial configuration, long-axis fields were then applied to determine the remanent state of each element, study the reversal behaviour and compare switching fields. The absolute field values obtained from these simulations are not particularly important as they usually differ significantly from experiment [123]. What is of interest, however, is the relative difference in switching field. The critical field for each geometry was determined to the nearest Oersted by running detailed simulations in 1 Oe field steps.

5.3.1 Rectangle

Rectangular cells have been known to support a wide variety of states at zero field [109]. The different metastable configurations from this set of simulations are shown as magnetisation vector maps in Fig. 5.6 but do not constitute a complete set. The transverse S (ground) state is shown for comparison. The calculated total system energy for each configuration is also given. These multi-domain states display S and C-like end domains i.e. parallel and anti-parallel. On application of a maximum 1000 Oe field parallel to the long axis, irreversible changes occurred resulting in the formation of the transverse S and C ground states shown in Fig. 5.2. The orientation of the end domains in the metastable states influenced the formation of these ground configurations. On switching the ground state with a reverse field of 424 Oe, the element continued to support the same type of configuration prior to field application, albeit with the central domain in the opposite direction. It is important to note that the field applied was not large enough to completely saturate the magnetisation of the element, but only to reverse it. If saturation had occurred, it is likely that either remanent ground state could have been formed as a result of the degeneracy. Typically, transitions between the transverse C and S states using a long-axis field occur via an intermediate 'flower state' [109,131].

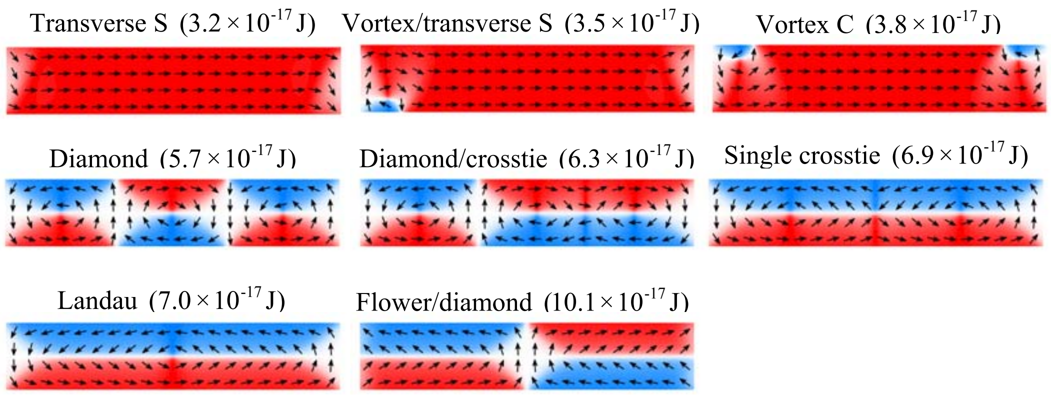

Fig. 5.6: Various metastable states formed in the OOMMF simulations by relaxing the rectangular element from different starting conditions.

The reversal sequences for an S and C state are shown in Fig. 5.7. As a result of the torque, magnetisation changes began at the ends of the element with the transverse domains increasing in size as the field was increased. At the critical field the x-component of magnetisation changed, but the y-component did not. After removing the field, the magnetisation relaxed to leave S and C states equivalent to those supported before field application.

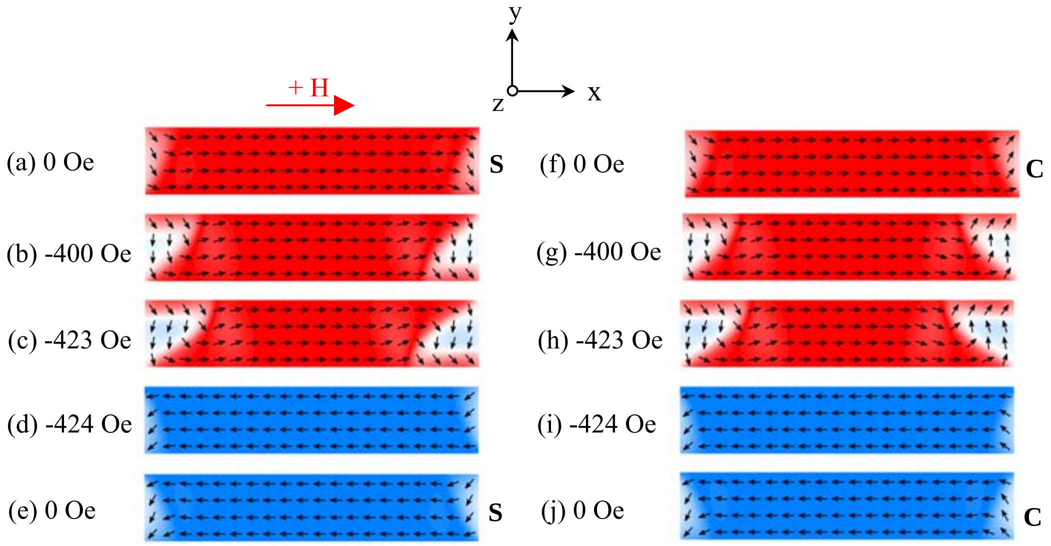

Fig. 5.7: Simulated reversal of the rectangular element from an (a)-(e) S and (f)-(j) C state using a long-axis field. Both states switched at the same field value via the same mechanism. The direction of positive field is shown.

To prevent charging, the domain walls were forced to change position. Without this adjustment, head-to-head and tail-to-tail magnetisation vectors create an unfavourable configuration at either end. Fig. 5.8 shows simplified schematics of the charge distribution around the domain walls of an S-state in the two orientations.

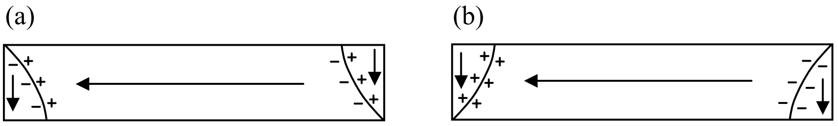

Fig. 5.8: Schematic diagrams showing the magnetic charge distribution around the domain walls with the walls oriented in their (a) new and (b) original positions. The latter configuration is energetically unstable and purely hypothetical.

Following long-axis reversal, a field was applied along the short-axis (Fig. 5.9) to try and uncover any changes in behaviour or different remanent states. This simulation was performed using larger field increments for efficiency. Starting from the transverse S configuration (Fig. 5.9a) and increasing the short-axis field strength saw the y-component of magnetisation increase from the end sections (Fig. 5.9b-c). At 1000 Oe, the formation of a short-axis flower state was evident (Fig. 5.9d). The field was increased further to 4000 Oe which was enough to align all but the corner regions with the applied field (Fig. 5.9e). On reducing the field to zero, the system collapsed into the flower-diamond state (Fig. 5.9f) seen previously in Fig. 5.6. When the field was applied in the opposite direction, two vortices were introduced (Fig. 5.9g) but were later annihilated as the field strength was increased (Fig. 5.9h). The rest of the cycle was the same as the outward path, albeit with the magnetisation in the opposite orientation (Fig. 5.9i-k). A similar simulation was performed using the transverse C state as the starting point. Apart from switching one end section at 200 Oe, the behaviour was identical to Fig. 5.9.

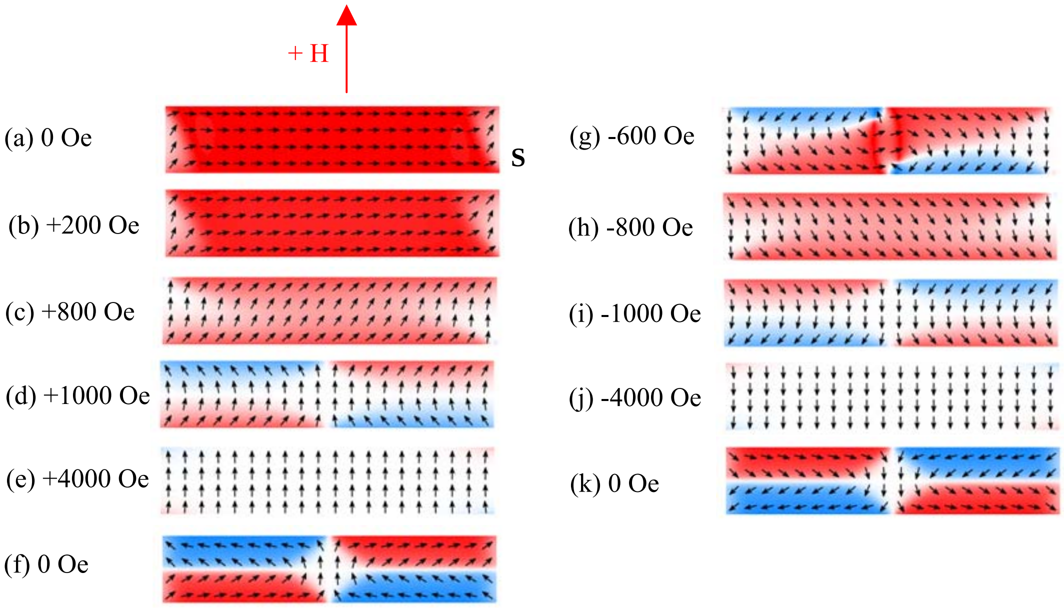

Fig. 5.9: (a)-(k) Simulated short-axis field application for the rectangular element from an initial S state.

5.3.2 Trapezium

Simulations were then performed with the trapezoidal and parallelogram geometries. The various metastable configurations observed after relaxing the trapezium from different starting conditions are shown in Fig. 5.10. The low energy ground state (transverse C) is also given. As can be seen, in comparison to the rectangular cell, the number of observed high energy states was much reduced. In addition, the difference in energy between the ground and lowest metastable state is greater for the trapezium.

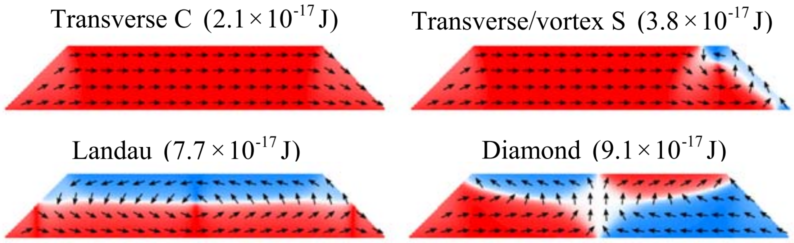

Fig. 5.10: Various states formed in the OOMMF simulations by relaxing the trapezium from different starting conditions.

As with the rectangular cell, long axis fields were applied to study the reversal mechanism and obtain an estimate for the switching field (Fig. 5.11). In a similar manner, reversal began at the ends of the element, causing an increase in the size of these domains (Fig. 5.11a-c). The spins with a greater perpendicular component were the first to rotate. However, as the shape anisotropy acts to align the magnetisation with the element edges, the magnetisation adjacent to the edges required a larger field to influence. This can be seen in the vector map at -523 Oe where, despite being aligned at 45° to the axis of applied field, the edge magnetisation at the ends of the trapezium remained relatively fixed (Fig. 5.11c). In contrast, the magnetisation near the centre of the end domains experienced a larger rotation at the same field value. As the field was increased to -524 Oe, the magnetisation switched (Fig. 5.11d). Unlike the rectangle, there was no need for the domain walls to change position and prevent charging, because the magnetisation in the end sections was forced to switch as a result of the local geometry. When the field was removed, the system relaxed to a remanent C state (Fig. 5.11e).

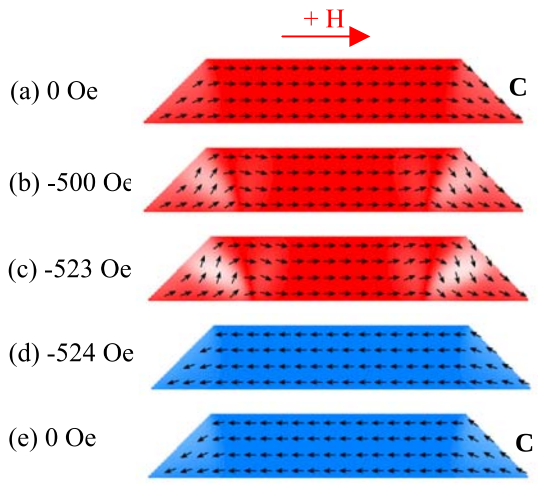

Fig. 5.11: (a)-(e) Simulated reversal of the trapezium from a C state using a long-axis field.

A hysteresis loop with the field applied at 90° to the long axis was later simulated. This sequence is shown in Fig. 5.12. From the initial C state (Fig. 5.12a), an increase in field strength caused the magnetisation to rotate (Fig. 5.12b). However, as a result of the end shape, the magnetisation at one end was oriented against the field direction. An increase in field to 800 Oe caused this region to switch, with the formation of a head-to-head transverse domain wall (Fig. 5.12c). A further increase in magnitude saw the spins gradually align with the field (Fig. 5.12d), before the system relaxed to form a remanent diamond configuration (Fig. 5.12e). This state is not unlike that observed with the rectangular element during the hard-axis cycle in Fig. 5.9. By applying the field in the opposite direction, two vortices were formed (Fig. 5.12f). At higher field these annihilated to leave a tail-to-tail transverse wall (Fig. 5.12g) which grew in length with increasing field strength (Fig. 5.12h). The remainder of this field cycle was the same as the outward path, with the magnetisation gradually aligning perpendicular to the length of the element (Fig. 5.12i) and then relaxing to form the previously observed diamond state (Fig. 5.12j).

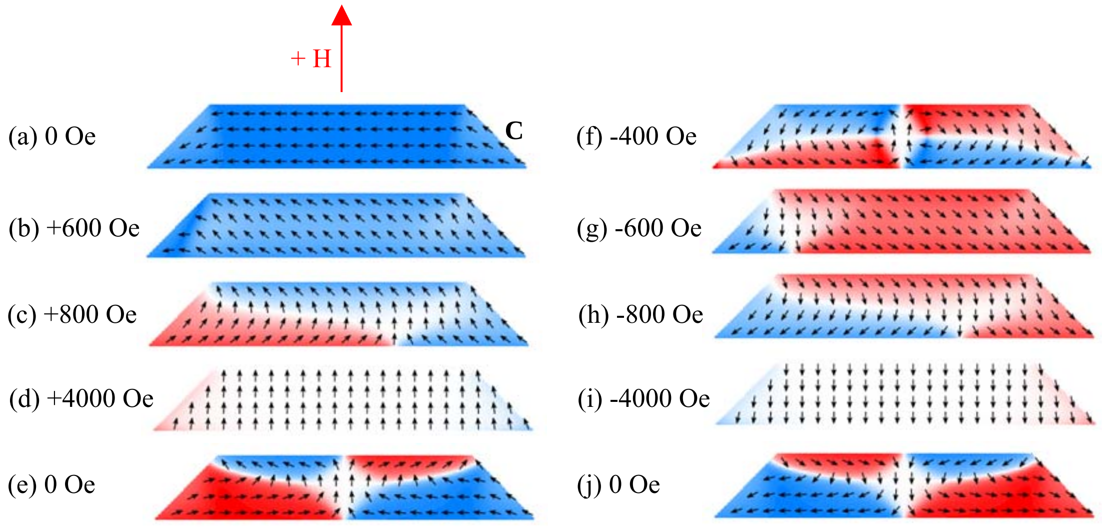

Fig. 5.12: (a)-(j) Simulated short-axis field application for the trapezoidal element from an initial C state.

5.3.3 Parallelogram

As with the trapezoid, the number of metastable remanent states that could be formed by the parallelogram was far fewer than the rectangular element. The different configurations are shown in Fig. 5.13 along with the transverse S ground state.

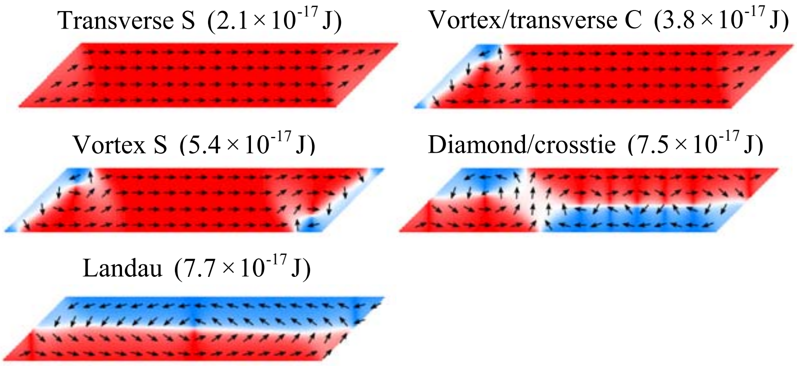

Fig. 5.13: Various states formed in the OOMMF simulations by relaxing the parallelogram from different starting conditions.

When a long-axis field of 1000 was applied, any vortices present from the initial relaxation were driven out, leaving the element in the ground state. The field was then applied in the opposite direction to study the reversal. The magnetisation vector maps depicting this behaviour are shown in Fig. 5.14. From the initial S state (Fig. 5.14a), spins near the centre of the end regions rotated to align with the field, increasing the size of these domains (Fig. 5.14b-c). At -524 Oe, the magnetisation of each domain switched (Fig. 5.14d). This field was of the same strength required to switch the trapezoidal element. After removing the field, the magnetisation relaxed to a transverse S state (Fig. 5.14e).

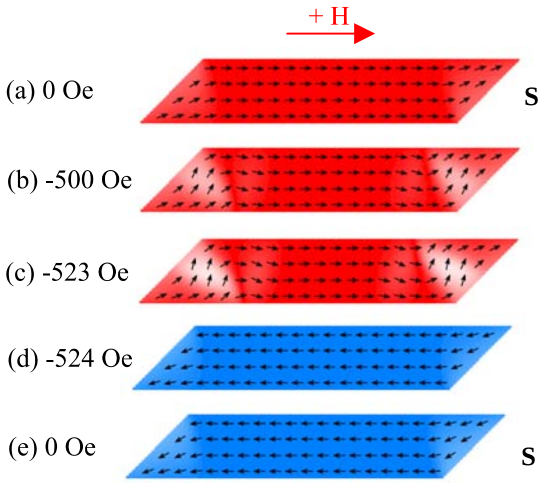

Fig. 5.14: (a)-(e) Simulated reversal of the parallelogram from an S state using a long-axis field.

Vector maps from the simulated short-axis hysteresis loop are given in Fig. 5.15. From a vortex S state (Fig. 5.15a), a field of 200 Oe was enough to remove both vortices and force a transverse S configuration (Fig. 5.15b). At 4000 Oe near-saturation occurred (Fig. 5.15c) before removal of the field allowed the system to relax to its ground state (Fig. 5.15d). With the field applied in the opposite direction, the magnetisation switched (Fig. 5.15f) instead of forming the diamond structure observed with each of the other geometries. A further increase in field strength saw an increase in the y-component of magnetisation (Fig. 5.15g) before the system collapsed to a transverse S state at zero field (Fig. 5.15h).

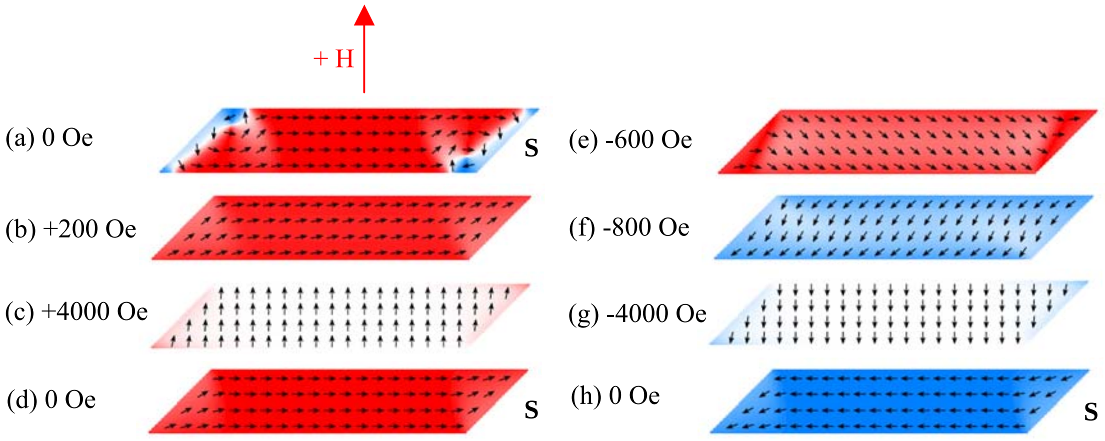

Fig. 5.15: (a)-(h) Simulated short-axis field application for the parallelogram from an initial vortex S state.

These micromagnetic simulations have shown that it is possible for rectangular elements to support a large number of different metastable configurations at zero field. In addition, depending on the orientation of the end vectors before long-axis field application, the element can relax into either the C or the S state. As explained, this irreproducibility is an unattractive property for storing bits [115]. The simulations have also revealed that the rectangular geometry can support a flower/diamond configuration during a short-axis cycle as a result of its mirror symmetry.

In comparison, the trapezoid and parallelogram were seen to support far fewer metastable configurations at zero field. Long-axis hysteresis loops showed these geometries to return to a single ground state; the trapezium a transverse C state and the parallelogram a transverse S state. With all three shapes, the majority of metastable configurations were found to exist only after the initial relaxation and the vortices were driven out by an applied field of relatively low strength. Like the rectangle, however, the trapezoid did support a diamond structure following hard-axis field application due to its symmetry plane. The formation of this state is probably due to the high symmetry/perfection of simulated structures and is unlikely to be observed in experiment. It could not be formed in the parallelogram.

Another important difference between the rectangular cell and the other geometries is the switching field. Whilst the rectangle switched at 424 Oe, the trapezium and parallelogram both required a field of 524 Oe for reversal. This 100 Oe increase can be attributed to the torque acting on the ends of the element. The end sections of the rectangle (Fig. 5.16a) have spins oriented perpendicular to the field, unlike the other geometries (Fig. 5.16b). Since the reversal was seen to begin at the ends of the element, it follows that the rectangle will begin to switch at a lower field than its less symmetric counterparts.

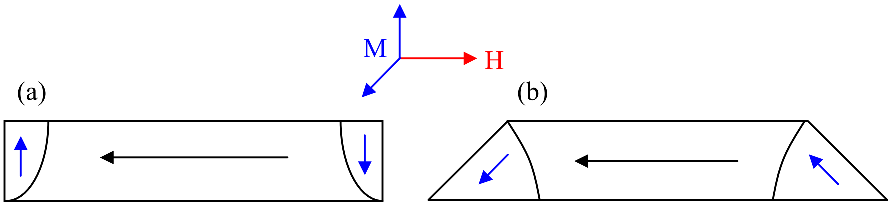

Fig. 5.16: The greater torque acting on the end domains as a result of the local geometry allowed the (a) rectangle to reverse at a lower field than the (b) elements with sloping edges.

These simulations have shown that by tailoring the elemental geometry, it is possible to remove the rectangular ground state degeneracy and allow the C and S states to exist as single ground configurations. This indicates, therefore, that single mode switching is likely in real elements of this type. Such structures have been fabricated on SiN membrane substrates and characterised using Lorentz microscopy. The results are presented in the next section.

5.4 Fabricated elements

Elements of the same size and shape as those used in the simulations were fabricated and studied using Lorentz microscopy. The in-plane dimensions were scaled up by two and three times to compare results with the smaller structures. Variation of the element size at constant aspect ratio seemed to have little effect on the magnetic behaviour, however, and the only notable difference was the switching field. As the Fresnel mode is suitable for studying larger structures, images taken from the largest elements are shown to summarise the data. As with the simulations, the rectangular geometry was studied as a benchmark for the other structures.

5.4.1 Rectangle

Figures 5.18-5.21 show the 600nm wide rectangular element. By saturating the magnetisation along the length of the structure and removing the field, the system relaxed to form a transverse C or S state. Subsequent reversal with a long-axis field then caused the nucleation of a vortex at either end, leaving a vortex C or S state as the remanent configuration. In agreement with the simulations, the orientation of the end vectors had a considerable effect on the magnetic state following field application. An initial transverse C state led to the formation of a vortex C state after switching at 70 Oe. Likewise, a transverse S state switched to its vortex counterpart at the same field strength. On repeated field cycles, the element was observed to maintain its vortex configuration so long as the applied field did not saturate the magnetisation. The switching field for vortex to vortex transition was around 25 Oe. At higher fields, the vortices were driven out of the structure, allowing the element to revert back to the transverse state. On occasion, reversal from a vortex C state resulted in the formation of a flux closure configuration. These were formed with various numbers of vortices and cross-ties. This was immediately surprising considering that the evaporator film thickness monitor (FTM) measured the permalloy thickness to be 20nm yet cross-ties only form in permalloy films with thicknesses of between 30 and 90nm. A subsequent calibration by Dr Nils Wiese using an atomic force microscope (AFM) revealed that the evaporator was depositing more material than the thickness monitor was detecting. The calibration graph shown in Fig. 5.17 shows that the elements were more likely to have been ~33nm thick than the 20nm initially intended. A measurement with the AFM later confirmed this. Nevertheless, the formation of cross-tie walls does not adversely affect the results and is therefore not a major issue in this particular study.

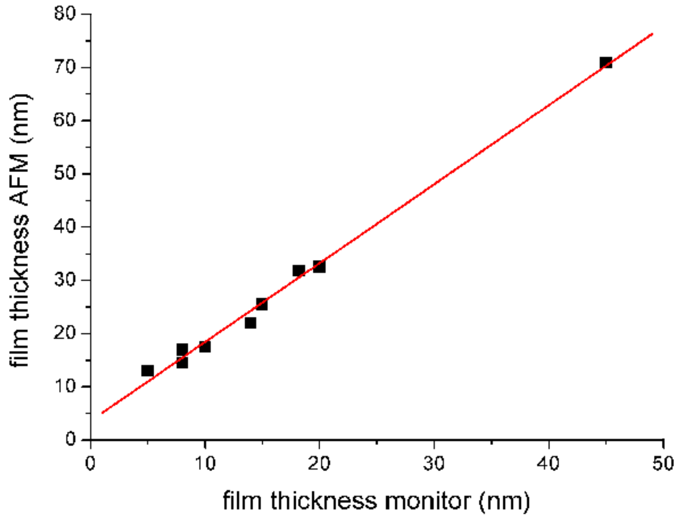

Fig. 5.17: NiFe film thickness measured using the AFM and FTM.

In some instances a single vortex core was observed, but in others as many as 4 vortices (and 3 cross-ties) were present at remanence. An increase in field to around 55 Oe, however, was enough to take the element to a vortex C state. The corresponding images are shown in Figs. 5.18-5.20.

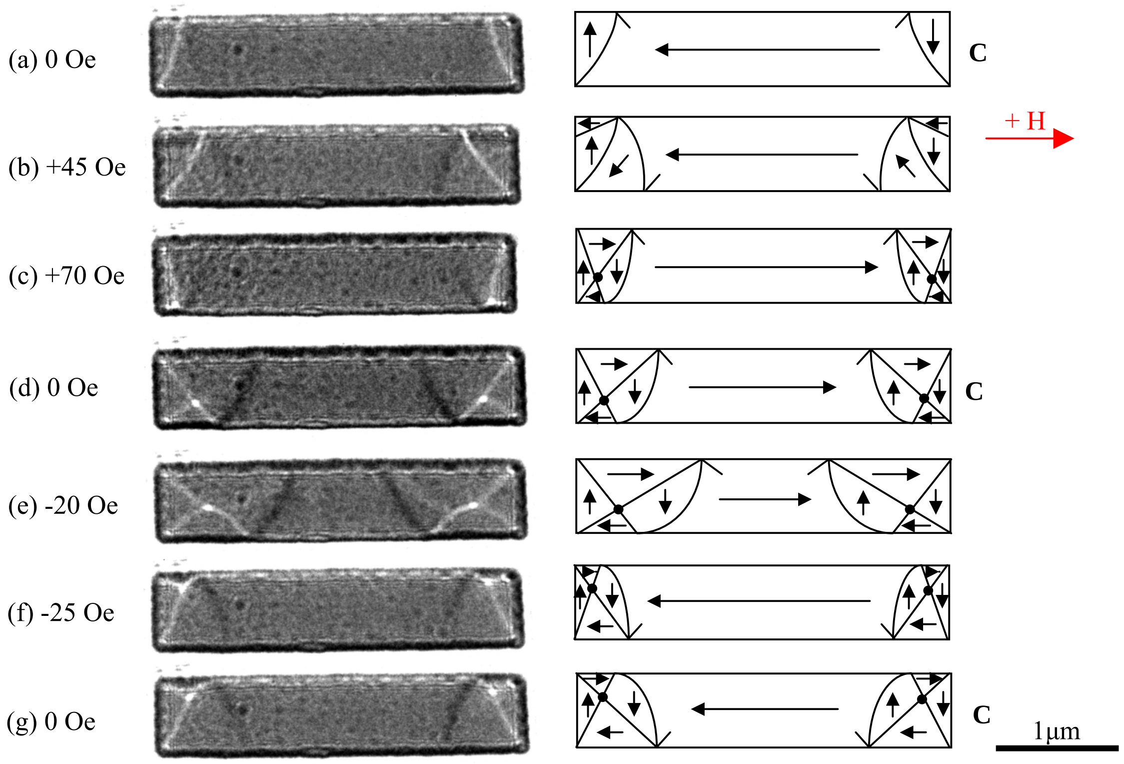

Fig. 5.18: (a)-(g) Reversal of the $3000 \times 600 \times 20\text{nm}^3$ wide rectangular element following saturation along the main axis. The magnetisation switched from a transverse C state to a vortex C state.

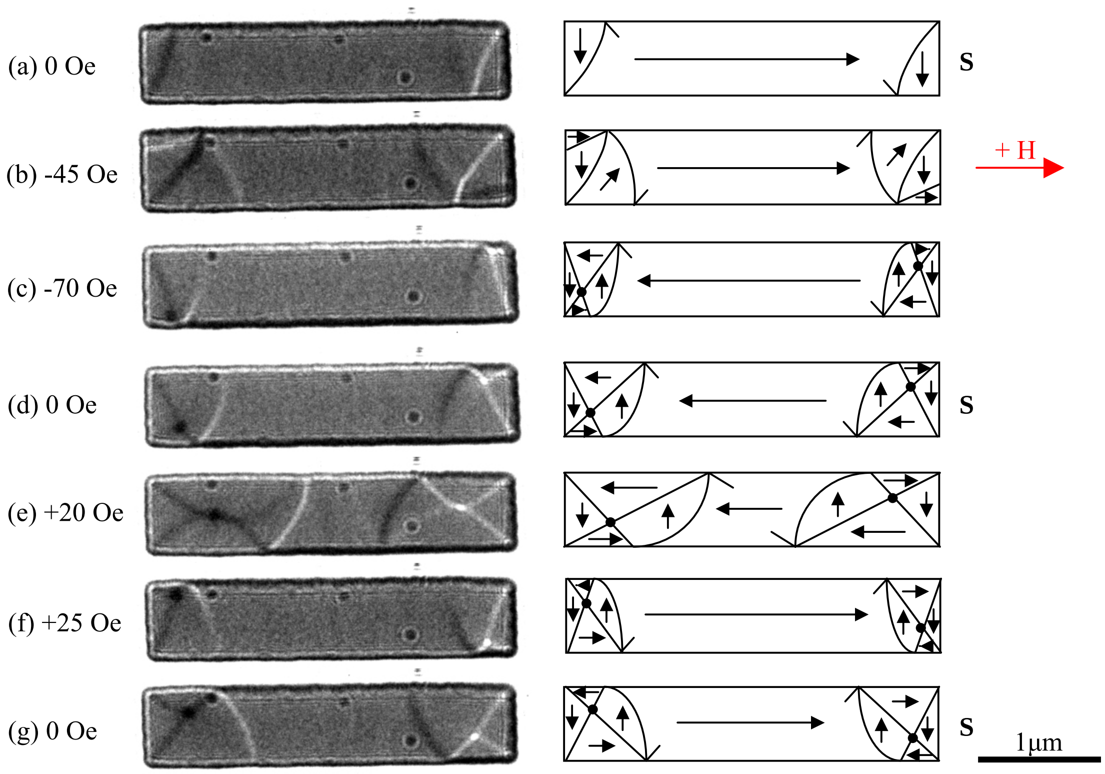

Fig. 5.19: (a)-(g) Reversal from a transverse S state to a vortex S state.

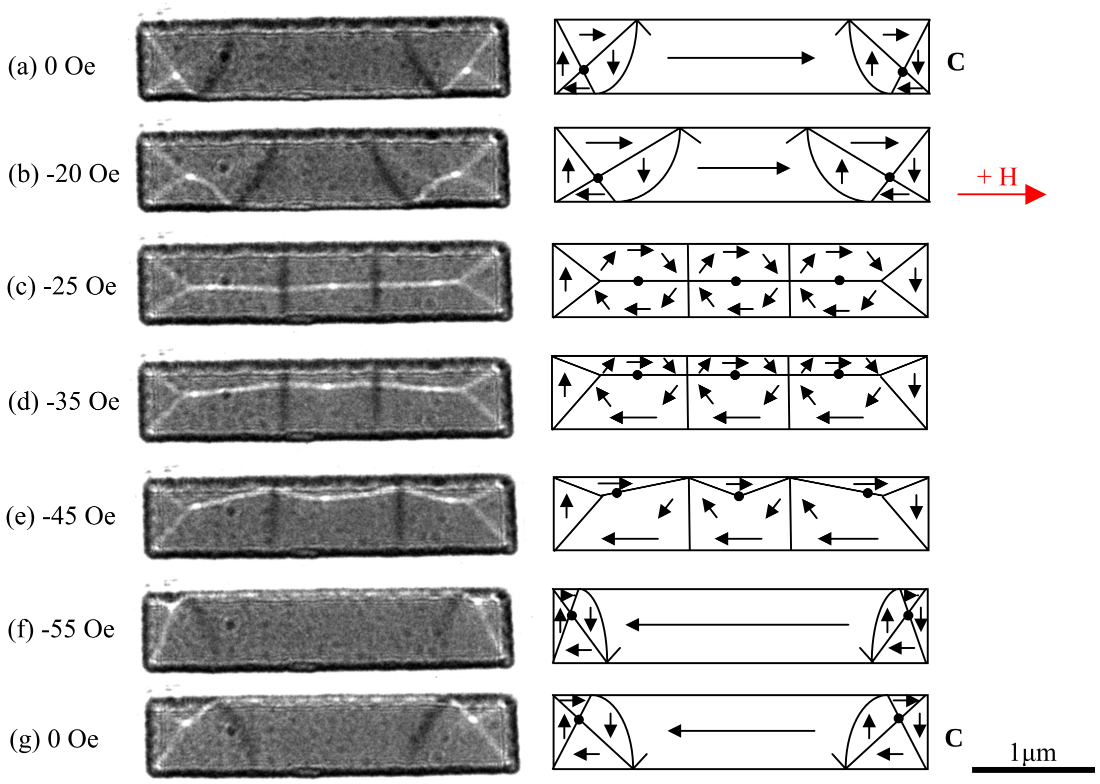

Fig. 5.20: (a)-(g) On occasion, the rectangle switched from a vortex C state to a flux closure configuration.

Short axis fields were then applied from initial transverse S and C states. Due to similarities in behaviour, only the C state field sequence is shown (Fig. 5.21).

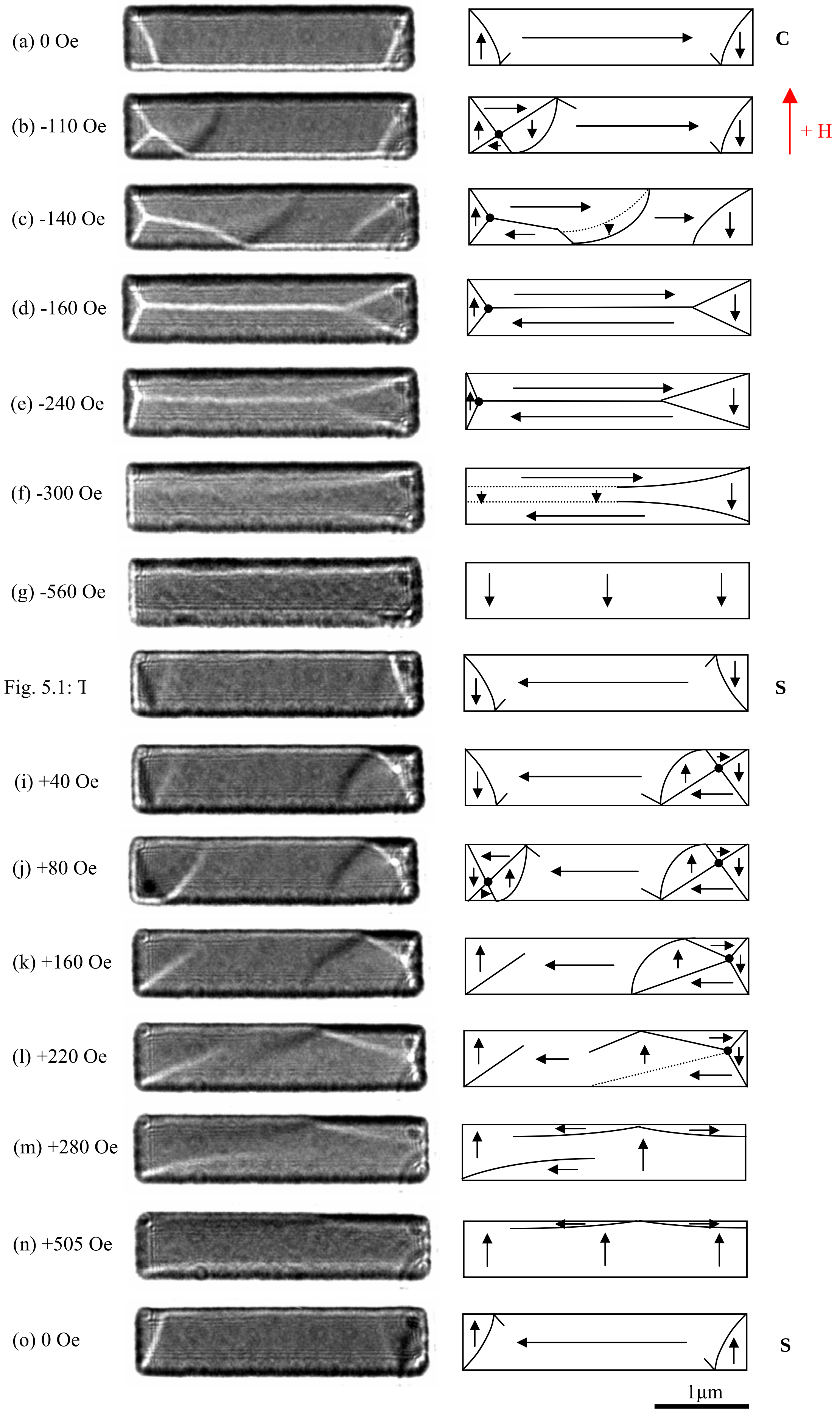

Fig. 5.21: (a)-(o) Short-axis reversal from an initial transverse C state.

At –110 Oe (Fig. 5.21b), a vortex was nucleated at the end section magnetised anti-parallel to the field, whilst the domain at the opposite end of the element increased in size. At –160 Oe, a distorted flux-closure state formed as seen previously (Fig. 5.21d). An increase in field then caused a reduction in size of the left hand domain (Fig. 5.21e) before annihilation at –300 Oe (Fig. 5.21f). Further domain wall annihilation took place at higher field, leaving a near-uniform configuration at –560 Oe (Fig. 5.21g). The element was then saturated at 2000 Oe and allowed to relax, forming a transverse S state with the central domain in the opposite orientation (Fig. 5.21h). By applying a field in the positive y-direction, vortices were introduced at the end regions as before (Fig. 5.21i,j) and subsequently driven out of the element at higher field. As the end domains were magnetised in the same direction, no flux closure state was possible. Instead, a flower-like domain pattern was formed at +280 Oe (Fig. 5.21m). Following saturation in this direction, the element relaxed to another transverse S state (Fig. 5.21o). The switching behaviour of the trapezium is discussed in the next section.

5.4.2 Trapezium

In agreement with the micromagnetic simulations, the trapezoid was not able to support a remanent S state following long-axis field application. In addition, as the end regions were sufficiently narrow, vortex formation was not observed. As will be seen in chapter 7, the nucleation of a magnetisation vortex is dependent on the width and thickness of material. Simulated phase diagrams of head-to-head domain walls have shown vortex formation in wider, thicker strips of permalloy, with transverse states favoured when these dimensions are reduced [134,135]. It is not surprising, therefore, that by tapering the end sections and reducing the element width in these regions, transverse domains were observed instead of vortices.

Fig. 5.22a shows the ground state following saturation along the main axis. By applying a field anti-parallel to the mean direction of magnetisation, domain wall contrast intensified and new walls were nucleated (Fig. 5.22b). Although faint contrast is visible in the large central domain, the magnetisation has been approximated as uniform in the corresponding schematic. This behaviour was also observed in the simulations, where reversal began at the end sections and the perpendicular component of magnetisation was able to rotate. At a field of 100 Oe, the magnetisation switched (Fig. 5.22c) before relaxing to an equivalent C state at zero field (Fig. 5.22d). Subsequent field application took the element round the hysteresis loop with an identical reversal mechanism in the opposite direction (Fig. 5.22e-g). No states other than the transverse C state were observed at remanence.

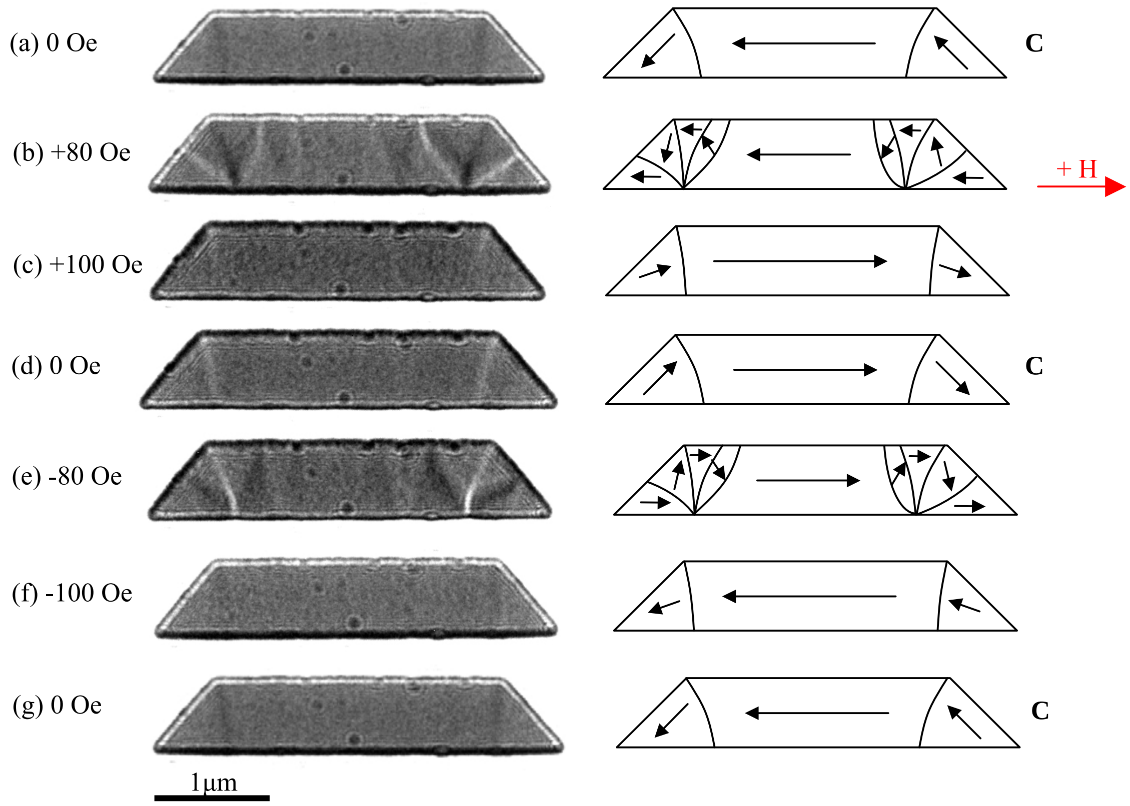

Fig. 5.22: (a)-(g) Reversal of the trapezoid between equivalent C state configurations.

Images captured during the short-axis experiment are shown in Fig. 5.23. From a transverse C state (Fig. 5.23a), a field in the negative y-direction caused the left hand domain to increase in size, whilst the right hand domain, aligned almost anti-parallel to the field direction, shrunk (Fig. 5.23b). A fourth domain was then nucleated, which grew with field strength until saturation (Fig. 5.23c-e). On removing the field a vortex formed in one corner (Fig. 5.23f), but was later annihilated, leaving the element in a transverse C state again (Fig. 5.23g). Increasing the field in the opposite direction took the magnetisation through a similar process until after saturation, the element relaxed to a transverse S state (Fig. 5.23l). This state is unlike the typical configuration observed in a rectangular element because of the difference in end shape, and is relatively unfavourable. A small field in the negative y-direction, however, was enough to switch the less stable end domain and force a transverse C state (Fig. 5.23m). This is slightly different behaviour to what the simulations predicted. In these we saw the formation of a diamond state following saturation in both directions.

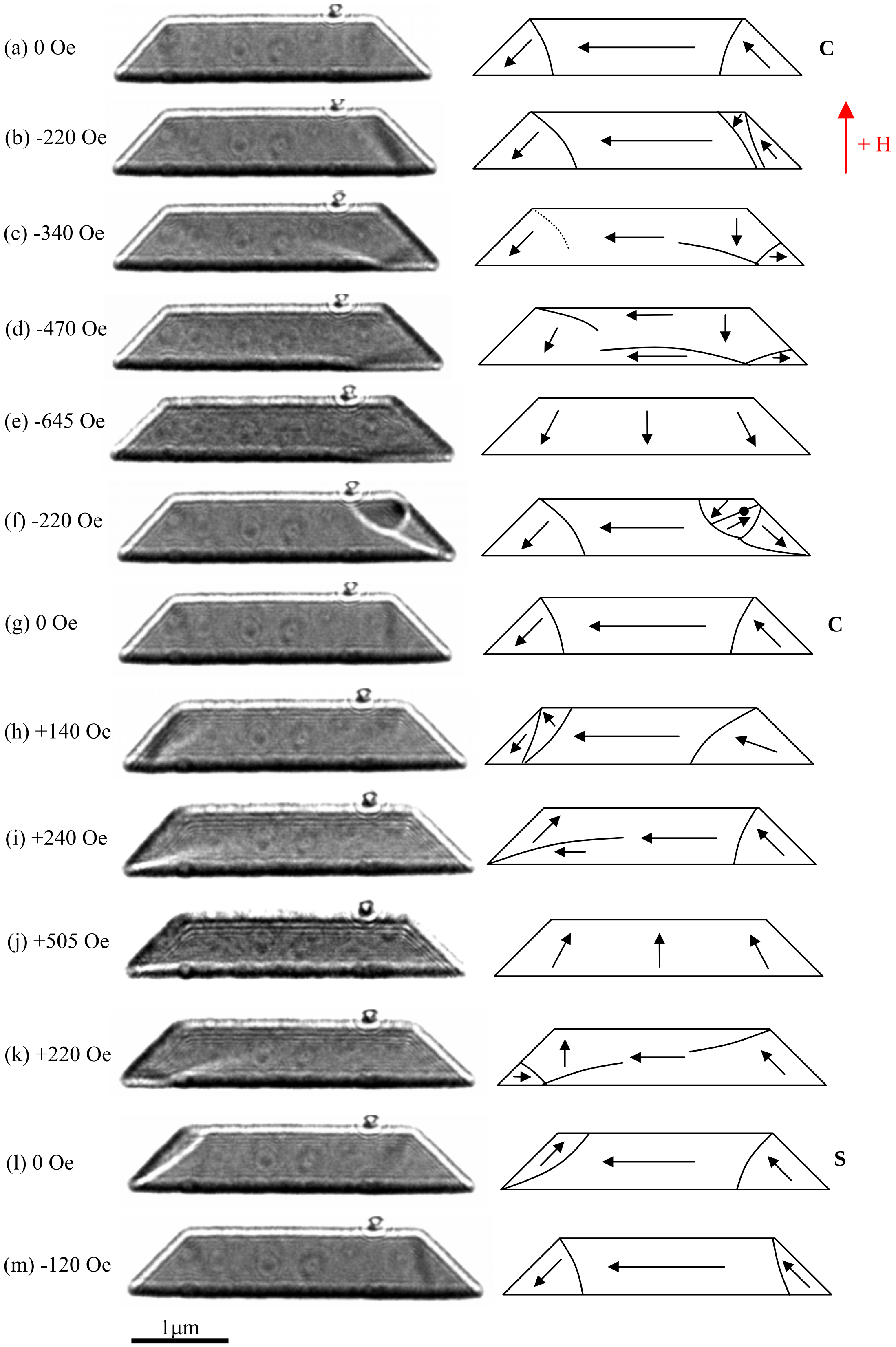

Fig. 5.23: (a)-(m) Short-axis reversal from an initial transverse C state.

5.4.3 Parallelogram

The behaviour of the parallelogram was very similar to the trapezoid. As a result of the slanted end sections, vortex formation was supressed and transverse end regions were observed. In accordance with the simulations, the system was forced to support an S state at remanence (Fig. 5.24a). Application of field anti-parallel to the net magnetisation direction then caused the domain wall contrast to increase around the corner regions (Fig. 5.24b) before reversal took place at 100 Oe (Fig. 5.24c). After removing the field, a transverse S state was observed (Fig. 5.24d). The return path of the hysteresis loop was identical, albeit with the magnetisation vectors oriented in the opposite direction (Fig. 5.24e-g). As with the trapezium, a slightly larger field was required to switch the element relative to the rectangular geometry, due to the absence of perpendicular magnetisation at the ends.

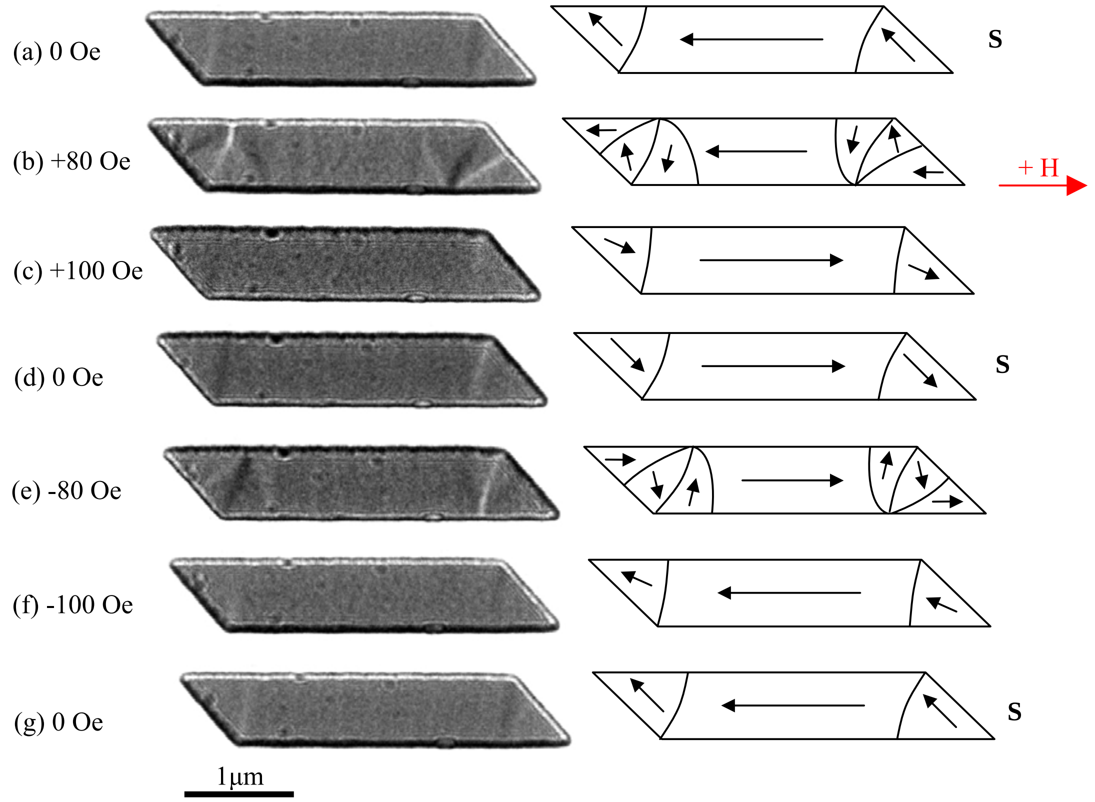

Fig. 5.24: (a)-(g) Reversal of the parallelogram between equivalent S state configurations.

From a transverse S state, a field was then applied in the negative y-direction (Fig. 5.25).

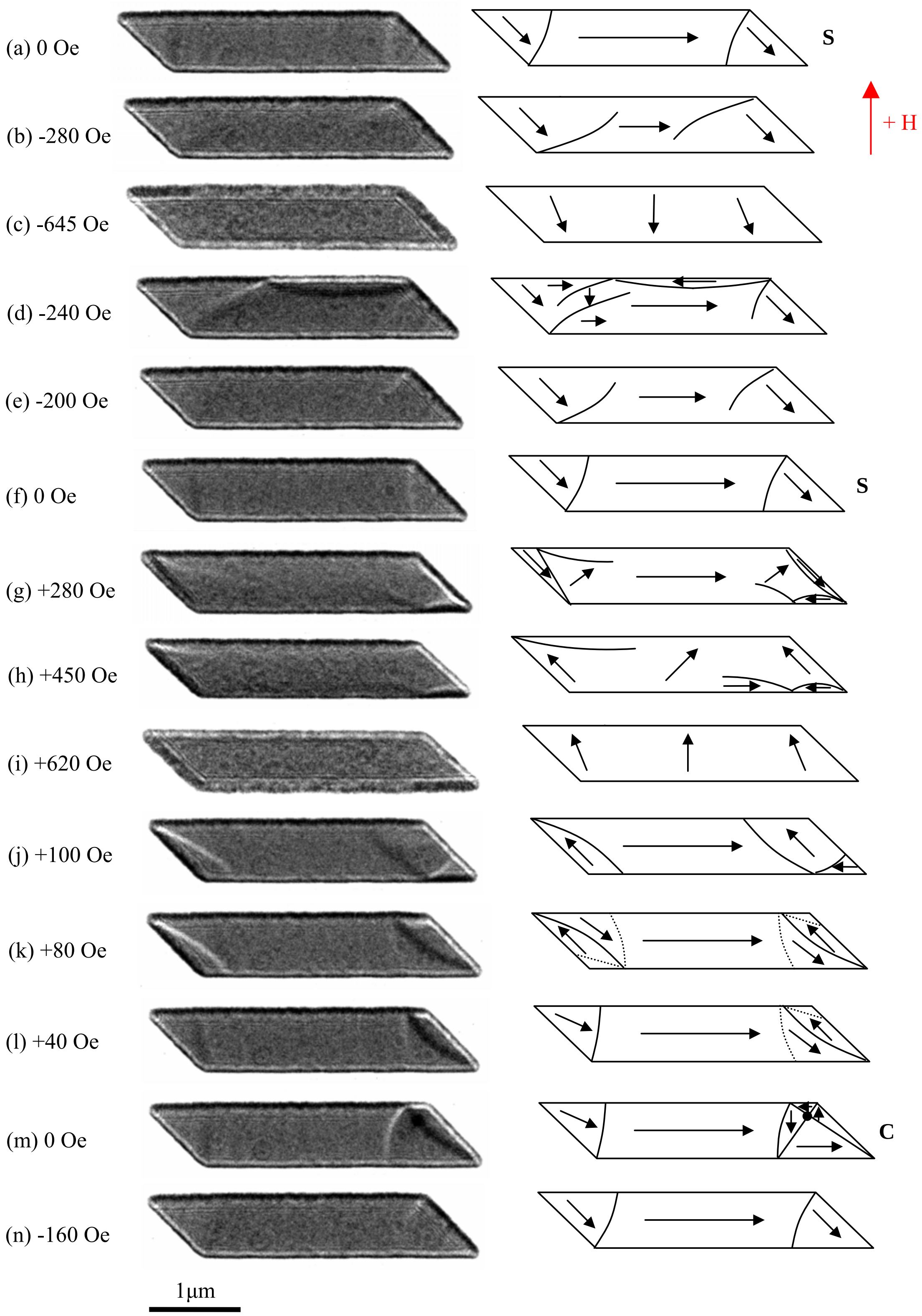

Fig. 5.25: (a)-(n) Short axis reversal from an initial transverse S state.

As the end sections were already oriented in the field direction, these domains expanded with increasing field strength (Fig. 5.25b). This was continued until saturation was reached. Following saturation, edge domains were formed as the field was reduced (Fig. 5.25d), but these were later annihilated leaving the element in the original S state (Fig.

5.25f). When the field was applied in the positive y-direction, new end domains were nucleated as the magnetisation aligned with the field (Fig. 5.25g). The field strength was then increased to uniformly align the magnetisation (Fig. 5.25h-i), but saturation was not achieved. As a consequence, the element did not switch as the simulation (Fig. 5.15) predicted. Instead, when the magnetisation relaxed (Fig. 5.25j-m), a vortex was introduced at one end, whilst the unfavourably aligned domain at the other end switched. A small field was then required in the negative y-direction to remove the vortex and take the element back to its original configuration (Fig. 5.25n).

5.5 Discussion

The experiments have revealed a number of points about the magnetic behaviour of these element geometries. As expected, there was some disagreement between the experimental and simulated results. One main difference was the formation of magnetisation vortices in the fabricated elements. Instead of vortex states, OOMMF predicted transverse configurations. This was also found in the study of domain wall trap structures (chapter 7), where head-to-head transverse walls were formed in the simulations, yet head-to-head vortex walls were observed in experiment for elements of the same dimensions. It must be noted, however, that in these calculations, the damping coefficient, α, was set to 0.5. In a recent collaboration with Prof. Thomas Schrefl on domain wall trap elements, on the other hand, finite element simulations performed using a damping coefficient of 0.1 readily predicted vortex formation. This suggests that reduced damping allows the magnetisation to further explore the energy surface without converging to the nearest state. Perhaps if α had been reduced in the finite difference simulations, vortex C and S states would have been calculated for the geometries studied in this chapter also. Unfortunately this could not be tested due to time constraints. Nevertheless, the simulated reversal from an initial transverse state did agree closely with experiment, albeit at largely different field values. A table summarising the switching field data is given below.

Geometry	Element width (nm)	Experiment/simulation	Switching field (Oe)
Rectangle	200	Simulation	423
Rectangle	200	Experiment	175
Rectangle	400	Experiment	102
Rectangle	600	Experiment	71
Trapezium	200	Simulation	524
Trapezium	200	Experiment	265
Trapezium	400	Experiment	156
Trapezium	600	Experiment	108
Parallelogram	200	Simulation	524
Parallelogram	200	Experiment	270
Parallelogram	400	Experiment	150
Parallelogram	600	Experiment	106

Table 5.1: Experimental and simulated switching field measurements for each geometry. The fabricated elements were switched 10 times each to provide an average result.

As expected, the switching field was larger for the trapezoid and parallelogram in comparison to the rectangle. From experiment, the field increased by 51% (54%), 53% (47%) and 52% (49%) for the 200nm, 400nm and 600nm wide trapezium (parallelogram) respectively, whilst the simulations on 200nm wide elements showed a 24% rise.

These magnetising experiments also proved that flux closure formation is possible in rectangular cells during long-axis field reversal. This transition was shown in Fig. 5.20 where the element switched from a vortex C state. Fields applied along the short axis also caused flux closure formation (Fig. 5.21). This has been observed before during studies of elliptical elements, where a hard-axis field took the magnetisation from a single domain state to the vortex configuration [112,113].

Whilst the trapezium and parallelogram underwent long-axis single mode switching between their ground configurations, different states were found to exist at remanence when fields were applied along the short axis. For example, in Fig. 5.23, the trapezoid was seen to support a transverse S state whilst a transverse-vortex C state was supported by the parallelogram under the same field conditions. These configurations proved relatively unstable and could be removed by a small field in the opposite direction. In the simulations, the only calculated remanent state other than the ground configuration was a diamond state in the rectangle and trapezium. As anticipated, this was not observed in the fabricated elements.

Under long-axis field application, therefore, it is safe to say that trapezium and parallelogram-shaped elements, of the dimensions considered here, can be reproducibly switched between their single ground state configurations with a slightly larger magnitude of field than that required to reverse the rectangular element.

5.6 Variation of inclination angle

After characterising the magnetic behaviour of the 45° trapezium and parallelogram, new elements were designed with different angles of inclination. These were then tested with simulations to determine their reversal behaviour and switching field, before the fabrication and imaging was performed. Here, fields were applied along the main axis only. The angle of inclination varied from 30° to 80° in 10° increments at constant element width. As before, 200, 400 and 600nm wide elements were studied, with Fresnel images of the largest structures being used to summarise the data.

5.6.1 Micromagnetic simulations

In the OOMMF simulations, each element was allowed to relax from a random configuration before being taken through a long-axis hysteresis loop. The field was varied in 50 Oe steps to observe the main transitions. Following this, a second simulation was performed in 1 Oe field steps around the switching point to accurately determine the critical field.

From these simulations, the magnetisation of each element was found to switch from one transverse ground state to the other via the same mechanism as Figs. 5.11 and 5.14. For this reason, only the 30° and 80° trapezium/parallelogram simulations are shown (Figs. 5.26-5.27).

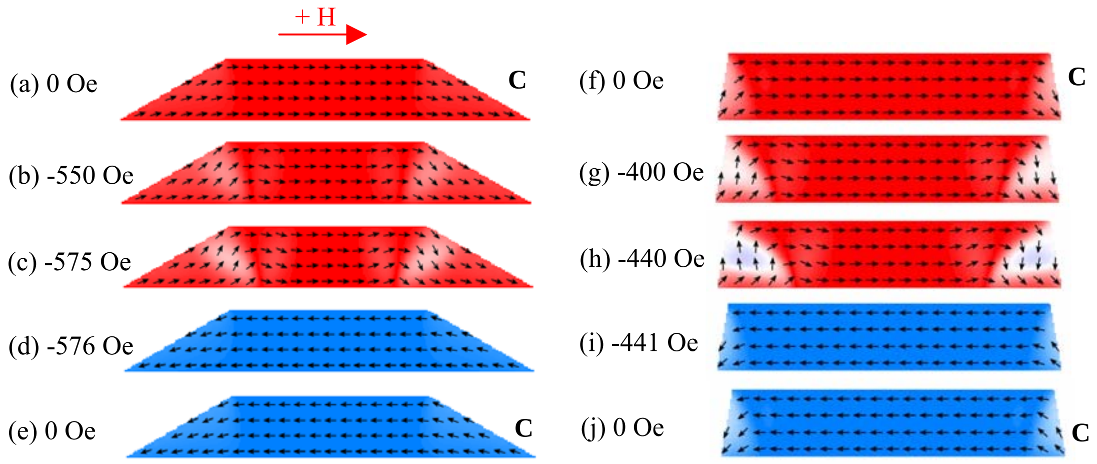

Fig. 5.26: Simulated reversal of the (a)-(e) 30° and (f)-(j) 80° trapezium.

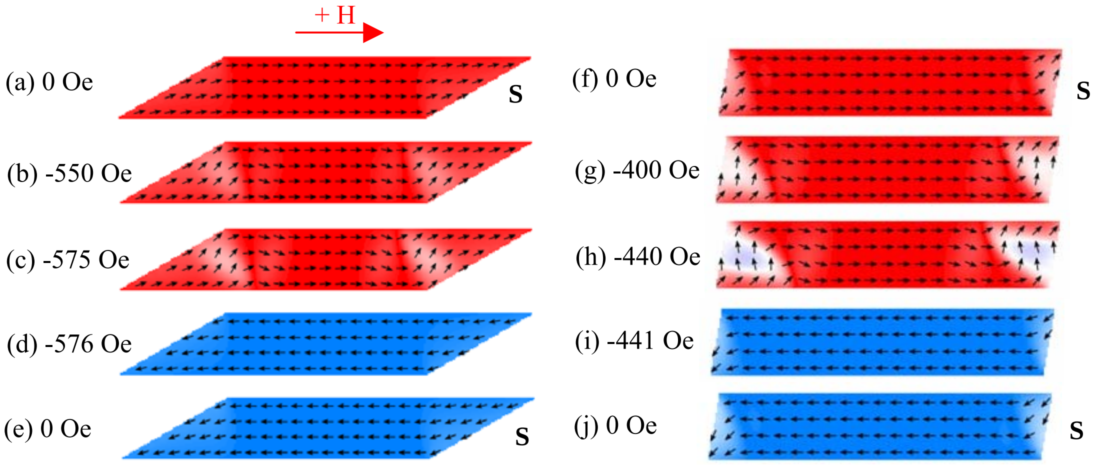

Fig. 5.27: Simulated reversal of the (a)-(e) 30° and (f)-(j) 80° parallelogram.

5.6.2 Fabricated elements

The long-axis reversal behaviour of the fabricated elements was then studied with Fresnel imaging. As a data gathering exercise, each 600nm wide element, including the rectangle and 45° trapezium and parallelogram, were saturated along their main axes before being allowed to relax in zero field. Following this, the elements were switched 10 times each (without saturating) to determine the remanent state after each reversal. This data is presented as bar graphs in Figs. 5.28 and 5.29. The behaviour of the 200 and 400nm wide structures was not analysed in as much detail, but was effectively the same as that of the 600nm elements.

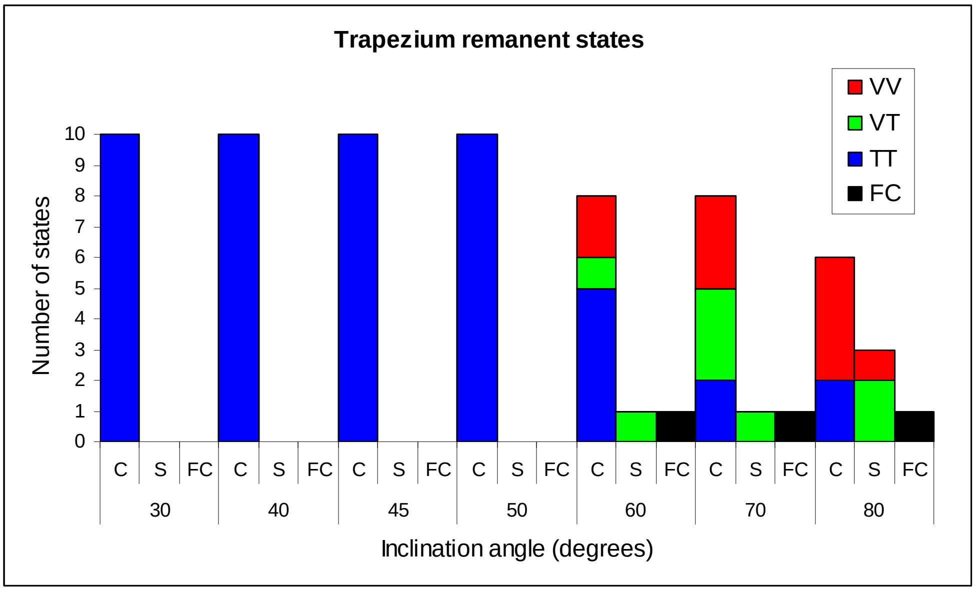

Fig. 5.28: Remanent state supported by each geometry of trapezium after switching.

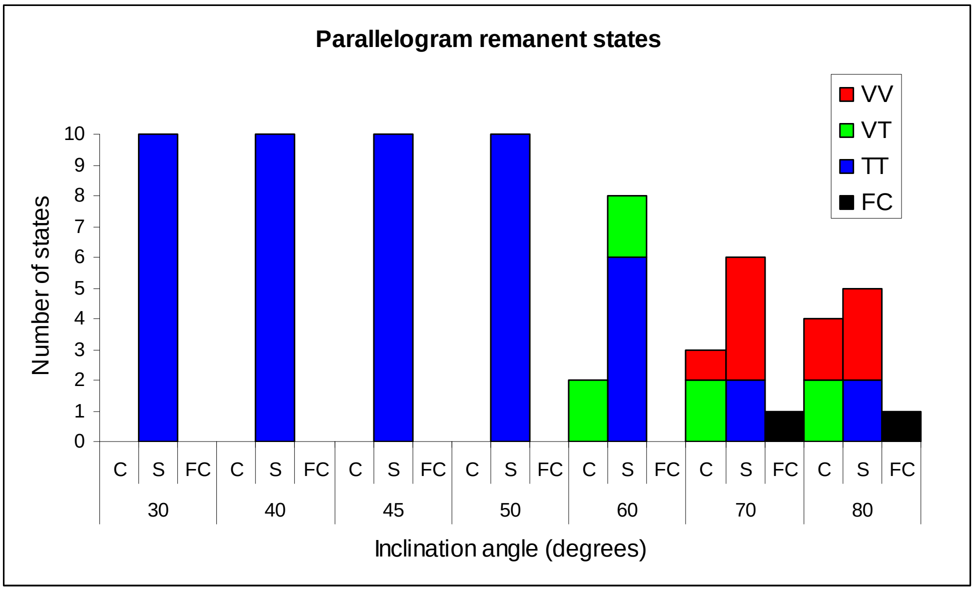

Fig. 5.29: Remanent state supported by each geometry of parallelogram after switching.

Within these graphs, the remanent states are represented by 2 letters to denote the type of end domain (vortex or transverse) and overall configuration (flux-closure). For example, when a vortex formed at either end of the element, the abbreviation VV has been used. Likewise, for two transverse end domains or a vortex-transverse mix the notation is TT and VT respectively. In circumstances where a flux-closure state was formed, the letters FC are given. After flux-closure formation, the field was increased to change the configuration to a C state before switching again.

From these data it can be seen, that in general, C states were favoured in the trapezium and S states were favoured in the parallelogram, for all angles of inclination. However, it was occasionally possible at angles above 50°, to form VVS or VTS states in the trapezium and VVC or VTC states in the parallelogram. The probability of this increased with angle. At 50° and below, the elements were only able to support their transverse, ground state configurations. This is because, at smaller angles the shape anisotropy is sufficiently strong that the magnetisation is less able to explore the energy surface and form other states. Also shown in the graphs is the formation of flux-closure states, which were possible in all of the 60° - 80° elements. As with the vortex C and S states, the probability of flux-closure formation increased with inclination angle.

Each element was then saturated along the main axis and allowed to relax to a transverse state. From here, a field in the opposite direction was applied to reverse the magnetisation. This process was repeated 10 times and the average switching field plotted in Fig. 5.30. These data show that as the inclination angle increased, the switching field decreased; a direct result of the spin orientation at the ends of the element. Also, in agreement with previous studies, the switching field was inversely proportional to element width. This stems from the shape anisotropy. In narrower geometries, the magnetisation is firmly held in place by the element edges and a large opposing field is required to force the spins to rotate. On the other hand, with wider elements, the magnetisation is able to follow the field direction and reverse domains are nucleated at a lower field. The simulation data on the 200nm wide elements have been included for comparison, and although the magnitude of field is very different, the trend is similar. Vortex states (with lower associated switching fields) also exist in the elements with wider end sections as shown in the image sequences. However, as they could not be supported by every geometry, they have been excluded from this analysis.

It can therefore be concluded, that although element geometries of lower symmetry may be an attractive alternative to rectangular cells in the sense that they exhibit more reproducible reversal behaviour, there is a price to be paid in switching field. This was also the case with tapered and elliptical elements, and is often undesirable in functional devices where it results in a larger power consumption.

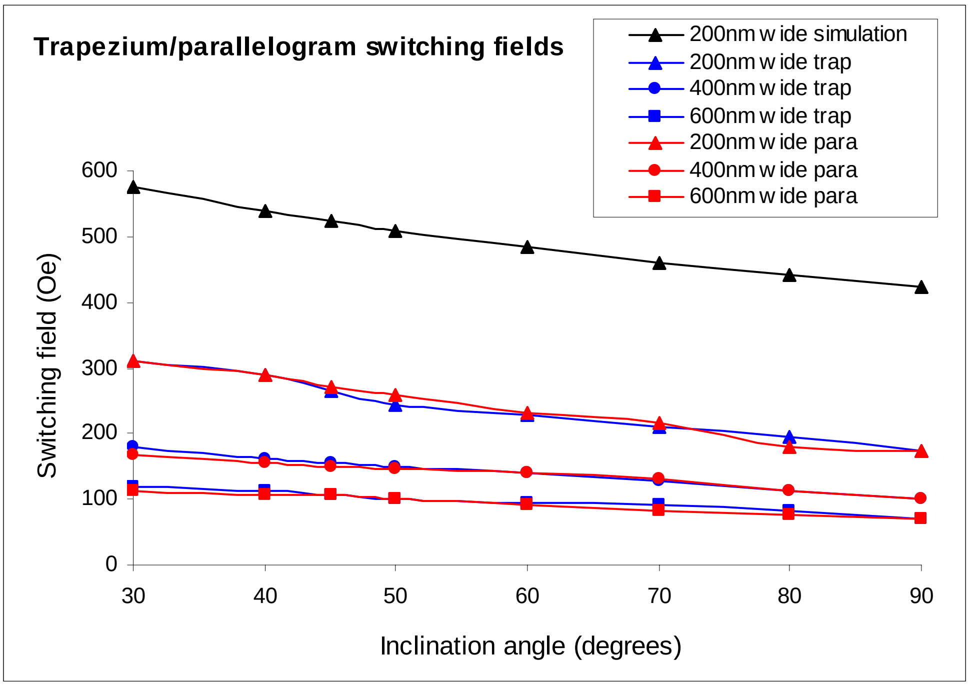

Fig. 5.30: Variation in switching field with increasing inclination angle.

Chapter 6

Using notches to pin domain walls

6.1 Introduction

The magnetic properties of rectangular ‘bar’ elements have been discussed in the previous chapter, with emphasis on the selectivity problem. Also presented were results from experiments and simulations on geometries with lower symmetry, where it was shown that the number of remenent states and modes of switching can be reduced, provided the end sections are sufficiently narrow. The increase in switching field associated with these elements, however, is an unattractive property. In this chapter, a different idea devised to control the magnetic switching is considered.

In recent years, there has been considerable interest in the modification of the magnetic properties of thin film structures by restricting their in-plane dimensions. Domain walls formed in these structures play a critical role in their behaviour. For example, in spin-dependent electronic devices, the walls contribute to the magnetoresistance [136-141]. In the case of highly constrained walls, extremely large magnetoresistance ratios have been reported [136,137]. Aside from applications, however, the domain walls are a topic of great interest in their own right. Theory predicts that wall widths in constrictions are smaller than those in continuous film, the wall structure being strongly influenced by the local geometry [142,143]. Such effects set in when the key dimensions in the fabricated structure become smaller than the wall width in continuous film. More important for this work though, is the pinning of domain walls [144]. Numerous studies have shown domain wall movement to be inhibited by notches [145-149], constrictions [150-157], traps [158-162] and defects [163-169]. These pinning sites act as a source of magnetic hardening but can also stabilise a particular spin configuration. Indeed, it is the latter effect that is being explored here. Previous studies involving notched micron-sized rings [144] have shown that notches create attractive potential wells for domain walls (Fig. 6.1a). These act as artificial pinning sites which can be used to force the element into a particular magnetic state. The idea is to include similar notches in the rectangular element and make either the C or the S state the ground configuration. In practise, the notches could take on a variety of different shapes (triangular, square, circular etc.), but this work focuses only on symmetric, triangular notches.

In the previous chapter, domain walls in the C and S states were found to exist at the ends of the rectangle. In the transverse state, they were connected between one corner of the element and a point on the opposite side. From the simulations, this point was at approximately 90nm from the short edges of the $1000 \times 200 \times 20\text{nm}^3$ rectangle. To try and pin the walls in place, in-plane notches of size $120 \times 70 \times 20\text{nm}^3$ have been included at either end. By placing the notches on opposite sides, the transverse S state should be favoured (Fig. 6.1b). With the notches on the same side, the C state should have the lower energy (Fig. 6.1c). These elements are labelled 'Notch1' and 'Notch2' for simplicity in the text. One concern about this method, nevertheless, is the reversal process. It was observed previously that the domain walls change position to avoid charging when the magnetisation switches. Therefore, the reversal mechanism will have to be closely observed with this in mind.

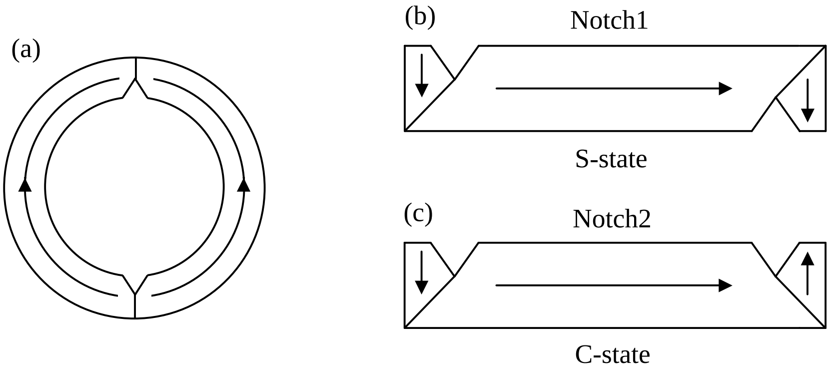

Fig. 6.1: (a) Notches have been used in magnetic ring structures to pin domain walls. The simplified (b) S and (c) C states induced by the addition of notches in the rectangular element.

6.2 Micromagnetic simulations

As with the basic rectangle, the spins of each element were randomised and allowed to relax to the nearest metastable energy state. Afterwards, 1000 Oe long-axis fields were applied to determine the remanent state, switching field and reversal mechanism. The hysteresis loops were simulated in 50 Oe field steps before the switching field was calculated to the nearest Oersted in a second, more detailed simulation.

6.2.1 Notch1

Despite the large number of metastable configurations supported by the rectangular element at zero field, there were very few states (other than the transverse S state) calculated by OOMMF [90] when the notches were introduced. Those formed are shown as magnetisation vector maps in Fig. 6.2.

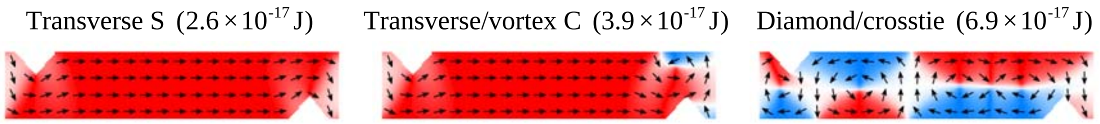

Transverse S $(2.6\times10^{-17}\,\mathrm{J})$ Transverse/vortex C $(3.9\times10^{-17}\,\mathrm{J})$ Diamond/crosstie $(6.9\times10^{-17}\,\mathrm{J})$

Fig. 6.2: Energy states formed in the OOMMF simulations by relaxing the Notch1 element from different starting conditions.

When the field was applied, any magnetisation vortices were driven from the element before removal of this field allowed the system to relax to a transverse S state. The fact that an S state was favoured over a C state indicates that the notches were inhibiting the degeneracy. The subsequent reversal sequence is shown in Fig. 6.3. On reversing the magnetisation with a field of 487 Oe, all three domains switched, taking the element to an equivalent S state in the opposite direction. The end domains were forced to switch as a result of the notch edges, rather like the short edges of the trapezium and parallelogram. New domain walls were then nucleated at the same position as the magnetisation rotated around the notch region. Instead of complicating the reversal, the notches actually simplified the process. The calculated switching field was larger for this element than it was for the basic rectangular cell (423 Oe), although still smaller than that of the trapezium and parallelogram (both 524 Oe). Such behaviour is in agreement with other studies which found notches to increase the magnetic hardness of an element [149]. This time the coercivity is not so much the result of a difference in torque, but is more to do with the domain wall energy and the local shape anisotropy. With the wall connected to the apex of the notch, its length and energy are minimised. Consequently, the wall remains in this position to maintain a favourable configuration. In addition, around the notch regions the magnetisation lies parallel to the edges to minimise the magnetostatic energy. However, when a field is applied to reverse the magnetisation, these spins rotate against their natural orientation and the dipole energy increases. Therefore, the edges of the notches act to prevent this rotation, causing the switching field to increase. The short-axis hysteresis loop was then simulated and is shown in Fig. 6.4.

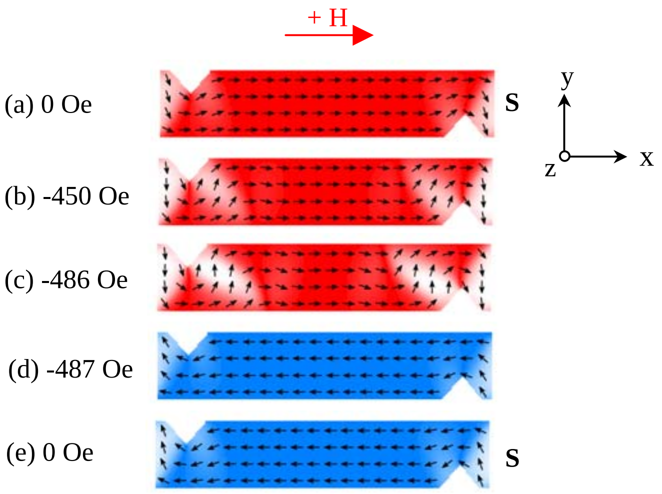

Fig. 6.3: (a)-(e) Simulated reversal of the Notch1 element using a long-axis field. The direction of positive field is shown.

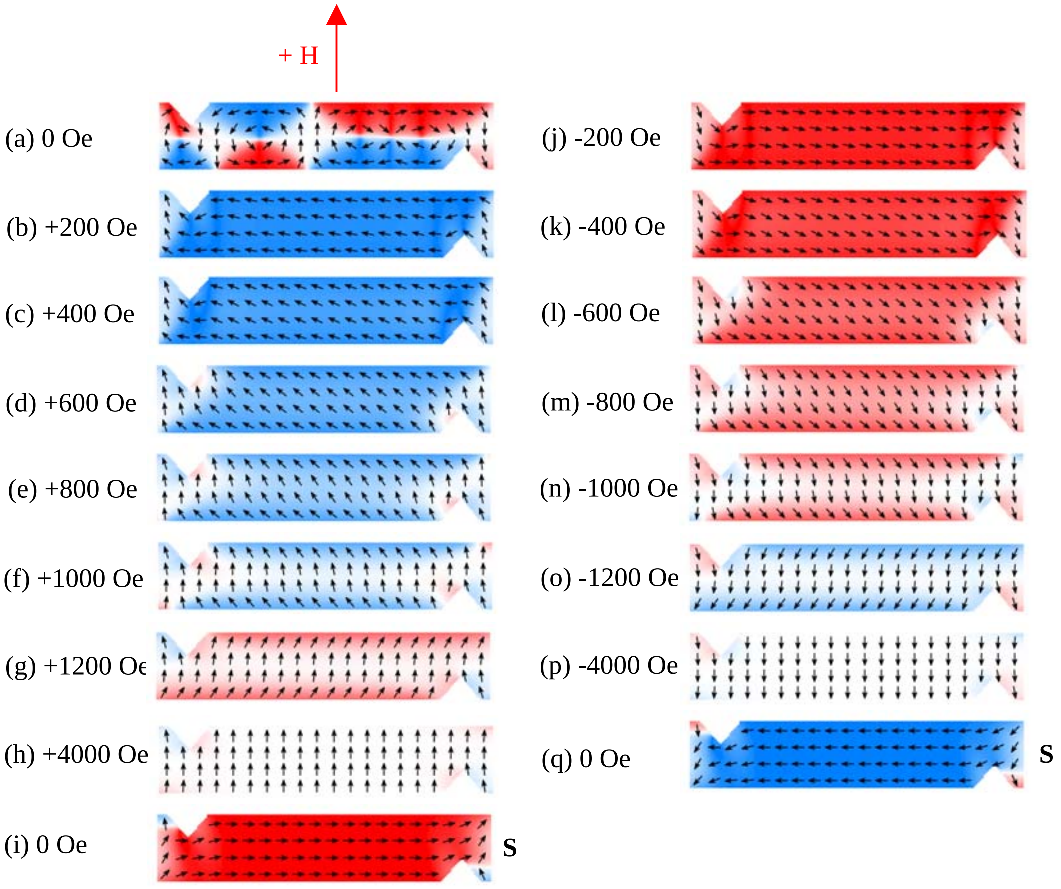

Fig. 6.4: (a)-(q) Simulated reversal of the Notch1 element using a short-axis field.

During the 90° hysteresis loop, the central section of the structure behaved in much the same way as the parallelogram, whilst the end sections, defined by the notches, were able to support flower-like corner domains (Fig. 6.4i). These domains are formed when the magnetisation follows the edges of the notch and is oriented in a different direction from the bulk of the spins. The magnetostatic energy of this metastable configuration was found to be 66% larger than that of the ground state. Application of a small negative field was enough to reverse the end regions (Fig. 6.4j).

6.2.2 Notch2

The same simulations were then performed using the Notch2 element. By relaxing the element several times from a random demagnetised state, the magnetisation was found to collapse into a transverse C and on one occasion, a transverse/vortex S state. These configurations are shown in Fig. 6.5.

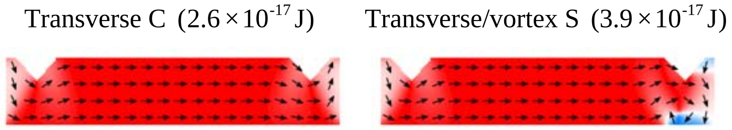

Transverse C (2.6×10^{-17} J) Transverse/vortex S (3.9×10^{-17} J)

Fig. 6.5: Energy states formed in the OOMMF simulations by relaxing the Notch2 element from different starting conditions.

On applying a long-axis field (Fig. 6.6), the magnetisation switched between equivalent C states. Again, this occurred at 487 Oe, the same magnitude of field required to switch the Notch1 geometry. With the application of a hard-axis field, a head-to-head domain wall was formed due to the inner edges of the notches (Fig. 6.7i). This configuration was also formed in the trapezoid where the short edges of the structure forced the magnetisation inward from either end.

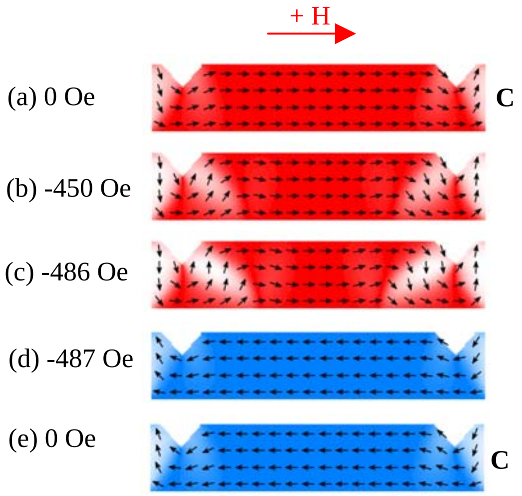

Fig. 6.6: (a)-(e) Simulated reversal of the Notch2 element using a long-axis field.

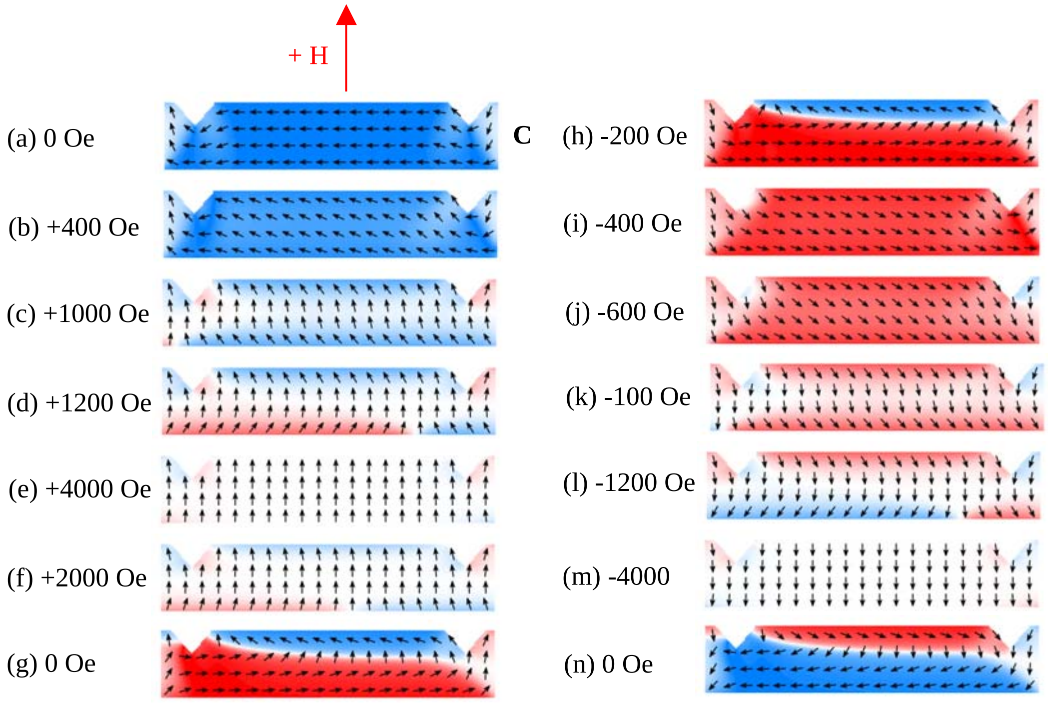

Fig. 6.7 (a)-(n) Simulated reversal of the Notch2 element using a short-axis field.

6.3 Fabricated elements

Elements of identical size and shape to those simulated were fabricated using electron beam lithography. As with the other structures, the pattern was repeated at two and three times magnification. Once again, the behaviour of each size of element at constant aspect ratio was very similar and only the largest (600nm wide) geometries are shown in the image sequences. The changes in switching field will be discussed in more detail at the end of the chapter.

The first noticeable thing about the fabricated elements was the frequent presence of vortices at the end sections. The formation of these magnetic configurations greatly complicates the problem. In the transverse state, a single wall exists at either end which can be pinned in place by the notch. However, as vortex end sections involve multiple domains/domain walls, they cannot be controlled in the same way.

6.3.1 Notch1

Starting with the Notch1 element, a large field was applied along the main axis to saturate the magnetisation. Afterwards, the field was removed, allowing the system to relax to a transverse state. In this case the notches appeared unable to force a particular configuration though, and both transverse C and S states were possible at remanence. When a reverse field was applied there was a high probability of vortex formation, although during repeated switching some vortex end domains were observed to change to transverse states. In terms of inducing a particular remanent state, the notches were unsuccessful. However, they did manage to prevent flux-closure formation during the long-axis magnetising cycle, which is a definite improvement over the rectangular element. Image sequences capturing these data are given in Figs. 6.8 and 6.9.

As the simulations predicted, the switching field of this element was slightly larger than that of the basic rectangular cell (71 Oe) but smaller than the field required to reverse the 45° trapezium (108 Oe) and parallelogram (106 Oe). To switch the magnetisation from a transverse S and C state, fields of around 90 and 85 Oe were required respectively, whilst a field of 35 Oe was able to reverse the element from an initial vortex configuration. With a vortex state at one end and a transverse domain at the other, an average field of 55 Oe was required.

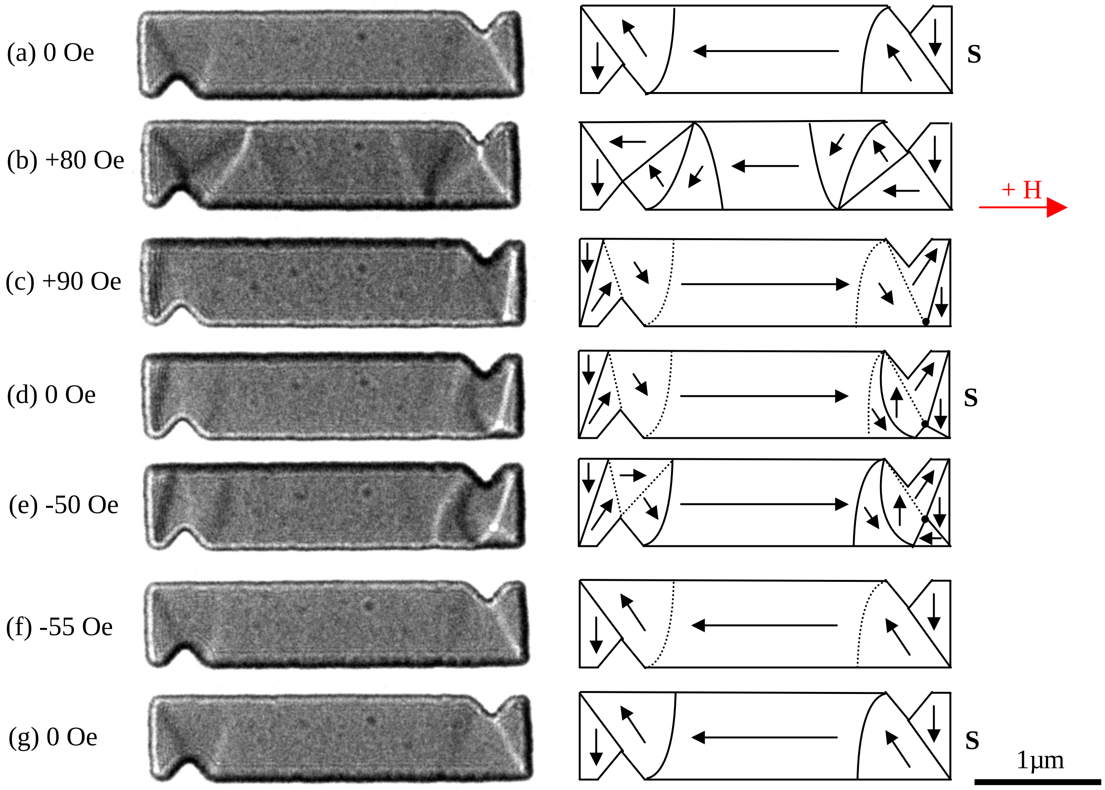

Fig. 6.8: (a)-(g) Reversal of Notch1 from an initial transverse S state.

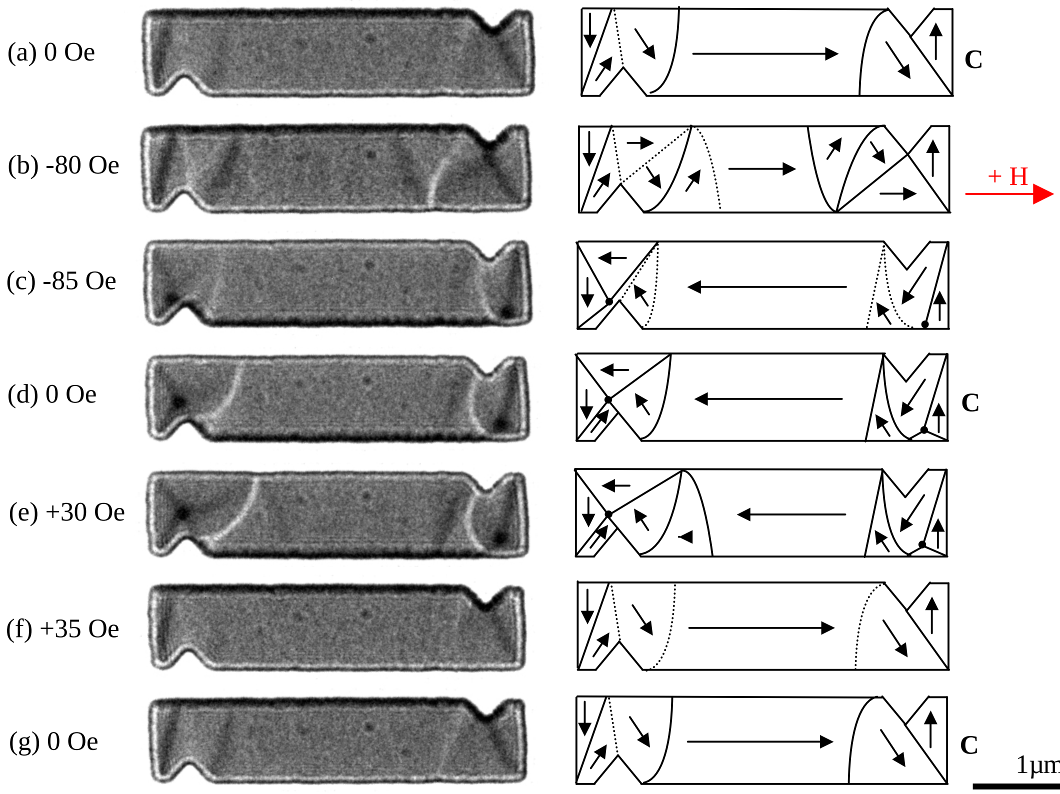

Fig. 6.9: (a)-(g) Reversal of Notch1 from an initial transverse C state.

As the simulations predicted, the switching field of this element was slightly larger than that of the basic rectangular cell (71 Oe) but smaller than the field required to reverse the 45° trapezium (108 Oe) and parallelogram (106 Oe). To switch the magnetisation from a transverse S and C state, fields of around 90 and 85 Oe were required respectively, whilst a field of 35 Oe was able to reverse the element from an initial vortex configuration. With a vortex state at one end and a transverse domain at the other, an average field of 55 Oe was required.

The short-axis field sequence is shown in Fig. 6.10. From a transverse S state (Fig. 6.10a), an applied field of 120 Oe caused the nucleation of a double vortex structure at one end (Fig. 6.10b). This was later annihilated at 180 Oe, resulting in the formation of a corner domain (Fig. 6.10c). These were formed at both ends of the element. As the field was increased, the magnetisation gradually aligned itself parallel to the short axis (Fig. 6.10d) before removal of this field saw the element relax to a quasi-S state with a flower domain in one corner (Fig. 6.10e). This was then removed by a 40 Oe field in the opposite direction (Fig. 6.10f). After increasing the field strength (Figs. 6.10g-k) and relaxing the magnetisation, a flux-closure state was formed (Fig. 6.10l). In agreement with the results in chapter 5, cross-ties were present within this domain structure. As the field approached zero, the number of vortices and cross-ties increased (Figs. 6.10m,n), demonstrating the additional freedom of the magnetisation.

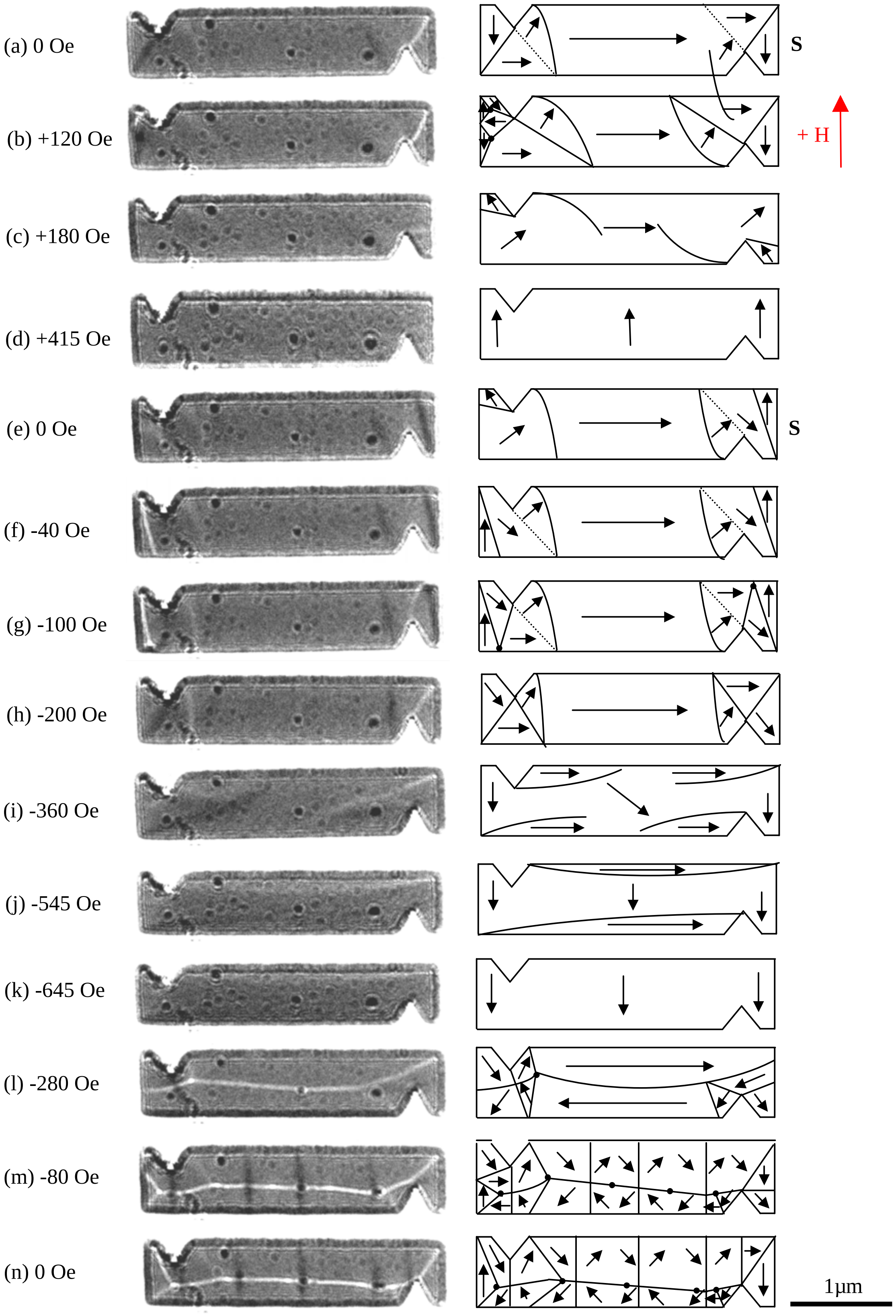

Fig. 6.10: (a)-(n) Reversal of the Notch1 element using a short-axis field.

6.3.2 Notch2

The Notch2 element was studied next and demonstrated analogous behaviour to Notch1. Long-axis reversal sequences from initial C and S states are shown in Figs. 6.11 and 6.12 respectively. As can be seen, the notches were unable to rule out S state formation, but did on some occasions manage to prevent the formation of vortex end domains. For example, in Fig. 6.11e,f the magnetisation switched from a vortex C state to a transverse C state. Here, the transverse state has a lower energy because the notches reduce the length of domain wall. In the basic rectangle, the magnetisation would have reversed to form another vortex C state.

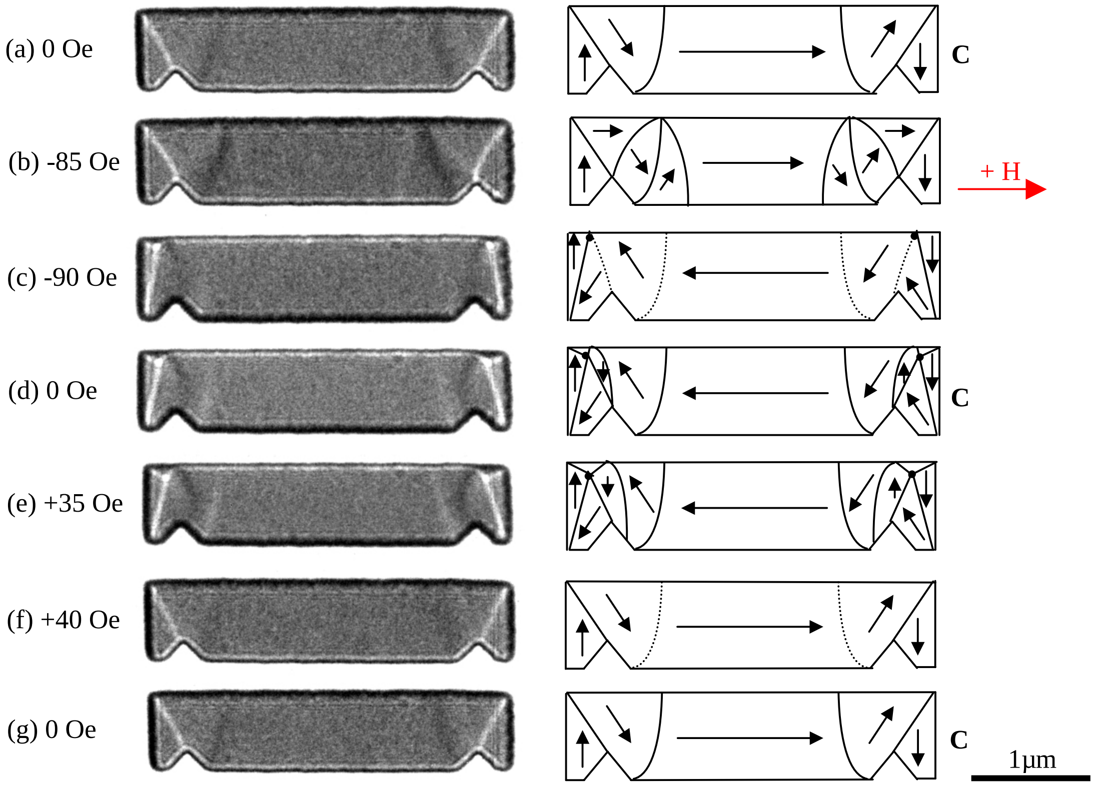

Fig. 6.11: (a)-(g) Reversal of Notch2 from an initial transverse C state.

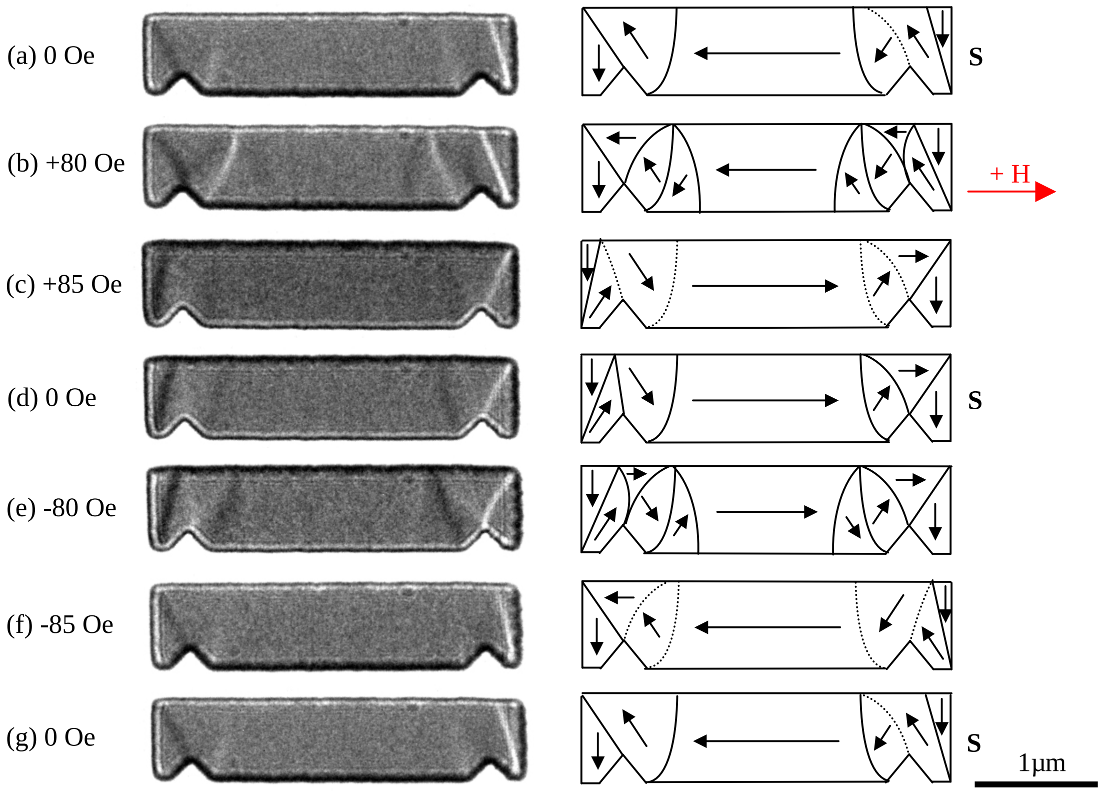

Fig. 6.12: (a)-(g) Reversal of Notch1 from an initial transverse S state.

The images recorded during the short-axis loop are shown in Fig. 6.13 and showed many similarities in behaviour to those from the Notch1 element. From an initial transverse C state (Fig. 6.13a), an increase in field caused the unfavourably aligned end domain to reverse. This occurred via the formation of two vortices (Fig. 6.13b), which were subsequently annihilated to leave a flower-like domain (Fig. 6.13c). By increasing the field further, the central region gradually aligned with the field (Fig. 6.13d-g) before the magnetisation relaxed to a flux-closure state (Fig. 6.13h). An 80 Oe field in the negative y-direction increased the number of vortices and cross-ties (Fig. 6.13i), but these were removed again at 240 Oe (Fig. 6.13j). At higher field the closure state was lost (Fig. 6.13k) and the y-component of magnetisation increased to saturation. A final reduction in field strength saw the system revert back to a flux-closure configuration which remained at zero field (Fig. 6.13p).

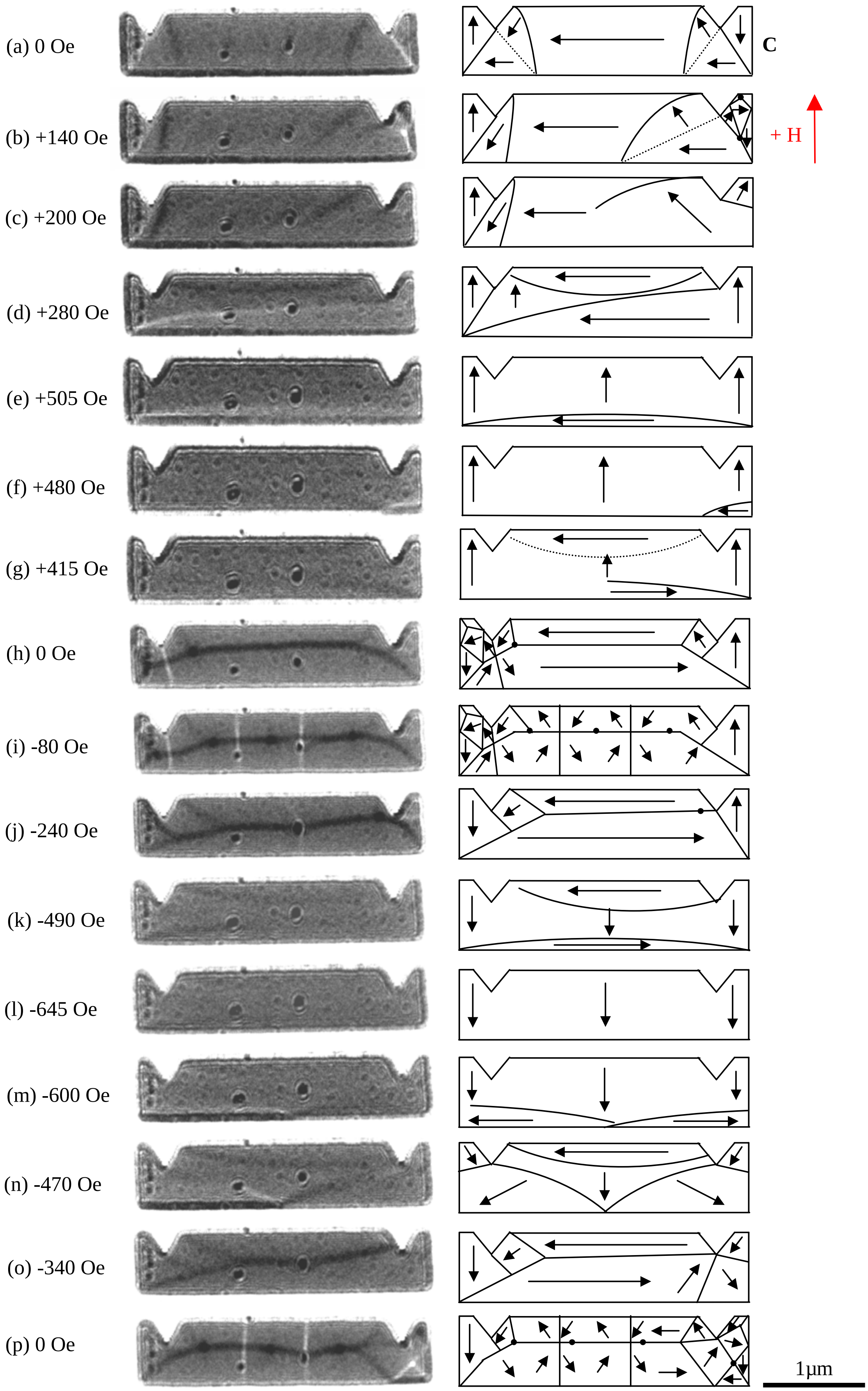

Fig. 6.13: (a)-(p) Reversal of the Notch2 element using a short-axis field.

6.4 Discussion

These in-situ magnetising experiments have shown that whilst the simulated Notch1 and Notch2 elements are able to reduce the number of remanent states and modes of switching, the fabricated structures do not display such perfect behaviour. This is largely due to vortex formation at the ends of the element. Instead of having to pin a single domain wall, the notches are faced with a three-wall configuration that cannot be easily controlled. Vortex end domains have also been observed with the element geometries in the previous chapter and are favoured in wider, thicker strips of material. These configurations were supported in all of the 200, 400 and 600nm wide elements studied. More complicated domain states were also observed during some of the field cycles as a result of vortex nucleation in the end sections. Again, these configurations were absent in the simulations. As mentioned in the last chapter, however, differences in behaviour between simulation and experiment may be caused by the chosen value of damping parameter in OOMMF.

Although the notches were unable to force the desired remanent state, they did prevent flux-closure formation during long-axis field cycles. In addition, during repeated switching, vortex states sometimes changed to transverse states as a result of the notches. In these situations, the reduced domain wall length makes the transverse state the ground configuration.

When short-axis fields were applied, simulation and experiment both showed the formation of flower-like domains in the corners of the element. As explained, these domains form because the edges of the notch prevent the magnetisation around this region from following the direction of the central domain. During hard-axis field cycles, flux-closure states were also formed as observed with the other element geometries.

Relative to the basic rectangular element, the switching field was larger for Notch1 and Notch2. This, as discussed in the chapter introduction, is due to the domain wall pinning effect and also the shape anisotropy of the notch edges. From experiment, the field increased by 63% (61%), 53% (61%) and 42% (49%) for the 200nm, 400nm and 600nm wide Notch1 (Notch2) element respectively, whilst the simulations on 200nm wide elements showed a 15% rise. Therefore, whilst the simulations predicted the notched elements would switch at a lower field than the trapezium and parallelogram, the experimental switching fields were around the same magnitude.

6.5 Variation of notch dimensions

Following characterisation of the original Notch1 and Notch2 geometries, the in-plane notch dimensions were varied to determine changes in the magnetic behaviour and switching field. In these experiments the x-dimension, denoted ‘length’, ranged from 60nm to 180nm in 30nm steps. At each of these lengths the y-dimension, denoted ‘width’, ranged from 30nm to 190nm in 40nm steps. Therefore in total, 25 sizes of notch were studied for both the Notch1 and Notch2 element shapes. At constant aspect ratio, these structures were fabricated at 1, 2 and 3 times magnification (200, 400 and 600nm wide elements) from 20nm thick permalloy. Each element was imaged in the Fresnel mode under long-axis field conditions only. Despite the extensive range in geometry, the behaviour varied only slightly. As a result, only a few image sequences are required to summarise the findings.

6.5.1 Micromagnetic simulations

Each element geometry was relaxed from a random magnetisation state before being taken through a long-axis hysteresis loop in 50 Oe field steps. Following this, a second simulation was performed around the switching point in 1 Oe field steps. From these simulations, the magnetisation of each element was observed to switch from one transverse state to another. However, there was found to be two different reversal mechanisms depending on the notch dimensions. In some geometries, the magnetisation of every domain switched at the same field value. This is the same reversal process observed with the Notch1 and Notch2 elements previously in the chapter (Figs. 6.3 and 6.6). With different elements, on the other hand, the central and end regions switched at separate magnitudes of field. This latter mechanism was exhibited by elements with notches of in-plane size $60 \times 30\text{nm}^2$ and $120 \times 190\text{nm}^2$ amongst others, and is shown in Figs. 6.14 and 6.15.

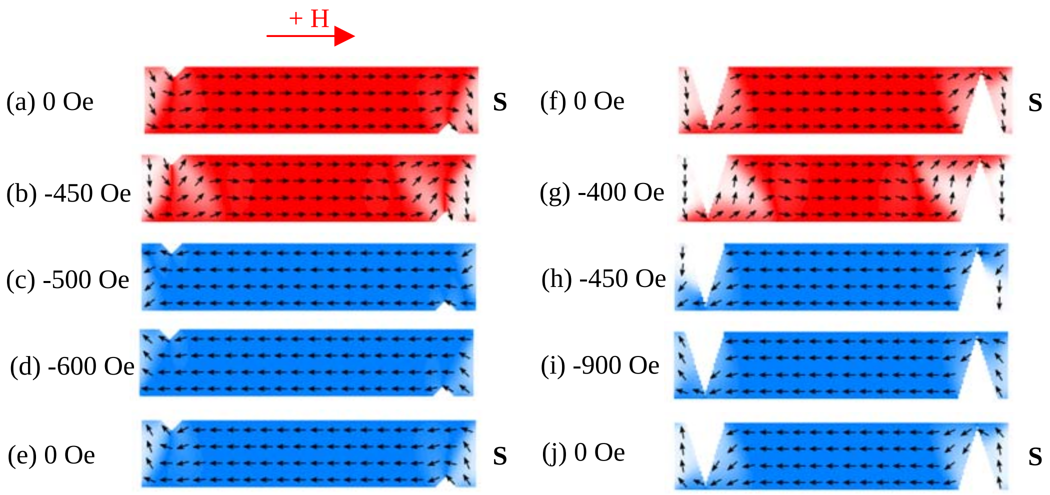

Fig. 6.14: Simulated reversal of the Notch1 element geometry with (a)-(e) $60 \times 30\text{nm}^2$ and (f)-(j) $120 \times 190\text{nm}^2$ notches.

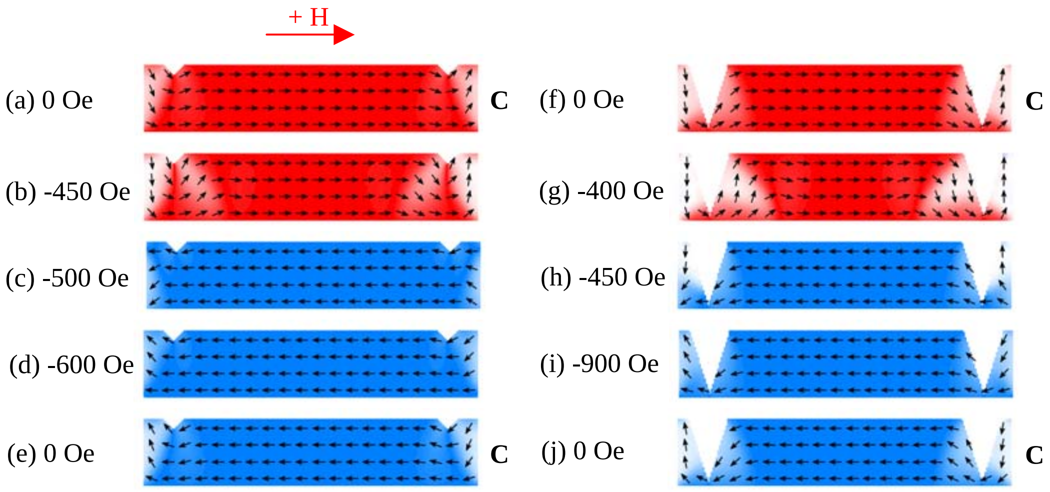

Fig. 6.15: Simulated reversal of the Notch2 element geometry with (a)-(e) $60 \times 30\text{nm}^2$ and (f)-(j) $120 \times 190\text{nm}^2$ notches.

The reversal process begins with the central section switching direction, causing the domain walls to change position (Fig. 6.14c). At higher field, the end sections then switch together, forcing the walls to move back to their original positions again (Fig. 6.14d). In the basic rectangular element, the end domains have no reason to switch during a long-axis loop because there is no short-axis field component. Instead, the domain walls shift position to minimise the surface charge. However, in the notched elements the magnetisation has to rotate around the notch region to minimise the magnetostatic energy, which affects the end configuration. The reason some sizes of notch favour a two-step reversal process over the typical single-step mechanism is not obvious, however. By analysing the results from each element, a partial phase diagram was created to summarise the data (Fig. 6.16). From this diagram it can be seen that there is a large range of length and width which allows a single-step reversal. Outside this zone in both dimensions there is a shift in behaviour. At very small sizes (in x and y) it may be that the notch is simply not large enough to pin the domain walls (Fig. 6.14a-e). On the other hand, with very large notches (especially in the y-dimension), the notch seems to separate the magnetisation of the end sections from that of the main body, effectively causing the system to behave as three separate elements (Fig. 6.14f-j).

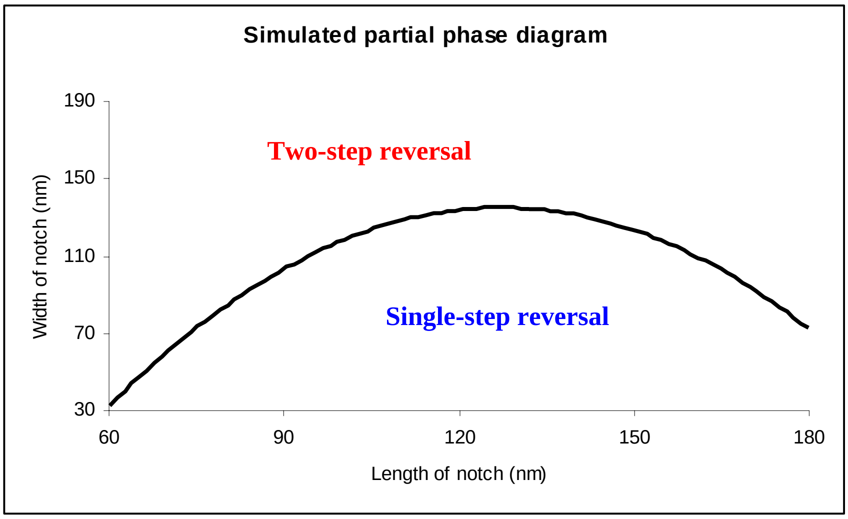

Fig. 6.16: Phase diagram produced from simulation data to show how the magnetisation reversal process differs with notch length and width.

To compare the switching fields of each element, the field was plotted against notch aspect ratio. The aspect ratio here is defined as notch length divided by notch width. These data are shown in Fig. 6.17 along with the switching fields for the 200, 400 and 600nm wide fabricated elements. The fabricated structures will be considered in the next section.

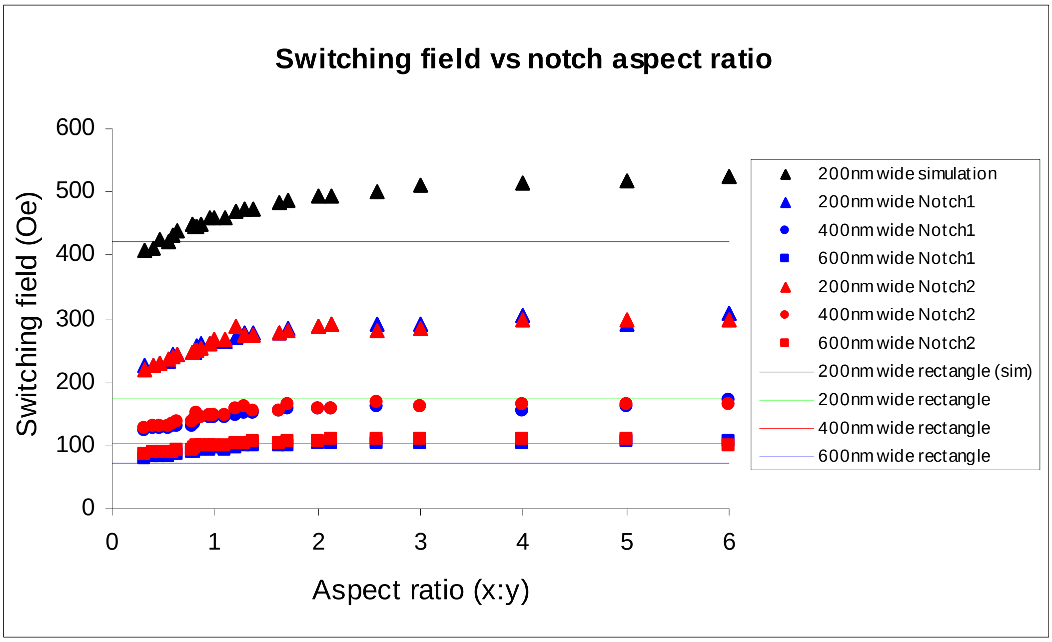

Fig. 6.17: Variation in switching field with notch aspect ratio.

The trend of simulated data points shows that the coercivity rises with increasing aspect ratio. This may relate to what was said in the last chapter about a change in torque with inclination angle for the trapezoid and parallelogram. This time, however, it is the angle of spins around the notch region with respect to the applied field direction that is important. For example, by comparing two notches of different length and equal width (Fig. 6.18a,b) we find a larger switching field for the magnetisation around the longer notch. At the notch edges the magnetisation of (a) is oriented at 75˚ to the x-axis as opposed to 56˚ for (b). Similarly, given two notches of different width (Fig. 6.18c,d), a larger field is required to reverse the element with the narrower notch. In this case the angles are 27˚ and 61˚ for (c) and (d) respectively. As well as torque, differences in domain wall length as well as variations in exchange and magnetostatic energy may also contribute to the coecivity. Although this was investigated with simulation data, there appeared to be no obvious trends and the results were inconclusive.

The switching fields for the rectangular elements are included in Fig. 6.17 for comparison. In the main, the coercivity increased by adding notches to the structure, but in some cases at low aspect ratio, the switching field was slightly smaller than for a rectangle of the same overall dimensions. This is an advantage over the trapezoids and parallelograms which were found to switch at higher fields than the rectangle for all angles of inclination.

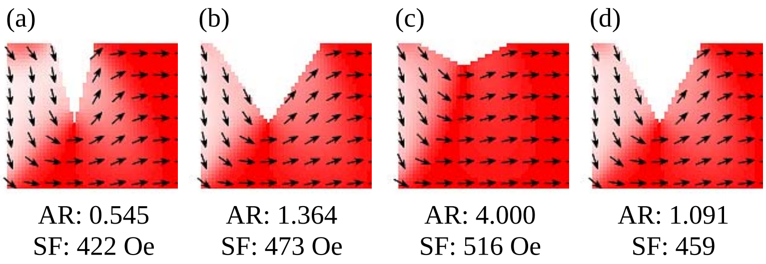

Fig. 6.18: (a)-(d) Magnetisation vector maps showing detail around the notch region for elements with different sized notches. The notch aspect ratio and switching field are given for each.

6.5.2 Fabricated elements

The fabricated elements were then studied in the Fresnel imaging mode. To collect data on the remanent states, the largest elements were saturated along their main axes and relaxed. Following this, the elements were switched ten times (without saturating) and the state at zero field was noted after each reversal. The data from this experiment is presented as bar graphs in Figs. 6.19 and 6.20. Within these graphs, letters have been used to denote the different states following the same notation as in the previous chapter. The number of states of each type are plotted against (in-plane) notch area instead of notch aspect ratio.

These data show that the configuration supported strongly depends on the absolute size of the notch. When the notch area is small, vortex end domains are favoured in both the Notch1 and Notch2 geometries. As the area increases, vortex formation becomes less probable and transverse or vortex-transverse states are formed. This arises because the volume of material decreases as the notches get larger, limiting the freedom of the spins. Instead, the shape anisotropy of the element edges aligns the magnetisation in a preferred direction. This ties in with the earlier argument about wide notches splitting the element into three separate sections. When the notches are large, the edges control the end configurations and the central section has little effect. Under these conditions, the ends are triangular in shape whilst the central section resembles either a trapezium or parallelogram (Fig. 6.21) depending on whether the notches are on the same side of the element or opposite sides respectively. As a result, the ends can be magnetised up or down and the main body of the element behaves in a similar manner to the structures considered in the last chapter.

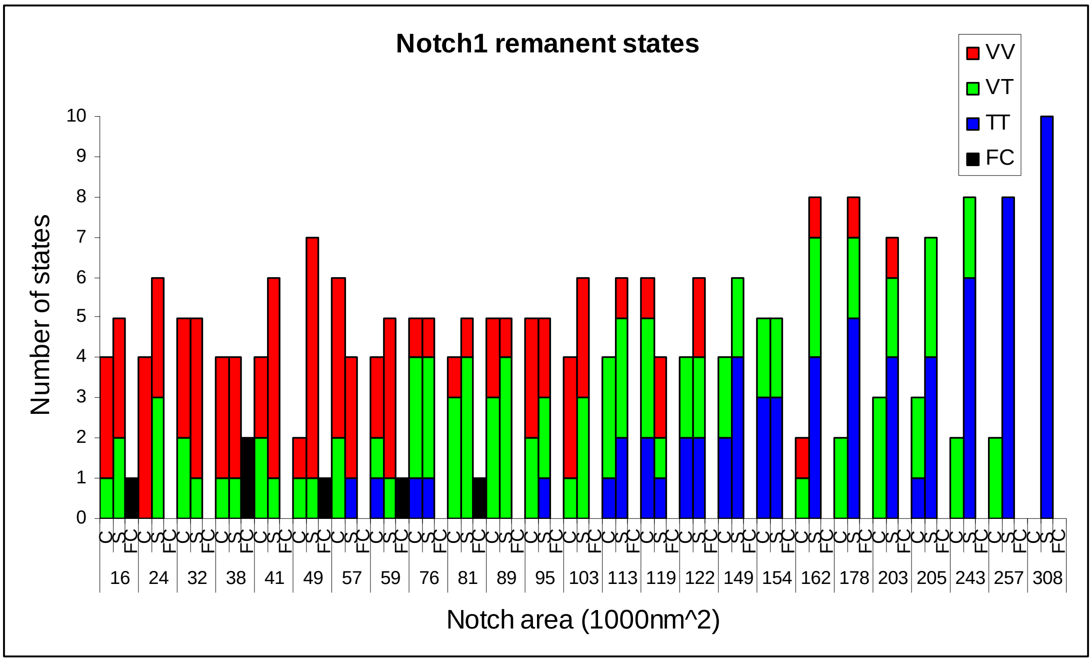

Fig. 6.19: The number of each remanent state formed after switching Notch1 elements with different sizes of notch.

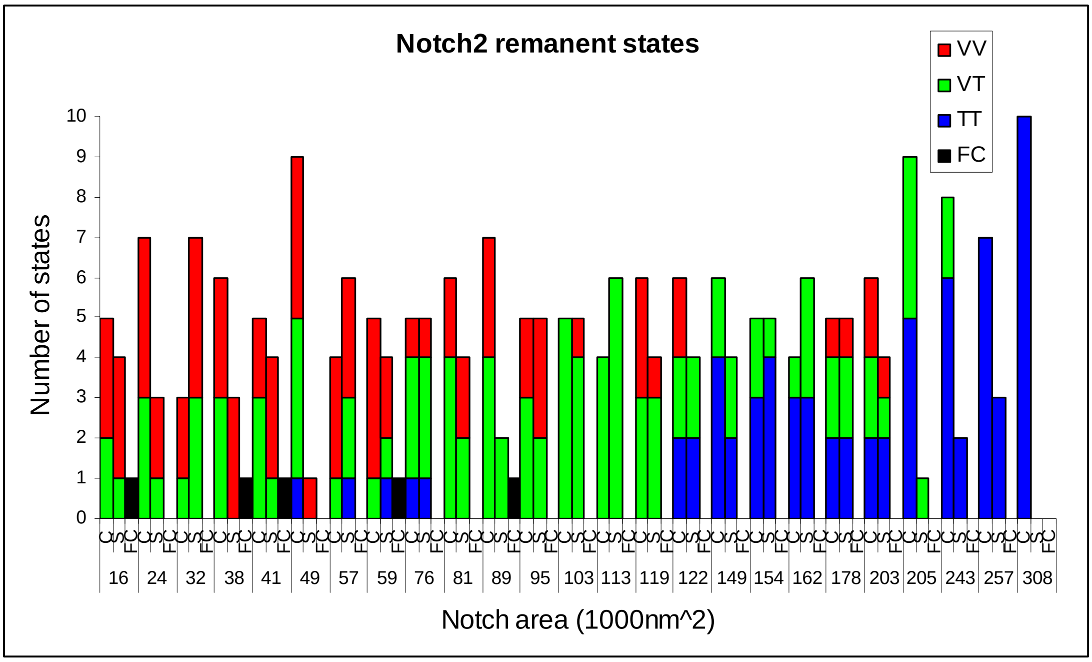

Fig. 6.20: The number of each remanent state formed after switching Notch2 elements with different sizes of notch.

Although the Notch1 element was designed to support a remanent S state and the Notch2 element a remanent C state, complete polarisation was not possible until the largest notches were used. At this size ($540 \times 570 \times 20\text{nm}^3$ for a $3000 \times 600 \times 20\text{nm}^3$ element), vortex formation was suppressed, and the transverse ground states were observed at zero field.

Below this size of notch it was possible to form both C and S states in their transverse and vortex configurations. Flux closure formation, on the other hand, occurred only with relatively small notches where vortex C states could be supported. As shown in the last chapter, vortex C states occasionally switch to closure states to minimise the magnetostatic energy of the system. Image sequences capturing the 'ideal' reversal behaviour in $3000 \times 600 \times 20\text{nm}^3$ elements with $540 \times 570 \times 20\text{nm}^3$ notches are shown in Figs. 6.22-6.23.

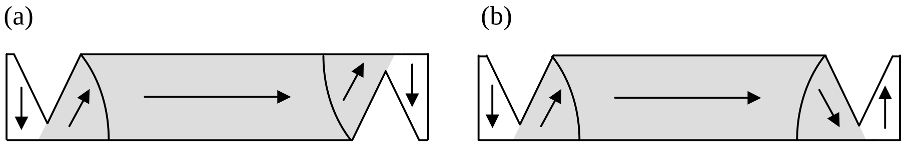

Fig. 6.21: When large notches are used, the element is split into three different sections that behave almost independently. In this situation, the main body of the structure follows the behaviour of a (a) parallelogram or (b) trapezium.

To determine the switching fields of the fabricated structures (Fig. 6.26), each element was saturated along the main axis and relaxed to form a remanent transverse state. Afterwards, a field was applied in the opposite direction to reverse the magnetisation. As in the previous chapter, this process was repeated ten times to obtain an average field value. The switching field increased gradually with notch aspect ratio. This trend is similar to the simulation results, although the magnitude of field was far lower for the fabricated elements. In agreement with the results from the last chapter, the switching field was also inversely proportional to element width. This can be attributed to an increased shape anisotropy when the element edges are closer together. For comparison, the data from the simulated and experimental rectangular cells have been included in the graph. In all experimental cases, the notched elements reversed with a larger field than the rectangle. This agrees with the micromagnetic simulations to a large extent, except for the elements with low aspect ratio notches, which were predicted to switch at a slightly lower field than the rectangle.

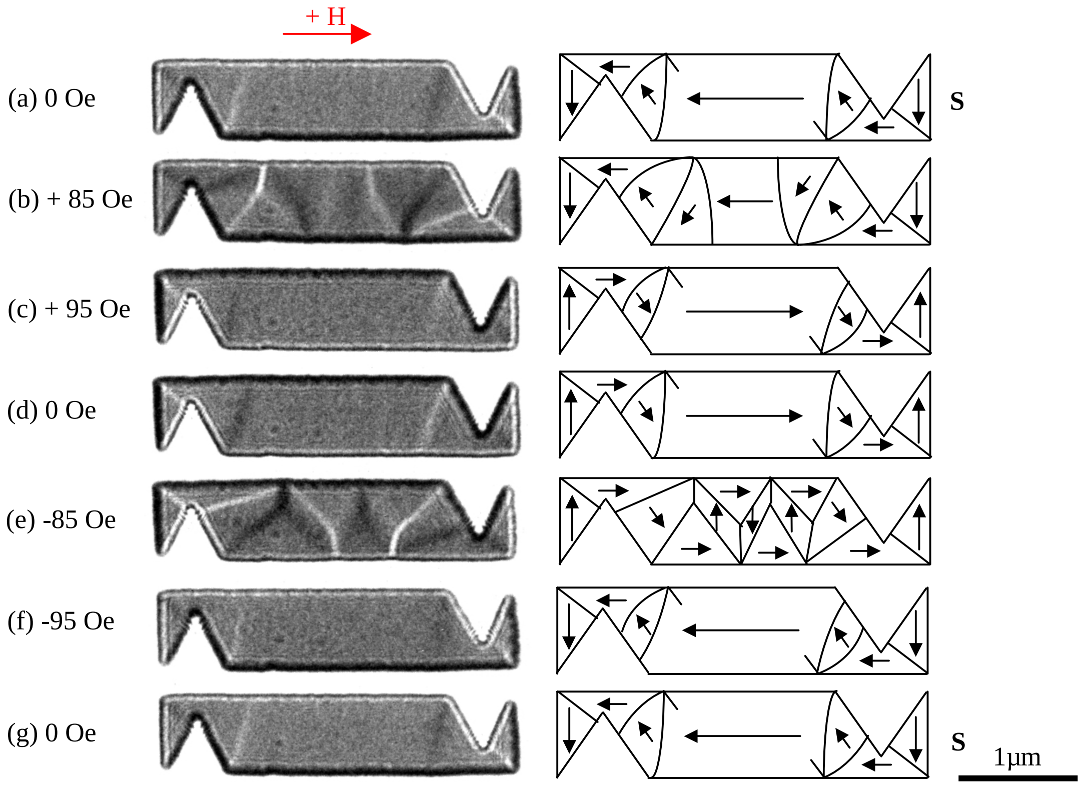

Fig. 6.22: (a)-(g) Reversal of the Notch1 element between transverse S state configurations.

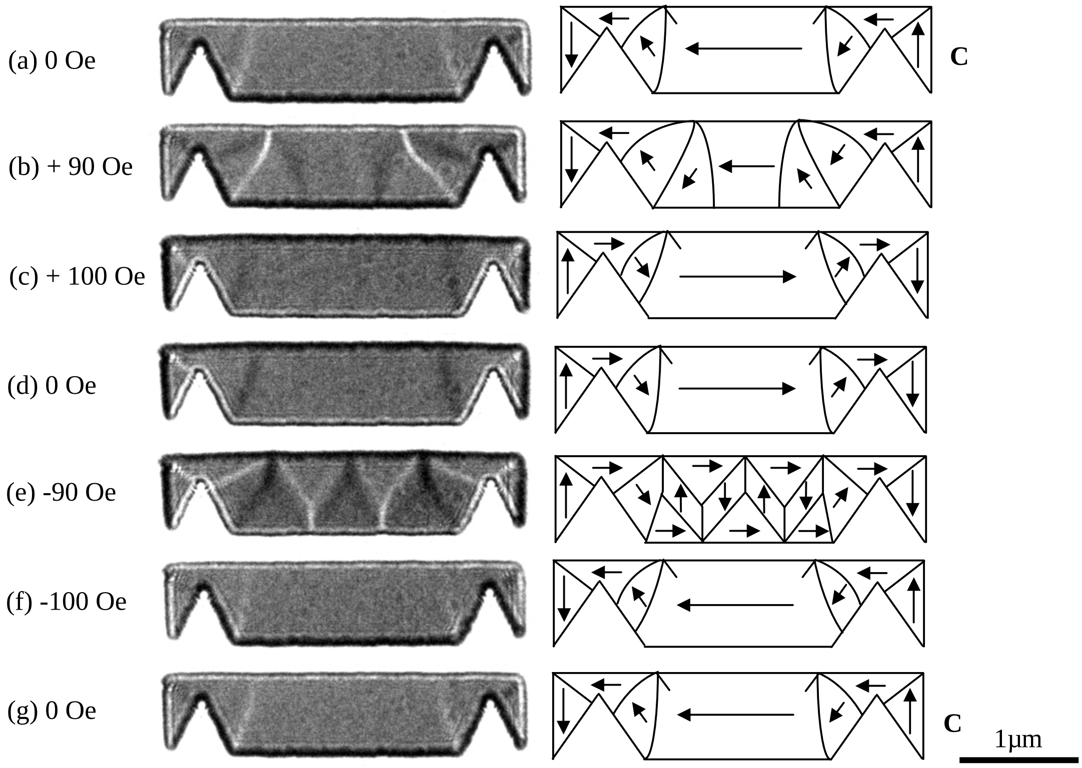

Fig. 6.23: (a)-(g) Reversal of the Notch2 element between transverse C state configurations.

In conclusion therefore, the addition of notches to a rectangular element can force the magnetisation into a particular remanent state and induce a single mode reversal process, but only when very large notches are used. In this study, merely those with the largest area were successful in achieving this. The experimental switching fields for these elements were very similar to those required to reverse the trapezoid and parallelogram, and all exceeded the coercivity of the basic rectangle.

Chapter 7

Domain wall traps

7.1 Introduction

The previous chapters have shown that whilst rectangular shaped elements can support a variety of remanent configurations and undergo different modes of reversal, the number of domain states may be reduced by breaking the element symmetry. Additionally, the inclusion of notches in a rectangular cell can force the element into a particular magnetic state by creating potential wells for domain walls. These artificial pinning sites make either the C or S state the ground configuration, but as with the trapezoids and parallelograms, cause an increase in switching field which is undesirable. In this chapter an alternative solution is introduced which uses a 'domain wall trap' element shape. The advantages of this approach are that it reduces both the element coercivity and the dependence of coercivity on element size. In addition, reversal can occur without the problem of irreproducible switching. The control of geometrically confined domain walls in constrictions or traps [149-152] is of great interest, both for solid state physics and device applications. In the domain wall trap (DWT) the idea is to create a head-to-head domain wall that can be moved reproducibly between two stable positions. The geometry consists of a narrow central section connected to wider ends as shown in Fig. 7.1. Creation of the wall is achieved by applying a saturating field perpendicular to the length of the central strip and then reducing it to zero. The geometry of the ends ensures that each end region becomes oppositely magnetised since the magnetostatic energy in these regions is minimised when the magnetisation lies parallel to the edges. Provided a head-to-head domain wall is formed in the central strip (Fig. 7.1a), magnetisation reversal within this region is achieved through movement of the trapped domain wall structure (Fig. 7.1b). Furthermore, the wider end sections are meant to ensure that there is a considerable energy barrier for the trapped wall to move into these regions, since the energy of a head-to-head wall increases with increasing element width. Therefore, the wall is preserved for switching to the opposite end of the element (Fig. 7.1c). Theory suggests that the fields required to move the domain wall are lower than those required to switch isolated elements [158].

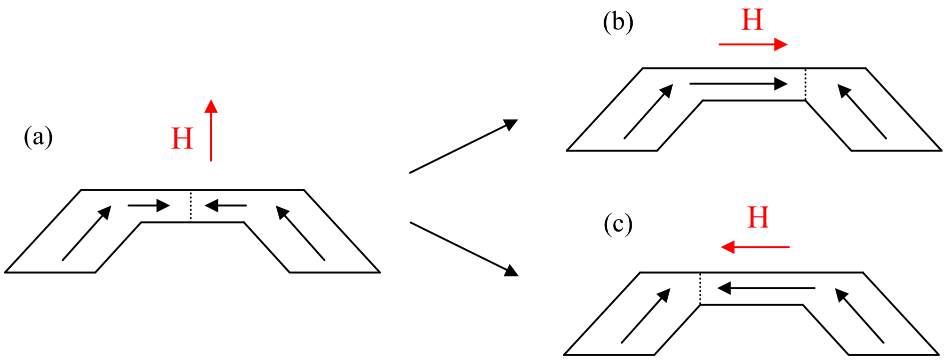

Fig. 7.1: After applying a short-axis field to form the wall (a), long-axis fields can be used to move the wall reproducibly between the ends of the domain wall trap element (b), (c).

Micromagnetic simulations of head-to-head walls [134,135] have predicted that both vortex and transverse wall configurations are possible depending on the width and thickness of the magnetic thin film. These wall configurations are illustrated in Fig. 7.2 and are named the vortex domain wall (VDW) and the transverse domain wall (TDW). The head-to-head VDW comprises three wall sections and can have clockwise (CW) or counter-clockwise (CCW) distributions as seen in Figs. 7.2a and 7.2b, respectively. The TDW comprises two wall sections and the central domain can be magnetised in opposite directions as shown in Figs. 7.2c and 7.2d. It should be noted, however, that these schematics are rather simplified and the detailed structure is discussed further in the next section.

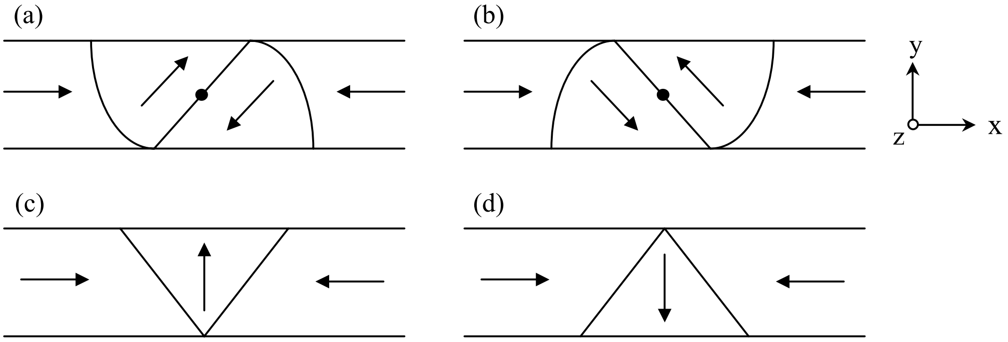

Fig. 7.2: Simplified schematic representation of (a) and (b) vortex and (c) and (d) transverse domain configurations for a head-to-head wall.

7.2 The domain wall trap elements

To form a head-to-head domain wall in the centre of the element experimentally, it was necessary to adjust the end shape from the dimensions proposed in reference [158]. Fabricated elements of the original design resulted in flux closure at the ends of the element with no head-to-head structures observed, so these sections were varied to induce significant shape anisotropy. Four different structures, each with a $1000 \times 200\,\text{nm}^2$ central section were studied in the TEM (Fig. 7.3). The first trap, labelled DWT1, is shown in Fig. 7.3a. The shape anisotropy associated with the long, parallel edges leads to the magnetisation being directed along the length of each section. The end regions are of the same width as the central section. In contrast, DWT2 was designed with end sections of varying width as can be seen in Fig. 7.3b. It was expected that this increasing width would keep the trapped wall within the central strip and reduce the danger of its complete removal by propagation into the end structures with consequent loss from the element. DWT3 (Fig. 7.3c) and DWT4 (Fig. 7.3d) were further variants on the same theme, the former having a higher symmetry than DWT2 but a comparable maximum width, whilst the end portion of the latter was significantly narrower. It is important to note the differences in local geometry where the central strip meets the end sections in each trap. Unlike the other structures, the central region of DWT1 exhibits a slightly shorter lower edge. The implications of this are described later.

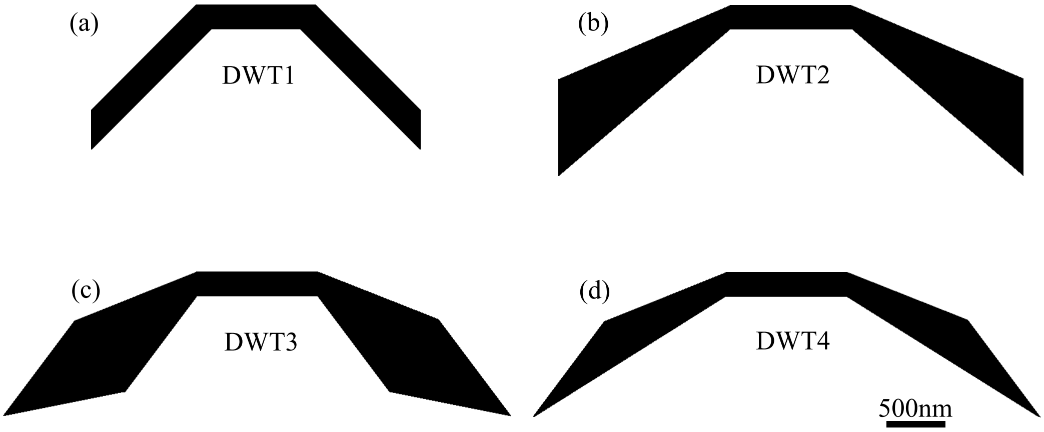

Fig. 7.3: The various domain wall trap structures studied.

OOMMF micromagnetic modelling [90] was utilised prior to fabrication as a means of testing the ability of each shape to support a head-to-head wall. Examples of some of the configurations simulated with the DWT1 geometry are shown in Fig. 7.4. The ground state for the element (Fig. 7.4a) has near-uniformly magnetised regions with low angle walls between them. In the case of the VDW and TDW states (Figs. 7.4b and 7.4c, respectively) each section is near-uniformly magnetised except for the head-to-head domain region where the vortex or transverse wall is observed. Both the VDW and TDW states are metastable and much higher in energy than the ground state, with the VDW exhibiting a slightly lower energy for the dimensions considered here. It should be noted that this is consistent with the previous calculations on idealised trapped walls [134]. Detailed magnetisation configurations of the VDW and TDW are shown in Figs. 7.4d and 7.4e which indicate that the simplified wall structures shown in Fig. 7.2 are a reasonable description of the magnetisation distribution.

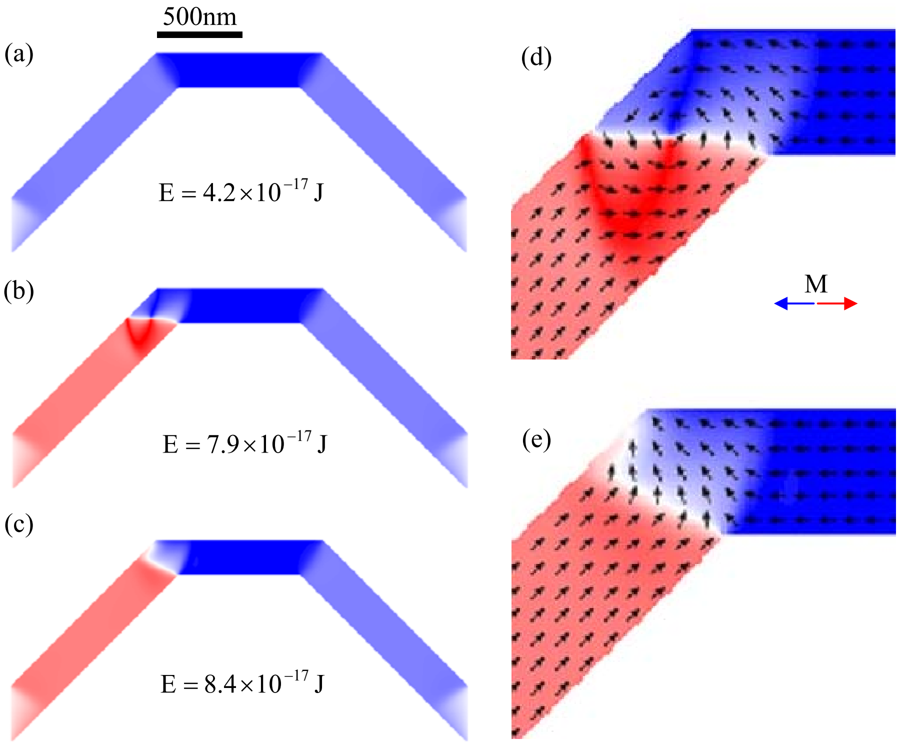

Fig. 7.4: OOMMF simulation of selected remanent states supported by DWT1: (a) near-uniformly magnetised, (b) head-to-head vortex and (c) head-to-head transverse states, and (d) and (e) more detail of the corner sections of (b) and (c). The calculated total system energies for (a)-(c) are given. Colours indicate the x-component of magnetisation whilst arrows are used to represent the magnetisation vectors.

Ten elements, 20nm thick, of each DWT geometry were then fabricated on SiN membrane substrates using electron beam lithography and lift-off. The material used was permalloy and deposition was by thermal evaporation. Following this, their magnetic structure was imaged using the Fresnel and DPC modes of Lorentz microscopy.

7.3 Formation of the head-to-head domain wall structure

When observed in the as-grown state, all of the elements supported the low-energy ground state structure equivalent to that shown in Fig. 7.4a. Formation of the head-to-head domain configuration was achieved by applying a field perpendicular to the long axis of the central strip and then relaxing the field to zero. The fields applied were not large enough to saturate the magnetisation along the y-axis but only to nucleate a VDW or TDW by switching the magnetisation in one of the end sections. This experiment determined the minimum field necessary to form the head-to-head structure in each element. All 10 elements of each geometry in the sample were observed and the field was increased gradually until the required structure was formed. The field values needed to achieve this (Table 7.1) reveal a strong dependence on end shape. The DWT1 elements required the largest fields to form the walls whilst the DWT3 elements required the smallest fields, consistent with the shape anisotropy of their respective end regions.

Element	Field to form wall (Oe)	Field to move wall between ends (Oe)	Field to remove wall from structure (Oe)
Axis of applied field	Y	X	X
DWT1	330	——	94
DWT2	295	31	83
DWT3	200	35	75
DWT4	285	36	67

Table 7.1: The critical field values required to form, switch, and remove a VDW in each of the DWTs. There is no field value in the third column for DWT1 because it was not possible to move the wall reproducibly between the ends of the strip in this element.

To understand more about the head-to-head structures supported, fields were applied at various angles to the y-axis to determine changes in the magnetic configuration with varying field orientation (Fig. 7.5).

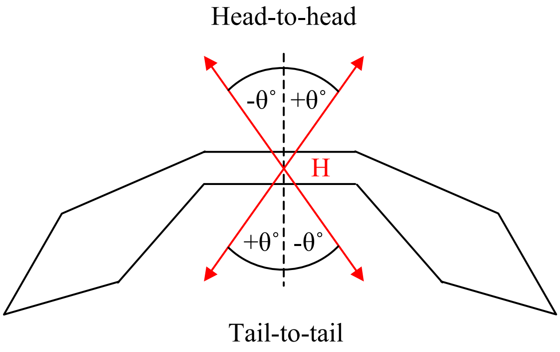

Fig. 7.5: Orientation of applied field during the wall-forming experiment.

Ten field orientations close to the positive y-direction and 10 close to the negative y-direction were chosen. In practice this involved rotating the specimen in its holder by 1° between field applications. In this, and in subsequent experiments, the sample was subjected to a field in its plane of ~7000 Oe, the maximum available. Observations were then made in zero field. The results of this experiment can be seen in Figs. 7.6-7.7. As the data obtained from DWTs 2, 3 and 4 were almost identical, only those from the DWT1 and DWT3 elements are shown. Fig. 7.9 shows the 5 locations where the head-to-head VDW can be formed in the strip.

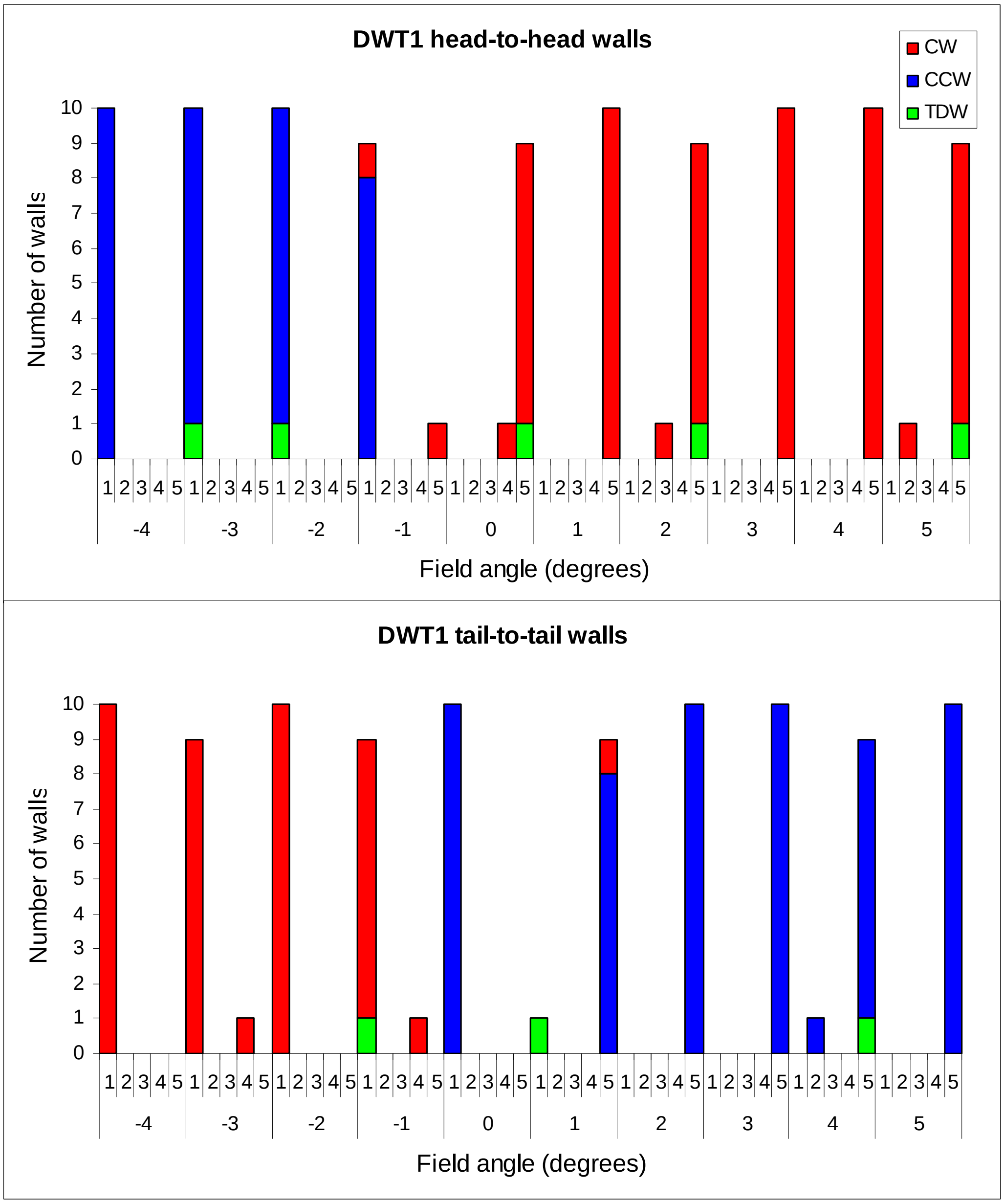

Fig. 7.6: The number/type of head-to-head and tail-to-tail walls formed at each of the 5 locations in the 10 DWT1 elements at different angles of applied field. The angles are measured with respect to the element short-axis.

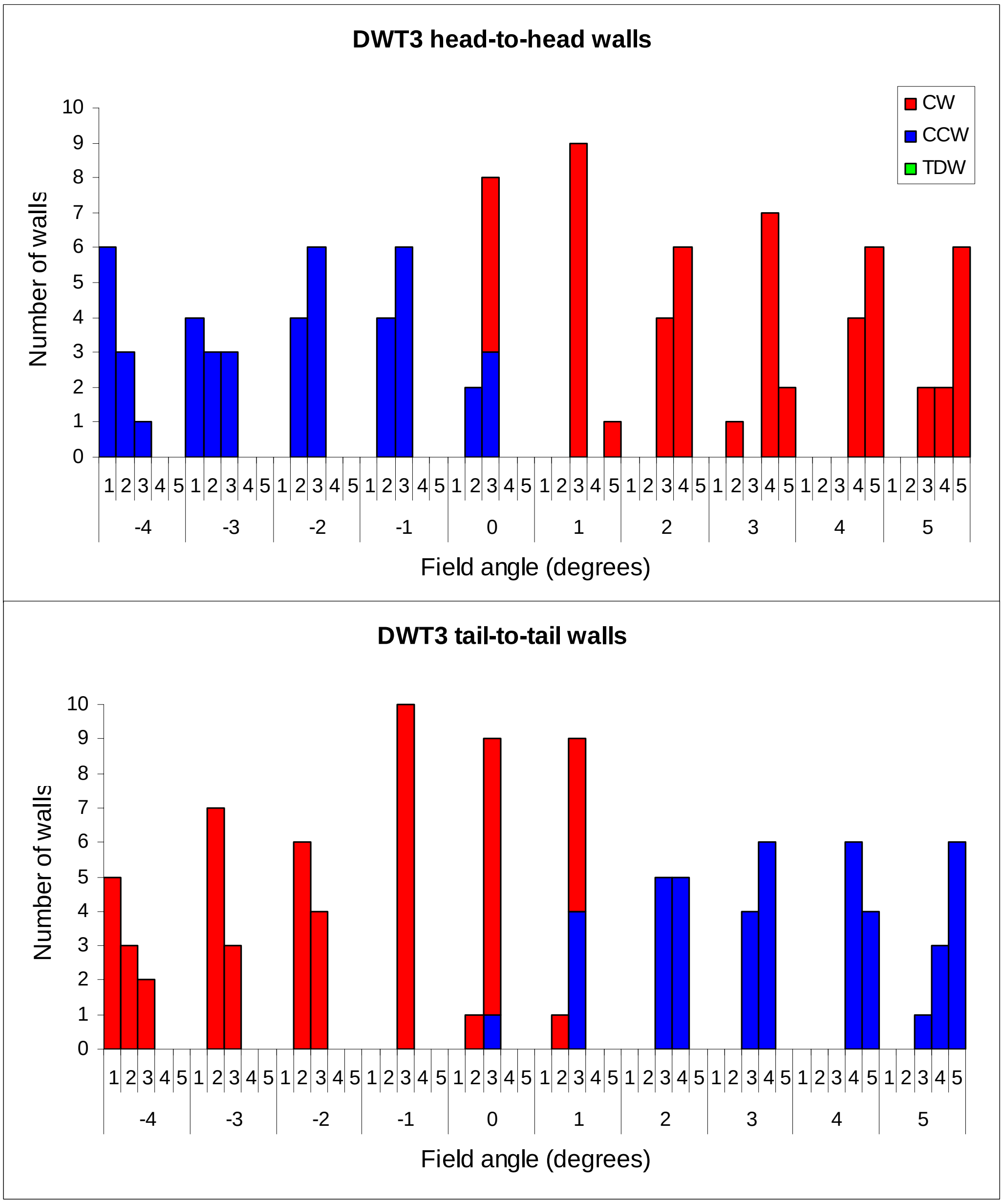

Fig. 7.7: The number/type of head-to-head and tail-to-tail walls formed at each of the 5 locations in the 10 DWT3 elements at different angles of applied field. The angles are measured with respect to the element short-axis.

One of the 200 observations (10 elements × 20 fields) of head-to-head structures in DWT3 is shown in Fig. 7.8. It was typical insomuch as the VDW structure was favoured over the TDW 99% of the time. This is in agreement with the energetics calculated by OOMMF and consistent with the original phase diagram that predicts vortex formation in a permalloy strip of this width and thickness [134]. It is interesting to note, however, that in the 1% of configurations where a TDW was nucleated, the structure was supported only by the DWT1 elements and not by any of the other geometries.

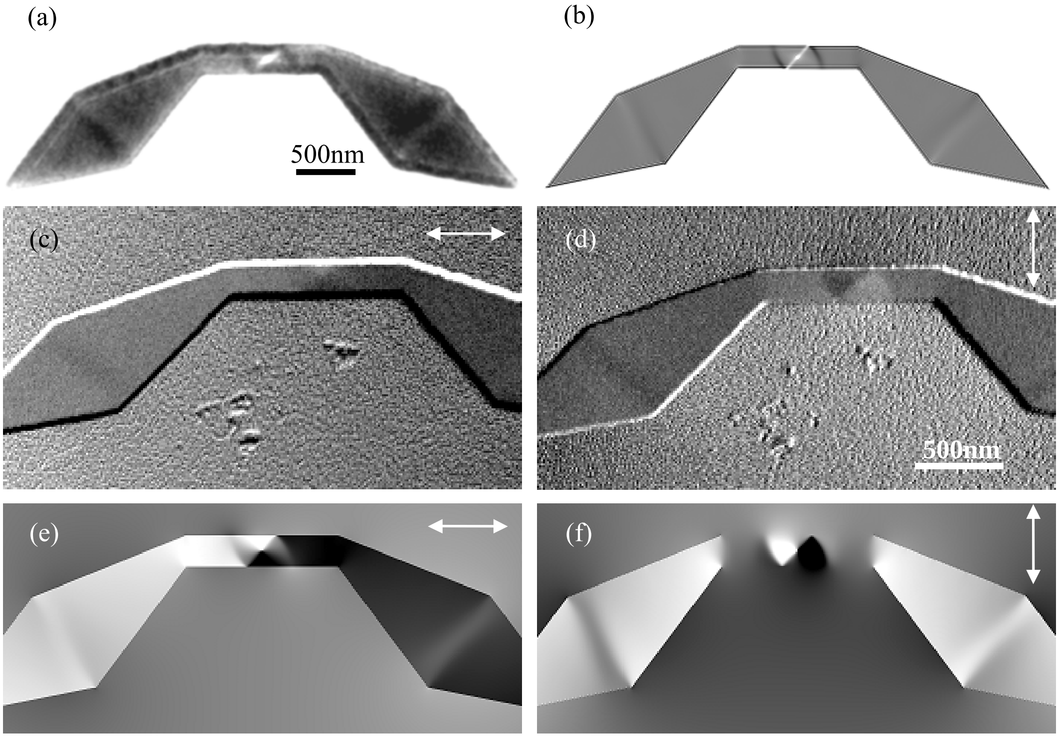

Fig. 7.8: (a) Experimental and (b) calculated Fresnel images of a head-to-head VDW localised in the centre of DWT3. (c)-(d) Experimental and (e)-(f) simulated DPC images of this configuration. Arrows in the DPC images denote the direction of mapped induction.

The VDW structure did not always form in the middle of the central strip, but was found to be stable at 5 different locations depending on the orientation of the field. These positions are depicted schematically in Fig. 7.9. Locations 1 and 5 spanned the apex between the central and end regions. Locations 2 and 4 were at the ends of the central strip but contained entirely within it, whilst location 3 was at the centre of the strip. In DWT1, the most favoured positions were locations 1 and 5. Although it was possible to form the structure in the other regions, these instances were rare (3% of the 200 observations). For each of the other DWTs there was a far greater spread but the data can be approximated as follows. Whilst for a field close to parallel to the short axis the VDW formed in the centre of the element, application of field at an angle of 2º away from this caused vortex formation at locations 2 and 4. By rotating the sample 4º away from the axis, the likelihood of forming the VDW at locations 1 and 5 increased.

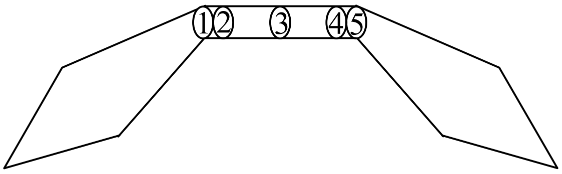

Fig. 7.9: Locations where the head-to-head VDW can be formed.

These experiments also revealed a correlation between the applied field direction and the sense of VDW rotation. The data indicate that application of the hard axis field exactly orthogonal to the central strip resulted in an equal mix of CW and CCW vortices distributed throughout the elements and located at the centre of each strip (location 3). However, when the applied field was slightly misaligned from this direction, a strong polarisation of the VDW sense of rotation was observed. For the head-to-head configuration (upwards field) a 1° misalignment clockwise from the hard direction resulted in formation of a CW VDW at location 3. For a counter clockwise misalignment we observed a CCW VDW at location 3. Fig. 7.10 shows Fresnel images of CW (Fig. 7.10a) and CCW (Fig. 7.10b) VDWs localised in the centre of DWT3. Further clockwise deviation of the angle to 2° and 4° produced CW VDWs at locations 4 and 5 respectively whilst counter clockwise deviation produced CCW VDWs at locations 1 and 2.

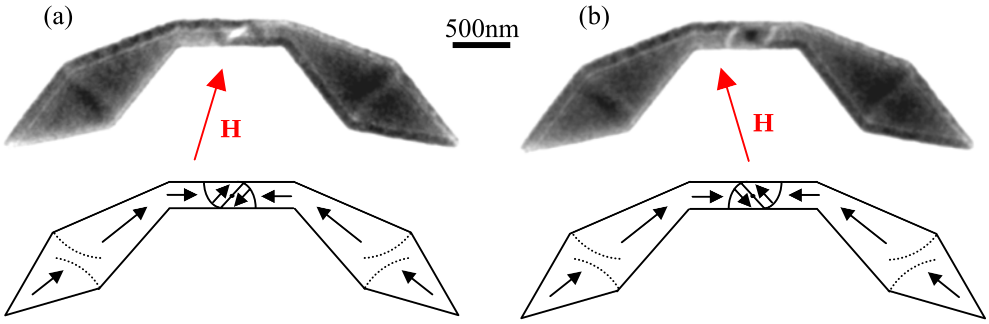

Fig. 7.10: (a) A clockwise and (b) counterclockwise VDW in DWT3. Schematics depict the magnetisation vectors in the corresponding Fresnel images. The direction of applied field used to initialise the different head-to-head structures is also shown.

7.4 Magnetic behaviour of DWTs 2, 3 and 4

Following initialisation of the head-to-head domain structures, in-situ magnetising experiments were carried out in the TEM to determine their stability. The fields required to move the VDW between the ends of the strip and completely out of the structure were noted. The various transitions are shown in Fresnel image sequences. These images show one of the DWT3 elements, but again, the behaviour of DWT2 and DWT4 was almost identical. As the behaviour of DWT1 was very different from the other geometries, it is considered in the next section. A summary of the critical fields for each geometry of domain wall trap is given in Table 7.1. N. B. the values shown have been averaged over several experiments using 10 elements of each geometry. In addition, no distiction has been made between the fields required to move the wall in different directions to take into account the asymmetry of the VDW and its interaction with the ends of the strip.

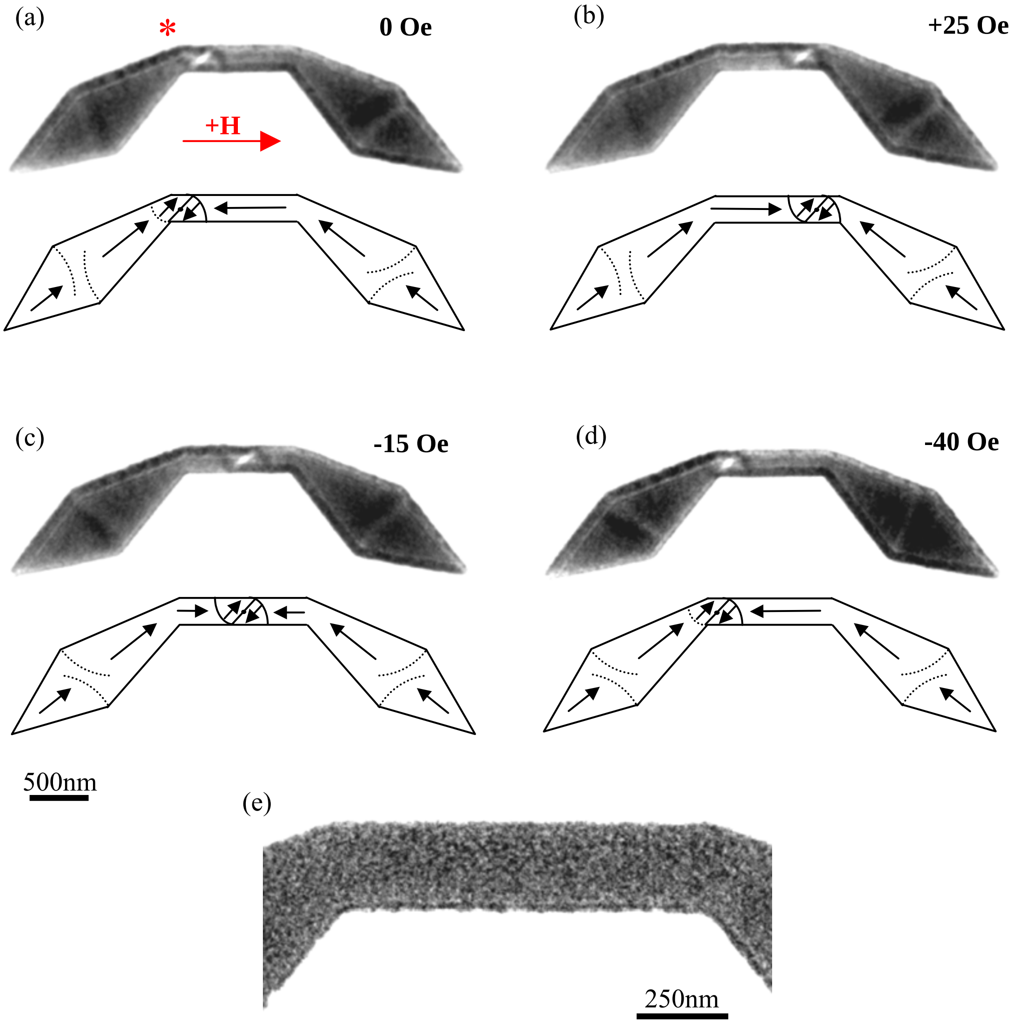

Fig. 7.11: (a)-(d) Fresnel images showing the movement of a VDW between the ends of the strip in DWT3. (e) Bright-field image taken at higher magnification revealing well defined edges in the fabricated element.

By applying a field parallel to the long axis of the central strip it was possible to move the VDW from one end to the other in a field of a few tens of Oersted. In Fig. 7.11a, a CW VDW can be observed at location 1 in the trap. At this location the direction of magnetisation in the end section and that of the adjacent part of the VDW resulted in a reduction in contrast of the left hand wall (starred) since the change in magnetisation orientation was small. Application of a field to move the structure caused an increase in length of the 180° domain wall before the VDW shifted to the opposite end of the strip (location 4) in a sudden move at a field of +25 Oe. This is shown in Fig. 7.11b. Thereafter a field of -15 Oe shifted the VDW to the middle of the strip (Fig. 7.11c) instead of back to its original position. The wall remained at this position until, at a field of 40 Oe, it moved back to location 1 (Fig. 7.11d). The inhibited movement at location 3 was observed in almost all of the experiments and occurred in the DWT2, DWT3 and DWT4 elements. Fig. 7.11e shows a bright field image of the central strip of a DWT3 element at higher magnification, the high quality of the edges being relevant to the discussion later.

In the next set of experiments larger fields were applied to try to force the VDW out of the central region. An example of this behaviour is shown in Fig. 7.12, again for DWT3. Starting with the head-to-head wall in the corner of the element (Fig. 7.12a), a field of -85 Oe (Fig. 7.12b) caused an increase in length of the left hand wall of the VDW before removing the structure from the trap at 95 Oe (Fig. 7.12c). As can be seen in Fig. 7.12b, this transition occurred via wall formation and movement in the end section at higher field values. This behaviour was also observed in DWT2 where the large volume of material permitted formation of more complex domain structures. With the head-to-head structure situated at location 4 (Fig. 7.13a), an applied field of 80 Oe in the positive x-direction varied the orientation of the magnetisation in the VDW (Fig. 7.13b) before removing it at a field of 100 Oe (Fig. 7.13c). Again, domains in one of the ends of the element played a role in this transition. A significant change in domain wall contrast can be observed prior to expulsion of the VDW out of the central strip (Fig. 7.13b). In the narrower DWT4 element, however, it was the VDW that moved during reversal of the end section. Here, the high shape anisotropy hinders rotation of the magnetisation whilst only a slight increase in the size of the VDW occurs as it moves into this region.

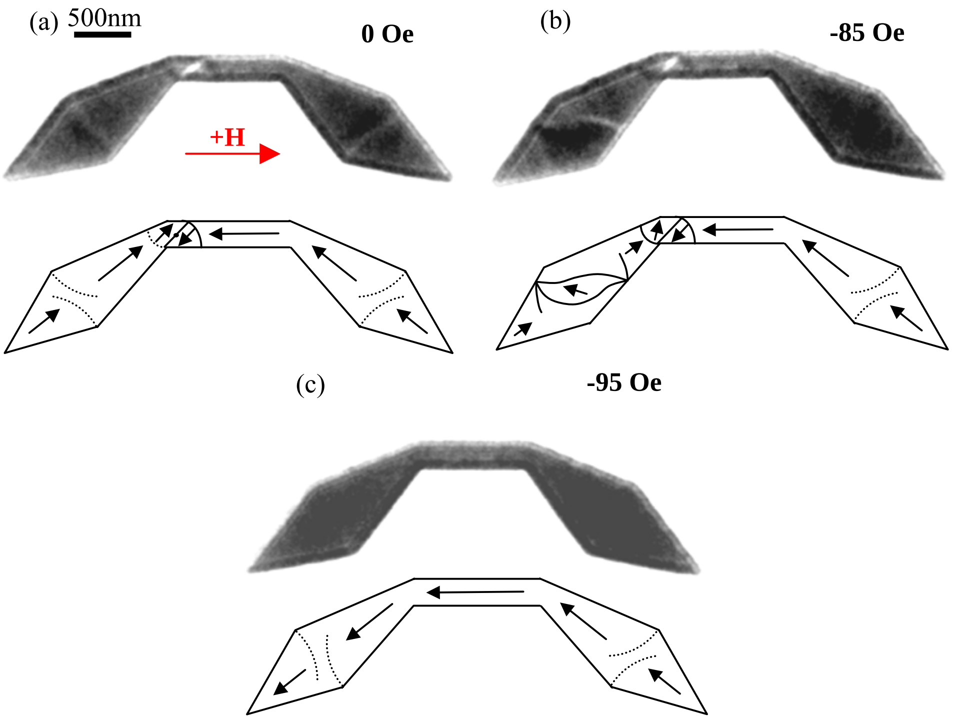

Fig. 7.12: (a)-(c) Fresnel images showing the removal of a VDW from the left hand side of DWT3.

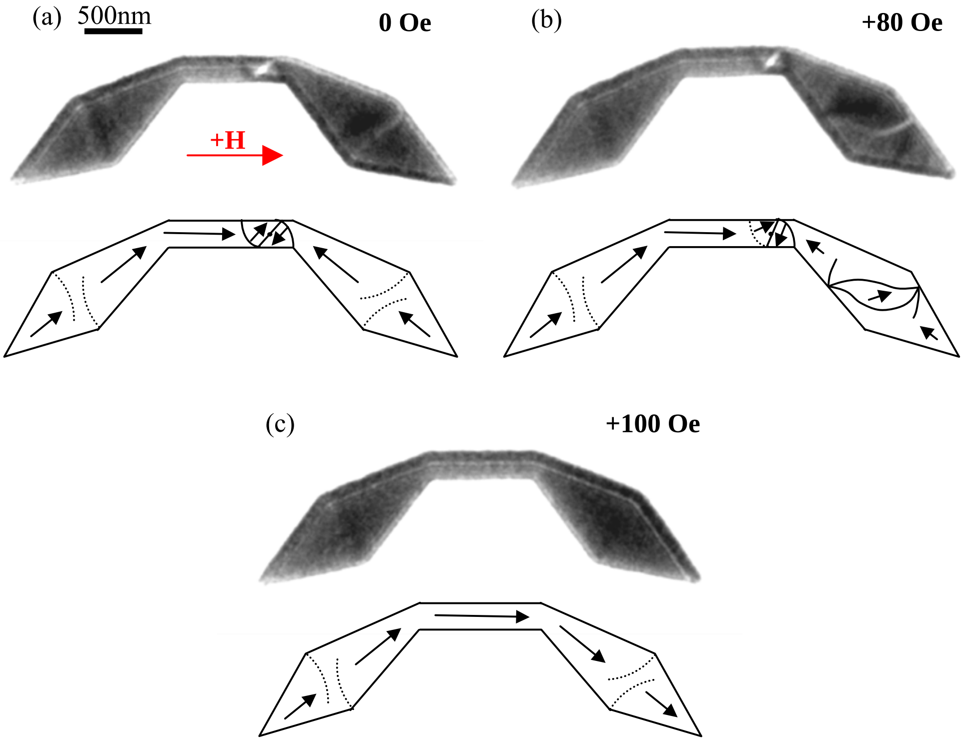

Fig. 7.13: (a)-(c) Fresnel images showing the removal of a VDW from the right hand side of DWT3.

In the majority of experiments on DWTs 2, 3 and 4 the VDW was not trapped in the end sections after moving past the corners, but was removed from the element completely. On the few occasions when the VDW was not completely removed, several complex domain configurations were observed instead. Four of these domain states are shown in the Fresnel images of Fig. 7.14.

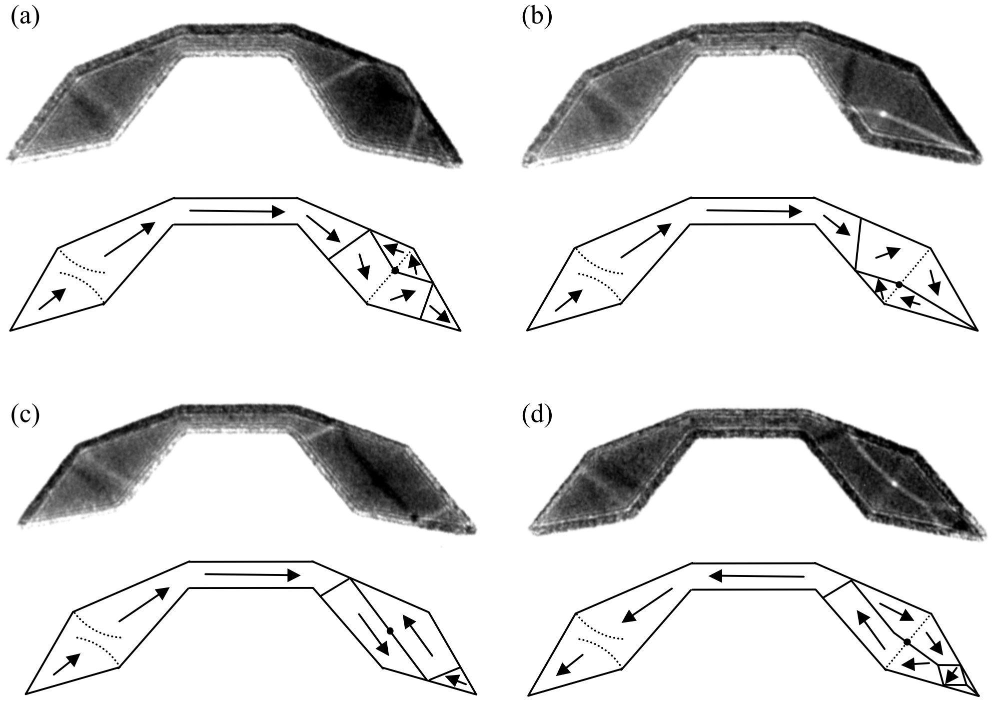

Fig. 7.14: (a)-(d) Four of the configurations observed when the VDW was moved out of the central strip but contained within the end section.

7.5 Magnetic behaviour of DWT1

The magnetic behaviour in DWT1 was quite different from that observed in each of the other traps. As mentioned previously, application of the initialisation field tended to form a VDW at locations 1 and 5 in the trap. In the tail-to-tail configuration, clockwise vortices favoured location 1 (Fig. 7.15a) whilst counter-clockwise vortices were observed at location 5. From the former configuration, application of a -80 Oe field parallel to the long axis resulted in the vortex being driven out of the element. Instead of switching to the opposite end of the strip, the VDW was stretched from the corner (Fig. 7.15b) until at a field of -115 Oe it was removed from the trap (Fig. 7.15c). In the majority of experiments with DWT1, the VDW could not be moved between the ends of the strip.

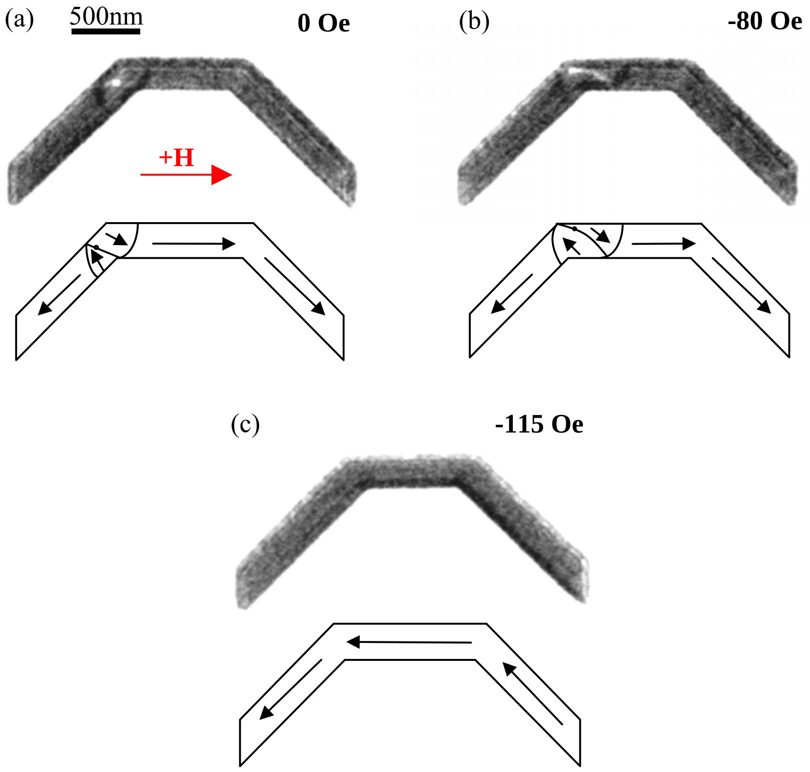

Fig. 7.15: (a)-(c) Fresnel images of the most common transition observed in the DWT1 elements. The VDW can be seen to extend before it is removed from the structure.

On some occasions, however, it was possible to form a head-to-head CW VDW at location 1 or a head-to-head CCW VDW at location 5 (Fig. 7.16a) using an exact hard-axis field. In these configurations the VDW was not as strongly stabilised. By applying a field to move the structure to the opposite end of the central section, three different kinds of behaviour were observed as shown in Fig. 7.16. In the first, the VDW was seen to move from location 5 to location 2 maintaining its structure (Fig. 7.16b). In the second case, the VDW behaved in a similar manner but was able to move completely into location 1 (Fig. 7.16c) without being hindered at the end of the central region. In the third sequence, the vortex switched both position and sense (Fig. 7.16d). This behaviour was observed in all of the DWT1 elements and occurred randomly. Experimentally, these behavioural types took place around the same field value (60 Oe) and appeared to be equally probable. It is important to stress that in most cases the head-to-head structure formed in DWT1 could not be moved reproducibly.

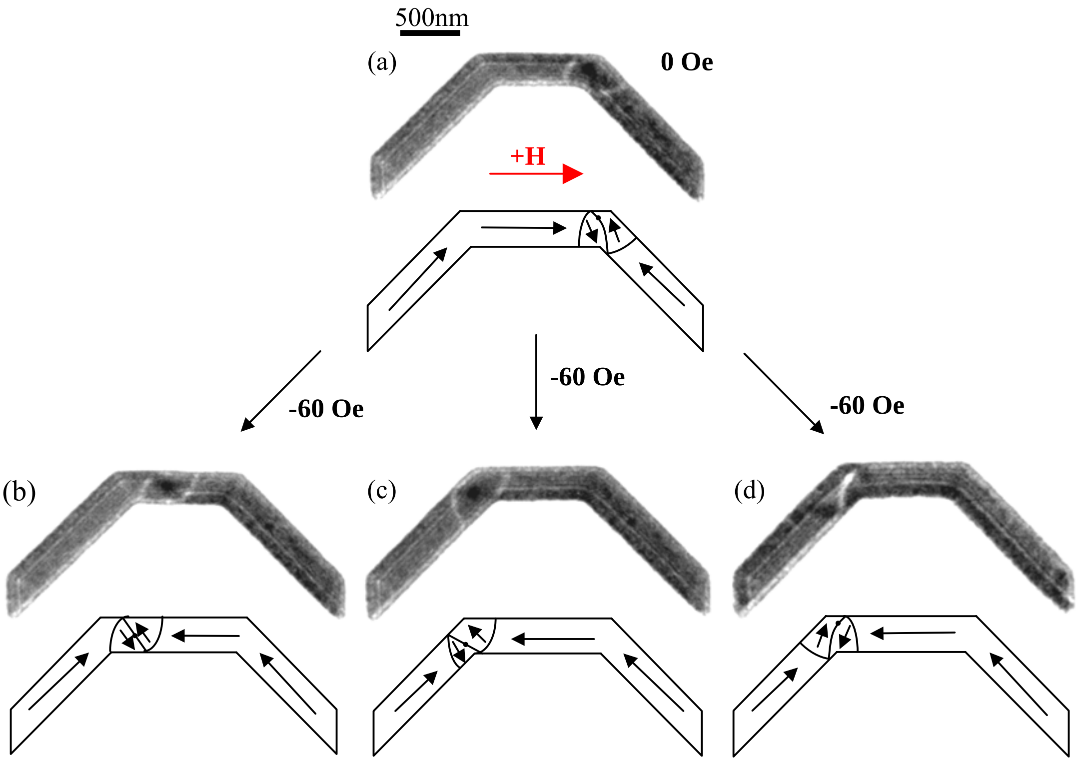

Fig. 7.16: (a)-(d) The three transitions observed when a field was applied to move the less stable VDW to the opposite end of the strip. These occurred around the same field value.

A final observation on the DWT1 element relates to the movement of a TDW (Fig. 7.17a). By applying a field to shift the position of the structure, a vortex was nucleated and a further domain introduced, transforming the TDW to the lower energy VDW state at a field of -5 Oe (Fig. 7.17b). Once formed, the VDW behaved as described previously.

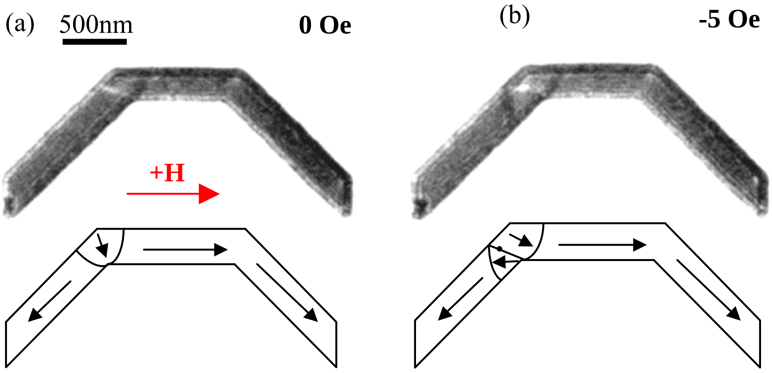

Fig. 7.17: Fresnel images of a (a) TDW in DWT1 transforming to the (b) vortex structure under the application of a small field.

7.6 Variation of strip width and thickness

To determine changes in the head-to-head wall structure with varying strip dimensions, a series of DWT3 elements were fabricated with strip widths of 50, 100, 150 and 200nm. All other in-plane dimensions were kept constant. These permalloy structures were deposited on membrane substrates at thicknesses of both 10 and 20nm. Head-to-head walls were initiated as before and imaged using low mag scanning (LMS) DPC. A simulated phase diagram [134] of thin permalloy strips predicts TDW formation in the thinner, narrower strips only, with VDWs forming as the width and thickess increases. Data extracted from this phase diagram and the experiment are shown in Table 7.2 with DPC images of each element given in Figs. 7.18 and 7.19.

Thickness (nm)	Width (Oe)	Simulated wall structure	Experimental wall structure
10	50	TDW	?
10	100	TDW	VDW
10	150	TDW	VDW
10	200	TDW/VDW	VDW
20	50	TDW	VDW
20	100	TDW/VDW	VDW
20	150	VDW	VDW
20	200	VDW	VDW

Table 7.2: Types of head-to-head wall formed in strips of various width and thickness.

From these images it can be seen that VDWs were formed in all of the 20nm thick strips despite the micromagnetic predictions. This discrepancy is likely to be the result of an inaccurate film thickness measurement. As discussed in chapter 5, the evaporator FTM underestimated the NiFe thickness, and was not detected until after the majority of experiments had already been completed. In the 10nm thick elements, the magnetic contrast was low, making it difficult to determine the domain wall structure. In addition, the 50 and 100nm wide strips of this thickness were found to be narrower than expected (~30 and 60nm respectively). Whilst a faint VDW can be seen in the 100, 150 and 200nm wide strips, the wall cannot be seen in the narrowest element. The reasons for low magnetic contrast in the 10nm film is 3-fold. A smaller Lorentz force is expected as a result of the thinner material, but metal flagging and a surface oxide were also present on this sample. Attempts to reveal further information from the 50nm wide strip using both

Fresnel and high mag scanning (HMS) DPC proved unsuccessful. In HMS the signal is not as sensitive to changes in magnetic induction and the contrast is reduced, whilst in Fresnel the strong edge effects drowned out any magnetic information.

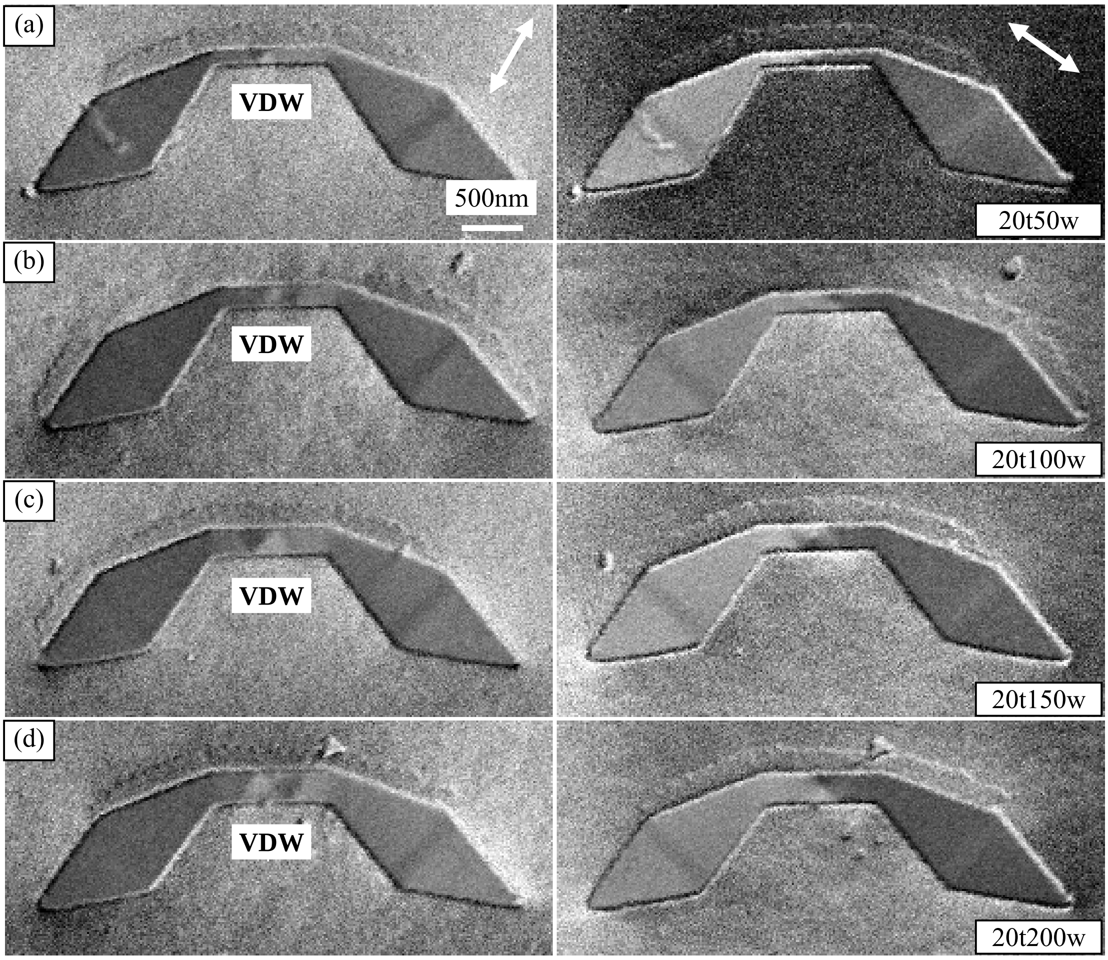

Fig. 7.18: DPC images showing the head-to-head domain wall structure in 20nm thick DWT3 elements with strips of various width.

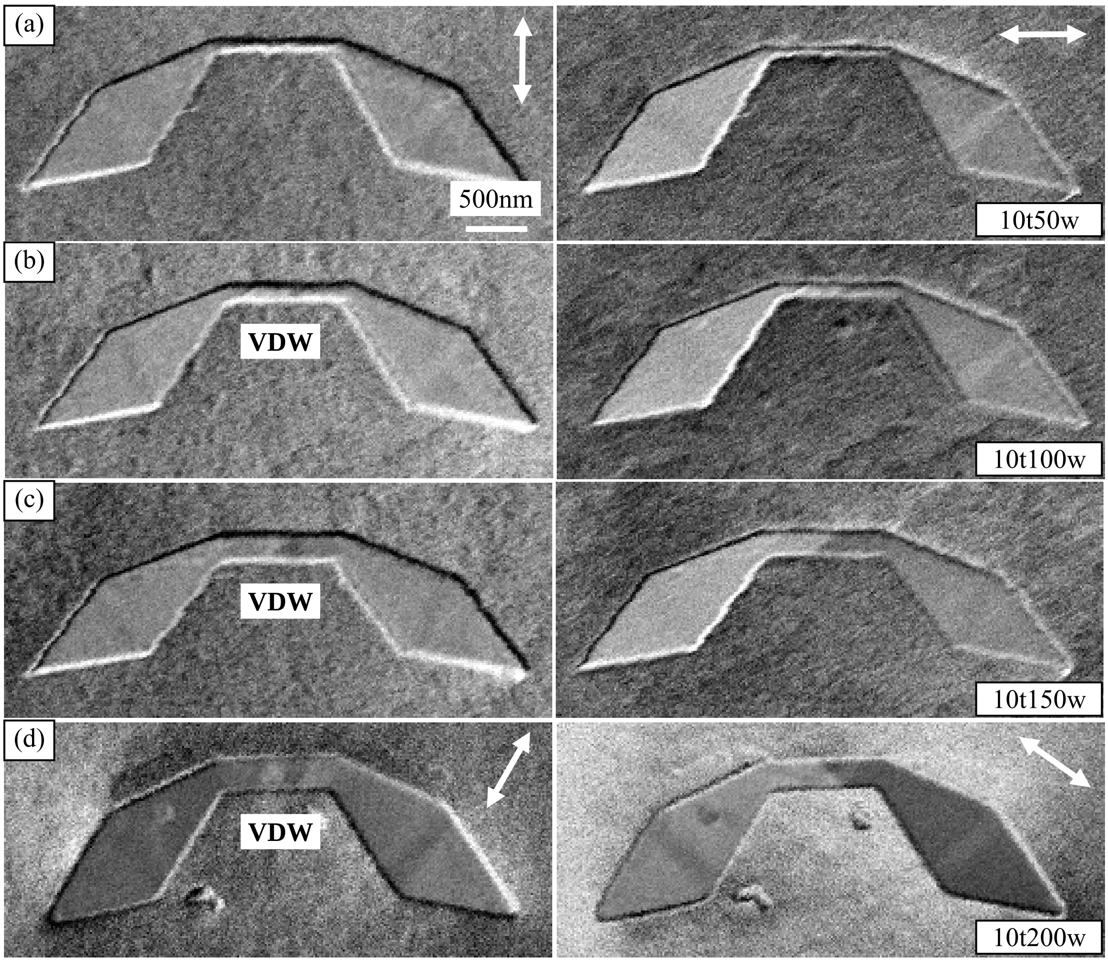

Fig. 7.19: DPC images showing the head-to-head domain wall structure in 10nm thick DWT3 elements with strips of various width.

7.7 Discussion of single bit DWT elements

It has been shown that it is possible to fabricate a variety of domain wall traps in which head-to-head or tail-to-tail wall structures can be nucleated and moved reproducibly using a relatively small magnetic field. Significant changes in the magnetic behaviour as a result of adjusting the geometry at the ends of the element have been observed.

Variation in end shape had an effect on the minimum field required to form the head-to-head domain wall. The field value necessary to reverse the end section is dependent on the width of this region and also the effective torque exerted on the magnetisation by the applied field. For example, by comparing elements of similar maximum end width (DWT1 with DWT4 or DWT2 with DWT3), a larger field was required to reverse the end sections that had an edge aligned parallel to the axis of applied field. As the magnetisation direction generally aligns with the element edges, it follows that the torque acting on the magnetisation towards the ends of DWT3 and DWT4 will be greater than on DWT1 and DWT2, in which the magnetisation was locally aligned anti-parallel to the direction of applied field. Also, by comparing end width for elements with similarly angled edges (DWT1 with DWT2 or DWT3 with DWT4) we observed smaller creation fields for the wider geometries. This reflects the shape anisotropy of the end sections.

When large fields were used to initialise the VDW it was shown that the precise field orientation had a strong influence on both the wall position and sense of vortex rotation. Following saturation in a given direction, the magnetisation relaxes to form a VDW or TDW at one of 5 possible locations within the strip. At the ends of the strip the Néel walls of the VDW structure interact with the corners of the element. There is also an additional reduction in the exchange energy associated with the magnetisation at the inner corner [158] which acts to stabilise the configuration. At location 3 in the centre of the strip, magnetostatic fields, generated by the end sections of opposing magnetisation, act on the VDW from opposite sides to create an energetically stable location for the domain wall. Stabilisation at this point was initially thought to be the result of physical roughness in the fabricated element, but bright field images have revealed a smooth edge with no obvious pinning sites (Fig. 7.11e).

The schematic diagrams given in Fig. 7.20 help to explain the biasing of the vortex rotation with applied field direction. Following saturation of an element as the field is reduced to zero, the magnetisation can rotate in one of two directions to form the VDW. With the field applied perpendicular to the length of the strip there is no preferred orientation and both CW and CCW configurations can be formed. By applying the field at a small angle to the short axis and relaxing, however, one ‘domain’ of the VDW is magnetised in a similar direction to the field (Fig. 7.20a) and the other is aligned anti-parallel to this. This alignment of magnetisation biases the orientation of the 180° wall of the VDW, and once this is established, the sense of rotation is determined by the direction of magnetisation in the adjacent sections of the element. For example, in Fig. 7.20a the magnetisation in the VDW must rotate clockwise to prevent charging in the outer Néel walls. If the magnetisation rotated in the opposite direction (Fig. 7.20b), individual head-to-head regions would exist at either side of the structure, resulting in a build-up of unnecessary positive charge in the VDW.

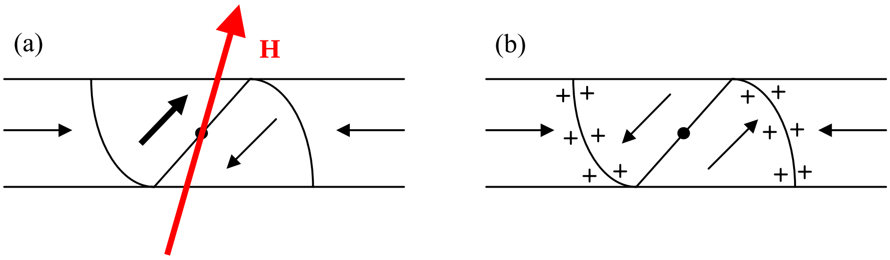

Fig. 7.20: The relation between the applied field orientation and the resulting VDW geometry: (a) favourable CW rotation and (b) unfavourable CCW rotation.

When fields were applied along the x-axis a difference in the magnitude necessary to move the VDW in different directions was observed. For example, in Fig. 7.11b a field of 25 Oe was required to move the CW VDW from location 1 to location 4, whilst in Fig. 7.11c a field of only 15 Oe was required to move it away from this end. This 10 Oe difference can be related to the asymmetry of the VDW and its interaction with the corners of the element. At location 1, two of the three walls which make up the VDW are attached to the inner corner of the DWT3 element compared with only one of the walls at location 4. This results in the two 'domains' of the VDW having a favourable/non-favourable orientation with respect to the end sections. In addition, there is also a lower exchange energy associated with this VDW at location 1 compared with any of the other positions and it is a combination of this and the domain wall pinning that is responsible for the difference in field.

The magnetic behaviour of the DWT1 element was quite different from that associated with the other elements and needs to be discussed further. The first notable point is the strong tendency for the wall to form at locations 1 and 5, as opposed to any of five locations in each of the other geometries. This indicates a greater degree of corner stability that is most likely the result of local geometry. DWT1 exhibits a shorter lower edge in the central strip giving different x co-ordinates to the upper and lower corners of a given end. It is possible that the total length of domain wall is smaller at locations 1 and 5 than elsewhere in the strip, resulting in a lower energy for the configuration at these positions.

In the DWT1 element, it was possible, on occasion, to form a TDW in the corners of the structure. The reason for this is probably related to the symmetry of both the TDW and the corner of the element. The TDW consists of three domains separated by two Néel walls. In a narrow strip of uniform width, these walls are usually of equal length and the configuration has mirror symmetry about a line perpendicular to the strip. A TDW localised in the corner of DWT1 is symmetric in shape with Néel walls of equal length. A schematic diagram depicts this configuration in Fig. 7.21a. In each of the other element shapes, however, the local geometry around the corner means that a TDW would have walls of different lengths, destroying the symmetry of the structure and rendering the configuration less favourable. A TDW localised in an element with ends of increasing width is shown schematically in Fig. 7.21b. Such local geometry is exhibited by DWTs 2, 3 and 4 around the corner regions. To enable Néel walls of equal length, the wall adjacent to the end section of the element could tilt slightly, but this would increase the length (and energy) of the wall and the size of the central domain (Fig. 7.21c). Instead, the wall nearest the central strip could be reduced in length by moving closer to the outer corner (Fig. 7.21d), but the symmetry of the TDW is still broken by the local geometry. An alternative option would be to move the complete TDW structure further into the central strip (Fig. 7.21e). In this position, however, the magnetisation in the adjacent end section would likely rotate to form a VDW. As our experiments show only formation of head-to-head VDWs in DWTs 2, 3 and 4, we can assume that none of the described configurations are energetically favourable.

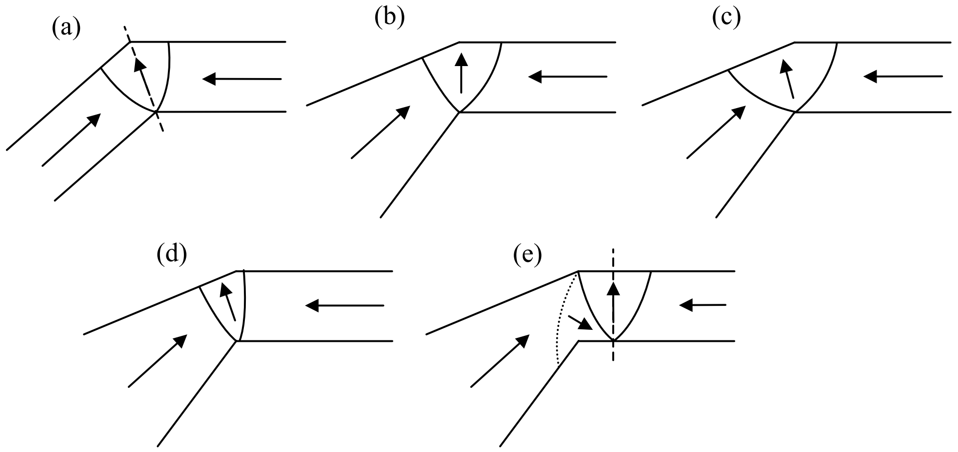

Fig. 7.21: (a) Schematic representation of a TDW localised in the corner of a DWT1 element and (b)-(e) hypothetical energetically unfavourable structures in the other DWTs.

When fields are applied along the easy axis of the strip, the behaviour of the trapped wall is dependent on how strongly it is pinned to the corners of the element. With a strongly stabilised wall (Fig. 7.15a), the structure was stretched and then removed completely. This demonstrates that the energy barrier which has to be overcome to de-pin the domain walls is sufficiently large that neither any magnetostatic energy minimum in the centre of the element nor any pinning at the opposite end of the strip are sufficient to arrest the reversal. A contributing factor to the loss of the VDW is the width of the end section in this element. Whilst the wider ends of DWTs 2, 3 and 4 help prevent this from occurring, the ends of

DWT1 offer little resistance to the domain wall motion. With a less favourable and more weakly pinned VDW on the other hand (Fig. 7.16a), the wall was able to move across the strip with a relatively small applied field and was pinned at the opposite end.

The TDW to VDW transition presented in Fig. 7.17 is also considered here. When the field is applied parallel to the strip length it affects the TDW in two ways. Firstly, it exerts a torque on the central domain of the TDW. Due to the local geometry at the ends of DWT1, however, the magnetisation in this region is oriented towards the outer corner and not perpendicular to the axis of applied field. As a result, the torque acting on opposite sides of the TDW is different, and the magnetisation within the domain rotates incoherently, possibly accounting for VDW formation. The applied field also acts to move the TDW along the central strip, with the energy required dependent on the level of pinning at the corner. As a result, the behaviour of the TDW under the influence of an applied field depends on where it is situated within the element. This transition has also been observed in finite element simulations performed by Bance *et al* [160]. In these experiments a clockwise rotating field of variable frequency was able to change reproducibly a transverse configuration to either a CW or CCW VDW as a function of field strength. In addition, the simulated application of static fields along the length of the strip was able to move the TDW from one corner to the other, with transition to a VDW occurring midway between the ends of the strip.

By varying the width and thickness of strip in the DWT3 element, a VDW was observed in every geometry apart from the (designed) 10nm thick, 50nm wide strip. The magnetic contrast in this film was inherently low, but fabrication problems caused the actual width of the element to be smaller than expected, and combined with metal flagging and a surface oxide layer, made determination of the domain wall structure difficult. These results disagree somewhat with the simulations which predict transverse wall formation in the thinner, narrower strips. However, given the inaccuracy of the FTM at the time of this experiment, it is not fair to compare the results directly.

From the four different geometries considered in this study, the DWT3 element was most successful in terms of its ability to support a head-to-head domain structure that could be moved reproducibly with field. The small fields required to nucleate and move the VDW (200 Oe and 35 Oe respectively), combined with the resistance to domain wall motion created at the ends of the trap by the increasing end width (75 Oe), make this element more suitable than the others for device applications. Despite the interesting, and rather unusual, behaviour exhibited by DWT1, this element geometry is less suitable for applications due to the inability to move the VDW reproducibly between the strip ends. The DWT2 geometry could, however, be used as a domain wall trap element and its behaviour was very similar to DWT3. The drawback here is the large initialisation field associated with the end shape (295 Oe). Finally, although DWT4 was based directly on the DWT3 design, the narrower end sections do not provide enough resistance to large applied fields (67 Oe). In domain wall traps, it is desirable to have a large range of field in which the head-to-head wall is fixed at the end of the strip, as this prevents accidental loss after switching. With DWT4, the difference in field required to move the wall between the ends of the strip and to remove it from the structure completely (31 Oe) is not sufficient for practical applications.

7.8 DWT chains

To be able to store sufficient data in an MRAM chip [171], the magnetic bits (binary digits) have to be fabricated in a 2D array (Fig. 7.22). However, due to magnetostatic interactions between neighbouring cells, the packing density is limited. Previous studies on rectangular elements have shown that a separation of greater than or equal to one width is advisable between elements in the same row, and in excess of one length between each row [114,130]. Therefore, when the domain wall traps are moved closer together, problem areas would likely arise between adjacent elements (Fig. 7.23a). As magnetostatic interactions tend to align neighbouring moments anti-parallel, this could potentially affect the formation of the head-to-head configuration.

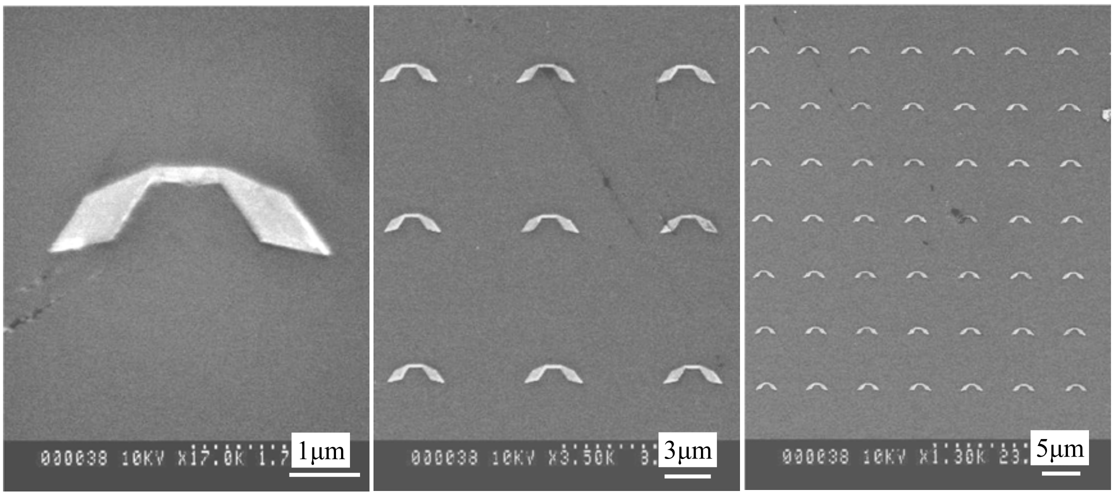

Fig. 7.22: SEM images of a fabricated array of DWT3 elements on the surface of a Si substrate at different magnifications.

A simple solution would be to alternate the orientation of adjacent elements in the y-direction so as the field lines favour the configuration, but local fields would be required to form the domain walls (Fig. 7.23b). In the global setup, problem regions would still exist because the ends are magnetised in a similar direction (Fig. 7.23c). An alternative approach, as proposed in one of the early papers [158], would be to link up the elements in a given row to form a series of traps attached end-to-end that share the same end sections. A schematic diagram of this arrangement is shown in Fig. 7.23d. In a DWT chain, the end sections are separated by 1μm strips which reduces their interaction. As has been observed previously in this study, however, stray fields from these regions act on each strip with an equal and opposite force, inhibiting the VDW slightly as it moves (Fig. 7.11c). On the other hand, a small increase in field was enough to overcome this 'magnetostatic pinning' effect, so it is more a minor complication than a serious problem. Also, although maximising the packing density with this setup, each chain would still have to be sufficiently separated (~2μm) along the y-axis.

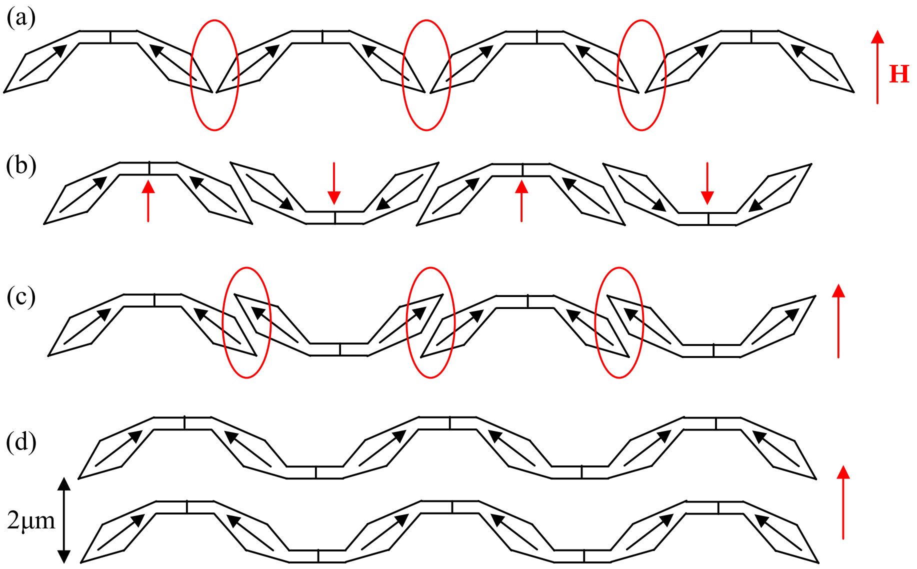

Fig. 7.23: (a) Stray field interactions may prevent the formation of a head-to-head configuration in a closely packed array unless the bits are oriented in alternating directions. This would require local fields to magnetise the cells in (b) opposite directions otherwise (c) magnetostatic effects would still cause problems. (d) A series of DWT3 elements connected as a long magnetic strip. The chain spacing is still an important dimension if stray fields are to be negligible.

A series of 20nm thick connected DWT3 elements were fabricated with 5 and 10 elements in each chain. Fields were then applied to nucleate and manipulate the domain walls. Application of a short-axis field produces alternating head-to-head and tail-to-tail walls in each of the strips, and thereafter long-axis fields affect every wall in the chain. To control the state of a single bit requires the application of a local field. Such control would be achievable using the word/bit line architecture used in current MRAM devices but this was not possible in the microscope. Instead, global fields were applied as before to study the behaviour of the complete structure.

Fig. 7.24 shows a series of VDWs moving between the ends of each strip in a single DWT chain. The domain wall contrast reveals that every head-to-head wall had a CCW rotation and every tail-to-tail wall a CW rotation. This implies that the initialising field was oriented at a small angle CCW to the positive y-direction instead of exactly along the short axis. The walls did not move at exactly the same field strength, but were observed to switch over a range of about 20 Oe. The reversal behaviour of each strip was the same as described earlier. Stars are used in the images to highlight transitions at the various field steps.

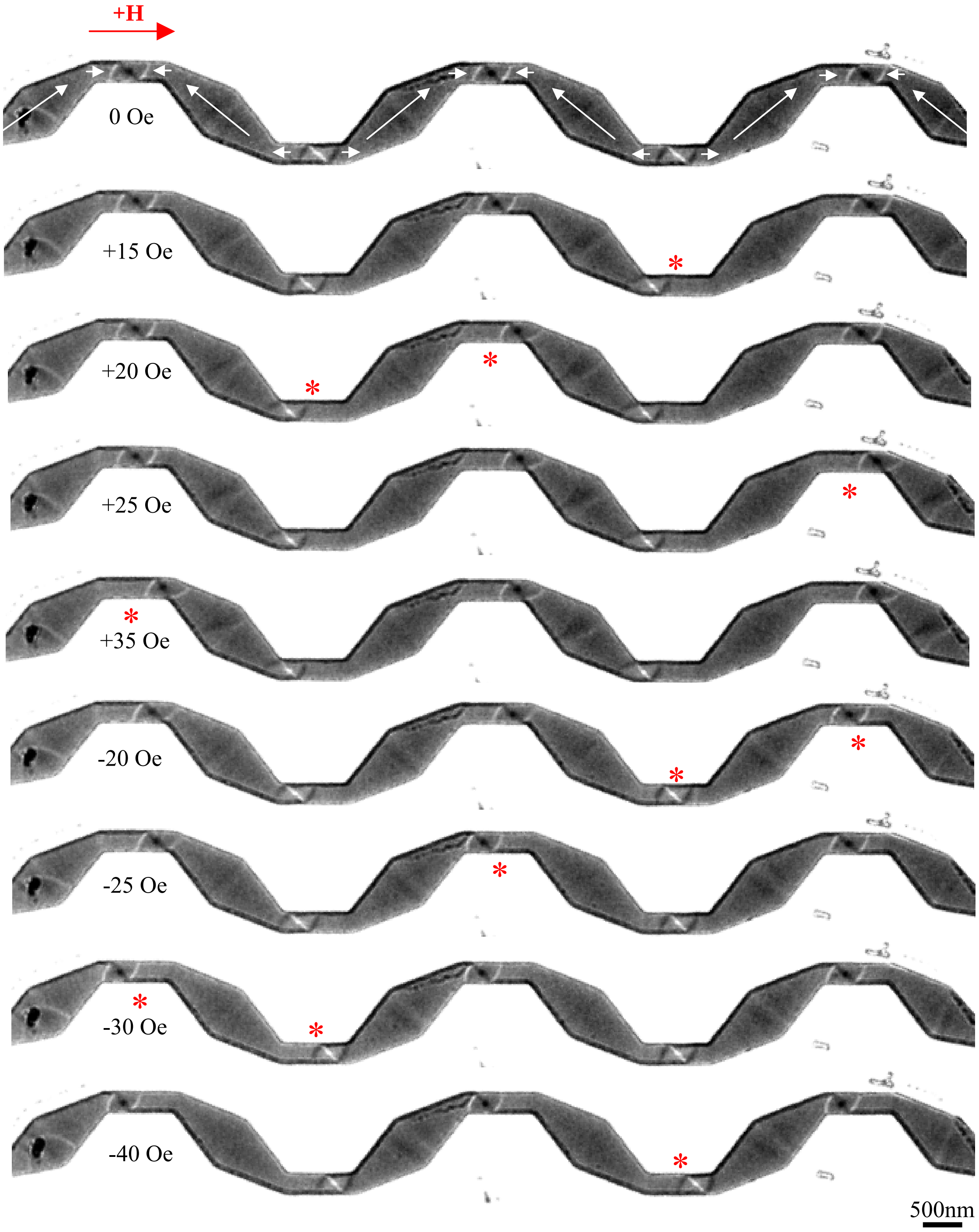

Fig. 7.24: Fresnel images showing VDW movement between the ends of the each strip in a DWT chain.

After this, larger fields were applied to remove the domain walls. This behaviour was captured in Fresnel image sequences for both positive (Fig. 7.25) and negative (Fig. 7.26) long-axis fields. Earlier it was shown that head-to-head and tail-to-tail walls move in opposite directions under the influence of an applied field. In DWT chains, therefore, neighbouring walls will annihilate one another provided they are not first removed by walls in the end sections. It has also been shown with the isolated DWT elements, that depending on end width, removal of the VDW can occur either by annihilation with walls in the end sections or by propagation (DWT3 vs DWT1). With DWT3 chains, annihilation with domain walls in the wider regions was the dominant process. Stars are used in the images to highlight domain wall removal at the various field steps. In Fig. 7.25, all VDWs in the field of view were observed to annihilate at 95 Oe. With the field applied in the opposite direction (Fig. 7.26), the walls were removed at different field values.

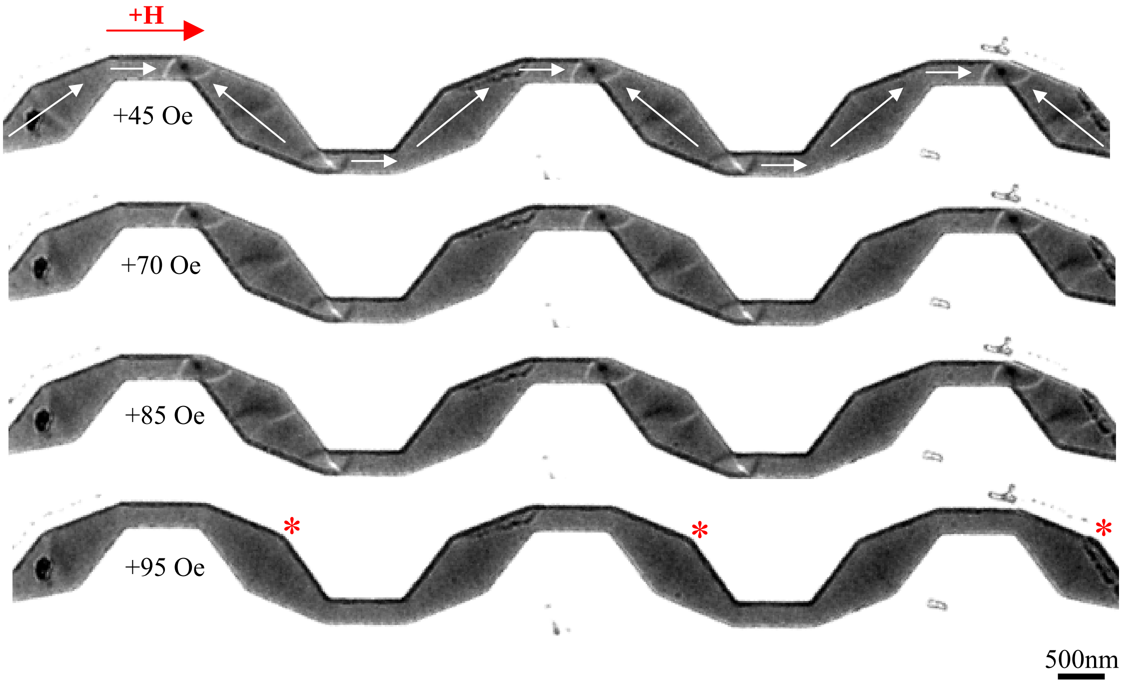

Fig. 7.25: Fresnel images showing VDW annihilation with domain walls in the wider regions of the structure when the positive field was increased. Removal of each wall took place around the same field strength.

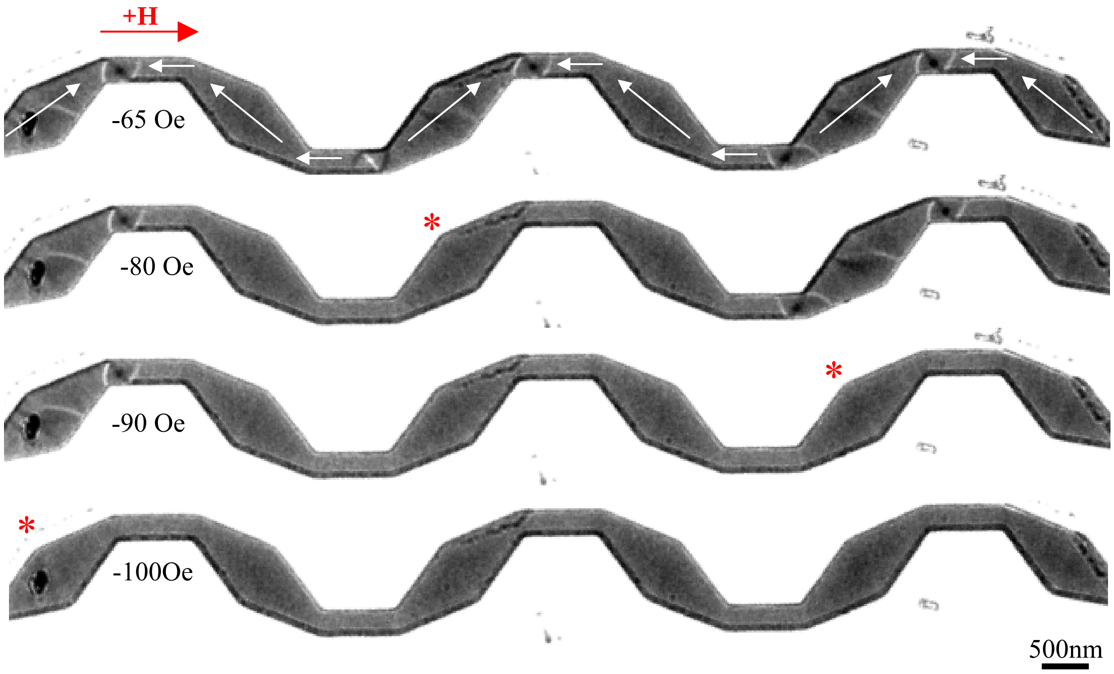

Fig. 7.26: Fresnel images showing VDW annihilation with domain walls in the wider regions of the structure when the negative field was increased. The walls were removed at different field values in this particular experiment.

7.9 Domain wall injection

As well as investigating the potential of domain wall trap elements as MRAM storage cells, their fundamental magnetic behaviour is also of interest. Currently, the study of domain walls in elements with restricted dimensions [172] is a hot research topic. The structure [134], width [142,143] and motion [173] of the wall can change dramatically depending on the physical size and shape of material. With this in mind, DWT chains have been used to investigate the injection of a single head-to-head wall, as well as the movement of this wall through the structure. After attempting this with the basic DWT3 chain geometry, new elements incorporating an injection pad at one end were also studied. Several groups have performed similar investigations on magnetic nanowires, so the results of these experiments should be of general interest.

Starting with a chain of 5 connected DWT3 elements (no injection pad) in a uniform state, long-axis fields were applied anti-parallel to the magnetisation direction in an attempt to introduce and direct a wall along the length of the chain. Fresnel images capture this behaviour in Fig. 7.27. From the near-uniform configuration (Fig. 7.27a) an increase in field saw the nucleation of low-angle domain walls in the wider sections of each DWT (Fig. 7.27b). Increasing the field strength further then caused the magnetisation of the complete chain to switch (Fig. 7.27c). This was the most commonly observed reversal process. On occasion, however, individual regions within the chain reversed without affecting the magnetisation of the neighbouring sections. This behaviour took place at a slightly lower field strength (110 Oe) than that required to switch the complete structure and caused formation (starred) of a VDW (Fig. 7.27d) and also some more complex configurations (Fig. 7.27e). These complicated domain structures could not be moved and increased field application resulted in their annihilation.

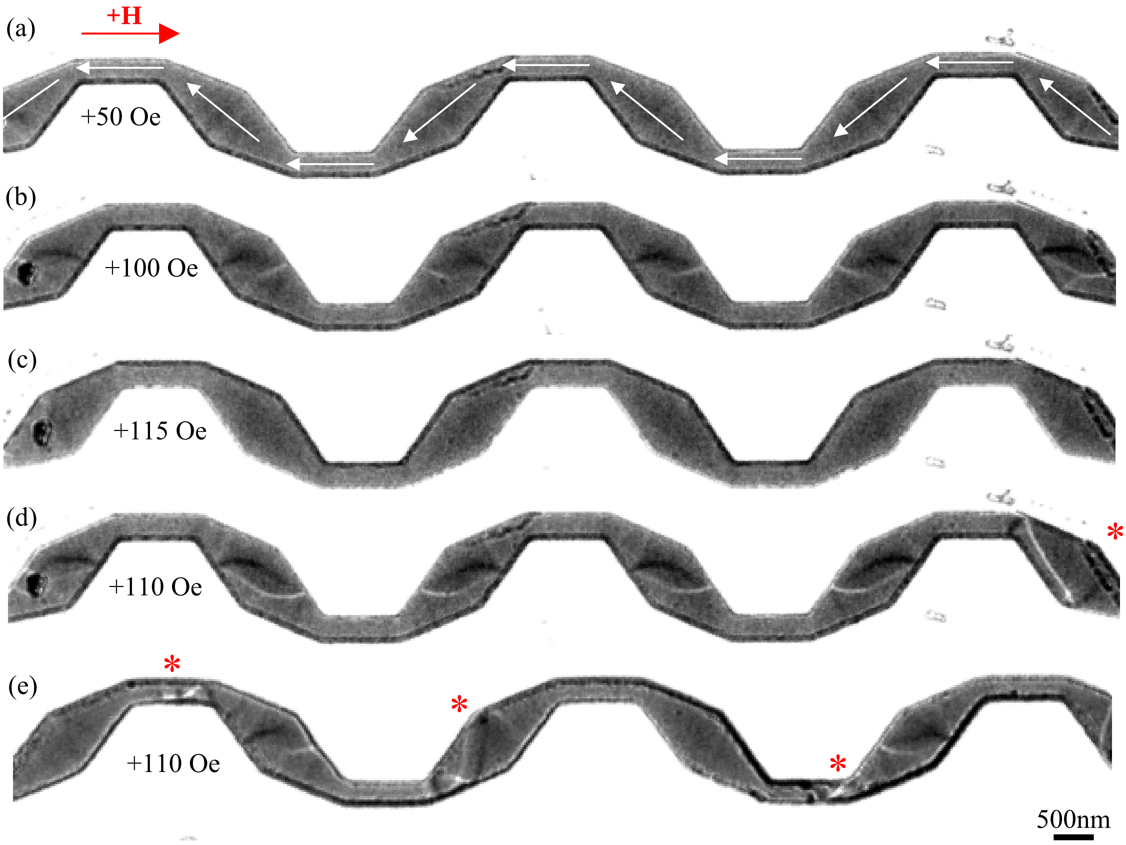

Fig. 7.27: (a)-(c) Typically, application of field anti-parallel to the near-uniform magnetisation caused reversal of the complete DWT chain. Occasionally, however, individual sections switched at slightly lower fields to form a (d) VDW and (e) more complex domain structures.

The use of a so-called injection pad at one end of the DWT chain was then investigated. An injection pad [174-177] is a wider section of material attached to the end of a narrow element. It can take various forms, but typically circular, elliptical, square, rectangular or diamond geometries are used. Since the field required to nucleate a domain wall depends on the element width, a wide pad can form a wall at fields smaller than the nucleation field of the wire. In this work, diamond-shaped pads with a diagonal width of 2μm were attached to one end of each DWT chain.

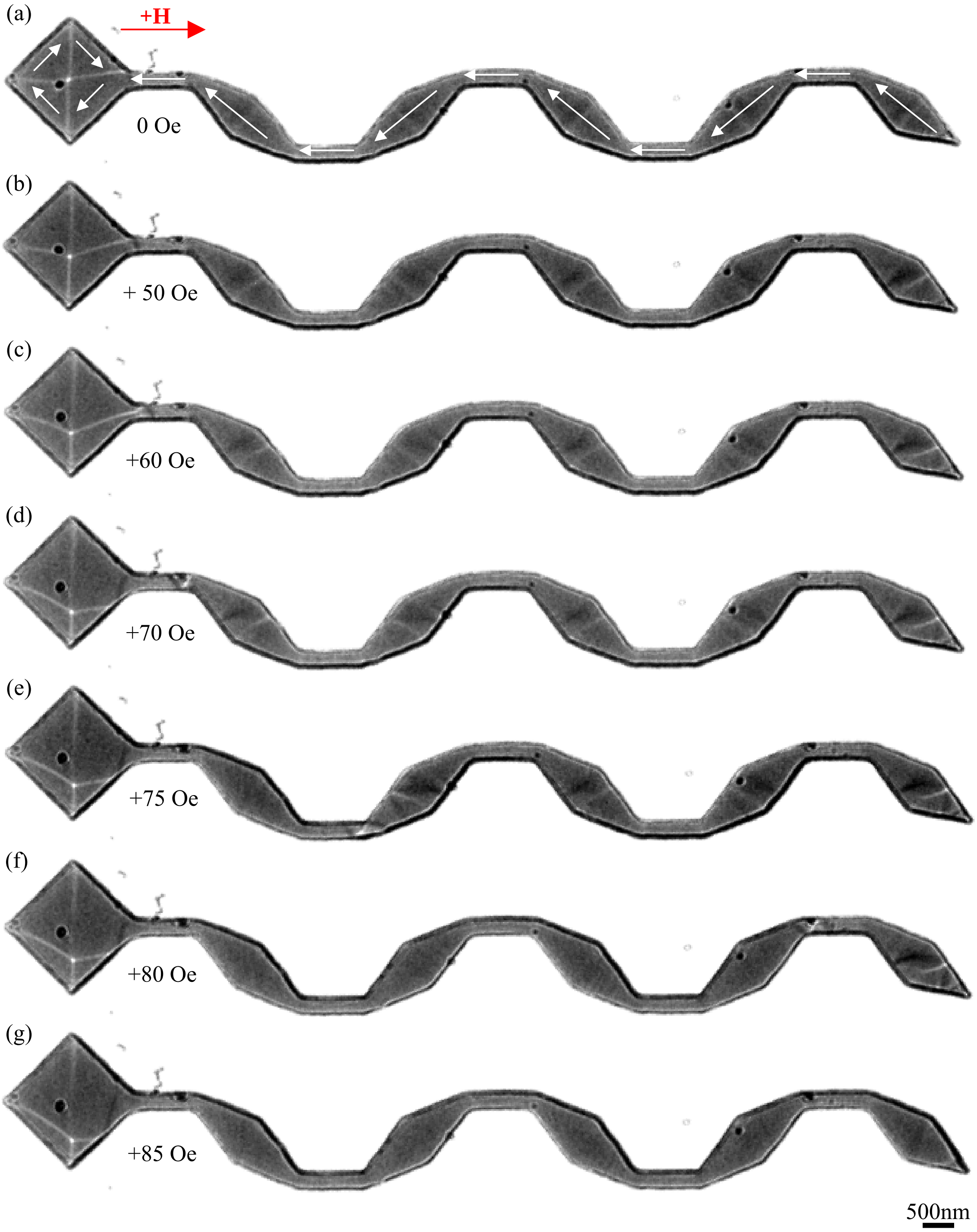

Fig. 7.28: The introduction of a VDW to a DWT3 chain. Although the wall could be moved through the length of the element using an applied field, its motion was abrupt.

The element was first saturated along the length of the chain and allowed to relax. A flux-closure state was supported at remanence in the pad with the magnetisation of each DWT segment approximately uniform (Fig. 7.28a). Following this, a field was applied in the opposite direction and increased gradually. Changes in the magnetisation of the pad were noticeable at low field, with an increase in the size of the domains oriented close to the field direction (Fig. 7.28b). At 60 Oe, the right hand wall in the pad was stretched and a head-to-head domain wall formed at the connection point between the pad and the chain (Fig. 7.28c). A further increase in field to 70 Oe caused the right hand wall to change position from the upper edge of the pad to the lower edge, with the nucleation of a vortex and the injection of a head-to-head VDW. This came to rest at the end of the first strip (Fig. 7.28d). At 75 Oe, this wall propagated through the wide section of the trap and into the second strip (Fig. 7.28e). At a field of 80 Oe, it had moved through the third and fourth strips before stopping at the fifth (Fig. 7.28f). The head-to-head wall maintained its structure and sense of rotation throughout each transition. Finally, at an applied field of 85 Oe, the wall was driven from the element completely, leaving the magnetisation in a near-uniform state (Fig. 7.28g). A schematic diagram depicting the magnetisation changes in the injection pad as the field was increased is shown in Fig. 7.29.

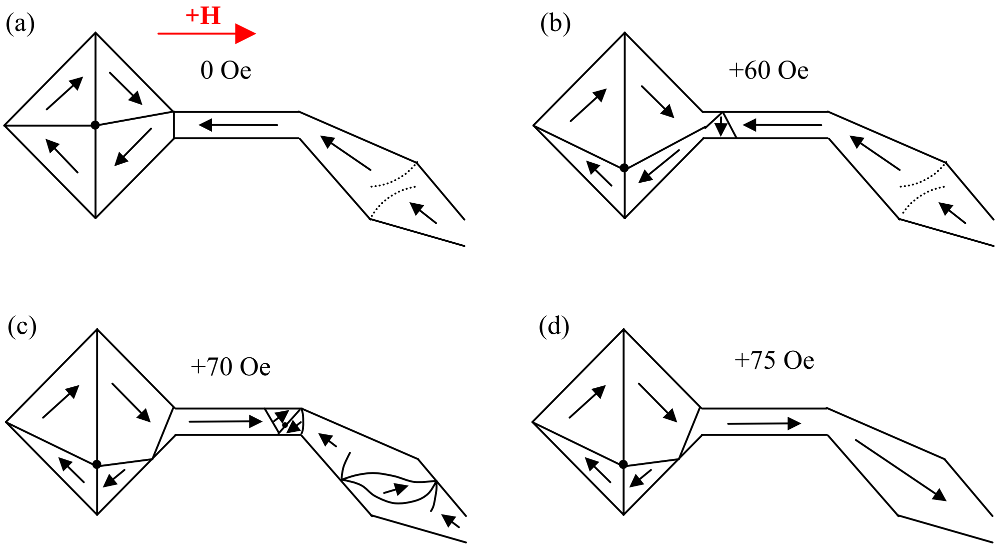

Fig. 7.29: The introduction of a VDW to the DWT chain using a diamond-shaped injection pad.

As a comparison to this, DWT1 chains were fabricated with injection pads to determine if the uniform width would allow an injected wall to move more reproducibly through the structure. Fresnel images of their behaviour can be seen in Fig. 7.30. As with the previous element, domain wall injection proceeded via movement of the right hand wall in the pad. This time, however, the magnetisation vortex rotated counter-clockwise and so the wall moved from the lower edge of the pad to the upper edge. Once formed, the VDW was trapped at the end of the first strip but managed to move completely into the narrow end section. A further increase in field then saw the head-to-head wall propagate out of the element without pinning at any of the corner regions.

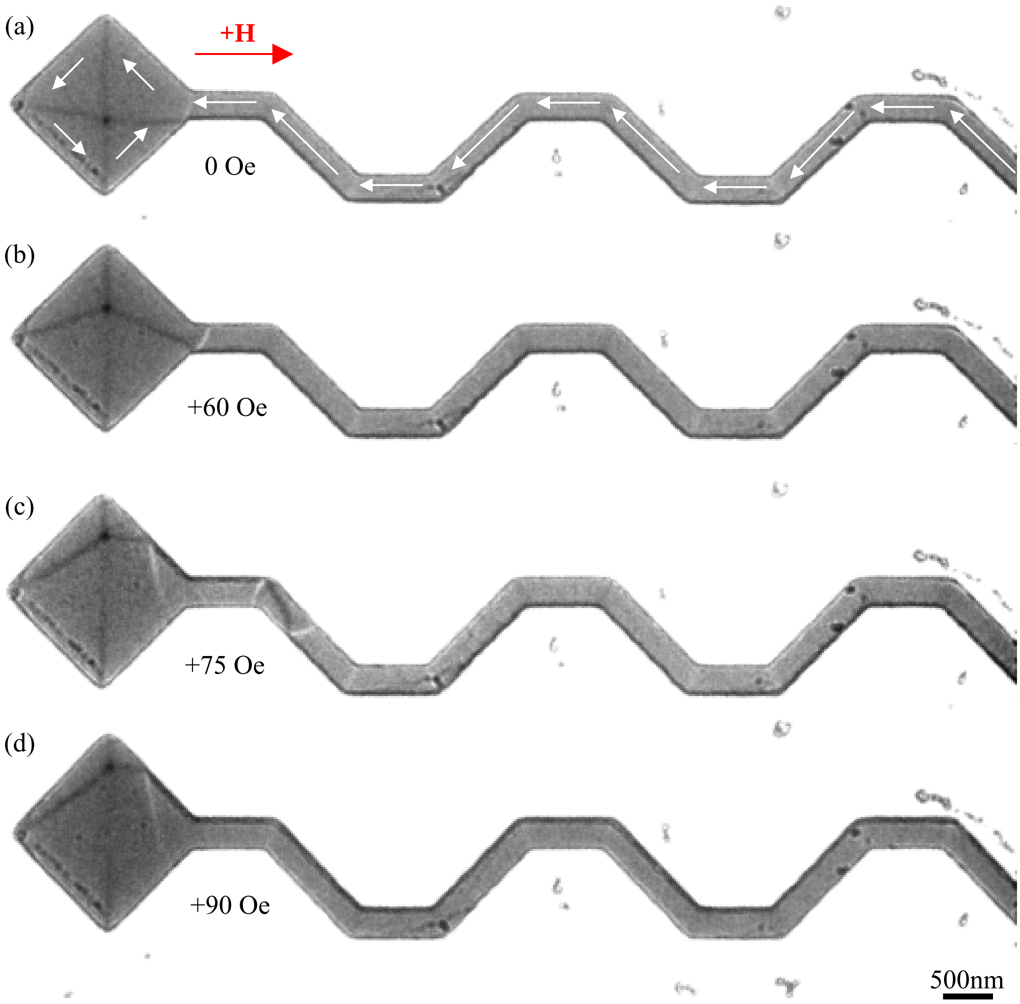

Fig. 7.30: The introduction of a VDW to a DWT1 chain. Once formed, the wall was removed from the element completely in a single field step.

7.10 Discussion of DWT chains

The last few sections of this chapter have shown that it is possible to connect several DWT3 elements together to form a chain that maximises the packing density. By using this design, head-to-head domain walls can be moved between the ends of each strip reproducibly without strong adverse magnetostatic interactions. The magnetic behaviour of each bit in the chain was the same as that of the isolated elements. However, local fields would be required to switch the individual bits if these structures were to be used in a magnetic memory device.

Attempts to inject a single head-to-head wall into the standard DWT3 chain proved unsuccessful. The inclusion of an injection pad at one end was later able to overcome this problem. However, whilst a single wall could be introduced, it was difficult to manipulate the wall between the different sections of the structure. This behaviour is a result of the wide DWT3 end regions. Although they provide resistance to the domain wall motion during switching, the field required to drive the wall past each strip gives it sufficient energy to bypass other traps in the element. As a result, the VDW ‘jumps’ between the different sections in a non-reproducible manner.

On the other hand, the DWT1 geometry allowed the VDW to move uninhibited through the structure. Although the end regions of DWT1 are sufficiently narrow that the wall can pass through, they do not provide adequate resistance to the wall motion, and the wall is easily lost. Furthermore, it was shown in Fig. 7.15 that the local geometry at the corner regions of DWT1 provides additonal stability for the VDW causing it to stretch before its removal at higher fields. Given that the corners of the DWT1 chain are of the same geometry, this is a likely contribution to the wall being removed after propagating past the first end section.

In order to inject a head-to-head wall that can be reproducibly moved through a DWT chain, therefore, it will be necessary to adjust the end regions of each DWT unit. A compromise between the DWT1 and DWT3 geometries may be successful. One solution might be to keep the basic DWT3 shape, but narrow the ends slightly. On doing this, the barrier could be reduced without compromising its ability to stop the wall after propagation to the next strip. In theory, this would allow a small field to drive the VDW past the end sections without giving the wall sufficient energy to bypass the neighbouring traps. Unfortunately, time limitations have prevented the study of this geometry here.

Chapter 8

Magnetic tunnel junctions incorporating an artificial antiferromagnet in the free layer

8.1 Introduction

Néel or 'orange-peel' coupling (Fig. 8.1) is a magnetostatic interaction between ferromagnetic (FM) layers in multilayer films that occurs when the surface is rough and there is intralayer exchange coupling. Under these conditions, magnetic surface charge develops at the interfaces because the magnetisation cannot follow the surface profile. When the roughness has a conformal or correlated waviness (implying no phase, amplitude or correlation length differences in topology between the various layer surfaces) through a spacer layer of uniform thickness, the interface normals are locally opposite. With the layers magnetised in the same direction, the magnetic charges of opposite polarity in adjacent films are closer together than if the magnetisation was anti-parallel. In this situation, stray field lines connect both inter and intralayer charges. When the magnetisation is anti-parallel, none of the field lines cross the spacer layer and the field energy is larger [33]. Therefore, orange-peel coupling favours a FM alignment.

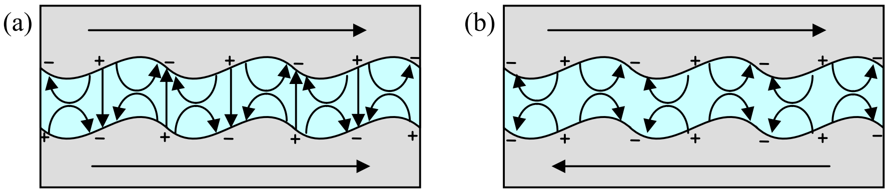

Fig. 8.1: Néel coupling in multilayer films with the layers aligned (a) parallel and (b) anti-parallel.

Due to the FM coupling between the free and pinned layers, the free layer hysteresis loop is shifted away from zero field. In the original Néel model (Fig. 8.2), this offset field is given by,

$$H_O = \frac{\pi^2 h^2 M_P}{\sqrt{2}\lambda t_F} \exp\left(\frac{-2\sqrt{2}\pi t_S}{\lambda}\right) \tag{8.1}$$

for a correlated waviness with amplitude h and wavelength λ, where t_F and t_S are the thickness of the free and spacer layers respectively, and M_P is the saturation magnetisation of the pinned layer [32]. This model has been found to give a reasonable description of the free and spacer layer thickness dependence. The offset field can be reduced by increasing the thickness of these layers, but this has disadvantages. Increasing the free layer thickness results in a higher switching field and hence greater power consumption, whereas a thicker tunnel barrier increases the resistance of the stack.

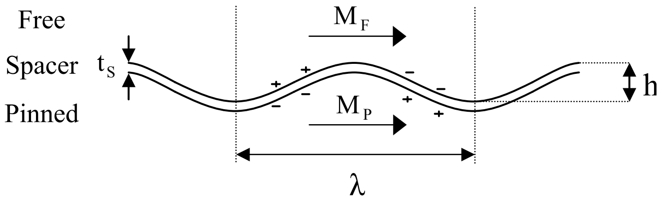

Fig. 8.2: Néel model for magnetic films of infinite thickness separated by a thin spacer layer.

A more refined analysis has been proposed [35] which takes into account the finite thickness of the ferromagnetic layers (Fig. 8.3), since charges created at the outer surfaces of the magnetic layers also interact. Again, assuming conformal waviness, the offset field is described by,

$$H_O = \frac{\pi^2 h^2 M_P}{\sqrt{2}\lambda t_F}[1-\exp(\frac{-2\sqrt{2}\pi t_F}{\lambda})][1-\exp(\frac{-2\sqrt{2}\pi t_P}{\lambda})]\exp(\frac{-2\sqrt{2}\pi t_S}{\lambda}) \qquad (8.2)$$

which includes a dependence on the pinned layer thickness, t_P. As the thickness of the pinned layer is increased, the Néel coupling and offset also increase.

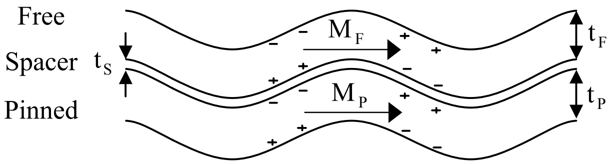

Fig. 8.3: Refined model for magnetic films of finite thickness separated by a thin spacer layer.

It has been shown in recent studies that a reduction in coupling can be realised by the addition of small amounts of oxygen in the sputtering gas as a surfactant (surface active agent) [178], by smoothing the layers during deposition [179] using an argon gas cluster ion beam (GCIB), or by pre-oxidation of the pinned layer to reduce intermixing with the tunnel barrier [180]. A different technique utilising an AAF in the pinned layer has also proven to alleviate the interlayer coupling [181]. These consist of two FM layers separated by an extremely thin non-magnetic spacer, usually ruthenium. The bottom layer is in contact with a natural antiferromagnet and there is strong AF Ruderman-Kittel-Kasuya-Yosida (RKKY) coupling across the ruthenium, provided the spacer is of the correct thickness. By including an AAF, magnetic charges of opposite polarity can be brought closely together at the interface between the pinned and spacer layers to partly compensate each other. Although this solution is effective, the AAF layer closer to the barrier has to be far thinner than the bottom layer. A further advantage of a pinned layer AAF is its increase in rigidity relative to a single layer film of the same material and thickness. The rigidity amplification can be expressed by the Q-factor,

$$H_C(\mathrm{AAF}) = QH_C(\mathrm{SL}) \tag{8.3}$$

where

$$Q = \frac{M_1 t_1 + M_2 t_2}{\left|M_1 t_1 - M_2 t_2\right|} \tag{8.4}$$

$H_C(\mathrm{AAF})$ and $H_C(\mathrm{SL})$ are the AAF and single layer coercivities respectively and M and t are the magnetisation and thickness of the two AAF layers [182]. Therefore, for identical materials, maximum rigidity is achieved when $t_1 = t_2$. However, in order to effectively compensate the charge and reduce the Néel coupling, robustness in high magnetic field is compromised. This is undesirable, as the pinned layer orientation should not vary with applied field during normal device operation.

8.2 The MTJ samples

In this study, an alternative method to reducing the offset field was investigated. Previous work using a vibrating sample magnetometer (VSM) has shown that by including an AAF in the free layer (Fig. 8.4) of the stack instead of the pinned layer, it is possible to reduce the offset field by up to 36% without affecting the pinned layer rigidity [183]. Taking into account the AAF, the offset field can be expressed as,

$$\begin{aligned} H_O = {} & \frac{\pi^2 h^2 M_P}{\sqrt{2}\lambda(t_{F1} - t_{F2})}[1 - \exp(\frac{-2\sqrt{2}\pi t_{F1}}{\lambda})][1 - \exp(\frac{-2\sqrt{2}\pi t_P}{\lambda})]\exp(\frac{-2\sqrt{2}\pi t_{AlO}}{\lambda}) \\ & -[1 - \exp(\frac{-2\sqrt{2}\pi t_{F2}}{\lambda})][1 - \exp(\frac{-2\sqrt{2}\pi t_P}{\lambda})]\exp(\frac{-2\sqrt{2}\pi t_{AlO+F1+Ru}}{\lambda}) \end{aligned} \tag{8.5}$$

where t_{F1} and t_{F2} are the thicknesses of the lower and upper layers of the free layer AAF and t_{AlO} and t_{Ru}, the thicknesses of the tunnel barrier and AAF spacer layer respectively. The first term of this equation describes the interactions between F1 and the pinned layer whilst the second term deals with the F2-pinned layer interactions. Also, as the third exponential in each term includes a dependence on the thickness of material separating the free and pinned layers, the second term must consider the Al_2O_3, F1 and Ru layers and not just the Al_2O_3.

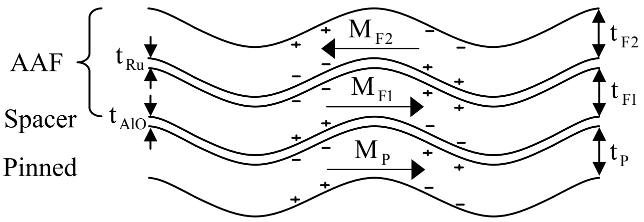

Fig. 8.4: Coupling model for MTJ with free layer AAF.

There are two important consequences of this equation on the behaviour of the stack. Firstly, the negative sign in the second term, which describes the F2-pinned layer interactions, explains the reduction in offset field when compared to equation 8.2. Secondly, the $1/(t_{F1} - t_{F2})$ factor affects the sign of the offset when the order of the AAF layers are changed. In this work, the net magnetic moment of the free layer was kept constant for comparison to a stack with single free layer. Three different MTJ films (Fig. 8.5) were deposited onto Si_3N_4 membrane substrates for TEM analysis. This differs from the VSM experiments where thermally oxidised Si was the chosen substrate. The first sample, labelled MTJ1, was a standard junction and the second and third samples, MTJ2 and MTJ3, contained an AAF in the free layer,

MTJ1: 3.5Ta/2NiFe/6IrMn/2.5CoFe/0.9AlO/5NiFe/3.5Ta
MTJ2: 3.5Ta/2NiFe/6IrMn/2.5CoFe/0.9AlO/3NiFe/0.8Ru/8NiFe/3.5Ta
MTJ3: 3.5Ta/2NiFe/6IrMn/2.5CoFe/0.9AlO/8NiFe/0.8Ru/3NiFe/3.5Ta

where the layer thicknesses are in nanometres. During growth, the field used to induce an easy axis aligned all FM layers parallel to one another. On removal of this field, F1 remained magnetised in this direction as a result of the orange-peel coupling. In the case of the basic junction (MTJ1), the single free layer was aligned parallel to the exchange bias layer. With two layers in the free layer (MTJ2 and MTJ3), F2 coupled anti-parallel to F1 through the Ruthenium. Therefore, the net direction of free layer magnetisation depended on the relative thickness of the two AAF layers. With the thick layer on the bottom (MTJ3), the net direction of free layer magnetisation was the same as that of the basic junction. As a result, the free layer offset was in the same direction for both films. With the layers interchanged (MTJ2), however, the net moment and offset were in the opposite direction.

Since the physical structure of a material greatly influences the magnetic properties, the MTJs were grown on top of a buffer system consisting of a Ta seed and magnetically dead (non-FM) NiFe layer. This system was used to encourage (111) texturing, which has been found to minimise the in-plane magnetocrystalline anisotropy [184]. In addition, Ta capping layers were deposited to help protect the magnetic films against atmospheric gases [185].

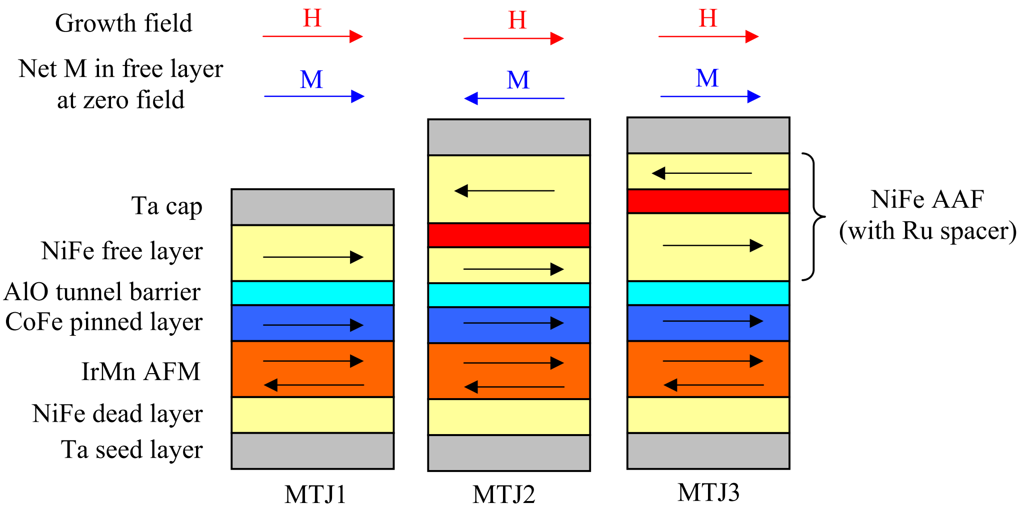

Fig. 8.5: Layer structure of the different MTJ samples.

8.3 Magnetic characterisation

To determine the magnetic behaviour of each MTJ, the samples were imaged in the Fresnel and differential phase contrast (DPC) modes of Lorentz microscopy. They were positioned in the specimen rod and rotated until their direction of magnetisation (at zero field) was aligned with the axis of applied field. A maximum in-plane field of ±50 Oe was applied in-situ to observe switching of the free layer. The fields required to switch the pinned layer and decouple the AAF have previously been determined as 700 and ~600 Oe respectively [183]. Therefore, throughout the free layer reversals, it was assumed that the pinned layer magnetisation was unaffected and that the constituent layers of the AAF were always aligned anti-parallel. In order to properly induce exchange bias, it was necessary to anneal each stack to 300°C in an applied field of 2000 Oe. This heating and field-cooling cycle was performed in a specially designed TEM specimen holder. The samples were then imaged as before to determine the effect of annealing on the magnetisation reversal. At each setting, a 2160 lines/mm cross grating was used for magnification calibration purposes. The images of each reversal are shown, complete with coloured arrows to indicate the direction of applied field (red) and magnetisation (blue).

As Fresnel imaging can be applied easily at low magnification, the first image sequence covered reversal of the film over the whole of the $100 \times 100\,\mu\text{m}^2$ membrane to provide a general understanding of the switching mechanism and magnetic structure. Following this, DPC was performed with a second specimen of the same type but at a higher magnification to reveal finer details of the reversal process. Slight differences in morphology can occur between different samples of the same type during deposition, so examination of multiple samples provides a better representation of how each of the stacks reverse. From these images, a measure of the prominent wavelength and dispersion angle of the magnetisation ripple was obtained to provide a more detailed comparison of the dispersion spectra.

From the image sequences, experimental values of the offset (H_O) and coercivity (H_C) were deduced in the following way. For each set of images, the switching field was noted for the increasing and decreasing field sections of the magnetisation cycle. Denoting these fields by H^+ and H^- respectively (Fig. 8.6), H_O and H_C were calculated using,

$$\text{H}_\text{O} = \frac{(\text{H}^+ + \text{H}^-)}{2} \tag{8.6}$$

$$\text{H}_\text{C} = \frac{(\text{H}^+ - \text{H}^-)}{2} \tag{8.7}$$

When the magnetisation reversed by domain wall nucleation and motion, the coercive field was assumed to be that at which the number of domain walls over the entire field of view was greatest [186]. On the other hand, when the magnetisation reversed by rotation, this field was taken when the magnetisation vector was oriented perpendicular to the axis of applied field.

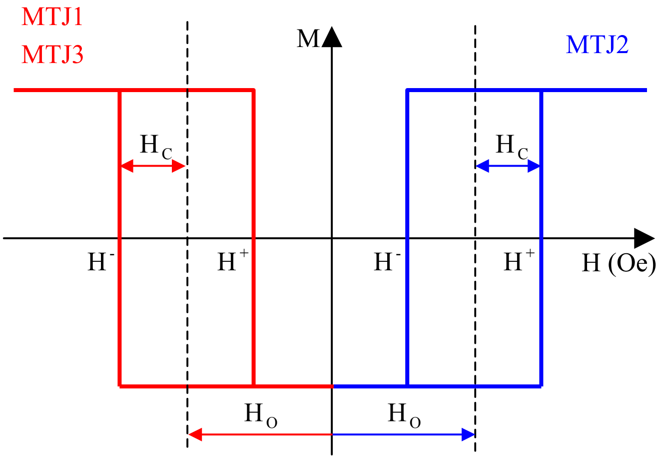

Fig. 8.6: Minor hysteresis loops for the different MTJs defining H_O and H_C.

8.3.1 MTJ1

Beginning with the Fresnel images of pre-annealed MTJ1, it can be seen that magnetisation ripple was present across the sample at zero field (Fig. 8.7a). On applying a negative field of -23 Oe (Fig. 8.7b), the ripple intensified together with modest rotation of the magnetisation. Following this intensification, domains of reverse magnetisation were observed at -25 Oe (Fig. 8.7c). By increasing the magnitude of applied field, the reversal proceeded with the formation of a number of long domain walls oriented at 33° clockwise (CW) to the field direction (Fig. 8.7d). As the field increased further (Fig. 8.7e), the reverse domains increased in size as domain wall annihilation took place until, at a field of -40 Oe (Fig. 8.7f), several of the walls had collapsed into 360° domain walls. These wall structures required larger fields to remove and will be described later in the chapter. On the return path, the ripple contrast intensified on going from an applied field of -40 Oe (Fig. 8.7g) to -25 Oe (Fig. 8.7h) followed by domain wall formation as before (Fig. 8.7i). This time, however, the walls were oriented at 38° counter-clockwise (CCW) to the applied field (Fig. 8.7j) direction. As the field was reduced to -12 Oe (Fig. 8.7k), a complex domain structure was observed in the previously unreversed regions, with the walls having no obvious preferred orientation. At zero field (Fig. 8.7l), the magnetisation had returned to its initial configuration, but with the presence of 360° domain walls. These 360° wall loops appeared at different locations from those formed during the initial reversal. The images indicate a free layer easy-axis hysteresis loop centred around -21 Oe with a coercivity of 7 Oe.

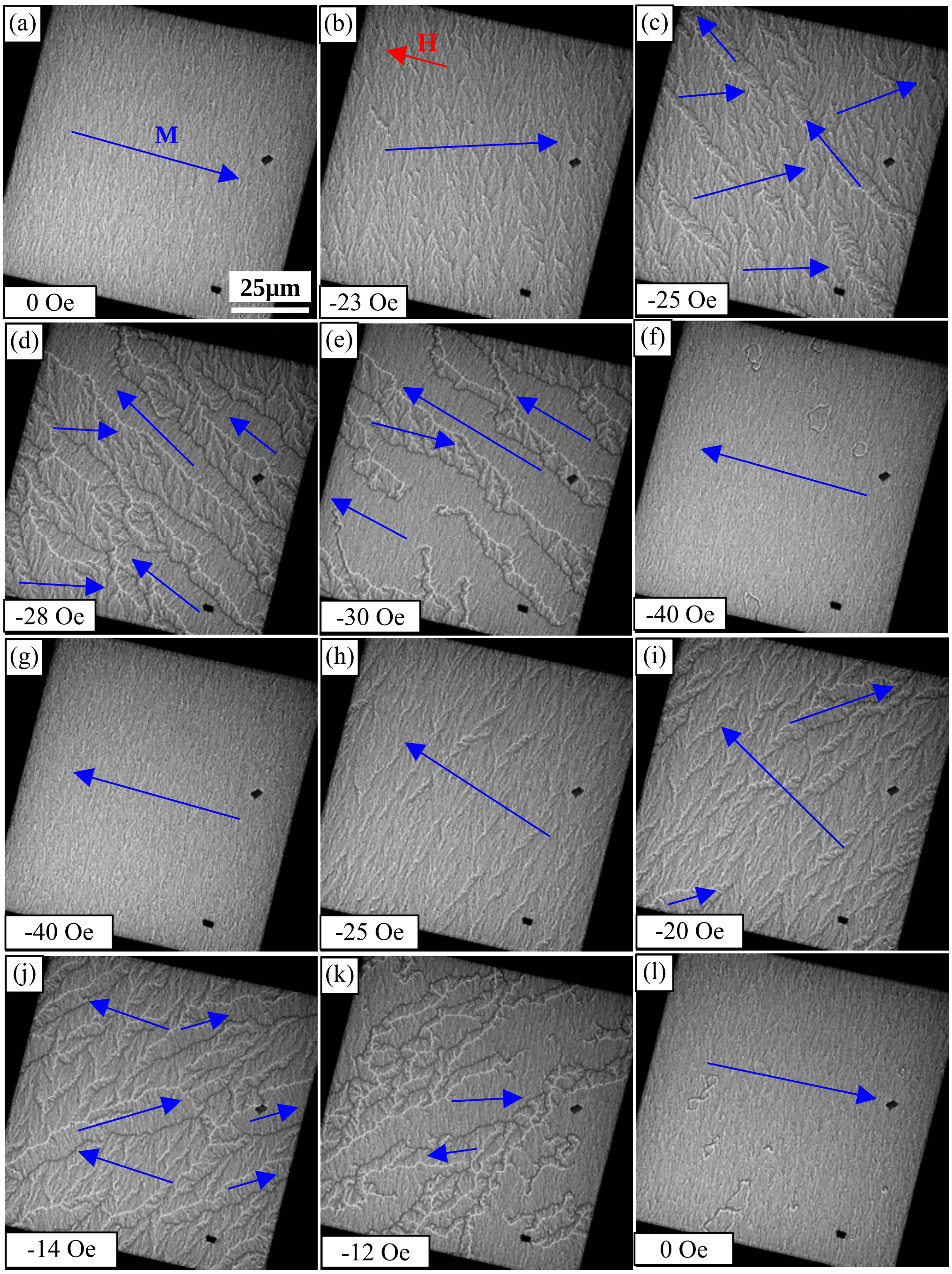

Fig. 8.7: Fresnel image sequence of the MTJ1 free layer before annealing.

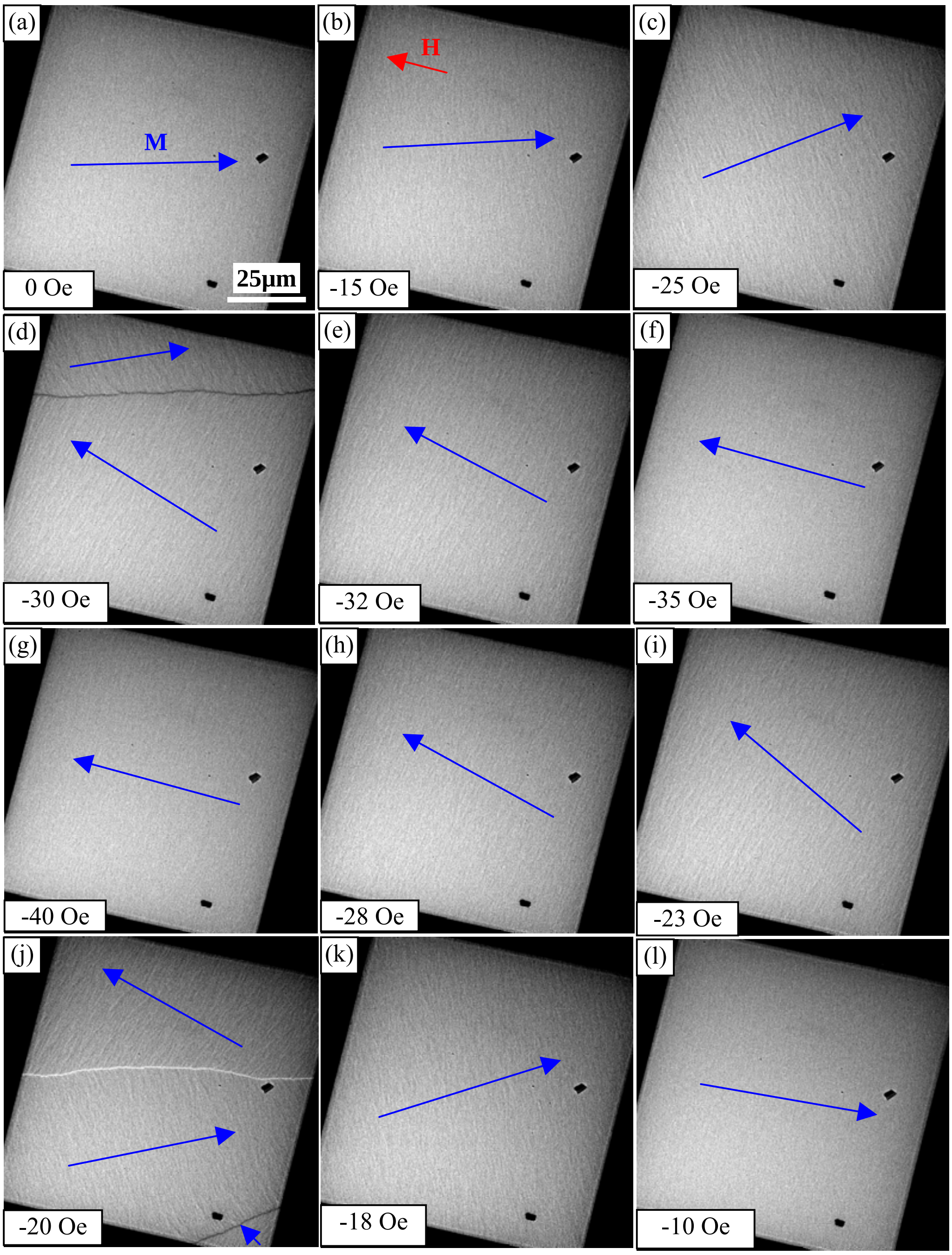

Fig. 8.8: Fresnel image sequence of the MTJ1 free layer after annealing.

After annealing MTJ1 in an applied field along the easy axis, the specimen was imaged under identical conditions to before. At zero field (Fig. 8.8a), modest magnetisation ripple was observed. The reduction in ripple contrast was the first noticeable change in the sample. By changing the field to -15 Oe (Fig. 8.8b) and then -25 Oe (Fig. 8.8c), the intensity of ripple increased as before, albeit on a much finer scale. The direction of magnetisation also rotated slightly. At an applied field of -30 Oe (Fig. 8.8d), reversal of the magnetisation occurred suddenly, with the nucleation and movement of a single, relatively straight domain wall oriented at 14° CCW to the field direction. At -32 Oe the wall had progressed through the entire field of view (Fig. 8.8e), before the magnetisation rotated to align with the field. At -35 Oe (Fig. 8.8f), the magnetisation was completely reversed, without the formation of 360° walls. By reducing the field from -40 Oe (Fig. 8.8g) to -28 Oe (Fig. 8.8h), the ripple intensified slightly. At -23 Oe, the magnetisation vector was seen to rotate (Fig. 8.8i), before two straight domain walls appeared which were aligned in similar directions to the wall on the outward path (Fig. 8.8j). The reverse domain, defined by these walls, then grew in size at the expense of the neighbouring domains until near uniform magnetisation was observed at -18 Oe (Fig. 8.8k). As before, further reduction of the field allowed the magnetisation to rotate and align itself with the easy axis (Fig. 8.8l). From these images, H_O and H_C are calculated to be -25 Oe and 5 Oe respectively.

DPC images of a second MTJ1 sample before annealing are shown in Fig. 8.9a-j. At each field value, a pair of images map the induction in orthogonal directions as indicated by the white arrows.

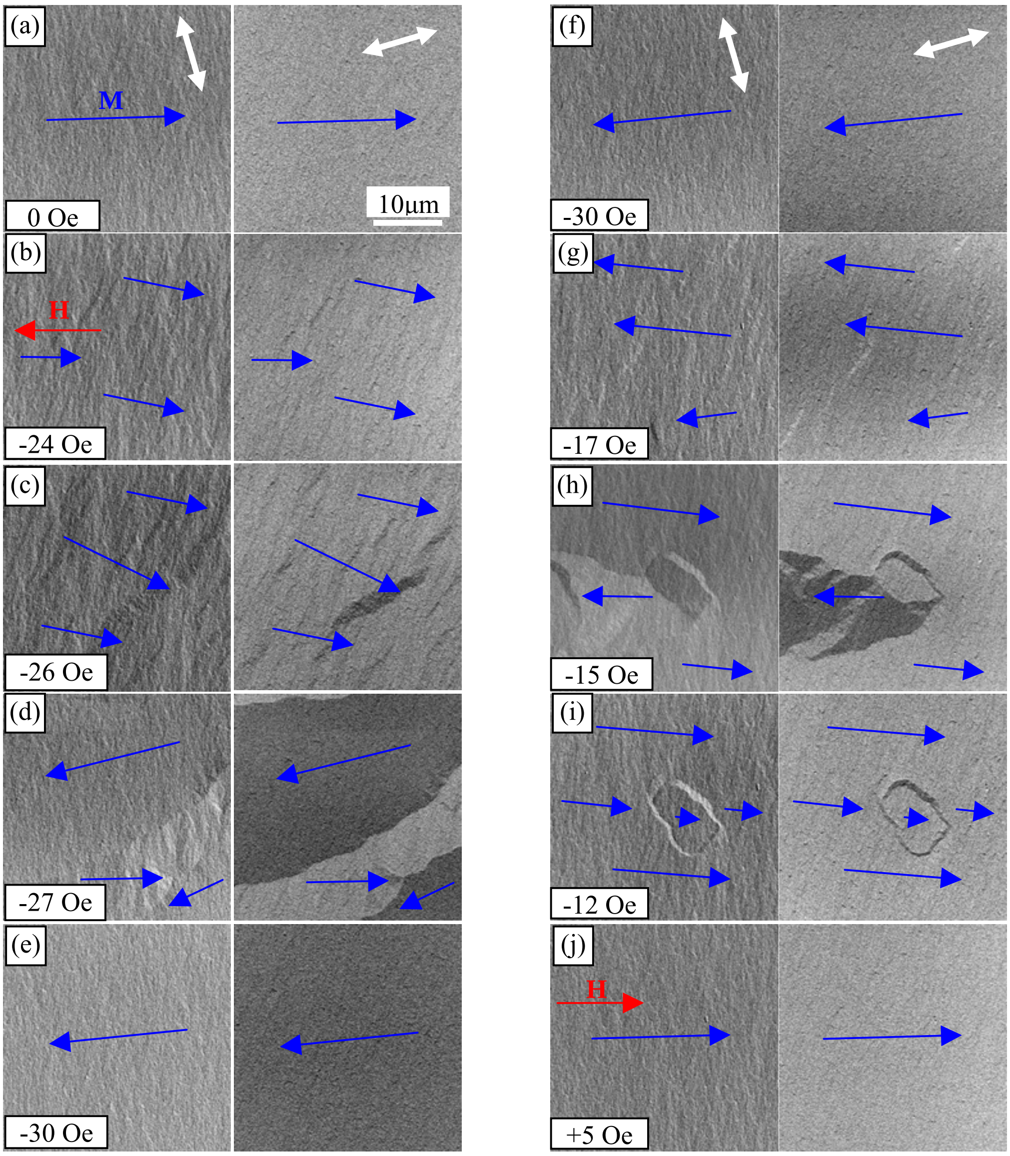

Fig. 8.9: DPC image sequence of the MTJ1 free layer before annealing. The white arrows indicate the direction of sensitivity of the mapped induction components.

The reversal of this specimen proceeded in a similar manner to the previous samples. Of note from these images is the 360° domain wall loop captured in Fig. 8.9i, where, as the applied field was decreased on the reverse path of the magnetising cycle, the wall was removed (Fig. 8.9j). These images suggest H_O and H_C to be -21 and 6 Oe respectively.

After heat treatment, the sample was imaged in the DPC mode under identical conditions. The corresponding images can be seen in Fig. 8.10a-j, but provide little additional information on the reversal mechanism. There is, however, local domain wall pinning visible in Fig. 8.10h which may be caused by excessive roughness from the underlying layers. The corresponding hysteresis loop is centred at -27 Oe with a coercivity of 3 Oe.

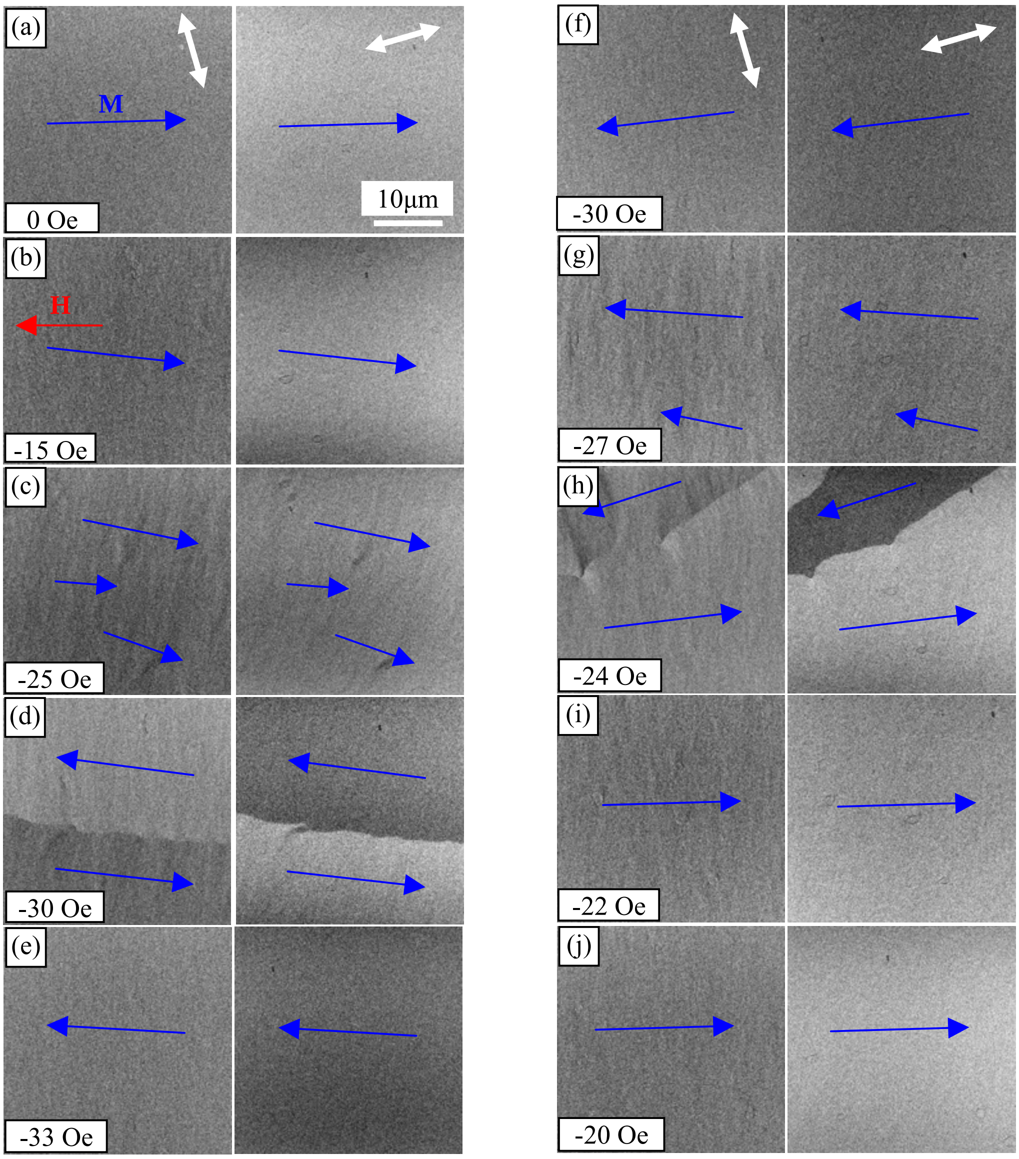

Fig. 8.10: DPC image sequence of the MTJ1 free layer after annealing.

8.3.2 MTJ2

The above experiment was repeated with MTJ2. The pre-annealed images reveal a very different dispersion spectrum to that of MTJ1.

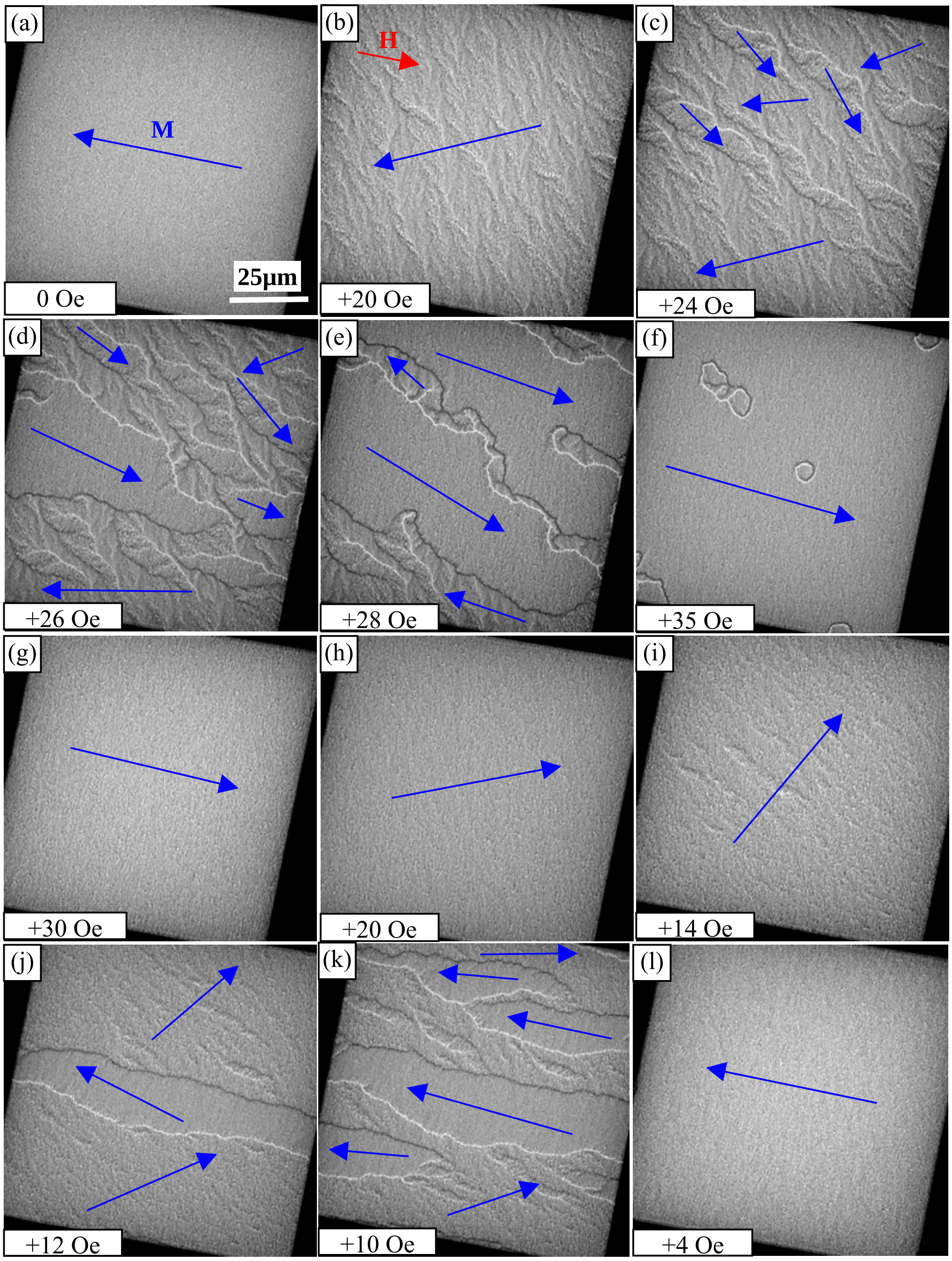

Fig. 8.11: Fresnel image sequence of the MTJ2 free layer before annealing.

At zero field (Fig. 8.11a), the magnetisation ripple was barely visible, but under a positive field of +20 Oe, the nature of the ripple spectrum became quite different (Fig. 8.11b). The change in sign of applied field with respect to the previous stack reflects the difference in net direction of the AAF magnetisation as discussed earlier. At a field of +24 Oe (Fig.

8.11c), domain walls were seen to develop. These walls were oriented at 10° CW to the direction of applied field. Within each domain, the direction of magnetisation was not as easily identified as with MTJ1 due to the reduction in ripple contrast. When the field was increased further, the reversed domains continued to grow in size until at +35 Oe (Fig. 8.11f), the reversal was almost complete. Several 360° domain walls were formed, some of which linked together to form a chain structure.

On the reverse path, similar behaviour was observed. This time, however, the domain walls appeared in the field of view parallel to the direction of applied field (Figs. 8.11j-k). As the field was reduced to +4 Oe, the magnetisation was oriented in the initial direction without the presence of any 360° walls (Fig. 8.11l). The hysteresis loop is centred at +18 Oe with a coercivity of 8 Oe.

The images in Fig. 8.12 were taken directly after the annealing cycle on MTJ2. At remanence, the ripple contrast was very low and the magnetisation uniform (Fig. 8.12a). As the field was increased, so did the dispersion. At +18 Oe, the magnetisation rotated by 40° (Fig. 8.12b) before domain walls began to appear. A single reverse domain (Fig. 8.12c) increased in size (Fig. 8.12d), gradually covering the whole area of the membrane (Fig. 8.12e) apart from regions where long 360° wall segments formed (Fig. 8.12f). These walls were seen to extend over distances greater than 100μm and could only be removed at larger fields. On the reverse path, ripple contrast increased as the field was reduced from +30 Oe (Fig. 8.12g) to +20 Oe (Fig. 8.12h). At +18 Oe (Fig. 8.12i) the ripple was oriented in different directions, forming low angle domain walls. This unusual ‘swirling’ configuration was then destroyed as two ~180° walls swept through the sample (Fig. 8.12j). Further reduction of the field saw the formation of a near uniform configuration, but with the presence of the 360° wall sections around the edges of the ‘window’ (Fig. 8.12k). The magnetisation was oriented back in the original direction at +4 Oe (Fig. 8.12l). After annealing, therefore, the MTJ2 hysteresis loop exhibited an offset of +18 Oe and coercivity of 2 Oe.

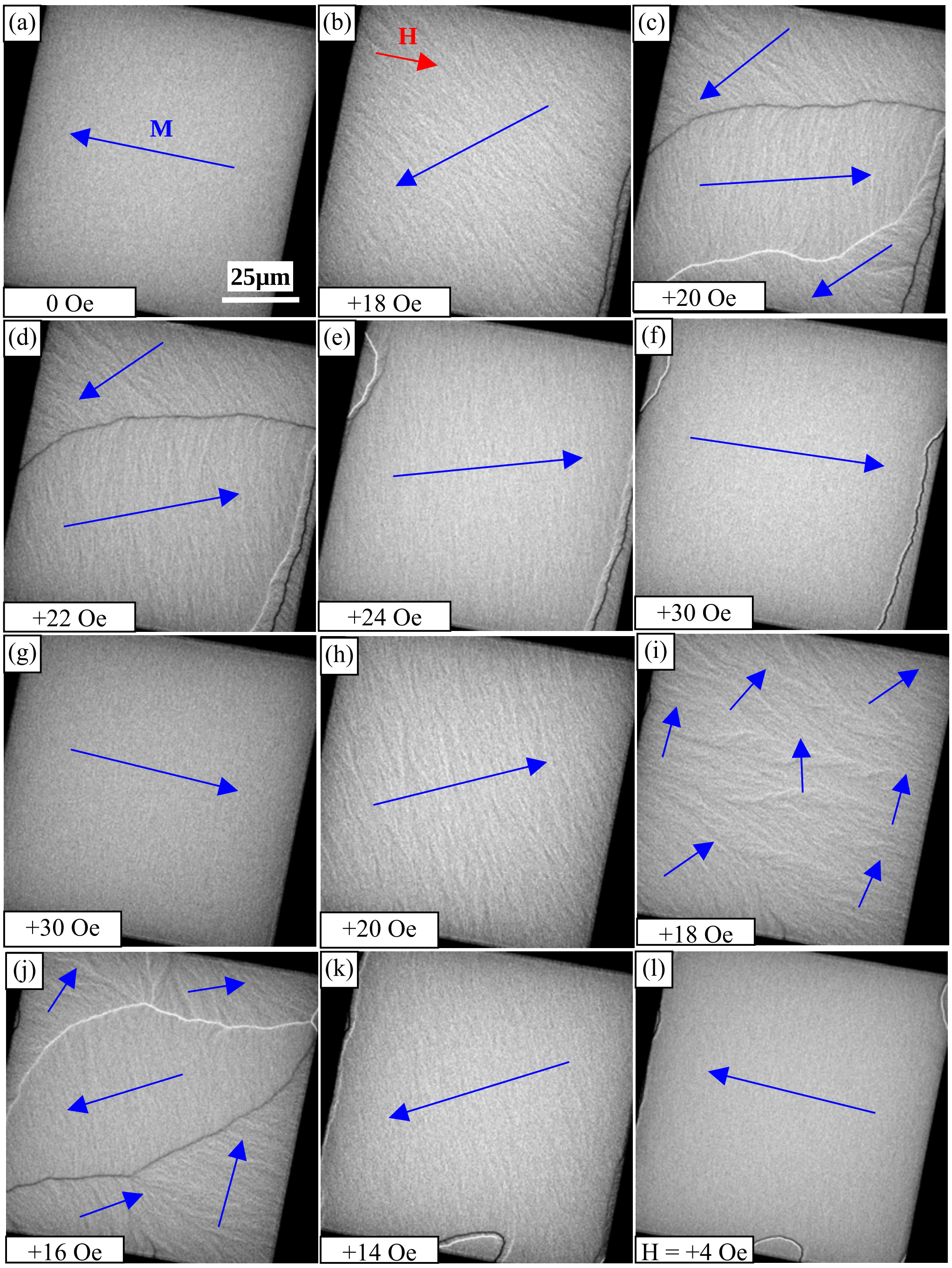

Fig. 8.12: Fresnel image sequence of the MTJ2 free layer after annealing.

Fig. 8.13a-j shows DPC images of another MTJ2 sample. Once again, compared with MTJ1 before annealing, the high frequency ripple contrast was very low at zero field. When the field approached the critical values in the forward and reverse directions, ripple contrast of a lower spatial frequency increased, together with a slight rotation of the magnetisation vector. As expected, this was followed by the formation of a relatively complex domain structure which collapsed into a number of 360° domain walls. H_O and H_C are +16 and 8 Oe respectively.

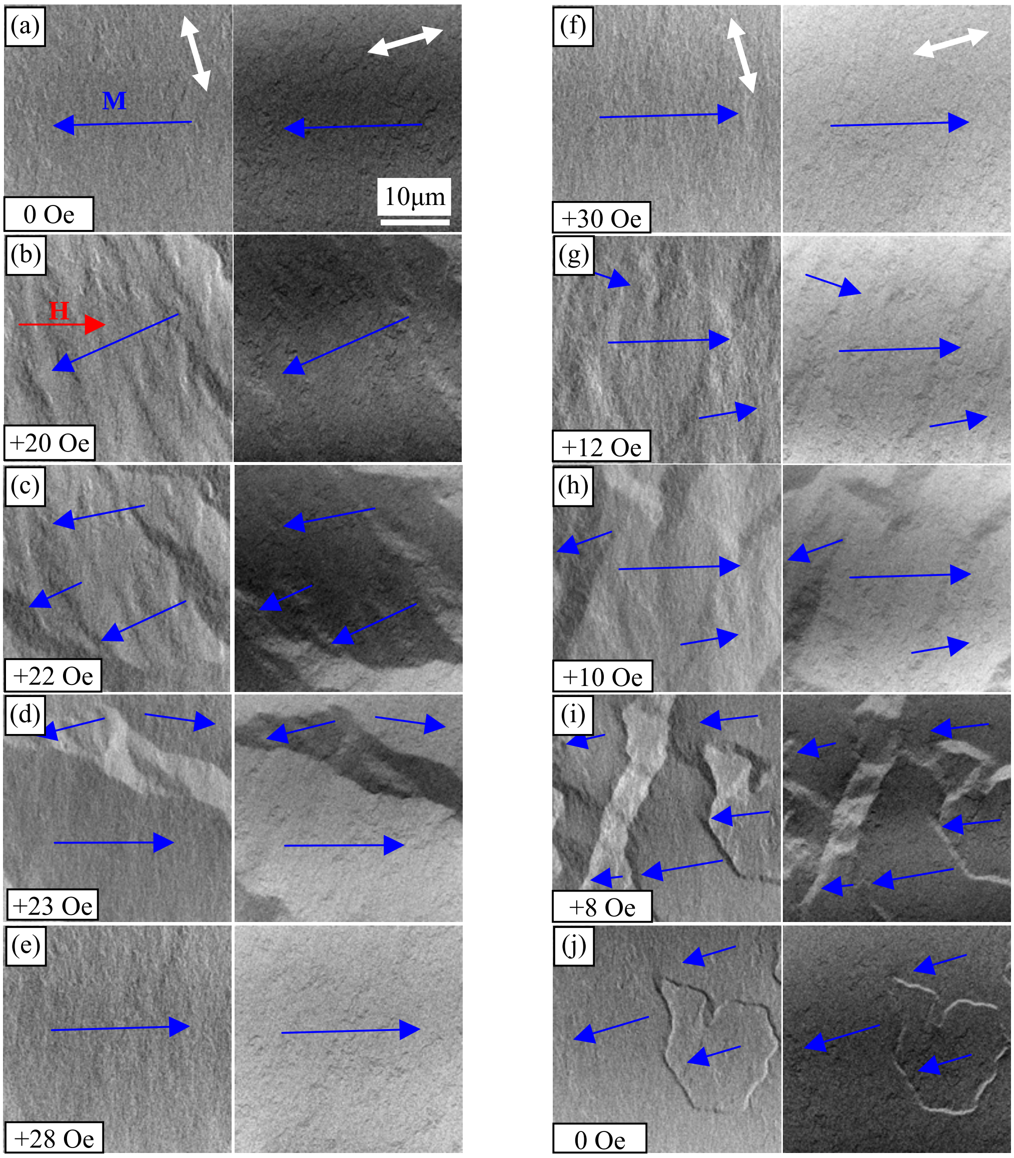

Fig. 8.13: DPC image sequence of the MTJ2 free layer before annealing.

After heat treatment (Fig. 8.14a-j) the local deviation of magnetisation from the net direction did not appear to have been dramatically varied, again, since the initial degree of ripple was noticeably low. The reversal process was effected by the nucleation and movement of a small number of domain walls which switched the film rather suddenly. These walls on the forward and reverse paths were oriented at 28° CW and 43° CCW to the applied field direction. As can be seen in Fig. 8.14i-j, a 360° wall was formed after the magnetisation reversed back to its original direction. From these images, H_O and H_C are estimated to be +18 and 1 Oe respectively.

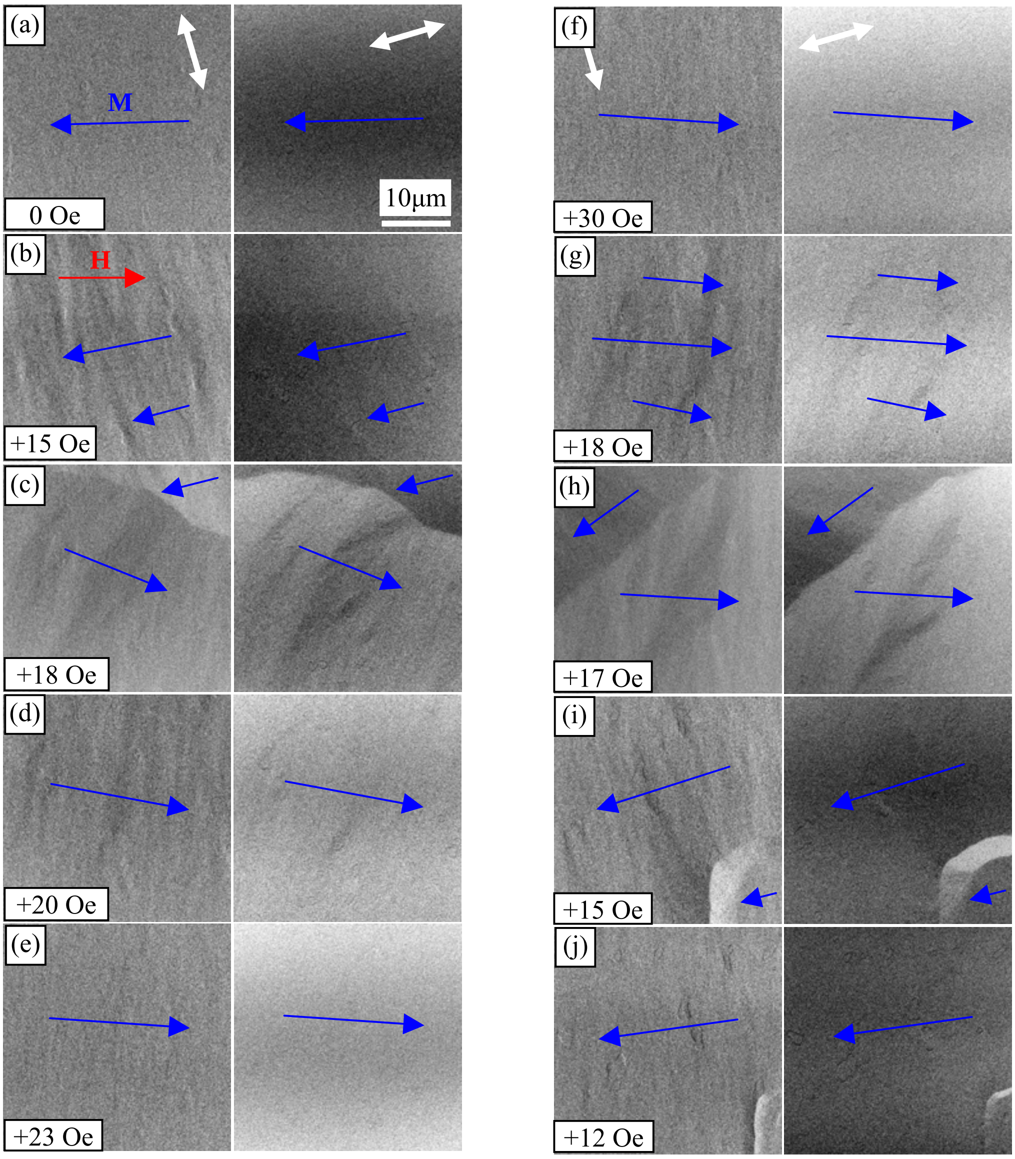

Fig. 8.14: DPC image sequence of the MTJ2 free layer after annealing.

8.3.3 MTJ3

To complete this set of experiments, MTJ3 was studied before and after the annealing cycle. The images reveal a similar behaviour to the first stack.

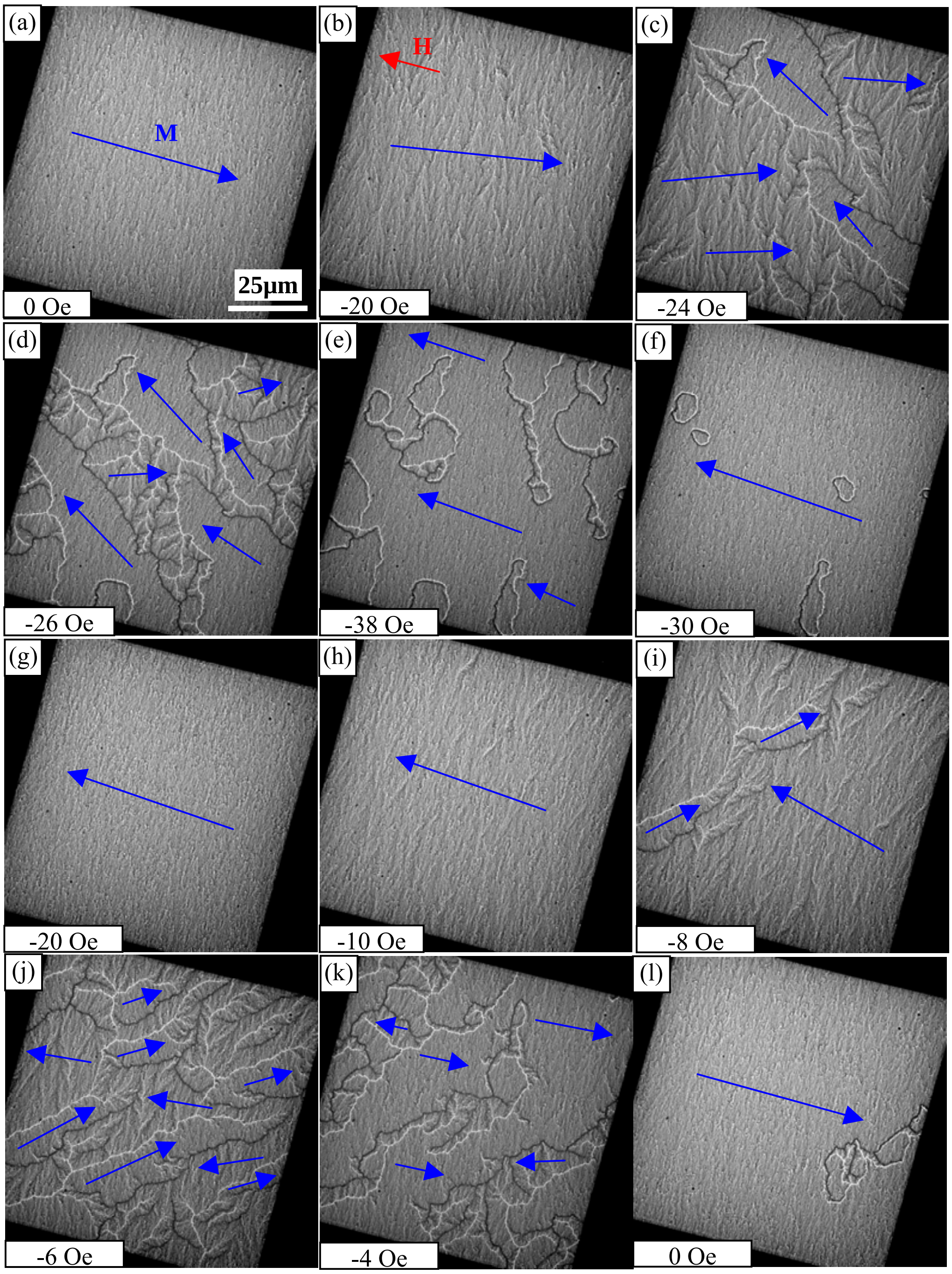

Fig. 8.15: Fresnel image sequence of the MTJ3 free layer before annealing.

Prior to heating (Fig. 8.15i-j), a relatively large deviation of the local magnetisation from the mean direction resulted in significant ripple contrast at zero field (Fig. 8.15a). On applying a negative field, the ripple was seen to intensify at –20 Oe (Fig. 8.15b) before the formation of domains of reverse magnetisation (Fig. 8.15c). At a field of –26 Oe (Fig. 8.15d) the reversal was half complete with the formation of a complicated domain configuration. A further increase in field strength saw the complex structure split up into a number of 360° domain wall chains (Fig. 8.15e), many of which annihilated at –30 Oe (Fig. 8.15f), leaving isolated walls that were persistent up to higher fields. The backward path proceeded in much the same way. Ripple intensification occurred on going from –20 Oe (Fig. 8.15g) to –10 Oe (Fig. 8.15h), followed by domains at –8 Oe (Fig. 8.15i). The complex domain configuration (Fig. 8.15j) then started to collapse into 360° walls (Fig. 8.15k) at –4 Oe, with some chains remaining at zero field (Fig. 8.15l). The images suggest a hysteresis loop centred at –16 Oe with a coercivity of 10 Oe.

After annealing the sample (Fig. 8.16i-j) the dispersion spectrum, in agreement with the results from MTJ1, changed dramatically.

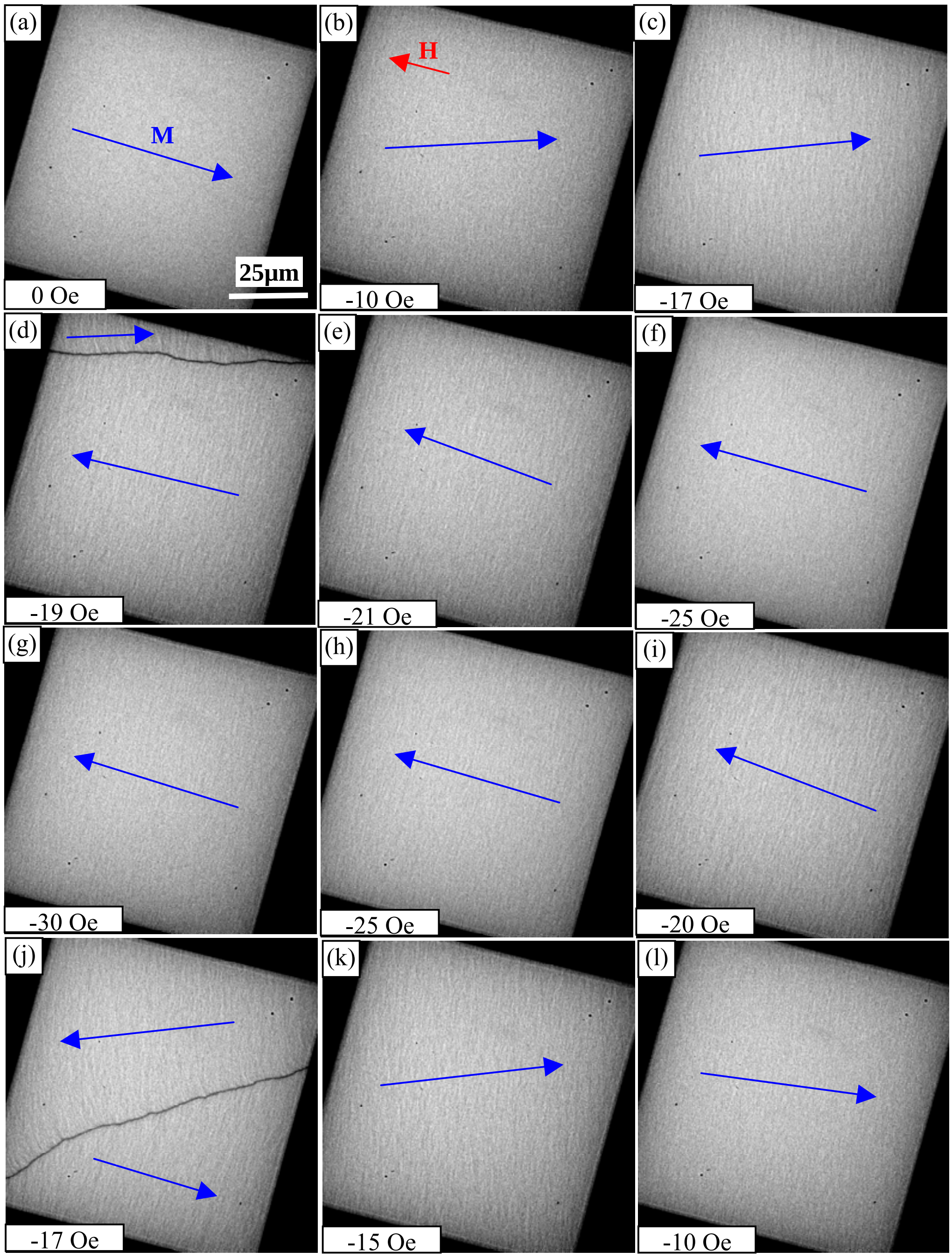

Fig. 8.16: Fresnel image sequence of the MTJ3 free layer after annealing.

At zero field (Fig. 8.16a), a very fine ripple was observed which intensified at –10 Oe (Fig. 8.16b), and even further at –17 Oe (Fig. 8.16c). A further increase in field to –19 Oe (Fig. 8.16d) resulted in a sudden reversal via the movement of a single and relatively straight domain wall, oriented at 12° CCW to the field. After passing through the film, the magnetisation appeared to be completely reversed at –21 Oe (Fig. 8.16e) without the formation of any 360° walls. Further increase of field caused a reduction in the ripple contrast (Fig. 8.16f). By reducing the applied field after saturation, almost identical behaviour occurred. Ripple intensification took place on decreasing the magnitude of field from –30 Oe (Fig. 8.16g) to –25 Oe (Fig. 8.16h) and –20 Oe (Fig. 8.16i), followed by the nucleation and movement of a single domain wall over the field of view (Fig. 8.16j). This domain wall was oriented at 35° CCW to the field direction. As in the forward path, the reversal took place over a very small field range. At –10 Oe the magnetisation was oriented in the original direction, again with the absence of 360° domain walls. The hysteresis loop for this free layer is centred at –18 Oe with a coercivity of 1 Oe.

From the DPC images (Fig. 8.17a-j) of MTJ3, the ripple contrast was very prominent prior to annealing. As shown in this sequence, the reversal proceeded with an increase in ripple coarseness before domain walls swept through the film. These walls were oriented at 23° CW and CCW to the field direction in the forward and reverse paths of the hysteresis loop. Very little rotation was evident in this particular experiment. The configuration during and after reversal were also surprisingly featureless. In the previous MTJ3 specimen, a highly irregular domain pattern collapsed to form 360° wall loops and chains. In this sample, no complicated structures were observed, although these images did only cover a small region of the film. The offset and coercivity are calculated to be –16 and 10 Oe respectively.

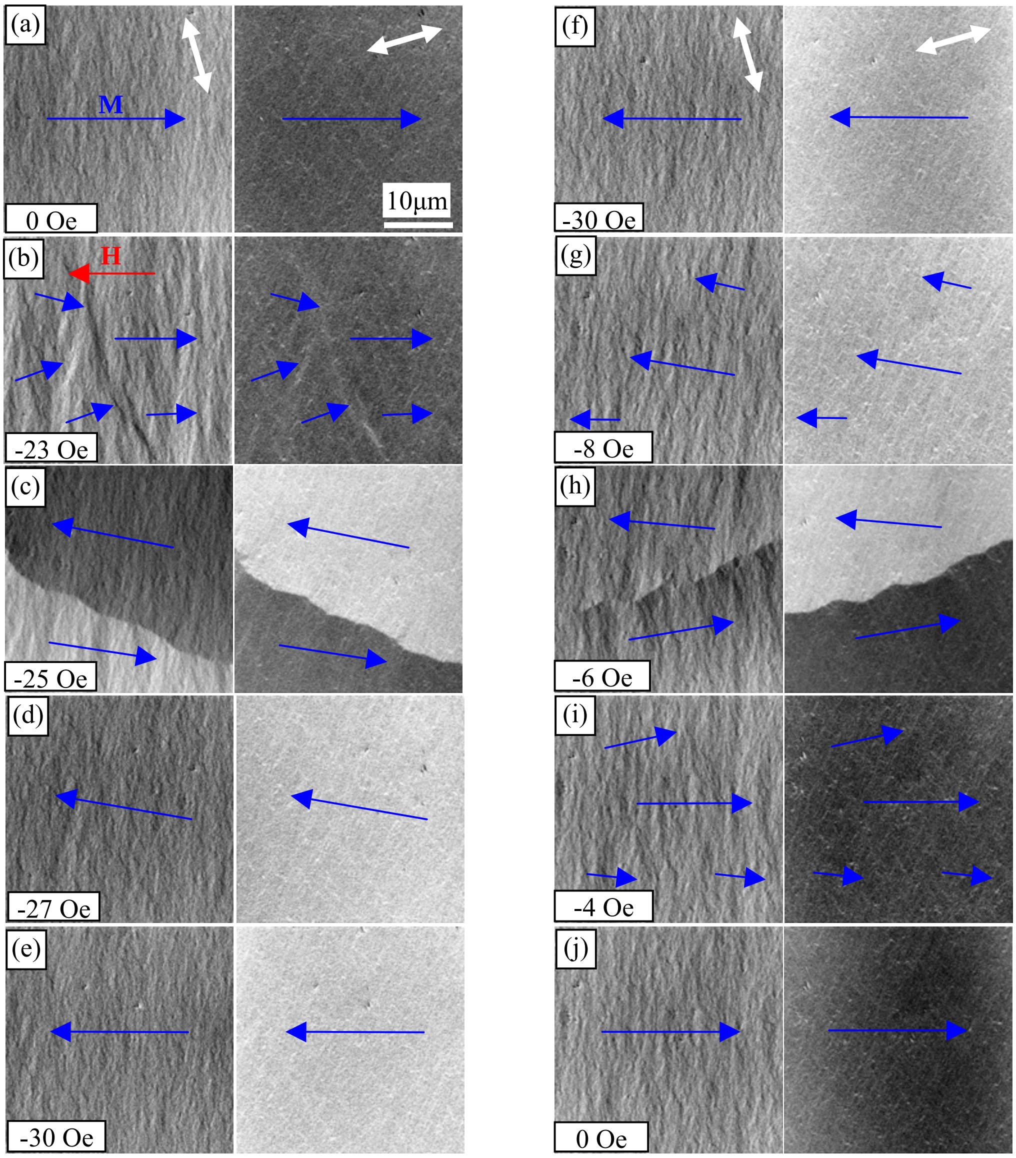

Fig. 8.17: DPC image sequence of the MTJ3 free layer before annealing.

The reversal process did not change very much on heating the sample as can be seen from the images in Fig. 8.18a-j. From these images, the only obvious differences were the reduction in ripple contrast as expected, and a change in domain wall orientation on the reverse path. During the outward path, the wall was oriented at 23° CW to the field direction as before, but on the return was parallel to the field. There was also a moderate degree of contamination present on the surface of this specimen, attributed to damage by the electron probe. As this was actually the first specimen studied, additional time spent trying to optimise the DPC imaging conditions meant that the film was subjected to more electrons than any of the other samples. This had no effect on the free layer reversal, however. The images suggest a hysteresis loop centred at –19 Oe with a coercivity of 2 Oe.

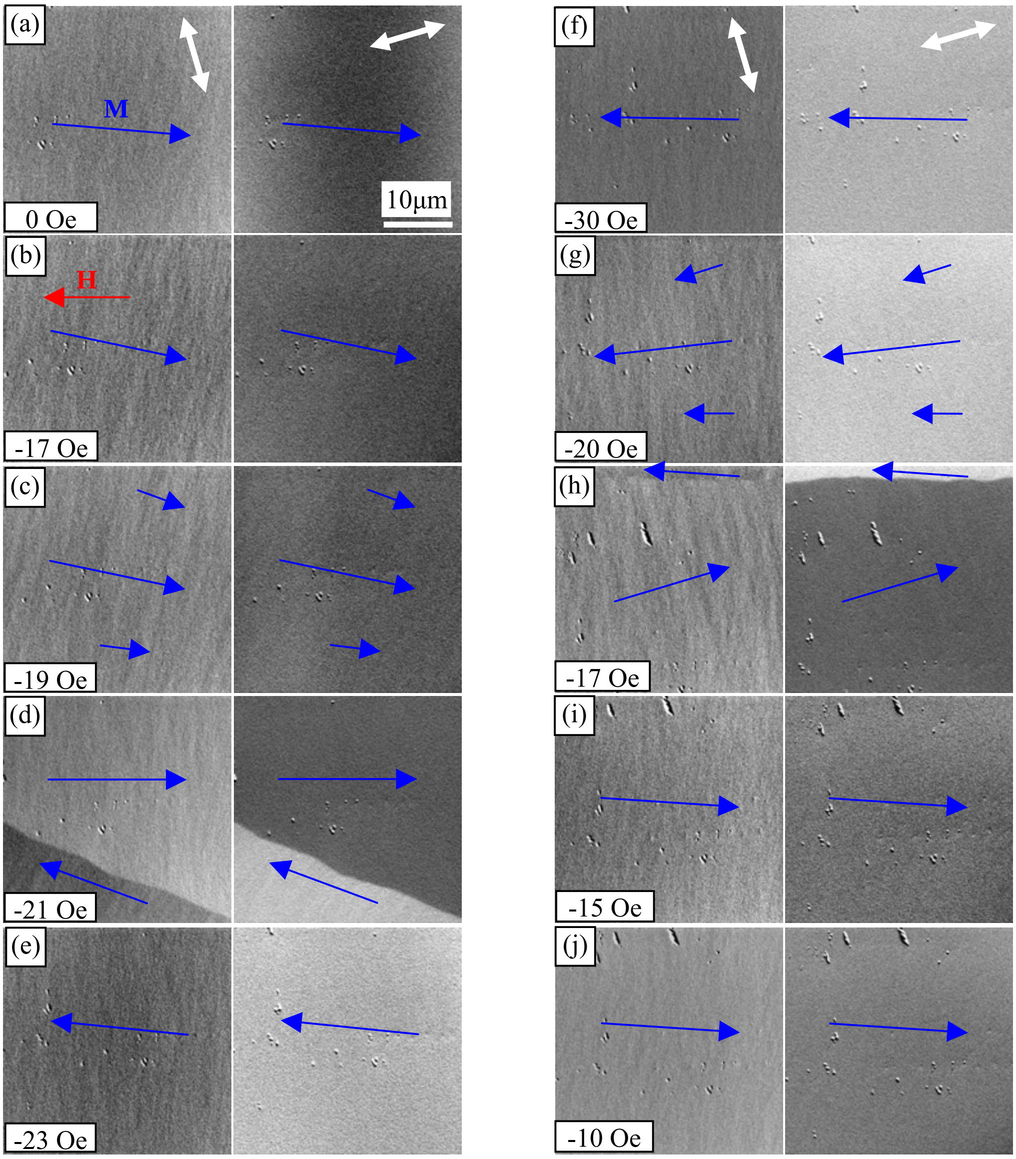

Fig. 8.18: DPC image sequence of the MTJ3 free layer after annealing.

8.3.4 Comparison of the magnetisation ripple

In order to study the effects of heat treatment and applied field on the magnetisation ripple as well as a comparison of dispersion between the different stacks, estimations of the most prominent ripple wavelength and dispersion angle were made from the Fresnel images. For a one-dimensional variation in magnetisation, the Fresnel contrast approximates to,

$$C(y) = \frac{et\lambda\Delta}{h}\left|\frac{dB_x(y)}{dy}\right| \qquad (8.8)$$

where t is the FM film thickness, λ is the electron wavelength, Δ is the defocus distance and B_x is the x-component of magnetic induction [187]. In this equation, the effects of inelastic scattering and finite electron source size are ignored which has been shown to underestimate the magnitude of dispersion in the past. Additionally, measurements of the ripple wavelength must be taken with care as the transfer function in the Fresnel mode oscillates strongly at large defoci. However, despite these criticisms, the Fresnel images can still provide useful information on the dispersion. Firstly, the finite source of a field emission TEM is effectively point-like, leading to negligible error in comparison to those fitted with thermionic emitters. Inelastic scattering remains a problem though, unless the microscope is equipped with an energy filter. The Philips CM20 used in this work unfortunately has no such filter and so the contrast measured is lower than equation 8.8 suggests. Despite this, although the Fresnel images do not allow absolute determination of the dispersion angle, they do provide a good method of obtaining information in arbitrary units. By assuming that the ripple is sinusoidal with amplitude $M_s\delta$ and wavelength Λ, the contrast can be expressed as,

$$C(y) = \frac{et\lambda\Delta}{h}\frac{\mu_0 M_s 2\pi\delta}{\Lambda}\cos(\frac{2\pi y}{\Lambda}) \tag{8.9}$$

with the standard deviation of intensity given by,

$$\sigma = \frac{et\lambda\Delta}{h}\frac{\mu_0 M_s 2\pi\delta}{\Lambda} \tag{8.10}$$

where M_s is the saturation magnetisation and δ is the root-mean-square (rms) dispersion angle. Since the only varying quantities in equation 8.10 are the FM thickness (between samples) and ripple wavelength, $\sigma \propto t\delta/\Lambda$. However, as the two AAF FM layers in MTJ2 and 3 are unlikely to be perfectly correlated through the Ru spacer, only the thicker of the layers should be taken into account.

It is possible to use the DPC mode to supplement the Fresnel calculations. This in-focus technique can provide more reliable information on the ripple spectrum and an absolute measurement of the dispersion. However, this analysis was not well suited to the image sequences shown here. In many of the DPC images acquired, there appeared to be a relatively large background intensity gradient. This noise was caused by a descan alignment error related to lens aberrations in the microscope during the time of this experiment and unfortunately could not be avoided. A second problem was that the difference images were obtained using an electronic mixer system which introduced a signal offset and gain to optimise the contrast. Such a system is invaluable during experiment as it allows the user to observe difference signals in real-time during the scan without the need for subsequent processing. Therefore, any corrections to the imaging conditions can be made immediately. In hindsight, a better idea would have been to take the signal from each quadrant of the detector and create the desired difference images using computer software, without modifying the data.

As the images were recorded digitally using a charge-coupled device (CCD) camera, analysis of the pixel intensity was quick and straightforward. The ripple was longitudinal in nature, so the average wavelength was estimated by taking a linetrace parallel to the axis of magnetisation and counting the number of intensity peaks. This was performed for each image of the Fresnel sequences. As we are dealing with a dispersion spectrum, a variety of different wavelengths were present in the images. However, only the most prominent variations were taken into account. To estimate the difference in dispersion angle between the images, the standard deviation of intensity taken from a line trace was weighted by the measured value of Λ and the (larger) free layer FM thickness.

The variation in ripple wavelength and rms dispersion angle for the forward and reverse paths of each sample before and after heat treatment are given in Fig. 8.19 and Fig. 8.20 respectively. The values at zero field are given in Table. 8.1. Studying the wavelength data first, each specimen showed a substantial increase in period as the field approached that required to reverse the magnetisation. After reversal, this value then dropped suddenly and levelled out at higher field. These graphs are offset as a result of the Néel coupling. The wavelengths appeared to fluctuate about similar values for each MTJ albeit with different peak magnitudes at the coercive field. Before annealing the stacks MTJ1 exhibited the largest peak wavelength and MTJ2 the smallest, but after increasing the magnetic homogeneity with heat treatment, MTJ2 and MTJ3 showed the largest and smallest peak wavelengths respectively. Also, from these graphs it can be seen that the ripple wavelength for each sample decreased on annealing.

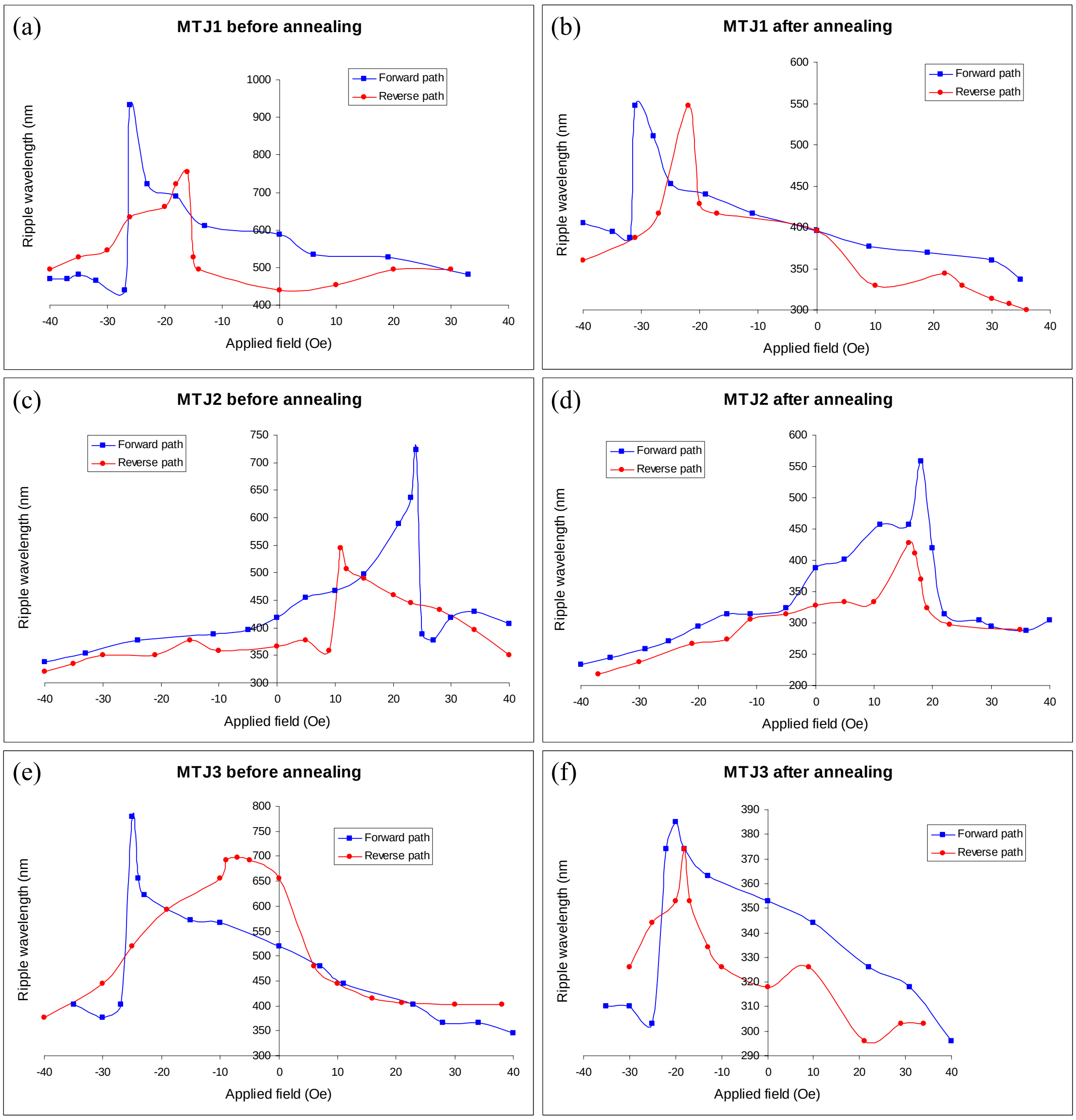

Fig. 8.19: Variation of ripple wavelength with applied field for (a)-(b) MTJ1, (c)-(d) MTJ2 and (e)-(f) MTJ3 before and after annealing.

The rms dispersion data showed a very similar trend, although the values for MTJ1 were far greater than the other stacks, both before and after annealing. Before annealing, MTJ2 exhibited the lowest peak dispersion angle as was obvious from the Fresnel and DPC images, but after annealing MTJ3 was more uniformly magnetised.

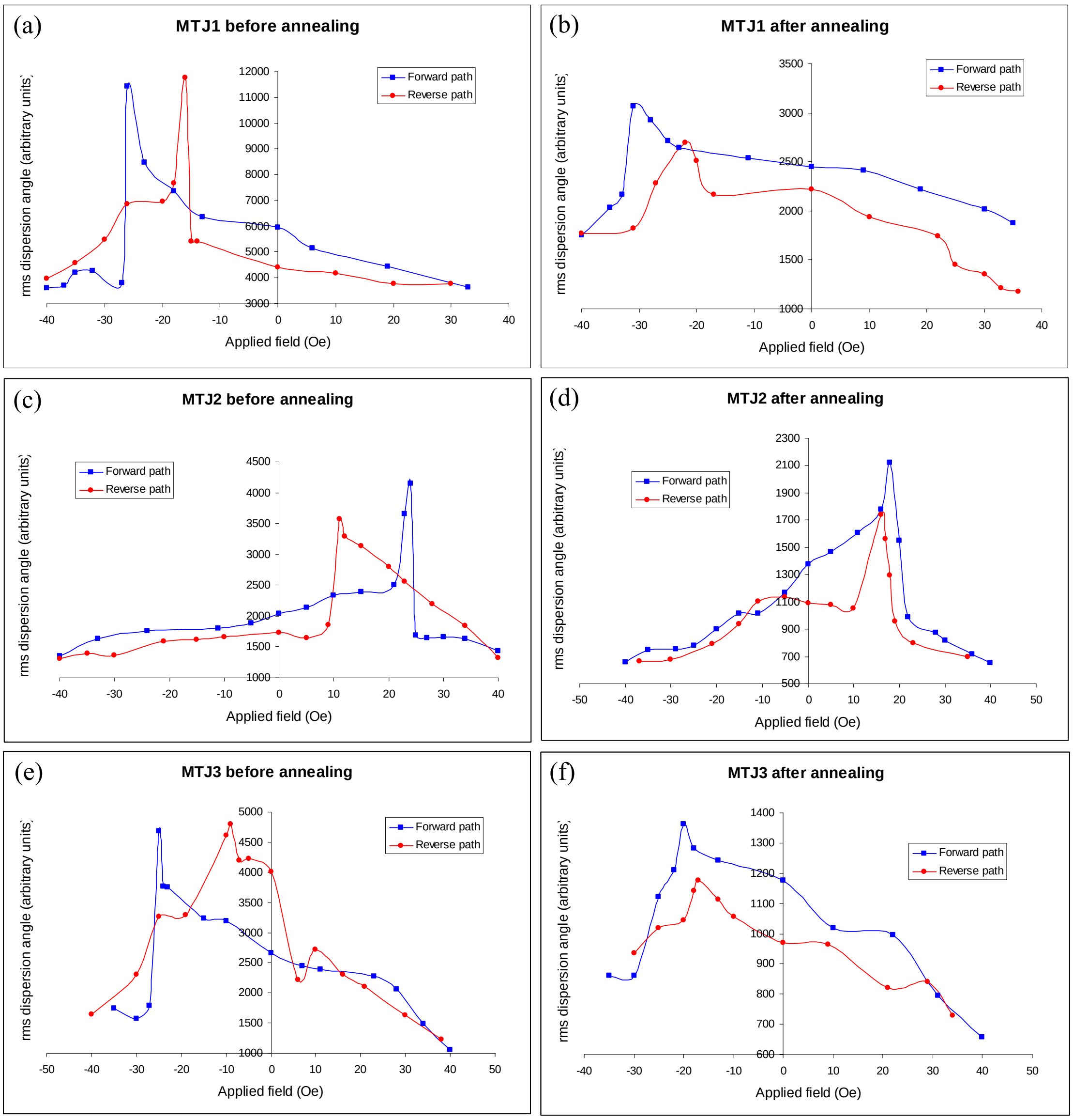

Fig. 8.20: Variation of the rms dispersion angle with applied field for (a)-(b) MTJ1, (c)-(d) MTJ2 and (e)-(f) MTJ3 before and after annealing.

8.4 Discussion of magnetic behaviour

The data presented here, and summarised in Table 8.1 (below) are very much in agreement with the previous VSM investigation by F. W. M. Vanhelmont and H. Boeve on the same MTJ samples [183]. The Fresnel and DPC images have revealed a number of interesting points about the magnetic behaviour of each stack and this section will attempt to explain the findings.

Sample	Before/after annealing	Offset (Oe)	Coercivity (Oe)	Ripple wavelength at remanence (nm)	rms dispersion angle at remanence (arbitrary units)
MTJ1	before	-21	6	514	5174
MTJ1	after	-26	4	396	2332
MTJ2	before	+17	8	393	1507
MTJ2	after	+18	1	358	988
MTJ3	before	-16	10	588	2667
MTJ3	after	-19	1	336	859

Table 8.1: Offset, coercivity, average ripple wavelength and rms dispersion angle at zero field for the free layer of each MTJ stack before and after annealing.

8.4.1 Offset and coercivity

These results clearly show a reduction in the offset field as a result of including an AAF in the free layer of the stack. Before heat treatment, this offset was reduced by 19% for MTJ2 and 24% for MTJ3, but these values improved to 31% and 27% respectively on annealing. That the reduction in offset increased after properly setting the exchange bias is a direct consequence of increasing the uniformity of the magnetisation in each FM layer. Effectively, many of the magnetic inhomogeneities are removed during this process leaving the AAF optimised for charge cancellation at the interfaces. The post-anneal data also show a greater reduction in field for MTJ2 over MTJ3. This result is caused by the thinner bottom AAF layer which allows the poles of opposite polarity to be brought closer to the tunnel barrier, thus compensating the charge more effectively [181]. Another point about the variation in offset is the increase in magnitude for the individual stacks after the samples were annealed. When the pinned layer is strongly magnetised in the plane of the film, the Néel coupling is enhanced relative to when the magnetisation is less uniform, and the offset field is increased. Also, as expected, the sign of offset was different for MTJ2 when compared to MTJ1 and MTJ3. This change in sign is the result of a difference in the direction of free layer net magnetisation at zero field when the AAF FM layer order is changed, as shown diagrammatically in Fig. 8.5.

Turning the attention now to the free layer coercivity, it can be seen that before annealing, addition of the AAF caused an increase in switching field but after annealing reduced the coercivity. Also, comparing the field values before and after heat treatment for each stack, it can be seen that the coercivity drops (substantially for MTJ2 and MTJ3) on annealing. In single layer polycrystalline films, the rigidity is affected by the local anisotropy of the crystallites which creates a frictional torque against rotation. With an AAF present, however, the magnetic rigidity is amplified by the Q-factor as shown in equation 8.3. The AAF rigidity is strongly affected by that of the constituent layers, and the larger the coercivity of these layers, the greater the rigidity of the AAF. As a result of the strong AF coupling, the magnetic stiffness of one layer is transferred to the other. This would explain the increase in coercivity from MTJ1 to MTJ2 or MTJ3 before annealing. After annealing, the decrease in coercivity with inclusion of the AAF is more difficult to explain. This result may be influenced by the Ru spacer. In an MFM/TMR study [188] of AAFs, Ru has been found to diffuse between the grains of the FM causing intermixing at the FM-Ru interface. This intermixing led to a decrease in the FM magnetisation and exchange coupling resulting in a lower coercivity. As atomic mobility increases with temperature, Ru diffusion is certainly a consideration during a heating cycle.

For each stack, the coercivity dropped once the samples were annealed in an applied field. This is caused by an increase in magnetic homogeneity for the free and pinned layers of the structure [189]. As can be seen in the Fresnel and DPC images prior to heat treatment, the magnetisation ripple was pronounced and the domain structure during reversal relatively complex. Previous studies [36,37] have shown that domain walls in one layer give rise to local charge accumulations which can pin walls in neighbouring layers. Therefore, interactions between the pinned and free layers create pinning sites for domain walls in the free layer that must be overcome for the reversal to go to completion. After annealing, the magnetisation in each layer is more uniform and the number of pinning sites reduced. As a result, the magnetisation undergoes a less complex reversal with a lower coercivity.

8.4.2 Reversal mechanism

The Fresnel and DPC image sequences show that in these samples, the free layer magnetisation reversed via the nucleation and movement of domain walls. In polycrystalline films, the local sense of rotation of the magnetic moments inside a layer can be influenced by thermal activation (though small at room temperature), variations in the exchange interaction and changes in the local anisotropy. Therefore, different regions spaced far enough apart to avoid direct exchange can rotate either CW or CCW resulting in domain formation [188]. The moments inside uniformly magnetised regions weakly coupled to their neighbours tend to rotate first followed by those tightly coupled at higher field. This model describes the behaviour of most of the MTJ samples studied here. However, as shown in Fig. 8.12, one MTJ2 specimen started to reverse via incoherent rotation, producing a swirl-like configuration before domain walls were nucleated. In another sample of this type (not shown), the complete reversal was by incoherent reversal. In this specimen, the magnetisation appeared to rotate differently in neighbouring regions, forming low-angle walls before further rotation caused their annihilation and precluded the nucleation of 180º walls. It is important to note here, however, that to perform the annealing experiments in the TEM, each sample had to be inserted manually into a specially designed heating rod. The down side to this procedure is that in-situ rotation of the specimen was not possible. Hence, the precision with which the orientation of the applied field could be set with respect to the original easy axis was limited to approximately ±2° [190]. In addition, during these reversals, the field was applied along the same axis as that used to set the direction of the pinned layer magnetisation throughout the heating cycle. However, it is possible that on removal of this aligning field, the easy axis of the free layer could have changed slightly, meaning that the field applied to reverse the film would not have been aligned exactly anti-parallel to this axis, increasing the chance of rotation. Therefore, by applying the field at a slightly different angle to before, the MTJ2 free layer magnetisation may have been aligned more anti-parallel to the field, resulting in a more typical reversal process.

Another point to mention about the image sequences is the orientation of domain walls during the forward and reverse paths. This change in orientation is not uncommon. In a previous study of spin valves [191], domain walls were inclined at ±25° angles to the easy axis. This was attributed to an easy-axis dispersion whereby the magnetisation in different regions rotated towards the applied field. In a study of IrMn/CoFe bilayers [189], similar behaviour was the likely result of an imperfect interface typical of multilayer polycrystalline films, giving rise to both unidirectional and biquadratic energy terms. Under these conditions asymmetric hysteresis occurs and a ‘natural angle’ emerges as a consequence of the FM passing through different effective fields on the forward and reverse paths.

Also, when the samples were annealed, the shape and length of the domain walls varied. Before annealing the walls were short and curved, whereas those imaged after heat treatment appeared to be relatively straight and extended over larger distances. This is again related to the increased uniformity of the magnetisation when the easy axis is properly set. Randomly oriented crystallites result in the formation of more complex configurations whereas a strongly induced easy axis favours long straight domain walls that are able to sweep through the film.

8.4.3 Magnetisation ripple

The Fresnel and DPC images show a lot of contrast from the magnetisation ripple of the FM layers. In polycrystalline magnetic materials, ripple results from local variations in the anisotropy direction between the coupled crystallites [192,193]. This gives a random contribution to the easy-axis direction of the magnetisation vector. With MTJs 1 and 3, the ripple contrast appeared to be very similar. However, with MTJ2, the intensity of ripple within each domain was much reduced, making an analysis of the magnetisation direction far more difficult. One possible explanation for this observation could be a change in grain size. In the previous VSM study, the AF coupling strength between the layers of the AAF increased with the thickness of the bottom NiFe layer. The explanation for this result was that renucleation occurred for grain growth on top of the Al_2O_3 [183]. As a result, the grain size at the Ru spacer was larger for a thicker bottom layer and the random disorder at grain boundaries was reduced, leading to an enhanced AF coupling strength. As magnetisation ripple is directly related to the crystallites, it is likely that the dispersion spectrum will also vary with grain size. Interlayer mixing may contribute as well, however. Each of the stacks are identical in structure up until the NiFe on top of the alumina barrier. In MTJs 1 and 3, the NiFe layer directly above the oxide is relatively thick compared to the second junction, which is only slightly thicker than the magnetically dead NiFe seed layer. In MTJ2, therefore, the 3nm layer is likely to be less uniform in structure than thicker layers of the same material, and it could be expected that defects and interlayer mixing at this part of the stack will affect the magnetic structure.

The variations in ripple both before and after annealing, and indeed between the samples, is likely to have a considerable effect on the reversal mechanism. It was observed in the pre-annealed images that domains of reverse magnetisation were formed from regions of intense ripple, and that the domain patterns involved could be quite complex in nature. The chain-like structures observed in all three stacks are one such example and have been found to be produced when lower mobility walls are pinned during reversal and orthogonal walls nucleated between them [191]. As magnetisation ripple has an associated surface charge that can affect the distribution of neighbouring layers [181,194], it is likely that the larger dispersion is partly responsible for the formation of these structures. When the ripple wavelength and dispersion angle decreased after annealing, a far simpler reversal took place via the movement of only one or two domain walls. In line with what has been discussed earlier on the variation in domain structure, this behaviour is indicative of a higher degree of homogeneity. In other MFM [195] and TEM [191] experiments performed on multilayer stacks, it was found that the incorporation of a natural antiferromagnet reduced the amplitude of dispersion. In the latter study, Néel coupling between the free and pinned layers of the spin valve was also expected to contribute.

The ripple spectrum was found to vary with applied field. As shown in Figs. 8.19 and 8.20, the wavelength and dispersion angle peaked just before reversal and then dropped in magnitude at the coercive field. This can also be seen in the images where the ripple contrast within the reversed part of the film was lower than that in the regions still to reverse. Such behaviour occurred for each film but was less noticeable once the samples had been annealed. This behaviour can simply be attributed to a variation in the Zeeman energy. As the field anti-parallel to the net magnetisation increases, the Zeeman energy also increases. The weakly coupled grains then start to rotate CW and CCW to align with the field, dragging the more strongly coupled grains behind them. This gradually increases the dispersion until, at a critical field, domain walls are nucleated and irreversible changes in the magnetic microstructure take place.

8.4.4 360º domain walls

A final point from the experimental observations that must be addressed is the presence of 360º domain walls. These walls were observed in each film and occurred more frequently before the samples were annealed. Such structures have been seen in numerous studies on samples containing AAFs [188,194-196] but can also be formed in different multilayer systems [197-200]. They occur between similarly magnetised domains and appear as two separate 180º Néel walls separated by a third domain oriented anti-parallel to its neighbours. As the magnetisation rotates continuously between the parallel domains, these structures can be considered as individual entities. Often 360º domain walls take the form of linear wall sections, but as has been shown here, they can just as easily link up to form 360º wall loops (Fig. 8.21) which are extremely stable [191].

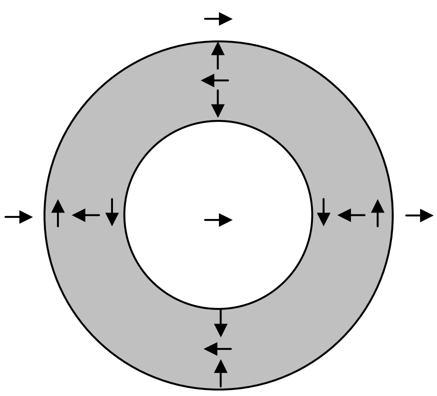

Fig. 8.21: A 360º domain wall loop.

The domain structure is initiated when Néel walls of opposite chirality come together as the reverse field is increased (Fig. 8.22a). In this situation, like charges from the walls preserve the central domain oriented anti-parallel to the applied field direction and the spins rotate continuously through 360° (Fig. 8.22b). When the Néel walls have the same chirality (Fig. 8.22c), on the other hand, opposite charges favour annihilation and the film becomes magnetised in the field direction (Fig. 8.22d).

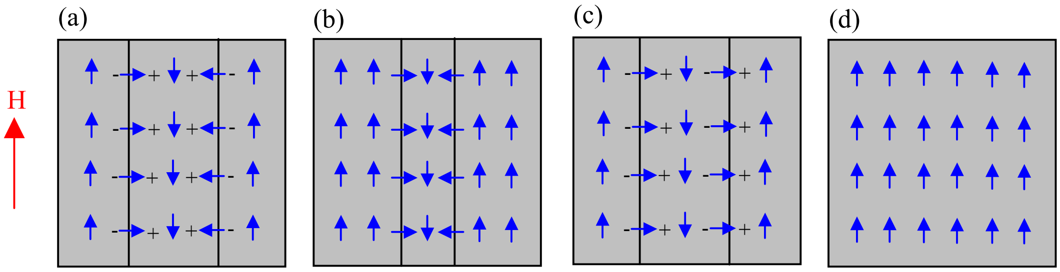

Fig. 8.22: Mechanism for the formation of 360° domain walls.

Although 360º walls are formed in single layer films, they are more abundant in samples containing AAFs because the AF coupling adds an additional contribution to their nucleation and stability [188]. They are nucleated in the bottom AAF FM layer where they are stabilised by charges of opposite polarity created by the interface roughness at the tunnel barrier. In this layer, the magnetisation at the centre of the wall is opposite to the field direction. This configuration is then mirrored in the upper AAF layer with the centre of the wall magnetised parallel to the field, creating a configuration with reduced magnetostatic energy. In addition, due to roughness at the Ru spacer, local variations in the AF coupling prevent coherent reversal of the film and act as nucleation and wall-pinning centres. This is a further reason why AAFs show a greater density of 360º walls than single layer films.

Once formed, their stability is dependent on the balance between the Zeeman, domain wall and AF coupling energies. As the field is inceased, the Zeeman and domain wall energies become unfavourable for the wall in the bottom of the AAF and its central domain decreases in size. However, the AF coupling preserves the wall and acts as a pinning source until the field strength dominates, causing it to collapse. In the upper layer, the applied field is parallel to the magnetisation at the centre of the wall, enhancing its stability. Nevertheless, expansion of this central domain is prevented by the strong AF coupling to the bottom AAF layer which is now uniformly magnetised in the field direction. Only at very high field does an unfavourable domain wall energy cause the upper wall to collapse. This enhanced wall stength may be the reason why 360º loops were observed at the end of the reversal sequences of both MTJ2 and MTJ3 but disappeared at low field for MTJ1 in Fig. 8.9j.

8.5 Physical characterisation

In order to confirm the arguments on grain size and interlayer mixing in the previous section, it was necessary to analyse the physical structure of the MTJ samples. This was performed using BF and DF TEM with electron diffraction. First, diffraction patterns were obtained from each sample to check for any obvious structural differences and ensure that (111) texturing was indeed induced by the seed layers. This was then repeated after the samples had been annealed to examine the physical effects of heat-treatment. Following this, in-plane grain size estimations were made from several BF and DF images acquired by passing the beam through the complete stack. Such estimations do not give any information on the grains within the individual layers of the film, but do provide an average result which can highlight any major changes in morphology. To analyse the structure of the different layers in each sample, cross-sections were fabricated by Mr Brian Miller and imaged in BF and DF by Dr Ian MacLaren. The cross-sectional images were also used to examine the layer roughness and compare values of amplitude and wavelength with those obtained from the VSM experiments performed at Philips.

8.5.1 Electron diffraction

Diffraction patterns taken with each sample at 0°, 15° and 30° tilt are shown in Fig. 8.23 before and after annealing. Only one set of diffraction patterns are shown because the ring structure was identical for each stack. As can be seen, the heat treatment had no effect on the pattern. When the tilt angle was increased, the contrast changed noticably, indicating that a high degree of texturing was present as a result of the seed layers. For each pattern, the radii of the rings were measured and the rings indexed by plotting R^2 against (h^2+ k^2+ l^2) since,

$$R^2 = (\frac{\lambda L}{a})^2 (h^2 + k^2 + l^2) \qquad (8.11)$$

where R is the radius, λ is the electron wavelength, L is the camera length, a is the material lattice parameter and h,k,l are the Miller indices. As the experimental parameters are known, Miller indices can be deduced from a knowledge of the crystal structure and the x-coordinates of each point at which R^2 cuts the gradient of the graph (Fig. 8.24).

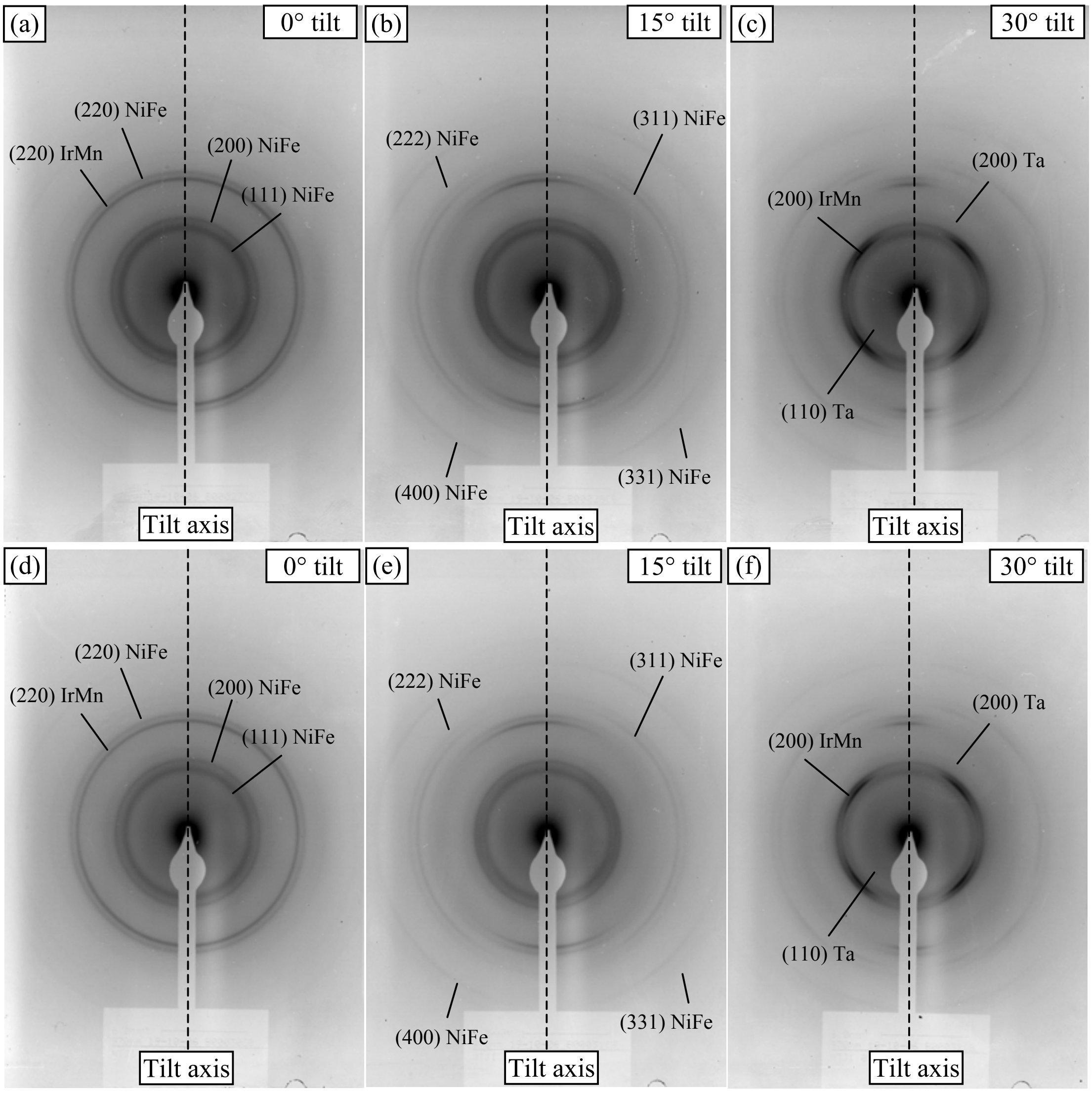

Fig. 8.23: Electron diffraction patterns taken before annealing at (a) 0°, (b) 15° and (c) 30° tilt and after annealing at (d) 0°, (e) 15° and (f) 30°.

Typically, electron diffraction patterns are difficult to index for multilayer samples because the electron distribution is a projection through the complete stack. However, this was simplified greatly by acknowledging that the stack thickness was dominated by NiFe and IrMn, both of which are face centred cubic (fcc), and that the Ta and Al_2O_3 were amorphous. Also, as the CoFe pinned layer and Ru spacer were thin with respect to the NiFe and IrMn, they could be ignored. Therefore, the diffraction patterns shown are effectively a superposition of NiFe and IrMn electron distributions with some diffuse rings as a result of the Ta. As the NiFe and IrMn lattice parameters are 3.575 and 3.811 angstroms respectively, lattice mismatch was inevitable during growth and some of the reflections are split.

At 0° tilt, with the beam perpendicular to the film plane, the (111), (200) and (220) rings were visible and homogeneous. However, at 15° the (220) contrast was reduced (except along the tilt axis) and additional rings appeared corresponding to the (311), (222), (400) and (331) planes. By tilting the sample to 30° the (220) contrast practically disappeared and the (200) NiFe and IrMn rings became distinguishable. These intensity variations support the claim for [111] texturing. For the zero order Laue zone (ZOLZ), the electron beam direction [uvw] and the allowed Bragg reflection (hkl) satisfy the Weiss zone law [201],

$$hu + kv + lw = 0 \qquad (8.12)$$

Therefore, assuming the beam is incident along [111], the only planes which satisfy equation 8.12 are the set {220}. Essentially, if the films were 100% textured in the [111] direction, the (220) ring would be the only one visible at 0° tilt. In the patterns obtained, the (220) reflection is indeed strong, but other rings are also present because this level of texturing is physically impossible using the current sputtering tools. With the sample tilted at 15° (beam incident ~[331]), stereographic projections calculated using the Desktop Microscopist software predict that faint (311), (331) and (420) rings should be visible in the diffraction pattern, whilst at 30° tilt (beam incident ~[220]), contrast from the (111) and (200) rings should also increase. The experimental data are in agreement with this, but as before, other reflections were also visible. Details of the stereographic projection technique are not given here, but can be found in reference [48].

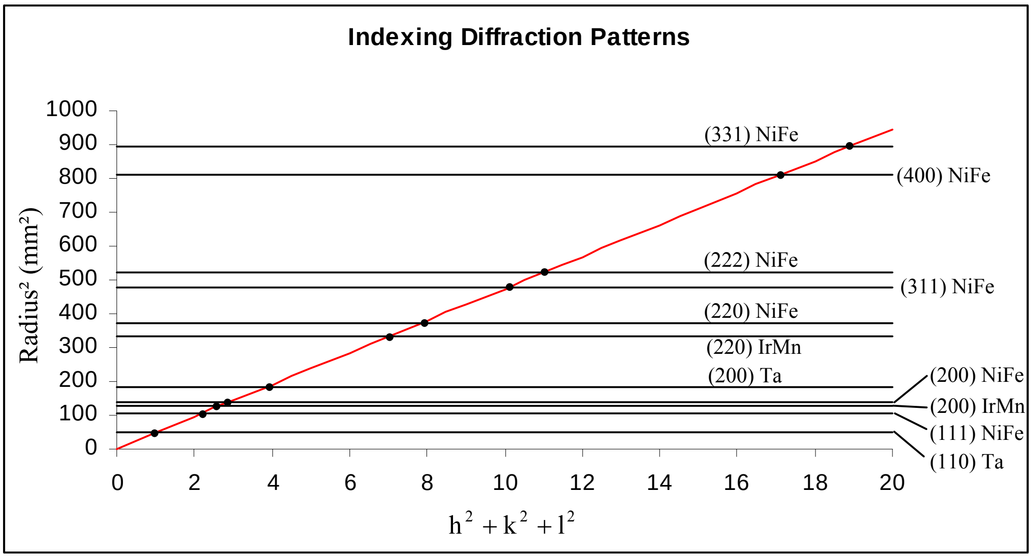

Fig. 8.24: Indexed diffraction pattern from the MTJ stacks.

8.5.2 Plan-view BF/DF imaging

By passing the electron beam through the complete multilayer stack, BF and DF images were acquired (Figs. 8.25-8.27). Whilst the BF micrographs were obtained by placing the objective aperture over the central part of the diffraction pattern, their DF counterparts were taken using electrons from the (220) reflection. As observed in Fig. 8.23a, this diffraction ring was intense, indicating that many of the crystallites satisifed the Bragg condition, allowing them to become clearly visible in the DF images. From several images of each sample, the mean grain size was determined using a particle analysis tool built into the Digital Micrograph software. To perform this analysis, a threshold is first selected which chooses the limits for the maximum and minimum grey-levels shown in the image. This is set so that only diffraction contrast from the strongly reflecting grains is visible. However, threshold selection is a matter of judgement, and care has to be taken not to omit the smallest grains from the calculations. In sputter-deposited films, the distribution of grain sizes often follows a log-normal variation, with probability expressed as,

$$P(D) = \frac{1}{\sqrt{2\pi}\sigma D}\exp\left[\frac{-(\ln(D)-\mu)^2}{2\sigma^2}\right] \qquad (8.13)$$

where D is the grain size and μ and σ are the mean value and standard deviation of ln(D) respectively. To achieve a realistic grain size estimation, data from previous studies on similar films were used as a guide to help set the threshold. The grain diameter was then calculated from statistics on the highlighted regions. It is important to stress that this technique provides only a rough estimate. The values for each sample are given in Table 8.2. These results show that the grain size was ~7nm for each sample and that the heating and field-cooling cycle caused no discernable change in the mean diameter.

Sample	Before/after annealing	Grain size (nm)				Roughness amplitude (nm)	Roughness wavelength (nm)
		Complete stack	Bottom free layer	Top free layer	Upper layers		
MTJ1	before	6.9	3.2	-	3.2	1.2	19.4
MTJ1	after	7.0	3.1	-	3.1	0.7	17.0
MTJ2	before	7.0	2.7	4.5	3.5	1.7	9.5
MTJ2	after	7.1	2.6	4.5	3.4	1.3	10.2
MTJ3	before	7.0	4.1	2.5	3.5	1.1	12.6
MTJ3	after	7.1	4.3	2.4	3.7	1.0	13.9

Table 8.2: Comparison of grain size and layer roughness between the different MTJ stacks.

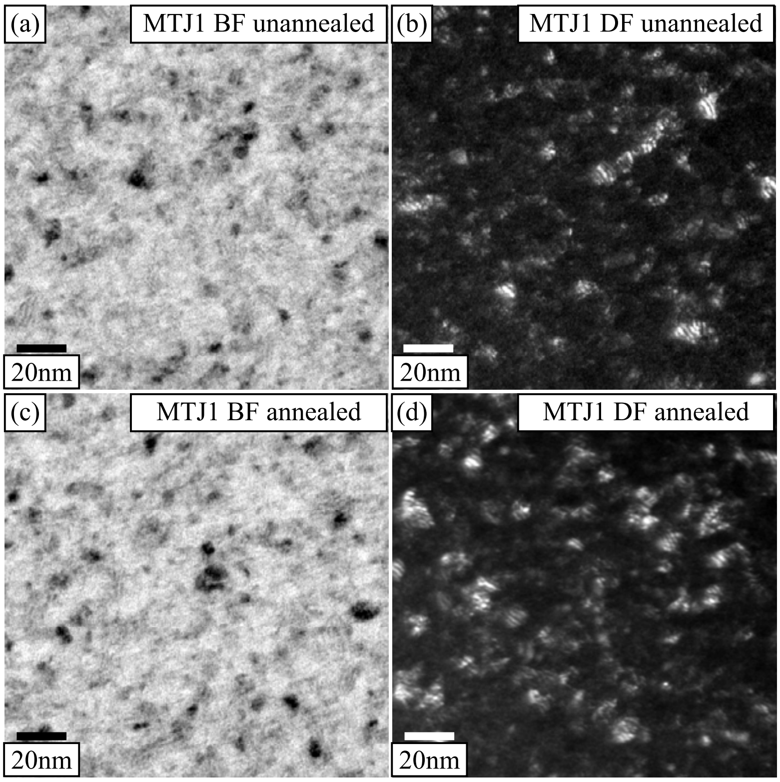

Fig. 8.25: BF and DF plan-view images obtained from MTJ1 (a)-(b) before and (c)-(d) after the annealing process.

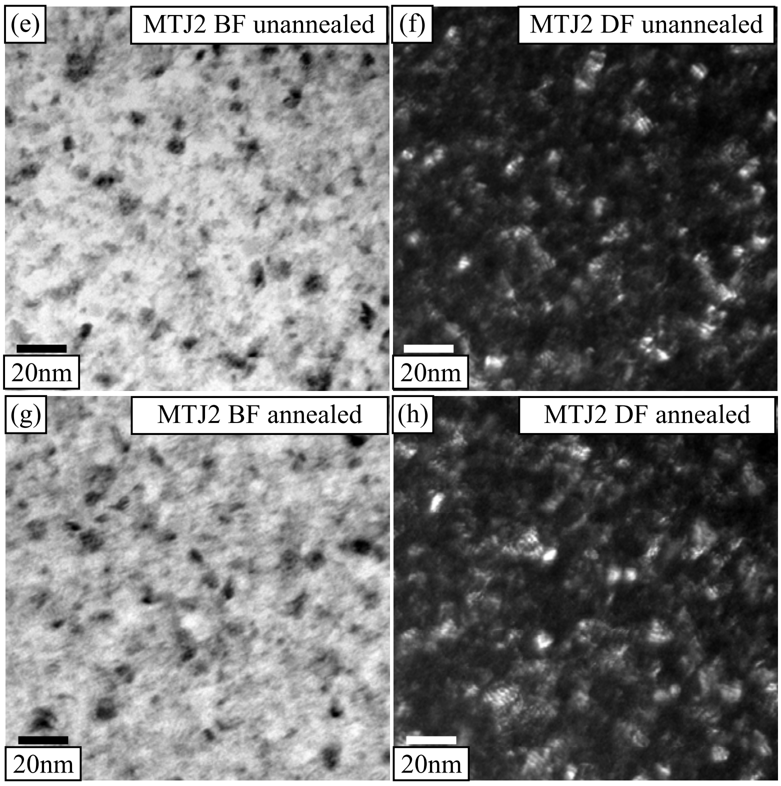

Fig. 8.26: BF and DF plan-view images obtained from MTJ2 (a)-(b) before and (c)-(d) after the annealing process.

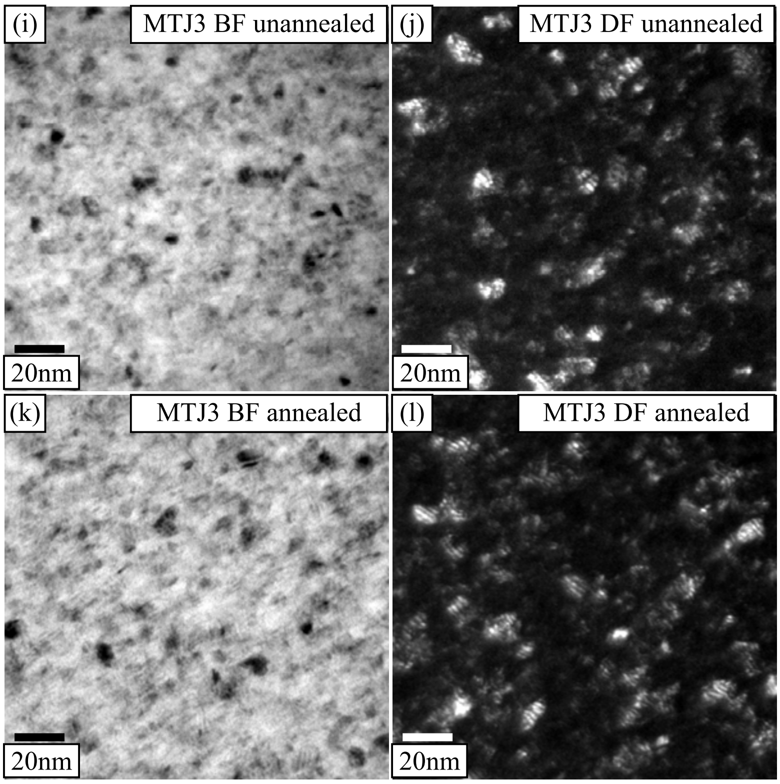

Fig. 8.27: BF and DF plan-view images obtained from MTJ3 (a)-(b) before and (c)-(d) after the annealing process.

As we are particularly interested in the grain structure of the free layer, however, a second batch of samples were fabricated onto Si_3N_4 membranes which included only the upper layers of the stack from the Al_2O_3 with the NiFe dead layer to induce [111] growth. For clarity, the layer structure (thicknesses in nanometres) and a schematic diagram are given below,

MTJ1’: 2NiFe/0.9AlO/5NiFe/3.5Ta
MTJ2’: 2NiFe/0.9AlO/3NiFe/0.8Ru/8NiFe/3.5Ta
MTJ3’: 2NiFe/0.9AlO/8NiFe/0.8Ru/3NiFe/3.5Ta

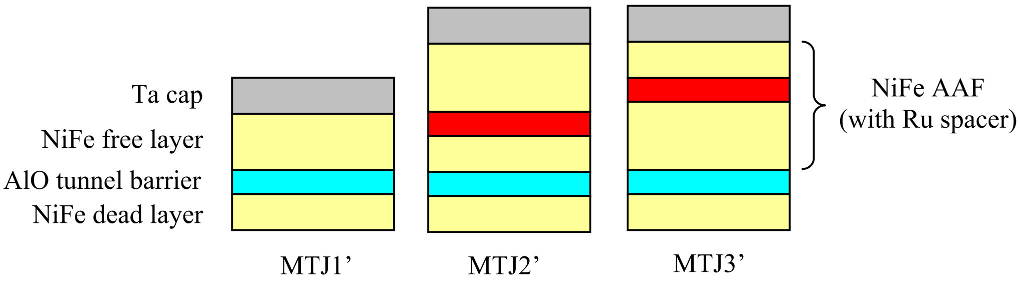

Fig. 8.28: Layer structure of the new MTJ’ samples.

The films were deposited by Dr Susana Cardoso at INESC-MN in Lisbon, Portugal. It is important to stress, however, that these samples were fabricated some time after the previous batch and were only intended for plan-view BF/DF imaging. Images showing diffraction contrast from the grains of the free layer are shown in Figs. 8.29-8.31. These were acquired before and after the same annealing process used earlier.

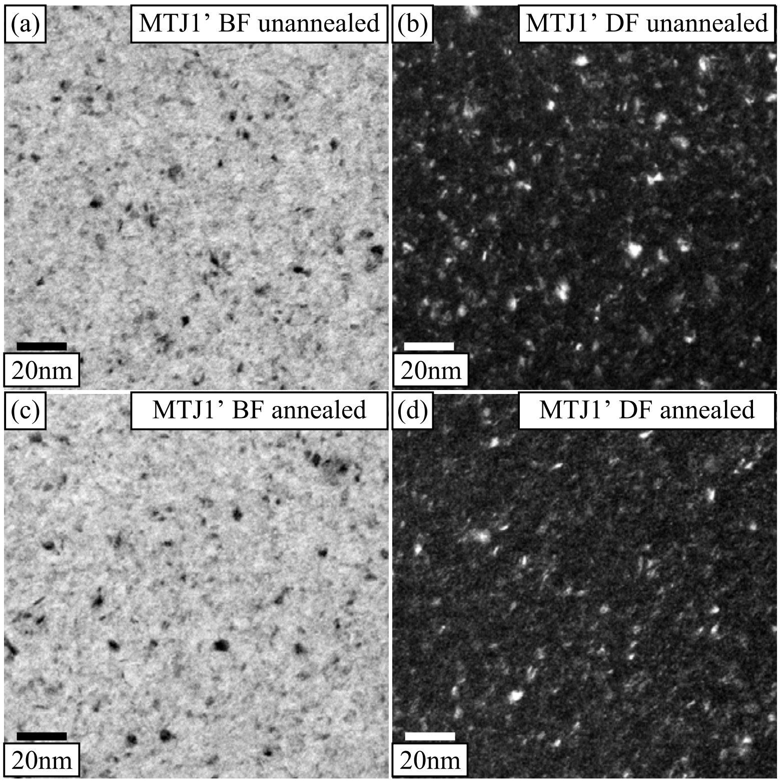

Fig. 8.29: BF and DF plan-view images obtained from MTJ1' (a)-(b) before and (c)-(d) after the annealing process.

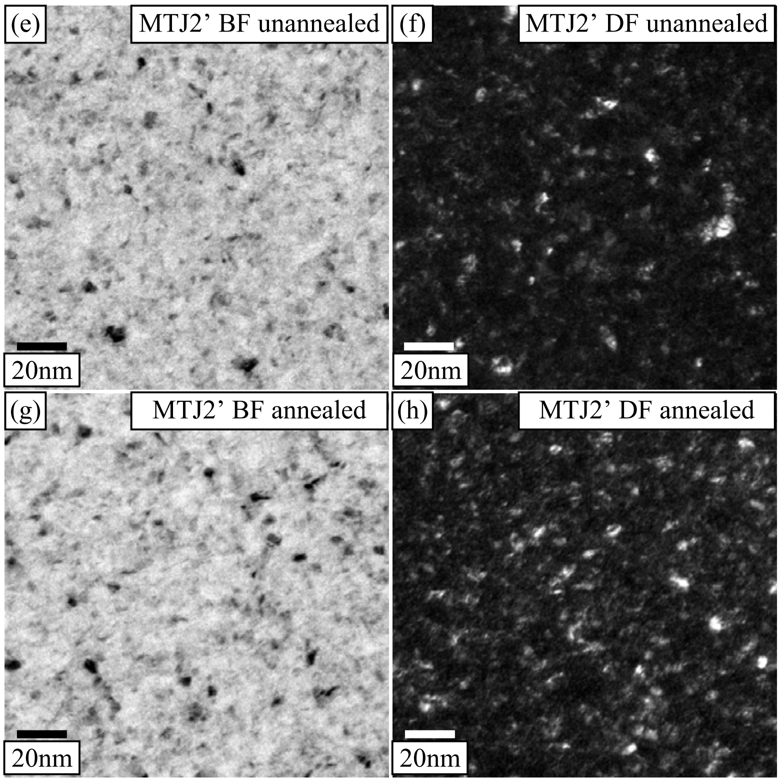

Fig. 8.30: BF and DF plan-view images obtained from MTJ2' (a)-(b) before and (c)-(d) after the annealing process.

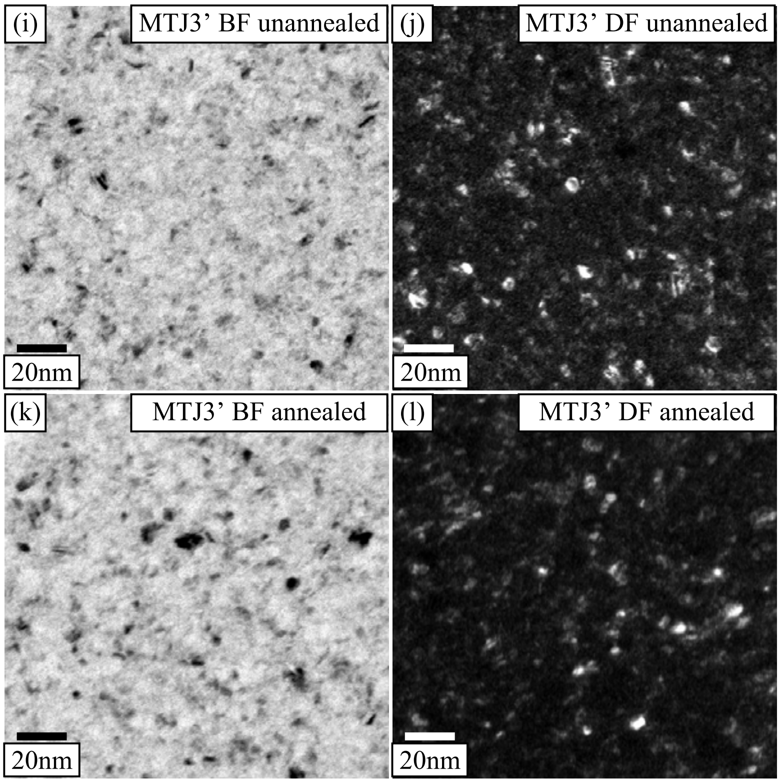

Fig. 8.31: BF and DF plan-view images obtained from MTJ3' (a)-(b) before and (c)-(d) after the annealing process.

The mean grain sizes are given in Table 8.2 and were all between 3-4nm. These values are around half the size of those measured from the complete stack showing that larger grains in the lower layers of the structure contributed greatly to the earlier image contrast. In addition, the grains in the single free layer of MTJ1 were slightly smaller than the grains of the AAF in MTJs 2 and 3. This was expected, since thicker layers of material allow the formation of larger crystallites. These images, however, did not reveal information on the grain structure within the separate AAF layers, so a cross-sectional analysis was necessary.

8.5.3 Cross-sections

Cross-sections were made from the membrane-supporting substrates using the encapsulation technique detailed in chapter 3. These were then imaged in bright and dark field to capture the diffraction contrast of the different layers and their constituent grains. Several BF and DF images were obtained from each specimen and analysed. A selection of these are shown in Figs. 8.32-8.34. In these images, contrast also arises from the SiN membrane, the oxide formed above the Ta cap and the epoxy resin used to glue the two substrate sections together during fabrication. As is evident from the grain structure, the only crystalline layers in the stack are NiFe, IrMn, CoFe and Ru. The other layers are amorphous and exhibit no crystallite contrast.

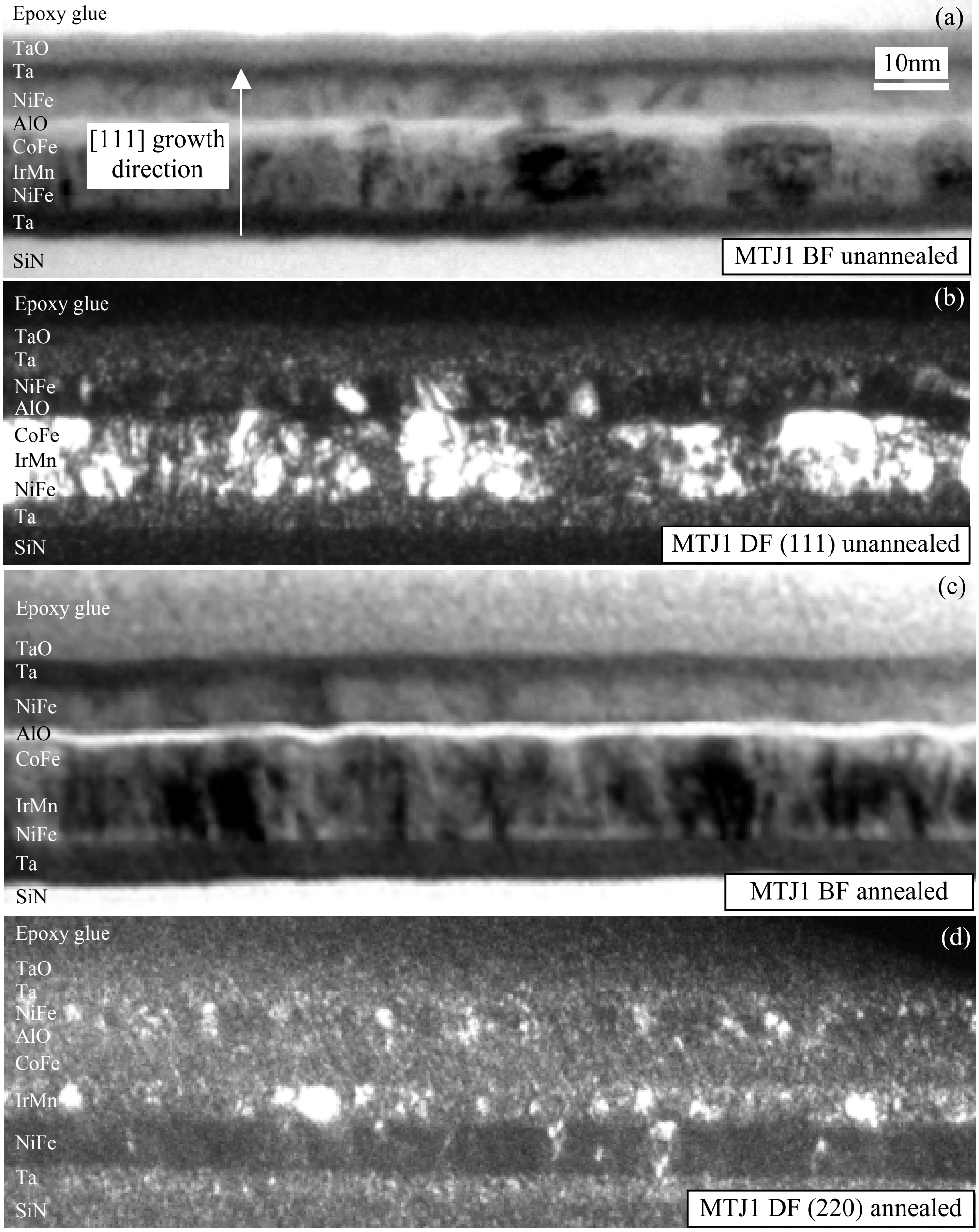

Fig. 8.32: (a), (c) BF and (b), (d) DF cross-sectional images obtained from MTJ1.

In the images of MTJ1, contrast between the NiFe dead layer, IrMn and CoFe is poor because many grains that were nucleated in the NiFe continued into the IrMn and CoFe, despite the differences in lattice parameter. The grain growth then stopped at the amorphous Al_2O_3 layer and new crystallites were nucleated in the NiFe free layer. As it was suspected that the grain size within this layer had an impact on the magnetic behaviour, their average diameter was calculated. The results from each sample are given in Table 8.2. Although heating cycles can cause a variation in the grain size of a polycrystalline film [202], this was not observable in these images. The mean free layer grain size was estimated to be 3.2nm before annealing and 3.1nm afterwards. Layer roughness initiated in the buffer system appeared to be correlated with that at the tunnel barrier. However, local fluctuations of a higher frequency were also present in the Al_2O_3 as a result of an uneven grain structure from the underlying NiFe, IrMn and CoFe layers. The roughness of the upper layers of the stack, on the other hand, seemed to be fairly consistent with the seed layer waviness. Since the grains in the free layer NiFe were relatively small, their structure did not cause additional local fluctuations.

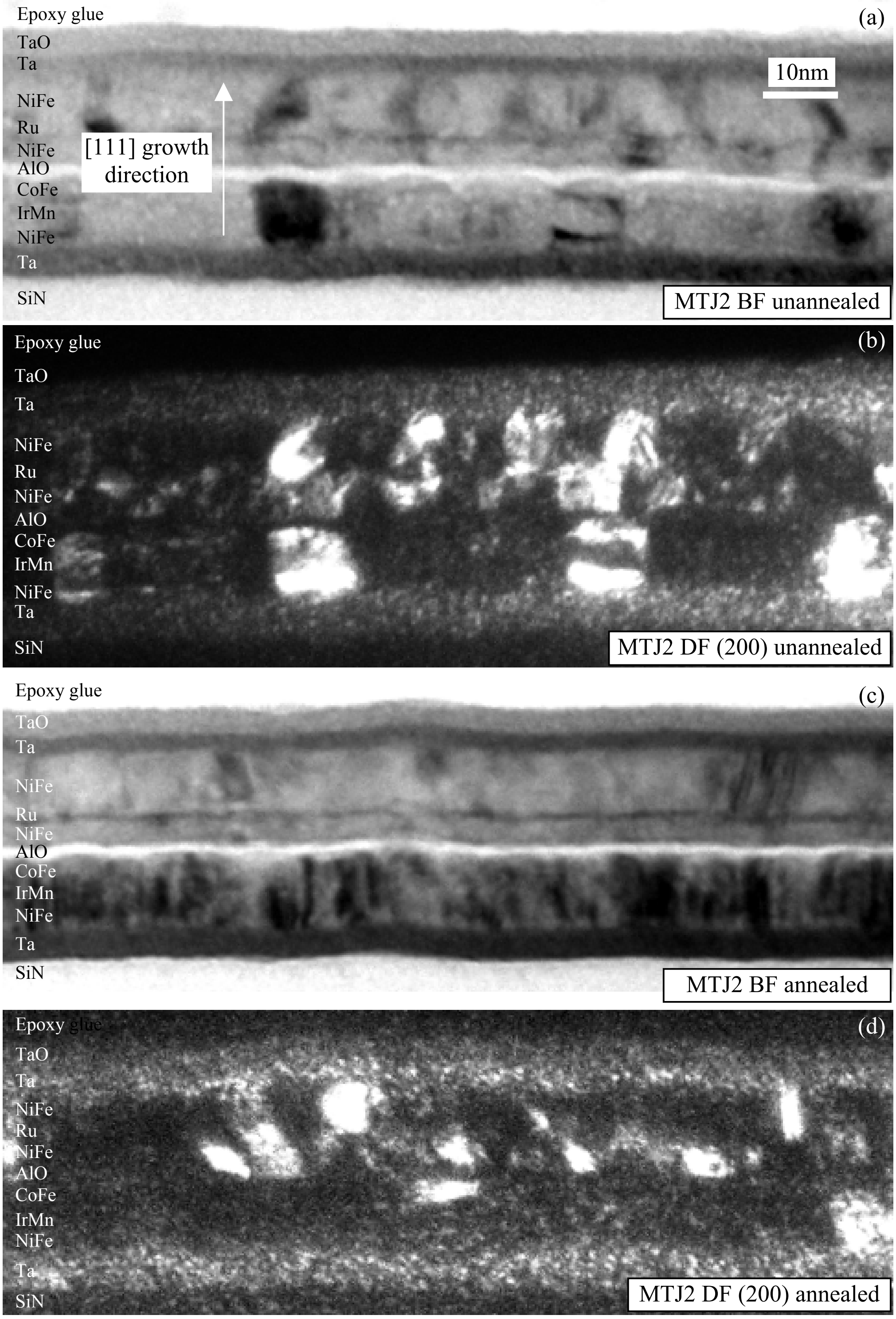

Fig. 8.33: (a), (c) BF and (b), (d) DF cross-sectional images obtained from MTJ2.

In MTJ2, the Ru roughness appeared to be conformal with the Al_2O_3 variations because the NiFe separating these two layers was thin, and the small grain size was insufficient to redefine the waviness. This roughness, however, did not continue up to the capping layer. Instead, a far smoother surface, exhibiting a more gradual undulation was observed. The Ru spacer and Al_2O_3 barrier may also have been discontinuous in places, which is not surprising considering their thickness. A previous TEM study on similar samples [184] has shown that the Al_2O_3 can vary in depth within the stack as a result of thickness changes in the underlying layers. These have also been known to cause irregularities in other layers of the structure. The images here reveal contrast to suggest analogous morphology. Unfortunately, it has not been possible to determine if interlayer mixing was present between the NiFe free layer and Ru spacer. Earlier it was discussed that intermixing may have been responsible for changes in coercivity and ripple contrast between samples, but further compositional characterisation using analytical TEM would be required. What is evident from these images, however, is that the order of the AAF layer does affect the grain size at the Ru spacer. With the thin NiFe layer adjacent to the oxide barrier, an average grain diameter of 2.7nm was calculated for this layer and a value of 4.5nm for the upper AAF layer. With MTJ3 on the the other hand, these sizes were 4.2 and 2.5nm respectively. Apart from this, the images of MTJ3 show many similarities to those taken with MTJ2. Also, whilst many of the grains in MTJ2 and 3 continue from the bottom AAF NiFe layer through into the Ru and top NiFe layer, others can be seen to renucleate on top of the Ru spacer which may be the result of lattice mismatch.

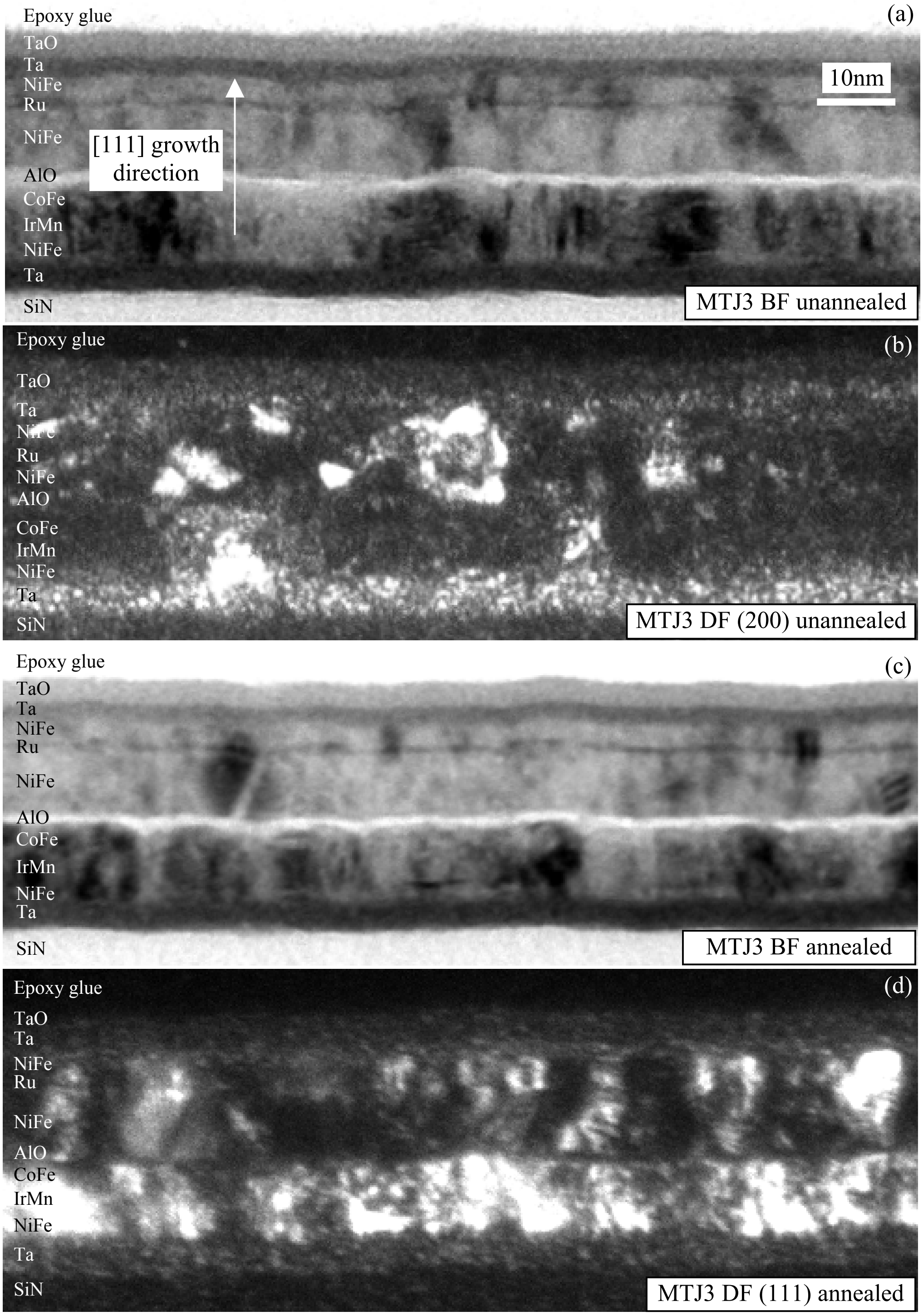

Fig. 8.34: (a), (c) BF and (b), (d) DF cross-sectional images obtained from MTJ3.

For comparison of the roughness amplitude and wavelength with the results obtained from the previous VSM experiments, measurements were made from the cross-sectional images of each sample. A least squares fit to the VSM data gave h and λ to be 0.16 and 9.8nm respectively [183]. These values correspond to a stack with single pinned layer exhibiting conformal waviness in each of the layers. To obtain an estimate from the cross-sections, many measurements of the distance from a reference line at the Si_3N_4 substrate to the centre of the Al_2O_3 tunnel barrier were made [41]. From these, the mean distance and standard deviation were calculated. In addition, the distances between each peak were noted and the mean wavelength determined. The results can be seen in Fig. 8.35 and Table 8.2.

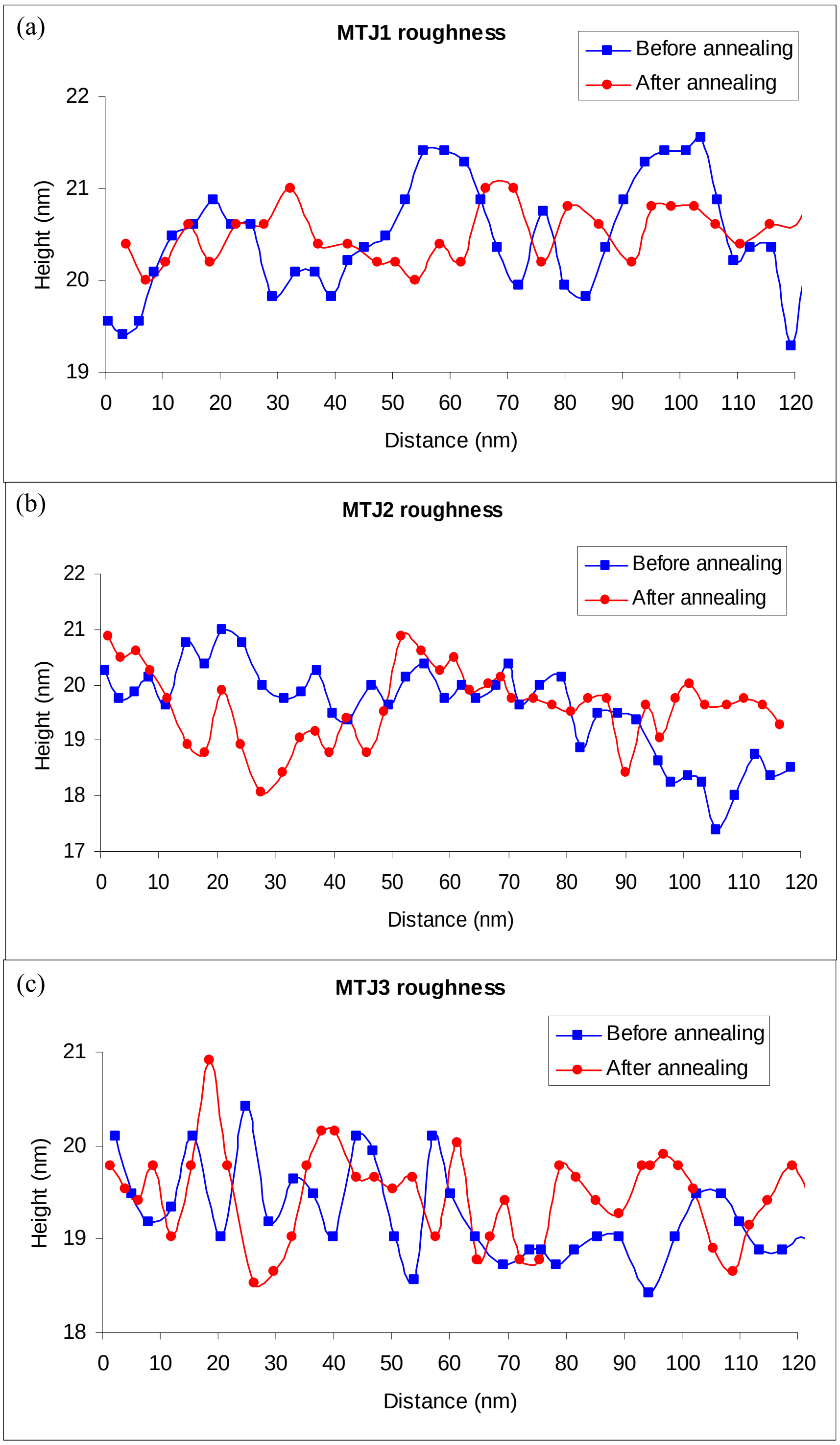

Fig. 8.35: Layer roughness at the AlO of (a) MTJ1, (b) MTJ2 and (c) MTJ3.

As can be seen in the roughness data, the amplitude measured for each stack was far larger than the previous estimation, but it is important to stress that these films were deposited on

Si_3N_4 membranes for TEM analysis and not bulk SiO_2 as used in the previous study. Therefore, substrate roughness variations may have influenced the results. In addition, the MTJ2 layers were found to be slightly rougher than the other stacks, both before and after the annealing process; yet another observable difference between these samples. The roughness wavelength on the other hand, was far closer to the VSM result. Although this measurement technique gives only an average approximation, the variation in roughness between samples is surprising. Each specimen was identical in structure up to the free layer of the stack, so layer growth was expected to be the same. One explanation could be an increase in stress acting on the seed layers when the single free layer of MTJ1 is exchanged for the thicker AAF system. The induced strain may cause displacement of the grains, but this does not explain the similarity in amplitude between MTJ1 and MTJ3. From the cross-sectional images, layer roughness does appear to be strongly influenced by the local grain structure of the underlying material. Whilst smaller crystallites result in a smoother stack, larger grains found in thicker layers do not conform to the pre-defined topology, but create a new, and typically rougher, base upon which subsequent layers grow. Grain sizes below the oxide barrier were not calculated, but perhaps changes in the grain diameter within the NiFe, IrMn and CoFe underlayers were responsible for the roughness variations in the Al_2O_3.

8.6 Discussion of physical structure

This physical characterisation has revealed a number of interesting points as well as testing the validity of the arguments in the magnetic discussion. Electron diffraction patterns obtained from each of the stacks at different tilts have confirmed that texturing in the [111] direction was induced by the seed layers, and that this did not change when the samples underwent heat treatment. The ring structure for each sample was identical, implying there were no major differences in structure. Plan-view images captured in the BF and DF modes then revealed a near identical grain size for each film when averaged over the complete stack. These estimates, however, were influenced strongly by the large grains in the bottom polycrystalline layers and a second calculation from the upper layers did show variations in the mean diameter. As a result of the thicker AAF with respect to the single NiFe layer, the grain size of MTJ2’ and MTJ3’ were larger than MTJ1’. Cross-sections were required to then analyse the grain structure within each layer. As expected, columnar growth of grains nucleated on top of the amorphous oxide took place, and the grain size was dependent on the layer thickness. This strengthens the argument for changes in magnetisation ripple being caused by a difference in grain size at the Ru spacer.

Interlayer mixing may still have played a part, however. If the Ru does indeed mix with the NiFe, then several monolayers either side of the spacer will become magnetically dead. In this situation the thin AAF layer of MTJ2 and MTJ3 will be further reduced in thickness causing the AAF to act more like the single free layer of MTJ1. If we then consider the thick AAF FM in the latter two stacks, we see that the base upon which the grains of the layer grow is very different. Whilst the crystallites of MTJ3 grow on top of the amorphous Al_2O_3 in the same way they do in MTJ1, those of MTJ2 grow on a magnetically dead crystalline bed. This additional ordering may be enough to reduce the ripple contrast.

Measurements were later made of the layer roughness at the tunnel barrier of each stack for comparison with the VSM data. Although the wavelengths calculated were not too far off the quoted value, the previously determined amplitude seems very underestimated. The images revealed an average roughness of ~7 times that deduced from the least squares fit, but this may be related to differences in the substrate material.

Chapter 9

Conclusions and future work

9.1 Introduction

In this thesis, the magnetic properties of single layer patterned elements and continuous multilayer films have been studied extensively using Lorentz microscopy. The thin film elements were specially designed to overcome difficulties in the switching behaviour of simple geometries. As well as demonstrating a level of success, they have also proven to be interesting specimens in their own right. Micromagnetic simulations were used throughout this work to aid interpretation of the results and provide a comparison to the experimental data. The investigation of magnetic tunnel junction (MTJ) samples in collaboration with Philips Research was also fruitful. These industrially relevant films have shown that the free layer offset field can be reduced by the compensation of magnetic surface charge at the layer interfaces. This chapter discusses the results of each experimental chapter and summarises the research. Following this is a section on new domain wall trap (DWT) sensor elements which, as well as being directly relevant to the work described in this thesis, could provide an exciting research project for the future.

9.2 Conclusions

In chapter 3, the different techniques used to fabricate continuous film specimens and thin film elements were described. With the main focus of this study on the magnetic behaviour of patterned films, it was necessary to develop the existing lift-off process further and optimise the quality of the magnetic structures. To recap, initial test samples showed poor feature definition and edge flags, as well as resist residue beneath the elements, all of which are problematic for this type of study. Good edge definition is vital when comparing different element geometries because changes to the shape strongly affect the magnetic behaviour. In addition, contamination above or below the ferromagnetic material leads to mass-thickness contrast in the TEM which can mask the magnetic microstructure we are trying to image. Metal flagging has been observed in previous studies and was attributed to an insufficient undercut in the resist profile. Experiments were therefore carried out to determine the most suitable resist combination necessary to achieve an undercut suitable for lift-off. In total, 18 different bilayers of resist were exposed to the electron beam. As well as PMMA, the most commonly used electron-sensitive polymer, ZEP and LOR were tested. Whilst ZEP is more sensitive to electron exposure than PMMA, LOR is unaffected by the beam. Instead, this layer is wet etched in CD26 after development of the imaging resist. From these experiments, a 40nm LOR/40nm PMMA bilayer produced the best results, as determined by both optical and scanning electron microscopy. This resist combination was almost able to eliminate edge flags completely and was used for the remainder of the fabrication in this thesis. To improve the patterning resolution, a 100kV electron beam was chosen over the original 50kV beam. In addition, a 30nm layer of Al was deposited on top of the resist stack prior to exposure. As Si_3N_4 membrane substrates are relatively unreflective, the light meter was unable to detect the specimen height and the beamwriter struggled to focus on the surface. On using the Al, however, the focussing and feature definition improved greatly. A secondary benefit of using Al is to dissipate surface charge. Si_3N_4 substrates charge during exposure because the material is electrically insulating. This can cause unwanted contrast, specimen drift and in extreme cases, substrate damage in the TEM, so it is important to provide an electrical path. A final adjustment to the fabrication procedure was the use of an oxygen plasma to remove resist residue after incomplete development. Organic material was removed in a matter of seconds with little adverse effect on the substrate.

The magnetic properties of rectangular elements and geometries of reduced symmetry were discussed in chapter 5. It was shown using simulations, that rectangles are able to support a wide variety of metastable configurations at zero field as well as degenerate ground states, due to their inherent symmetry. Fresnel image sequences later revealed that vortex end domains were favoured over transverse states in the fabricated elements and that on repeated switching, a vortex C state could reverse to form a flux-closure state. As discussed, this behaviour is potentially disastrous for storage devices as the information contained in the cell is effectively lost along with the net component of magnetisation. In contrast, the simulations predicted transverse end domains instead of vortex formation, though this may have been caused by an unrealistically high damping parameter. Excessive damping prevents the magnetisation from fully exploring the energy surface and instead forces the spins to converge to the nearest stable configuration. In addition, the simulated switching fields were found to be almost double in magnitude to those determined experimentally for elements of the same dimensions and initial configuration. Given that the micromagnetic computation deals with structurally perfect geometries and ignores thermal effects, however, this was not surprising. Different sizes of element were then fabricated at constant areal aspect ratio for comparison. Although the magnetic behaviour was similar for all sizes, the switching field increased with decreasing element width. This has been observed in numerous studies and is caused by an increase in shape anisotropy as the edges get closer together. The spins are held in place anti-parallel to the applied field direction until the Zeeman energy dominates and the element is forced to switch. One advantage the rectangular element has over other geometries is a low switching field. This is attributed to the perpendicular magnetisation at the ends of the element where the reversal begins.

After studying the rectangle, a 45° trapezium and parallelogram were investigated. By reducing the element symmetry, it was found that the number of metastable remanent configurations and modes of switching could be reduced. In addition, the ground state degeneracy of the rectangle was removed, resulting in a single preferred configuration. The shape anisotropy causes the magnetisation to lie parallel to the short edges. In effect, a transverse C state can be supported in the trapezium at zero field, whilst a transverse S state is the lowest energy configuration in the parallelogram. The switching fields of these structures were found to be higher than the rectangle, however. This occurred for two reasons. First, the orientation of the short edges with respect to the axis of applied field decreases the effective torque acting on the end domains. In the rectangle, these end sections were found to effect the reversal. Secondly, because of the shape anisotropy of the sloping edges, the adjacent spins are held in place and are reluctant to align with the field. Only at higher field strengths can they rotate against this magnetostatic energy barrier.

The angle of inclination was then varied for each structure as a comparison to the elements with 45° sloping edges. As the angle increased, the switching field dropped as a result of the larger torque. In addition, because of the increasing width at the ends of the element, the probability of vortex formation increased. At larger inclination angles, the trapezoid and parallelogram behaved in the same way as the rectangle, and flux-closure states were observed. At angles of 50° and below, the magnetisation switched between transverse states without the nucleation of vortices. Here, the element edges bias the spins in a preferred direction and limit their rotational freedom. Therefore, at these angles of inclination, the trapezium and parallelogram offered greater magnetic stability than the rectangle, but this came at the cost of a larger coercivity.

Cross-tie domain walls were observed in some of the images in chapters 5 and 6. This was surprising, as these only form in NiFe films with thicknesses of between 30 and 90nm and the deposited material was assumed to be 20nm. It was later discovered that the evaporator FTM was underestimating the film thickness, and in actual fact these elements were closer to 33nm in thickness.

Chapter 6 looked at how notches can be used to pin domain walls and stabilise particular spin configurations. Notches were added to the basic rectangle in an attempt to remove the ground state degeneracy and induce either a transverse C or S state at remanence. By using $120\times 70\times 20\text{nm}^3$ notches in the simulations, the number of metastable states was reduced and the elements underwent single mode switching. In experiment, however, similarly sizes notches were unable to force the desired behaviour, mainly because vortex end domains were supported instead of transverse regions. These complex wall structures cannot be controlled in the same way as a single transverse wall. Instead, the elements behaved much like the basic rectangle. Saying this, the notches did manage to prevent flux-closure formation during long-axis field cycles and by reducing the domain wall length, influenced a vortex to transverse reversal. The switching fields of these elements were found to be higher than the rectangular cell and around the same magnitude as the trapezium and parallelogram. This increase in coercivity is related to the domain wall energy and local shape anisotropy. When a wall is connected to the apex of the notch its length is minimised, rendering the configuration energetically favourable. Also, to avoid an increase in dipole energy at the edges, the notches act to prevent rotation of the spins, causing a further increase in switching field.

The in-plane notch dimensions were then varied in an attempt to uncover further changes in the magnetic behaviour. The simulations revealed two separate reversal mechanisms depending on the area of the notch. At very small sizes, the notches had little effect on the magnetisation of the element. Here, the central section switched first, followed by the end domains at higher field. This two-step reversal was also observed in elements with very large notches. In these structures, however, the notches were found to separate the ends from the bulk of the magnetisation, causing the different sections to behave almost independently. For intermediate sizes, we observed reversal of every domain at the same field value. From simulations and experiment, the coercivity was found to increase with notch aspect ratio. This appeared to be related to the torque on the spins adjacent to the notch, but differences in exchange and magnetostatic energy may also have had an effect. This data was later extracted from the simulations and analysed, but no clear trends were observed. In experiment, the notch dimensions had an influence on the remanent state and reversal behaviour. At small sizes, vortex end domains and flux-closure formation were possible, but as the area of the notch increased, the probability of vortex nucleation dropped. Instead, transverse states were favoured. With the largest notches, the ground state degeneracy was finally removed and the elements were able to switch reproducibly between single ground state configurations. Like the trapezium and parallelogram, however, this ideal behaviour came at the cost of a large coercivity.

Domain wall trap structures were investigated in chapter 7. This type of element had previously been studied using micromagnetic simulations and demonstrated superior behaviour to isolated elements of comparable size. This earlier work predicted reproducible switching behaviour at far smaller fields than is possible with rectangular cells, as well as a reduction in the switching field width dependence. As no experimental studies had been performed on these geometries, a part of this project was to characterise their magnetic behaviour using Lorentz microscopy. Domain wall trap elements were fabricated with the same dimensions as used in the original simulations. However, the shape anisotropy of the end sections proved insufficient to form a head-to-head domain wall and four new geometries had to be fabricated. Increasing fields were applied perpendicular to the central strip in small field steps to determine the magnitude required to form a head-to-head wall in each element. This value was found to be dependent on both the torque and shape anisotropy, with DWT3 requiring the smallest field. The simulations also predicted that two different domain wall structures were possible depending on the width and thickness of the central strip: a transverse domain wall (TDW) favouring narrower, thinner sections of material and a vortex configuration at larger dimensions. To study this experimentally, DWT3 elements were fabricated with strips ranging in width from 50 to 200nm, and film thicknesses of 10 and 20nm. These experiments showed vortex formation in all but the smallest strip, which itself exhibited insufficient contrast to determine the wall structure. Although this disagrees with the simulated phase diagram, fabrication problems may have influenced the results. The 200nm wide elements deposited at a thickness of 20nm were then used for the remainder of this study. Whilst vortex domain walls were found in every element, transverse walls were observed on occasion in DWT1. This was thought to be related to the local symmetry at the corners of the element. As the TDW has a mirror plane of symmetry and the corners of DWTs 2, 3 and 4 are asymmetric, the structure could not be supported. In the DWT1 geometry, however, the TDW symmetry is preserved, thus facilitating its formation.

Saturating fields of 7000 Oe were then applied at various angles to the short axis to characterise the sense of vortex rotation and domain wall position within the element. Fields were applied in both the positive and negative y-directions to nucleate head-to-head and tail-to-tail walls. The vortex domain wall (VDW) was found to be stabilised at five different locations within the strip. At the ends of the strip, the domain walls are pinned to the corners of the element and there is a reduction in exchange energy as a result of the local geometry. At the centre of the strip, on the other hand, magnetostatic fields act on the

VDW from opposite sides and create an energetically stable region. This experiment also revealed that the vortex sense of rotation can be controlled by the field direction. First the 180° wall is biased in one of two orientations by an off-axis field. Then, during the subsequent relaxation, its rotational sense is determined by the direction of magnetisation in the adjacent sections of the element.

Long-axis fields were later applied to study the switching of each element, and the images of DWTs 2, 3 and 4 showed identical behaviour. The VDW could be moved reproducibly between the ends of the strip without propagation into the adjacent sections. As a result of asymmetry in the VDW structure and its interaction with the corner regions, however, different field strengths were required to move the wall in opposite directions. In addition, the magnetostatic effect of the end sections inhibited movement of the wall at the centre of the strip, and a slightly larger field was necessary to overcome the energy barrier.

The switching behaviour of DWT1 was very different from the other geometries. This was attributed to the local geometry at the corners of the element which provided additional stability for the VDW. In general, it was not possible to move the wall reproducibly between the ends of the element. Instead, the head-to-head structure was stretched from the corner before propagating along the strip and out of the element at higher fields. The narrow end sections of this geometry were unable to provide adequate resistance to the wall motion, proving that ends of increasing width are more suitable for trapping domain walls. On occasion, it was observed that less strongly stabilised wall configurations (of higher energy) could be formed when the initialising field was applied along the short axis. In this situation the VDW sense and position are unbiased. These less strongly pinned wall structures could be moved to the opposite end of the element and were seen to switch sense as well as position. In situations where a TDW was formed, fields applied to move the structure were unsuccessful. Instead a vortex was nucleated, changing the TDW to a VDW and reducing the energy of the system.

Next, larger fields were applied to expel the head-to-head wall from each of the elements. It was found that removal of the VDW in DWTs 2 and 3 took place via annihilation with low angle walls in the end sections. In DWTs 1 and 4, on the other hand, the VDW was able to move past the corners of the element and right out of the structure. The reason for this difference in behaviour is down to the width of the end sections. It costs energy to force the VDW into the wider regions because of an increase in domain wall length. In addition, the spins in the centre of these sections can rotate to align with the field, so annihilation is by far the more favourable mechanism. In the narrower geometries the shape anisotropy prevents rotation of the magnetisation, so it is easier just to move the VDW. As the VDW length is kept relatively constant, there is no additional increase in energy. Overall DWT3 was most successful in terms of its ability to support a head-to-head wall that could be moved reproducibly with field. The small operational fields combined with the large domain wall resistance at the ends of the structure make this element more suitable than the others for device applications.

After characterisation of single elements, DWT chains were studied. These were formed by connecting several elements in a given row end-to-end. In this way, the end sections are shared between neighbouring strips which maximises the packing density without adverse magnetostatic effects. The DWT3 geometry was selected because of its symmetry and the success that these elements demonstrated as individual cells. First, short-axis fields were applied to form the walls. As a result of the chain geometry, alternate head-to-head and tail-to-tail configurations were nucleated. Subsequent long-axis fields then moved these structures in opposite directions. The control of a single DWT unit can be achieved only with a local field, and this was not possible in the microscope. The magnetic behaviour within each strip was found to be the same as observed with the individual elements. One notable observation, however, was that the walls moved at slightly different magnitudes of field over a 20 Oe range. At far higher fields, annihilation with low angle walls in the end sections was the dominant removal mechanism as expected.

As a final investigation into the behaviour of DWTs, domain wall injection was studied. Long-axis fields were applied from a near-uniform state to try and nucleate a single wall. During most of these attempts though, reversal of the complete chain took place and no walls were trapped. Still, on odd occasions it was possible to switch several sections of the chain, forming multiple head-to-head walls and also more complex domain structures. A diamond-shaped injection pad was later added to one end. These are usually connected to magnetic nanowires for studying domain wall behaviour. They are designed to reverse at a smaller field that the adjacent section of material, causing the nucleation of a single wall. By applying the long-axis field a head-to-head wall was introduced. However, movement of the VDW was abrupt and it ‘jumped’ between the different traps in the chain until it was driven from the element at higher field. To try and encourage smoother behaviour, similar elements were fabricated using the DWT1 end geometry. It was hoped that the uniform width would allow better control of the wall. Unfortunately, after the initial injection the VDW was stretched and removed from the element in a single step. This uninhibited movement is because narrow end sections do not provide adequate resistance to the wall motion; behaviour observed previously in the single DWT1 elements. It appears, therefore, that further adjustment of the end shape is required before controlled movement of a head-to-head wall is possible in DWT chains of this type.

As well as the work on thin film elements, this project involved the magnetic and physical characterisation of continuous film tunnel junctions. These samples were designed to reduce the Néel coupling by incorporating an artificial antiferromagnet (AAF) in the free layer. It was hoped that compensation of the magnetic surface charge would minimise the offset field without adversely affecting the magnetic behaviour of the film. Three different samples were deposited at Philips Research in Eindhoven, The Netherlands. The first sample, labelled MTJ1, was a standard junction and the second and third samples, MTJ2 and MTJ3, each included an AAF in the free layer. The only physical difference between MTJs 2 and 3 was the AAF layer order; 3NiFe/0.8Ru/8NiFe and 8NiFe/0.8Ru/3NiFe respectively, where the layer thicknesses are in nanometres. Both the magnetic and physical properties were studied before and after the samples were annealed, providing six data sets. The Fresnel and DPC imaging modes were used to probe the magnetic structure, whilst the physical structure was studied with BF/DF TEM and electron diffraction.

By adding an AAF to the stack, the image sequences revealed a 19% reduction in offset for MTJ2 before annealing and a 31% reduction afterwards. Likewise, MTJ3 demonstrated a 24% and 27% decrease. That the Néel coupling decreased further on annealing the stacks is one effect of an increased magnetic homogeneity. When the layers are more uniformly magnetised, the AAF is optimised for charge cancellation. Also, the offset was lower for MTJ2 than MTJ3 after annealing because the lower AAF ferromagnetic (FM) layer is thinner. This enables the poles of opposite polarity to be closer to the tunnel barrier, which compensates the charge more effectively. The coercivity was also affected by adding an AAF to the stack. This was attributed to the rigidity Q-factor. Such behaviour has been well documented, with theory suggesting a dependence on the magnetisation and thickness of the two AAF FM layers. After heat-treatment, however, the coercivity of MTJ2 and MTJ3 dropped below that of the basic junction. Although surprising, this was suspected to be caused by the diffusion of Ru atoms into the FM layers. As atomic mobility increases with thermal energy, it seems plausible that diffusion of the spacer material could reduce the magnetisation of the neighbouring layers.

In terms of the reversal behaviour, each sample was found to change orientation predominantly via the nucleation and movement of domain walls. In polycrystalline films, different regions spaced far enough apart to avoid direct exchange interactions rotate independently to align with the field. Effectively, weakly coupled grains rotate first, followed by those more tightly coupled, giving rise to complex domain configurations. As a result of an improved magnetic uniformity, the domain structure changed dramatically on annealing. Before annealing each sample, the domain walls were short and curved, and many were observed in the field of view. After heat-treatment, however, a small number of long straight walls were captured sweeping across the film. This may be related to the grain structure of the material, although the physical characterisation revealed no obvious changes in structure. Whilst randomly oriented crystallites produce a more complex reversal, a strongly induced easy axis favours a simpler mechanism. Also, the angle of domain walls with respect to the applied field direction was found to differ between the forward and reverse paths of the hysteresis loop. Recent studies on multilayer films have suggested that this could be the result of an imperfect interface giving rise to both unidirectional and biquadratic energy terms. In this situation, a natural angle emerges as the FM passes through different effective fields.

The magnetisation ripple contrast of MTJ2 was far lower than MTJ1 and MTJ3 before annealing. This was unexpected considering the similarities in layer structure between the samples. Initially grain size at the Ru spacer was thought to be responsible, since renucleation occurs on top of the amorphous Al_2O_3 barrier implying that there could be variations in magnetic order with FM layer thickness. A more likely explanation though, is interlayer mixing. If Ru diffused between the NiFe grains, then the thin AAF FM layer of MTJ2 and MTJ3 would become magnetically dead. Therefore, the magnetic contrast in the images would arise from the thicker FM layer. Given these conditions, the grains of MTJ3 grow upon the amorphous Al_2O_3 like MTJ1, but in MTJ2, they grow upon a magnetically dead crystalline base. This additional ordering in MTJ2 may be enough to reduce the ripple contrast relative to the other two samples, which appeared very similar. The magnetisation ripple was found to strongly influence the domain configuration during reversal. In particular, chain-like structures were observed in each film. After annealing, however, the induced easy-axis greatly reduced the ripple contrast allowing the magnetisation to reverse via the long, straight domain walls described previously. Again, this is a result of the improved magnetic homogeneity. To better compare the ripple structure between stacks, the wavelength and dispersion were analysed from Fresnel images. Although these images could not provide quantitative data, they did allow useful information to be obtained in arbitrary units. It was found that as the applied field (anti-parallel to the net direction of free layer magnetisation) approached coercivity, the ripple wavelength and dispersion angle increased. These then dropped suddenly at the critical field before levelling off. This behaviour can be attributed to the Zeeman energy. As the field increases, the weakly coupled grains rotate and drag the more strongly coupled grains behind them. This gradually increases the dispersion until domains are nucleated and irreversible changes take place.

Another observation from the magnetising experiments was the formation of 360° walls. These structures form when Néel walls of opposite chirality come together, and are often stable up to high fields. They occur in abundance in multilayer films containing AAFs because the AF coupling adds an additional contribution to their nucleation and stability. They tend to be nucleated in the bottom AAF FM where they are stabilised by surface charge from roughness at the tunnel barrier. This configuration is then mirrored in the top AAF FM, reducing the magnetostatic energy of the system. In addition, roughness at the Ru spacer causes local variations in the AF coupling which prevents coherent reversal and creates nucleation and pinning sites. Their robustness is down to a balance of Zeeman, domain wall and AF coupling energy terms. As the field increases, the Zeeman and domain wall energies become unfavourable for the wall in the bottom AAF FM. This causes a decrease in the central domain of the 360° wall. However, AF coupling preserves the wall structure until the field strength dominates, causing it to collapse. In the upper layer, the field is parallel to the magnetisation at the centre of the wall which stabilises the configuration. Because of AF coupling to the lower layer, however, this domain cannot grow in size. Only at very high field is the domain wall energy sufficient to remove the upper wall. This is the reason why 360° loops were observed at the end of the MTJ2 and MTJ3 reversal sequences, but disappeared at low field in MTJ1.

Following their magnetic characterisation, the physical structure of each MTJ sample was studied primarily to confirm the arguments on free layer grain size and interlayer mixing. First, electron diffraction was performed through the complete stack to check for obvious structural differences between the samples and to ensure that (111) texturing was induced by the seed layers. This was then repeated after annealing to examine the effects of heat-treatment. The diffraction patterns were identical for all samples both before and after the heat cycle, indicating no major variations in morphology. When the samples were tilted, the ring contrast changed noticeably indicating a high degree of texturing. Indexing of the rings later revealed that the texturing was indeed in the [111] direction.

Afterwards, in-plane grain size estimations were made from BF/DF images. This gives no information on the grains within the individual layers, but does provide an average measurement for each film. The mean grain diameter was the same for all samples and was found to be ~7nm. In addition, the heating and field-cooling cycle had a negligible effect on their size. To obtain an estimation of the free layer grain size without larger grains in the IrMn and CoFe layers influencing the result, a second batch of samples were fabricated including only the upper layers of the stack and a NiFe seed layer. A grain diameter of 3-4nm was measured for each sample, proving that grains in the lower layers of the stack were in fact contributing to the earlier image contrast. The grains in the MTJ1 single free layer were slightly smaller than those in the AAF of MTJs 2 and 3.

To obtain information on the grain structure within the separate layers, a cross-sectional study was necessary. Diffraction contrast in these BF/DF images revealed that only the NiFe, IrMn, CoFe and Ru layers of the structure were crystalline. Analysis of the crystallites in these layers then showed that the grain size was very dependent on layer thickness. This strengthens the argument for changes in ripple being related to differences in grain size at the Ru spacer. In terms of the film growth, many grains which started in the NiFe seed layer continued into the IrMn and CoFe, despite differences in the lattice parameter. These grains then stopped at the Al_2O_3 and new crystallites were nucleated in the free layer. In MTJs 2 and 3, most grains continued through the Ru and into the upper AAF FM, but some were seen to stop and renucleate at the spacer. This may have been caused by lattice mismatch at the layer boundary.

Layer roughness, responsible for the Néel coupling in these samples, was analysed last. Undulations at the Al_2O_3 were found to be correlated with those at the buffer layer. However, large grains in the NiFe, IrMn and CoFe produced additional local fluctuations of a higher frequency. In MTJs 2 and 3, the Ru roughness remained conformal with the tunnel barrier because the free layer grain size was insufficient to redefine the waviness. To quantify the Al_2O_3 roughness amplitude, distances between points at the centre of this layer and a reference line were measured. Following this, their mean and standard deviation were calculated. The average inter-peak distance was also determined to estimate the wavelength. The roughness of each stack was found to be far larger than the Philips VSM least squares fit had estimated, but the wavelength was similar.

One thing which could not be established from these cross-sections, however, was interlayer mixing. If Ru diffusion into the AAF NiFe had occurred, then this may have explained the differences in ripple contrast and reversal behaviour of MTJ2 relative to the other stacks. It was hoped that this information could be obtained from the BF/DF images, but in hindsight, compositional characterisation using analytical TEM may have been the better option.

9.3 Future work

In this section, a new idea involving domain wall trap elements is proposed. In chapter 7, it was shown that these structures support head-to-head domain walls that can be moved between the ends of the element to store information. However, instead of using these systems as storage cells, it may be possible to adjust their geometry to create elements that serve as one-dimensional magnetic field sensors. The basic concept uses the position of the head-to-head wall as a measure of the strength and direction of applied field. To achieve this, a larger strip of material would be required to enable detection over a reasonable field range. In addition, success of the system would rely on a smooth and reproducible domain wall movement with a high field sensitivity. As well as strip length, the width of the strip is an important issue. There must be a sufficient energy barrier for the wall to overcome as it moves along the strip, otherwise it will simply switch between the ends of the element (Newton's first law of motion). This would be the case if we were to take the basic DWT3 geometry and extend the central section (Fig. 9.1).

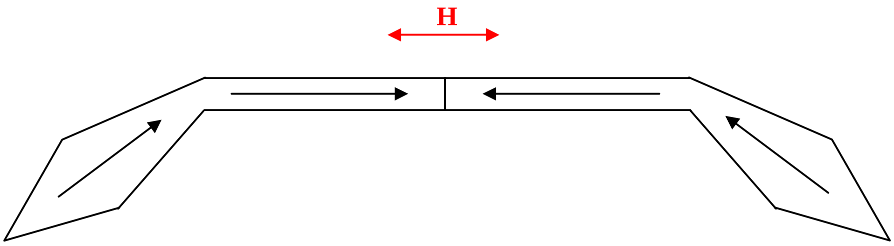

Fig. 9.1: Strips of uniform width provide little resistance to the domain wall motion and are unsuitable for this type of sensor device.

Therefore, what is required is an element where the strip width increases along the x-axis from the centre (Fig. 9.2).

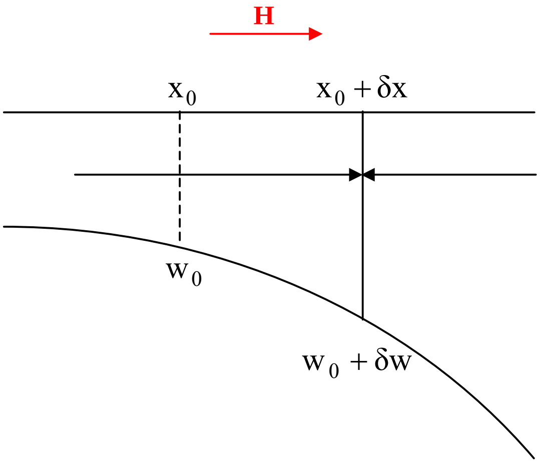

Fig. 9.2: Definition of the strip dimensions used in the derivation of equation 9.3.

In this case the domain wall length and energy increase as the wall progresses along the strip in either direction, which can only occur if the applied field is large enough to overcome the energy barrier. The change in energy as the wall moves can be formulated by taking into account the various energy terms. The saving in Zeeman energy as the wall propagates distance, δx, is given by,

$$\Delta E_Z = 2M_s Hwt\delta x \qquad (9.1)$$

whilst the gain in domain wall energy is,

$$\Delta E_W = \sigma\delta wt \tag{9.2}$$

where w and t are the strip width and thickness respectively, δw is the change in width and σ is the domain wall energy (area) density. For a linear response, we require $H = kx + c$, with k and c constants. By equating the two expressions, substituting for H and rearranging the equation, we obtain,

$$\frac{\delta w}{w} = \frac{2M_s(kx + c)}{\sigma}\delta x$$

Integrating both sides then gives,

$$\ln|w| = \frac{M_s x}{\sigma}(kx + 2c) + d$$

where d is a constant of integration. This can be rewritten as,

$$w = \exp[\frac{M_s x}{\sigma}(kx + 2c) + d] \tag{9.3}$$

So the width of the element must vary exponentially if linear behaviour is to be realised. Unfortunately this will involve a large element with very wide end sections (Fig. 9.3), so microstructure is likely to play a significant role. Whilst the theory may be convincing on paper, it would be interesting to see if this behaviour could be achieved in practise. Finite element simulations would be well-suited to this type of problem and could provide further information prior to fabrication.

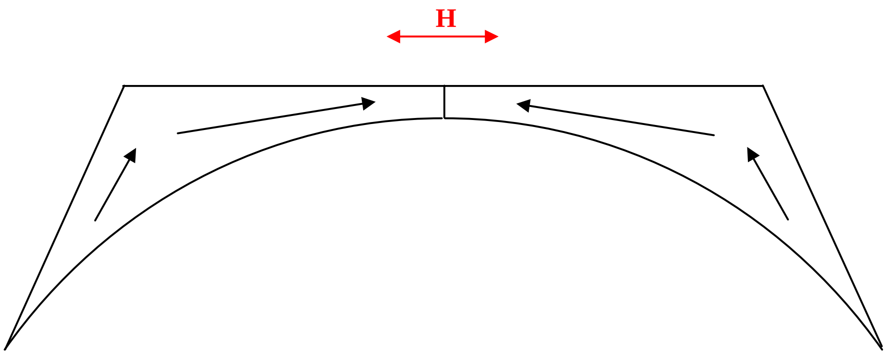

Fig. 9.3: An element with exponentially increasing width may be required to achieve the desired behaviour.

Appendix

This appendix provides the fabrication parameters for the PMMA/PMMA (Table A.1), LOR/PMMA (Table A.2) and ZEP/PMMA (Table A.3) lift-off processes, as well as detailed schematics of the FEI Tecnai T20 (Fig. A.1) and Philips CM20 (Fig. A.2) microscopes.

PMMA/PMMA process

Step	*Parameters*
Substrate clean	Acetone in 45°C hot water bath for 10mins IPA in 45°C hot water bath for 5mins Dry with N_2 gun
Resist application	Spin 2010 PMMA at 5000rpm for 60secs to deposit: 2.5% - 40nm 4% - 100nm 8% - 200nm Bake in 180°C oven for 1 hour Repeat spin and bake cycle for 2041 PMMA
Reflective coating	Evaporate 30nm of Aluminium
Exposure	Prepare design and layout files then submit job to beamwriter
Aluminium strip	CD26 for 60secs at 21°C RO water for 30secs Dry with N_2 gun
Development	MIBK:IPA 1:2.5 for 60secs at 21°C IPA for 30secs Dry with N_2 gun
Ash	35W for 60secs to remove 5nm of material
Metallisation	Evaporate 20nm of Permalloy
Lift-off	Acetone in 45°C hot water bath until material is removed IPA in 45°C hot water bath for 5mins Dry with N_2 gun
Gold coating	Sputter 4nm of Gold

Table A.1: Detailed fabrication process using PMMA/PMMA bilayers of resist.

LOR/PMMA process

Step	*Parameters*
Substrate clean	Acetone in 45°C hot water bath for 10mins IPA in 45°C hot water bath for 5mins Dry with N_2 gun
Adhesion promotion	Oxygen plasma ash, 35W for 60secs
Resist application	Spin 20% LOR-10A for 60secs to deposit: 7000rpm - 40nm 5000rpm - 100nm 3000rpm - 200nm Bake in 180°C oven for 10mins Spin and bake 2041 PMMA as described in Table A.1
Reflective coating	Evaporate 30nm of Aluminium
Exposure	Prepare design and layout files then submit job to beamwriter
Aluminium strip	CD26 for 60secs at 21°C RO water for 30secs Dry with N_2 gun
Development	PMMA - MIBK:IPA 1:2.5 for 60secs at 21°C IPA for 30secs Dry with N_2 gun LOR - CD26 for 60secs at 21°C RO water for 30secs Dry with N_2 gun
Ash	35W for 60secs
Metallisation	Evaporate 20nm of Permalloy
Lift-off	SVC-14 in 45°C hot water bath until material is removed methanol in 45°C hot water bath for 5mins IPA in 45°C hot water bath for 5mins Dry with N_2 gun
Gold coating	Sputter 4nm of Gold

Table A.2: Detailed fabrication process using LOR/PMMA bilayers of resist.

ZEP/PMMA process

Step	*Parameters*
Substrate clean	Acetone in 45°C hot water bath for 10mins IPA in 45°C hot water bath for 5mins Dry with N_2 gun
Adhesion promotion	Oxygen plasma ash to remove 5nm of material
Resist application	Spin ZEP 520A for 60secs to deposit: 25% at 4000rpm - 40nm 40% at 2500rpm - 100nm 60% at 2000rpm - 200nm Bake in 180°C oven for 1hour Spin and bake 2041 PMMA as described in Table A.1
Reflective coating	Evaporate 30nm of Aluminium
Exposure	Prepare design and layout files then submit job to beamwriter
Aluminium strip	CD26 for 60secs at 21°C RO water for 30secs Dry with N_2 gun
Development	PMMA - MIBK:IPA 1:2.5 for 60secs at 21°C IPA for 30secs Dry with N_2 gun ZEP - o-xylene for 60secs at 21°C IPA for 30secs Dry with N_2 gun
Ash	35W for 60secs
Metallisation	Evaporate 20nm of Permalloy
Lift-off	Acetone in 45°C hot water bath until material is removed IPA in 45°C hot water bath for 5mins Dry with N_2 gun
Gold coating	Sputter 4nm of Gold

Table A.3: Detailed fabrication process using ZEP/PMMA bilayers of resist.

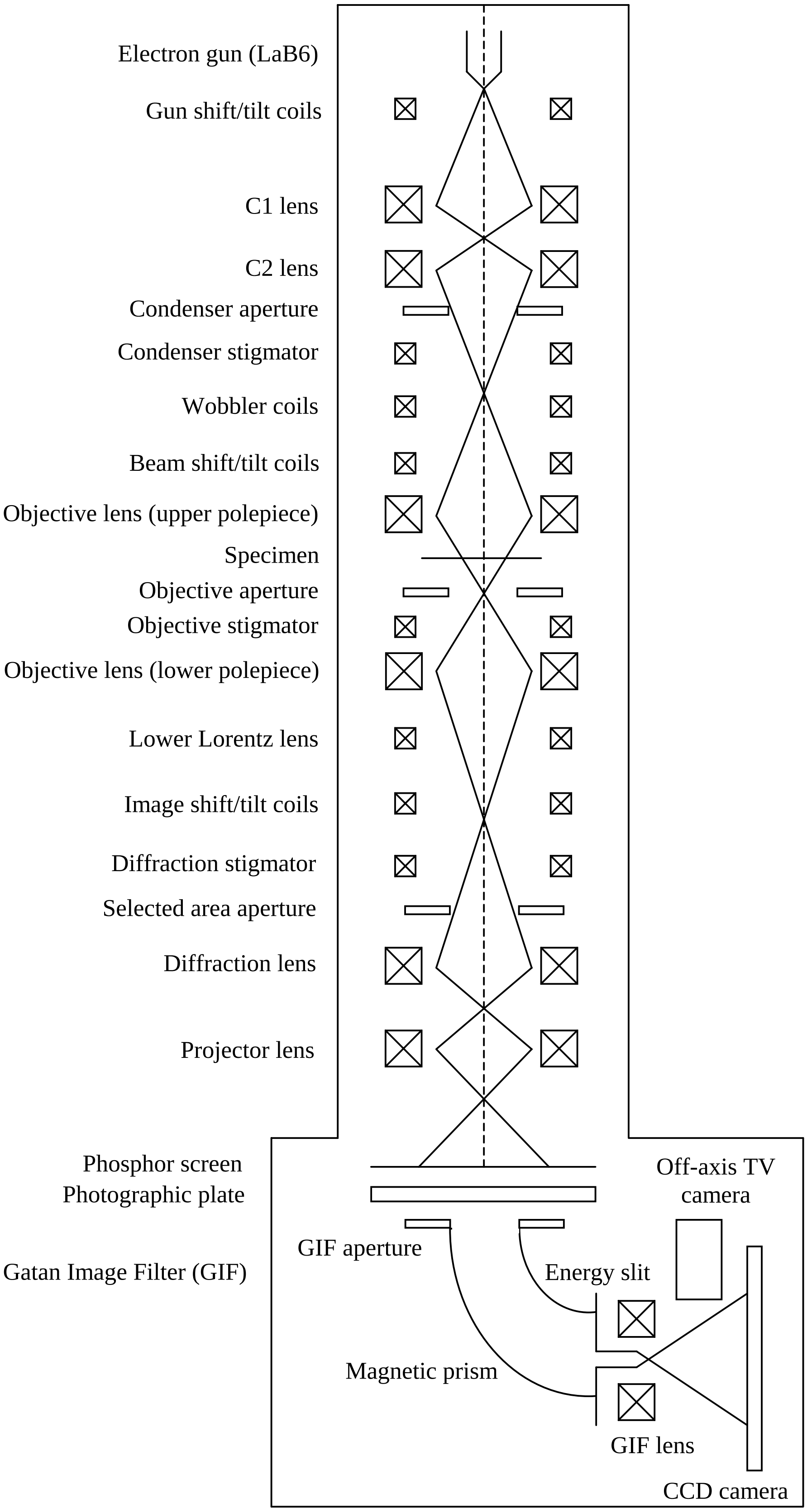

Fig. A.1: The FEI Tecnai T20 TEM column.

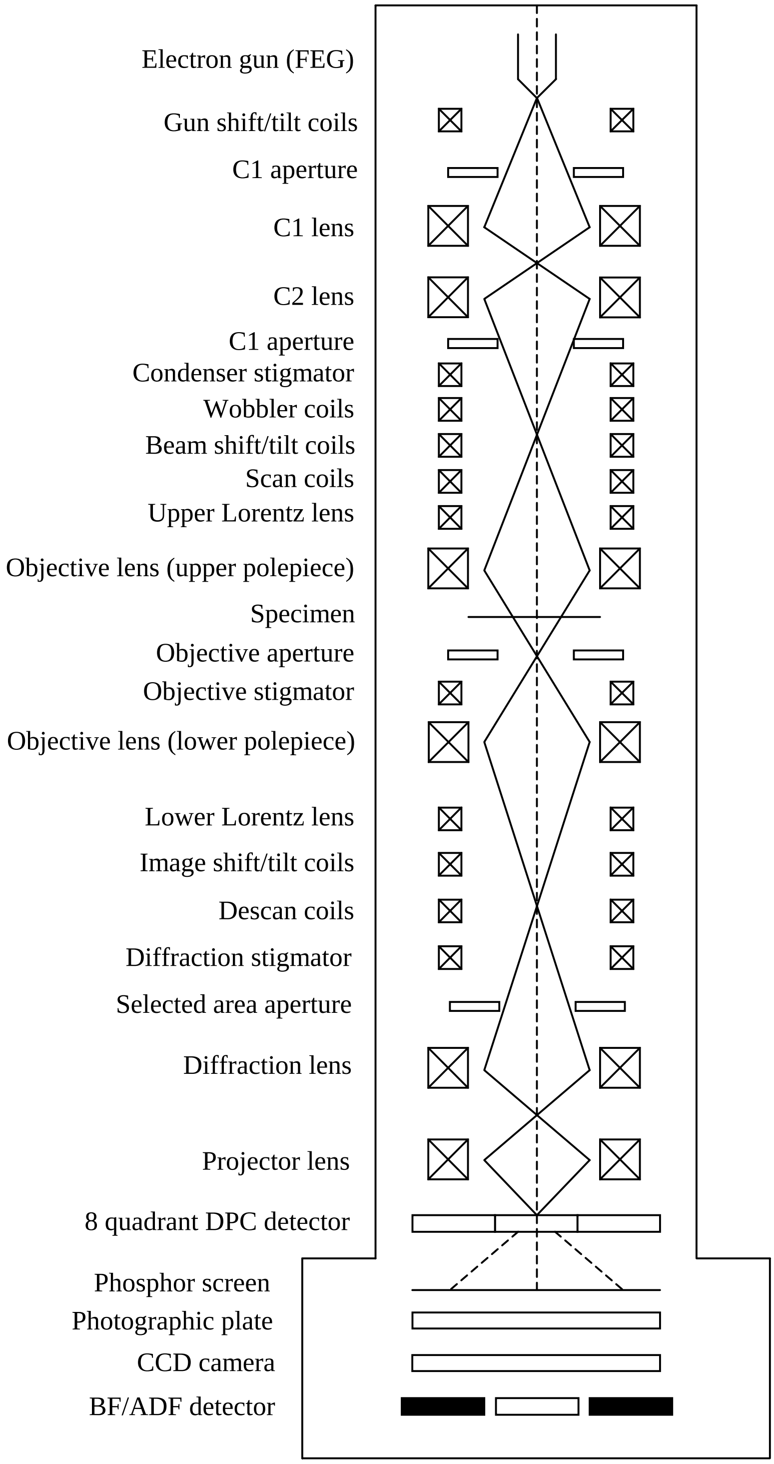

Fig. A.2: The Philips CM20 TEM/STEM column.

References

[1] P. Weiss, J. Phys. **6**, 661 (1907).

[2] W. Heisenberg, Z. Physik, **49**, 619 (1928).

[3] W. Pauli, Z. Physik, **31**, 765 (1925).

[4] H. W. Fuller and M. E. Hale, J. Appl. Phys. **31**, 238 (1960).

[5] J. Fidler, R. W. Chantrell, T. Schrefl and M. A. Wongsam, Encyclopedia of Materials: Science and Technology, Elsevier, 5642 (2001).

[6] D. K. Koltsov and M. A. Perry, Physics World, July, 31 (2004).

[7] R. Becker, Z. Phys. **67**, 253 (1930).

[8] F. Bitter, Phys. Rev. **38**, 1903 (1931).

[9] W. Rave and A. Hubert, IEEE Trans. Magn. **36**, 3886 (2000).

[10] M. Prutton, Thin Ferromagnetic Films, Butterworth (1964).

[11] E. E. Huber, D. O. Smith and J. B. Goodenough, J. Appl. Phys. **29**, 294 (1958).

[12] A. Hubert and R. Schafer, Magnetic Domains, Springer (1998).

[13] D. Jiles, Introduction to Magnetism and Magnetic Materials, Chapman and Hall (1998).

[14] E. C. Stoner and E. P. Wohlfarth, Phil. Trans. Roy. Soc. **A240**, 599 (1948).

[15] M. Labrune, J. C. S. Kools and A. Thiaville, J. Magn. Magn. Mater. **95**, 76 (1997).

[16] W. Thomson, Math. Phys. Papers, **2**, 267 (1856).

[17] T. McGuire and R. Potter, IEEE Trans. Magn. **11**, 1018 (1975).

[18] P. Grünberg, R. Schreiber, Y. Pang, M. B. Brodsky and H. Sowers, Phys. Rev. Lett. **57**, 2442 (1986).

[19] M. Julliere, Phys. Lett. **54A**, 225 (1975).

[20] R. von Helmolt, J. Weckberg, B. Holzapfel, L. Schultz and K. Samwer, Phys. Rev. Lett. **71**, 2331 (1993).

[21] E. Y. Tsymbal, O. N. Mryasov and P. R. LeClair, J. Phys.: Condens. Matter. **15**, R109 (2003).

[22] P. M. Tedrow, R. Meservey and P. Fulde, Phys. Rev. Lett. **25**, 1270 (1970).

[23] C. L. Platt, M. R. McCartney, F. T. Parker and A. E. Berkowitz, Phys. Rev. B **61**, 9633 (2000).

[24] J. F. Bobo, L. Gabillet and M. Bibes, J. Phys.: Condens. Matter. **16**, 5471 (2004).

[25] J. C. Slonczewski, Phys. Rev. B **39**, 6995 (1989).

[26] M. Pomerantz, J. C. Slonczewski and E. Spiller, J. Appl. Phys. **61**, 3747 (1987).

[27] J. Nogués and I. K. Schuller, J. Magn. Magn. Mater. **192**, 203 (1999).

[28] W. H. Meiklejohn and C. P. Bean. Phys. Rev. **102**, 1413 (1956).

[29] O. Massenet, F. Biragnet, H. Juretschke, R. Montmory and A. Yelon, IEEE Trans. Magn. **2** 553 (1966).

[30] J. F. Bobo, H. Kikuchi, O. Redon, E. Snoeck, M. Piecuch and R. L. White, Phys. Rev. B **60**, 4131 (1999).

[31] M. A. Ruderman and C. Kittel, Phys. Rev. **96**, 99 (1954).

[32] L. Néel, Comptes Rendus **255**, 1676 (1962).

[33] M. D. Stiles, J. Magn. Magn. Mater. **200**, 322 (1999).

[34] J. Zhang and R. M. White, IEEE Trans. Magn. **32**, 4630 (1996).

[35] J. C. S. Kools and W. Kula, J. Appl. Phys. **85**, 4466 (1999).

[36] H. W. Fuller and D. L. Sullivan, J. Appl. Phys. **33**, 1063 (1962).

[37] H. W. Fuller and L. R. Lakin, J. Appl. Phys. **34**, 1069 (1963).

[38] F. J. Friedlaender and L. F. Silva, J. Appl. Phys. **36**, 946 (1965).

[39] J. C. Slonczewski and S. Middelhoek, Appl. Phys. Lett. **6**, 139 (1965).

[40] S. Middelhoek, J. Appl. Phys. **37**, 1276 (1966).

[41] B. R. Craig, S. McVitie, J. N. Chapman, A. B. Johnston and D. O. O’Donnell, J. Appl. Phys. **100**, 053915 (2006).

[42] J. O. Oti and S. E. Russek, IEEE. Trans. Magn. **33**, 3298 (1997).

[43] T. Kimura, F. Wakay and K. Gamo, Jpn. J. Appl. Phys. **40**, 6357 (2001).

[44] T. Kimura and Y. Itagaki, Appl. Phys. Lett. **78**, 4007 (2001).

[45] K. Shigeto. T. Okuno, T. Shinjo, Y. Suzuki and T. Ono, J. Appl. Phys. **88**, 6636 (2000).

[46] M. W. Davidson and M. Abramowitz, Optical Microscopy, National High Magnetic Field Laboratory, FL, USA (1999).

[47] S. J. Pennycook, A. R. Lupini, A. Borisevich, M. Varela, Y. Peng, P. D. Nellist, G. Duscher, R. Buczko and S. T. Pantelides, Proceedings of the 2003 International Conference on Characterisation and Metrology for ULSI technology, **683**, 627 (2003).

[48] D. B. Williams and C. B. Carter, Transmission Electron Microscopy, Kluwer Academic/Plenum Publishing (1996).

[49] D. Chescoe and P. J. Goodhew, The Operation of Transmission and Scanning Electron Microscopy, Bios Scientific Publishers Ltd (1990).

[50] P. J. Goodhew, Introduction to Scanning Transmission Electron Microscopy, Bios Scientific Publishers Ltd (1997).

[51] I. MacLaren, Y. Ivanisenko, R. Z. Valiev and H. J. Fecht, J. Phys.: Conf. Ser. **26**, 335 (2006).

[52] R. Lindsay, J. N. Chapman, A. J. Craven and D. McBain, Ultramicroscopy, **80**, 41 (1999).

[53] J. N. Chapman, J. Phys. D: Appl. Phys. **17**, 623 (1984).

[54] K. Tsuno and T. Taoka, Jap. J. Appl. Phys. **22**, 1041 (1983).

[55] J. N. Chapman, A. B. Johnston, L. J. Heyderman, S. McVitie and W. A. P. Nicholson, IEEE Trans. Magn. **30**, 4479 (1994).

[56] J. N. Chapman, P. R. Aitchison, K. J. Kirk, S. McVitie, J. C. S. Kools and M. F. Gillies, J. Appl. Phys. **83**, 5321 (1998).

[57] J. N. Chapman and M. R. Scheinfein, J. Magn. Magn. Mater. **83**, 223 (1990).

[58] N. H. Dekkers and H. de Lang, Optik **30**, 452 (1974).

[59] N. H. Dekkers and H. de Lang, Philips Tech. Rev. **37**, 1 (1977).

[60] J. N. Chapman and G. R. Morrison, J. Magn. Magn. Mater. **35**, 254 (1983).

[61] J. N. Chapman, S. McVitie and I. R. McFadyen, Scanning Microscopy Supplement 1, J. Kirschner, K. Murata and J. A. Venables (eds.) AMF O'Hare, Chicago, 221 (1987).

[62] J. N. Chapman, I. R. McFadyen and S. McVitie, IEEE Trans. Magn. **26**, 1506 (1990).

[63] K. E. Drexler, Engines of Creation, Anchor Books (1986).

[64] P. Maury, M. Peter, V. Mahalingam, D. N. Reinhoudt and J. Huskens, Adv. Funct. Mater. **15**, 451 (2005).

[65] G. Decher, Science **277**, 1232 (1997).

[66] B. Khamsehpour, C. D. W. Wilkinson, J. N. Chapman and A. B. Johnston, J. Vac. Sci. Technol. B, **14**, 3361 (1996).

[67] C. P. Scott, A. J. Craven, P. Hatto and C. Davies, J. Microsc. **182**, 186 (1996).

[68] R. Menon, A. Patel, D. Gil and H. I. Smith, Materials Today, 26, February (2005).

[69] D. Macintyre and S. Thoms, Introduction to Ebeam Lithography training course, University of Glasgow (2003).

[70] T. H. P. Chang, J. Vac. Sci. Technol. **12**, 1271 (1975).

[71] D. R. Medeiros, A. Aviram, C. R. Guarnieri, W-S. Huang, R. Kwong, C. K. Magg, A. P. Mahorowala, W. M. Moreau, K. E. Petrillo and M. Angelopoulos, IBM J. Res. Dev. **45**, 639 (2001).

[72] H. Ito, IBM J. Res. Dev. **41**, 69 (1997).

[73] S-C. Chang and J. M. Kempisty, Mat. Res. Soc. Symp. Proc. **729**.

[74] B. Khamsehpour, C. D. W. Wilkinson and J. N. Chapman, Appl. Phys. Lett. **67**, 3194 (1995).

[75] K. Kinoshita, K. Yamada and H. Matsutera, IEEE Trans. Magn. **27**, 4888 (1991).

[76] M. Hatzakis, B. J. Canavello and J. M. Shaw, IBM J. Res. Dev. **24**, 452 (1980).

[77] M. Herrmann, S. McVitie and J. N. Chapman, J. Appl. Phys. **87**, 2994 (2000).

[78] S. A. Campbell, The Science and Engineering of Microelectronic Fabrication, Oxford University Press (2001).

[79] L. Landau and E. Lifshitz, Physik. Z. Sowjetunion. **8**, 153 (1935).

[80] W. F. Brown, Jr., Phys. Rev. **58**, 736 (1940).

[81] W. F. Brown, Jr., Phys. Rev. **105**, 1479 (1957).

[82] W. F. Brown, Jr., J. Appl. Phys. **29**, 470 (1958).

[83] W. F. Brown, Jr., J. Appl. Phys. **30**, 625 (1959).

[84] W. F. Brown, Jr., J. Appl. Phys. **33**, 3026 (1962).

[85] W. F. Brown, Micromagnetics, Wiley Interscience, New York (1963).

[86] T. L. Gilbert, Phys. Rev. **100**, 1243 (1955).

[87] M. d'Aquino, PhD thesis: Non-linear Magnetisation Dynamics in Thin Films and Nanoparticles, Università degli Studi di Napoli Federico II (2004).

[88] J. Fidler, R. W. Chantrell, T. Schrefl and M. A. Wongsam, Encyclopedia of Materials: Science and Technology, Elsevier, 5642 (2001).

[89] R. D. McMichael, Introduction to Micromagnetics, IoP meeting, London, December (2006).

[90] M. J. Donahue and D. G. Porter, NISTIR 6376, National Institute of Standards and Technology, Gaithersburg, MD (1999).

[91] J. Fidler and T. Schrefl, J. Phys. D: Appl. Phys. **33**, R135 (2000).

[92] Y. Aharonov and D. Bohm, Phys. Rev. **115**, 485 (1959).

[93] S. McVitie, G. S. White, J. Scott, P. Warin and J. N. Chapman, J. Appl. Phys. **90**, 5220 (2001).

[94] S. McVitie, Quantitative Lorentz TEM: The Transport of Intensity Equation, SSP Group Colloquium, Department of Physics and Astronomy, University of Glasgow (2005).

[95] S. McVitie and G. S. White, J. Phys. D: Appl. Phys. **37**, 280 (2004).

[96] R. E. Dunin-Borkowski, Ultramicroscopy **83**, 193 (2000).

[97] M. de Graef, Introduction to Conventional Transmission Electron Microscopy, Cambridge University Press (2003).

[98] M. de Graef and Y. Zhu, J. Appl. Phys. **89**, 7177 (2001).

[99] M. Beleggia, M. A. Schofield, V. V. Volkov and Y. Zhu, Ultramicroscopy **102**, 37 (2004).

[100] P. Donnadieu, M. Verdier, G. Berthomé and P. Mur, Ultramicroscopy **100**, 79 (2004).

[101] S. McVitie and M. Cushley, Ultramicroscopy **106**, 423 (2006).

[102] I. A. Beardsley, IEEE Trans. Magn. **25**, 671 (1989).

[103] V. V. Volkov, Y. Zhu and M. de Graef, Micron **33**, 411 (2002).

[104] M. Mansuripur, J. Appl. Phys. **69**, 2455 (1991).

[105] J. M. Cowley, Diffraction Physics, 2nd Edition, North Holland, Amsterdam (1975).

[106] J. H. C. Spence, Experimental High Resolution Electron Microscopy, 2nd Edition, Oxford University Press, New York (1988).

[107] M. R. Teague, J. Opt. Soc. Am. **73**, 1434 (1983).

[108] D. Paganin and K. A. Nugent, Phys. Rev. Lett. **80**, 2586 (1998).

[109] W. Rave and A. Hubert, IEEE Trans. Magn. **36**, 3886 (2000).

[110] J. Shi, S. Tehrani, T. Zhu, Y. F. Zheng and J. –G. Zhu, Appl. Phys. Lett. **74**, 2525 (1999).

[111] J. Shi, T. Zhu, S. Tehrani, Y. F. Zheng and J. –G. Zhu, J. Magn. Magn. Mater. **198-199**, 251 (1999).

[112] X. Liu, J. N. Chapman, S. McVitie and C. D. W. Wilkinson, Appl. Phys. Lett. **84**, 4406 (2004).

[113] X. Liu, J. N. Chapman, S. McVitie and C. D. W. Wilkinson, J. Appl. Phys. **96**, 5173 (2004).

[114] K. J. Kirk, J. N. Chapman, S. McVitie, P. R. Aitchison and C. D. W. Wilkinson, Appl. Phys. Lett. **75**, 3683 (1999).

[115] K. J. Kirk, Contemporary Physics, **41**, 61 (2000).

[116] S. McVitie and J. N. Chapman, Microsc. Microanal. **3**, 146 (1997).

[117] A. B. Johnston, J. N. Chapman, B. Khamsehpour and C. D. W. Wilkinson, J. Phys. D: Appl. Phys. **29**, 1419 (1996).

[118] J. N. Chapman, P. R. Aitchison, K. J. Kirk, S. McVitie, J. C. S. Kools and M. F. Gillies, J. Appl. Phys. **83**, 5321 (1998).

[119] R. D. Gomez, T. V. Luu, A. O. Pak, K. J. Kirk and J. N. Chapman, J. Appl. Phys. **85**, 6163 (1999).

[120] S. McVitie, L. Zhou and J. N. Chapman, J. Phys. D: Appl. Phys. **32**, 2714 (1999).

[121] H. Ardhuin, J. N. Chapman, P. R. Aitchison, M. F. Gillies, K. J. Kirk and C. D. W. Wilkinson, J. Appl. Phys. **88**, 2760 (2000).

[122] K. J. Kirk, J. N. Chapman, S. McVitie, P. R. Aitchison and C. D. W. Wilkinson, J. Appl. Phys. **87**, 5105 (2000).

[123] K. J. Kirk, M. R. Scheinfein, J. N. Chapman, S. McVitie, M. F. Gillies, B. R. Ward and J. G. Tennant, J. Phys. D: Appl. Phys. **34**, 160 (2001).

[124] T. Schrefl, J. Fidler, K. J. Kirk and J. N. Chapman, J. Magn. Magn. Mater. **175**, 193 (1997).

[125] K. J. Kirk, J. N. Chapman and C. D. W. Wilkinson, Appl. Phys. Lett. **71**, 539 (1997).

[126] M. Redjdal, P. W. Gross, A. Kazmi and F. B. Humphrey, J. Appl. Phys. **85**, 6193 (1999).

[127] J. Gadbois, J. –G. Zhu, W. Vavra and A. Hurst, IEEE Trans. Magn. **34**, 1066 (1998).

[128] M. Rührig, B. Khamsehpour, K. J. Kirk, J. N. Chapman, P. Aitchison, S. McVitie and C. D. W. Wilkinson, IEEE Trans. Magn. **32**, 4452 (1996).

[129] G. Yi, P. R. Aitchison, W. D. Doyle, J. N. Chapman and C. D. W. Wilkinson, J. Appl. Phys. **92**, 6087 (2002).

[130] K. J. Kirk, J. N. Chapman and C. D. W. Wilkinson, J. Appl. Phys. **85**, 5237 (1999).

[131] A. S. Arrott, Z. Metallkd. **93**, 963 (2002).

[132] H. Koop, H. Brückl, D. Meyners and G. Reiss, J. Magn. Magn. Mater. **272-276**, e1475 (2004).

[133] C. K. Lim, Y. S. Kim, N. Y. Park and J. Lee, IEEE Trans. Magn. **41**, 2670 (2005).

[134] R. D. McMichael and M. J. Donahue, IEEE Trans. Magn. **33**, 4167 (1997).

[135] Y. Nakatani, A. Thiaville and J. Miltat, J. Magn. Magn. Mater. **290-291**, 750 (2005).

[136] G. Tatara, Y.-W. Zhao, M. Munoz and N. Garcia, Phys. Rev. Lett. **83**, 2030 (1999).

[137] H. D. Chopra and S. Z. Hua, Phys. Rev. B **66**, 020403 (2002).

[138] D. A. Allwood, G. Xiong, M. D. Cooke, C. C. Faulkner, D. Atkinson, N. Vernier and R. P. Cowburn, Science **296**, 2003 (2002).

[139] N. Vernier, D. A. Allwood, D. Atkinson, M. D. Cooke, and R. P. Cowburn, Europhys. Lett. **65**, 526 (2004).

[140] J. Grollier, D. Lacour, V. Cros, A. Hamzic, A. Vaurès, A. Fert, D. Adam and G. Faini, J. Appl. Phys. **92**, 4825 (2002).

[141] J. Grollier, P. Boulenc, V. Cros, A. Hamzic, A. Vaurès, A. Fert, D. Adam and G. Faini, Appl. Phys. Lett. **83**, 509 (2003).

[142] P. Bruno, Phys. Rev. Lett. **83**, 2425 (1999).

[143] Y. Labaye, L. Berger and J. M. D. Coey, J. Appl. Phys. **91**, 5341 (2002).

[144] M. Kläui, C. A. F. Vaz, J. A. C. Bland, W. Wernsdorfer, G. Faini and E. Cambril, J. Appl. Phys. **93**, 7885 (2003).

[145] M. Kläui, J. Rothman, L. Lopez-Diaz, C. A. F. Vaz, J. A. C. Bland and Z. Cui, Appl. Phys. Lett. **84**, 1910 (2004).

[146] L. Lopez-Diaz, M. Kläui, J. Rothman and J. A. C. Bland, Physica B, **306**, 211 (2001).

[147] M. Kläui, C. A. F. Vaz, J. Rothman, J. A. C. Bland, W. Wernsdorfer, G. Faini and E. Cambril, Phys. Rev. Lett. **90**, 097202 (2003).

[148] M. Kläui, C. A. F. Vaz, J. A. C. Bland, W. Wernsdorfer, G. Faini, E. Cambril, L. J. Heyderman, F. Nolting and U. Rüdiger, Phys. Rev. Lett. **94**, 106601 (2005).

[149] C. C. Faulkner, M. D. Cooke, D. A. Allwood, D. Petit, D. Atkinson and R. P. Cowburn, J. Appl. Phys. **95**, 6717 (2004).

[150] A. J. Zambano and W. P. Pratt, Jr., Appl. Phys. Lett. **85**, 1562 (2004).

[151] D. Lacour, J. A. Katine, L. Folks, T. Block, J. R. Childress, M. J. Carey and B. A. Gurney, Appl. Phys. Lett. **84**, 1910 (2004).

[152] S. H. Florez, M. Dreyer, K. Schwab, C. Sanchez and R. D. Gomez, J. Appl. Phys. **95**, 6720 (2004).

[153] C. C. Yao, D. G. Hasko, Y. B. Xu, W. Y. Lee and J. A. C. Bland, J. Appl. Phys. **85**, 1689 (1999).

[154] A. Hirohata, Y. B. Xu, C. C. Yao, H. T. Leung, W. Y. Lee, S. M. Gardiner, D. G. Hasko, J. A. C. Bland and S. N. Holmes, J. Appl. Phys. **87**, 4727 (2000).

[155] A. Hirohata, Y. B. Xu, C. C. Yao, H. T. Leung, W. Y. Lee, S. M. Gardiner, D. G. Hasko, J. A. C. Bland and S. N. Holmes, J. Magn. Magn. Mater. **226-230**, 1845 (2001).

[156] M. Kläui, C. A. F. Vaz, A. Lapicki, T. Suzuki, Z. Cui and J. A. C. Bland, Microelectron. Eng. **73-74**, 785 (2004).

[157] Y. C. Chen, Y. D. Yao, S. F. Lee, Y. Liou, J. L. Tsai and Y. A. Lin, Appl. Phys. Lett. **86**, 053111 (2005).

[158] R. D. McMichael, J. Eicke, M. J. Donahue and D. G. Porter, J. Appl. Phys. **87**, 7058 (2000).

[159] C. Brownlie, S. McVitie, J. N. Chapman and C. D. W. Wilkinson, J. Appl. Phys. **100**, 033902 (2006).

[160] S. Bance, T. Schrefl, G. Hrkac, D. Suess, C. Brownlie. S. McVitie, J. N. Chapman and D. A. Allwood, IEEE Trans. Magn. **42**, 2966 (2006).

[161] M. Hara, J. Shibata, T. Kimura and Y. Otani, Appl. Phys. Lett. **89**, 192504 (2006).

[162] Y. B. Xu, C. A. F. Vaz, A. Hirohata, C. C. Yao, W. Y. Lee, J. A. C. Bland, F. Rousseaux, E. Cambril and H. Launois, J. Appl. Phys. **85**, 6178 (1999).

[163] A. O. Adeyeye, J. A. C. Bland and C. Daboo, Appl. Phys. Lett. **70**, 3164 (1997).

[164] T. Jourdan, F. Lançon and A. Marty, Phys. Rev. B **75**, 094422 (2007).

[165] A. Aharoni, J. Appl. Phys. **58**, 2677 (1985).

[166] D. I. Paul, Phys. Lett. **64**, 485 (1978).

[167] X. Chen and P. Gaunt, J. Appl. Phys. **67**, 4592 (1990).

[168] J. A. Jatau and E. Della Torre, J. Appl. Phys. **73**, 6829 (1993).

[169] M. Kersten, Z. Phys. **124**, 714 (1948).

[170] M. Kläui, C. A. F. Vaz, W. Wernsdorfer, E. Bauer, S. Cherifi, S. Heun, A. Locatelli, G. Faini, E. Cambril, L. J. Heyderman and J. A. C. Bland, Physica B **343**, 343 (2004).

[171] T. M. Maffitt, J. K. DeBrosse, J. A. Gabric, E. T. Gow, M. C. Lamorey, J. S. Parenteau, D. R. Willmott, M. A. Wood and W. J. Gallagher, IBM, J. Res. & Dev. **50**, 25 (2006).

[172] S. H. Florez, C. Krafft and R. D. Gomez, J. Appl. Phys. **97**, 10C705 (2005).

[173] D. Atkinson, D. A. Allwood, C. C. Faulkner, G. Xiong, M. D. Cooke and R. P. Cowburn, IEEE Trans. Magn. **39**, 2663 (2003).

[174] K. Shigeto, T. Shinjo and T. Ono, Appl. Phys. Lett. **75**, 2815 (1999).

[175] C. C. Faulkner, D. A. Allwood, M. D. Cooke, G. Xiong, D. Atkinson and R. P. Cowburn, IEEE Trans. Magn. **39**, 2860 (2003).

[176] D. A. Allwood, G. Xiong and R. P. Cowburn, Appl. Phys. Lett. **85**, 2848 (2004).

[177] L. Thomas, C. Rettner, M. Hayashi, M. G. Samant, S. S. P. Parkin, A. Doran and A. Scholl, Appl. Phys. Lett. **87**, 262501 (2005).

[178] W. F. Egelhoff, Jr., P. J. Chen, C. J. Powell, M. D. Stiles, R. D. McMichael, J. H. Judy, K. Takano and A. E. Berkowitz, J. Appl. Phys. **82**, 6142 (1997).

[179] J. J. Sun, K. Shimazawa, N. Kasahara, K. Sato, T. Kagami, S. Saruki, S. Araki and M. Matsuzaki, J. Appl. Phys. **89**, 6653 (2001).

[180] W. F. Egelhoff, Jr., R. D. McMichael, C. L. Dennis, M. D. Stiles, A. J. Shapiro, B. B. Maranville and C. J. Powell, IEEE Trans. Magn. **42**, 2664 (2006).

[181] T. Dimopoulos, C. Tiusan, Y. Henry, V. da Costa, K. Ounadjela and H. A. M. van den Berg, J. Magn. Magn. Mat. **242-245**, 512 (2002).

[182] N. Wiese, T. Dimopoulos, M. Rührig, J. Wecker, H. Brückl and G. Reiss, Appl. Phys. Lett. **85**, 2020 (2004).

[183] F. W. M. Vanhelmont and H. Boeve, IEEE Trans. Magn. **40**, 2293 (2004).

[184] M. MacKenzie, J. N. Chapman, S. Cardoso, H. Li, R. Ferreira and P. P. Freitas, J. Phys. D: Appl. Phys. **38**, 1869 (2005).

[185] K. –M. H. Lenssen, D. J. Adelerhof, H. J. Gassen, A. E. T. Kuiper, G. H. J. Somers, J. B. A. D. van Zon, Sensors & Actuators, **A85**, 1 (2000).

[186] J. P. King, J. N. Chapman, M. F. Gillies and J. C. S. Kools, J. Phys. D: Appl. Phys. **34**, 528 (2001).

[187] A. Gentils, J. N. Chapman, G. Xiong and R. P. Cowburn, J. Appl. Phys. **98**, 053905 (2005).

[188] C. Tiusan, T. Dimopoulos. K. Ounadjela, M. Hehn, H. A. M. van den Berg, V. da Costa and Y. Henry, Phys. Rev. B, **61**, 580 (2000).

[189] P. Gogol, J. N. Chapman, M. F. Gillies and F. W. M. Vanhelmont, J. Appl. Phys. **92**, 1458 (2002).

[190] C. K. Lim, J. N. Chapman, M. Rahman, A. B. Johnston and D. O. O’Donnell, J. Appl. Phys. **95**, 1510 (2004).

[191] M. F. Gillies, J. N. Chapman and J. C. S. Kools, J. Appl. Phys. **78**, 5554 (1995).

[192] H. Hoffmann, J. Appl. Phys. **35**, 1790 (1964).

[193] K. J. Harte, J. Appl. Phys. **39**, 1503 (1968).

[194] C. Tiusan, T. Dimopoulos, L. Buda. V. da Costa. K. Ounadjela, M. Hehn and H. A. M. van den Berg, J. Appl. Phys. **89**, 6811 (2001).

[195] H. Brückl, J. Schmalhonst, H. Boeve, G. Gieres and J. Wecker, J. Appl. Phys. **91**, 7029 (2002).

[196] H. Boeve, L. Esparbe, G. Gieres, L. Bär, J. Wecker and H. Brückl, J. Appl. Phys. **91**, 7962 (2002).

[197] L. J. Heyderman, J. N. Chapman and S. S. P. Parkin, J. Appl. Phys. **76**, 6613 (1994).

[198] L. J. Heyderman, J. N. Chapman and S. S. P. Parkin, J. Phys. D: Appl. Phys. **27**, 881 (1994).

[199] J. N. Chapman, M. F. Gillies and P. P. Freitas, J. Appl. Phys. **79**, 6452 (1996).

[200] H. S. Cho, C. Hou, M. Sun and H. Fujiwara, J. Appl. Phys. **85**, 5160 (1999).

[201] K. Knowles, Indexing Diffraction Patterns, Dissemination of IT for the Promotion of Materials Science (DoITPoMS), University of Cambridge.

[202] M. MacKenzie, J. N. Chapman, S. Cardoso, M. Rickart, P. Diaz and P. P. Freitas, Inst. Phys. Conf. Ser. **26**, 169 (2006).